The University of Sheffield

Synthesis of new oxyfluoride phases, a possible new family of fluoro-LISICON Li^+ conductors

A thesis submitted for the degree of Doctor of Philosophy

Xiaoyuan Zhu

Supervisor: Prof. Anthony R. West

Department of Material Science and Engineering

Feb 2023

Acknowledgments

I would like to take this opportunity to express my heartfelt gratitude to my supervisor, Professor Anthony R. West, for his unwavering support, encouragement, and help throughout my master's degree and Ph.D. research. His experience and creative thinking offered me valuable feedback and suggestions that not only helped me shape and refine my ideas but also showed me how to become a scientist. I am incredibly grateful for his mentorship.

I would like to thank the technician staff in our research group and department for their kind help on my experiments, especially Dr. Dawei Wang and Dr. Ge Wang for their contributions to synthesis and characterization techniques, Dr. Linhao Li for impedance measurement and analysis, and Dr. Nik Reeves-Mclaren, Dr. Robert D. Moorehead, and Dr. Lewis Owen for their work on X-ray diffraction testing and analysis.

Warm thanks to all members of our functional ceramics group, former and present. I enjoyed five years of study in Sheffield with you.

My deepest thanks to my family and friends for your unwavering love, encouragement, and care.

Abstract

Lithium ion conducting solid electrolytes are of great potential interests for possible all solid state lithium battery applications. Several families of materials are being considered including LISICONs, garnets and argyrodite. This thesis focuses on the synthesis and characterisation of new oxyfluoride materials in the LISICON family following the recent report of high-lithium ion conductivity in Li_5SiO_4F.

Studies on Li_5SiO_4F have given four new sets of results. (i) Samples heated for extended times show evidence of Li_2O loss in the electrical property data with the appearance of a lithium-deficient grain boundary phase. (ii)The equivalent circuit analysis of high frequency impedance data shows contribution of a dipole reorientation effect to ac conductivity. (iii) Attempts to dope Li_5SiO_4F with a range of di-, tri-, tetra- and penta-valent cations yielded a large number of new, previously unreported oxyfluoride phases that appear to belong to the LISICON family. (iv) The detailed structure of the two polymorphs of Li_5SiO_4F is not known, but the X-ray diffraction pattern of the low temperature, α-polymorph has a very strong subcell with hexagonal symmetry that appears to be closely related to the ZnO structure. This is the first example of a tetrahedral, LISICON-based structure with a hexagonal subcell that exhibits complete disorder of both cation and anion positions.

A detailed study on the compositions in the ternary system: Li_2O-SiO_2-LiF found four new phases in addition to previously reported Li_5SiO_4F. These are: Phase B, γ-Phase B, Phase T and Phase N. Phase B, with approximate stoichiometry Li_2O:SiO_2:LiF=47:28:25, also has a ZnO-like hexagonal subcell and a modest ionic conductivity of ~5.6×10^{-8} Scm^{-1} at 100 °C. The high temperature polymorph of Phase B, labelled γ-Phase B formed over a wide solid solution range. γ-Phase B has an orthorhombic subcell with doubled volume that is clearly derived from the ZnO-like hexagonal subcell of Phase B. Nevertheless, the supercell structures of both Phase B and γ-Phase B are still unknown. γ-Phase B had an ionic conductivity of ~1.1×10^{-6} Scm^{-1} at 100 °C. Phases T and N had similar composition to Li_5SiO_4F but significantly different XRD

patterns and electrical properties, the desired composition for single Phase N had not been found. Phase T showed a poor ionic conductivity similar to that of Li_4SiO_4.

A preliminary survey of the Li_3PO_4-Li_4SiO_4-LiF system found three possible new phases labelled Phase S, γ-Phase S and Phase A. Phase S was also indexed on a ZnO-like hexagonal subcell. γ-Phase S is closely related to Phase S but it is probably thermodynamically metastable and quickly decomposes/transforms to Phase A. Impedance results showed that Phase S and Phase A have only poor ionic conductivity similar to that of bulk Li_4SiO_4; γ-phase S shows an ionic conductivity which is approximately 2 orders of magnitude lower than that of γ-Li_5SiO_4F. The preliminary phase diagram study of this system also showed evidence of a significant range of F^- doped Li_3PO_4-Li_4SiO_4 solid solution. The substitution mechanism is not known for certain, but may involve a novel mechanism with replacement of $(PO_4)^{3-}$ by $(LiF_4)^{3-}$ tetrahedra.

The various new phases reported in this study, which include Phase S, γ-Phase S, Phase A, Phase B, γ-Phase B, Phase T and Phase N, and Li_5SiO_4F may all belong to a new oxyfluoride family which have subcell structures derived from hexagonal ZnO, leading to a possible new family of fluoro-LISICON Li^+ ion conductors. Phase S, Phase B and α-Li_5SiO_4F were categorised as belonging to the β-structure family, while γ-Phase S, Phase A, γ-Phase B, Phase T, Phase N and γ -Li_5SiO_4F belong to the γ-structure family. The β family would have cations only in one set of tetrahedral sites, T_+, whereas in γ family, both of the tetrahedral sites, T_- and T_+, are partially occupied. All of these structure have a cation:anion ratio greater than the 1:1 ratio in ZnO. This mains that the structures also contain extra Li^+, probably in interstitial sites, and this may be the reason for the observed high level of Li^+ ion conductivity. We do not know if the O^{2-}, F^- distribution is random. However, the stoichiometry of Li_5SiO_4F suggests that the O, F arrangement is ordered and in particular, this phase may be regarded as containing $(SiO_4F)^{5-}$ pentagonal bipyramids instead of the more common SiO_4 tetrahedra.

Content

Chapter 1. Literature Review

1.1. Lithium ion battery and its components

Lithium ion batteries with their widespread applications as the reliable power source for different devices and facilities, stationary energy storage and promising alternative to petrol/diesel derived vehicles, are indispensable in current life [1-2]. The Nobel Prize in Chemistry 2019 was awarded jointly to John B. Goodenough, M. Stanley Whittingham and Akira Yoshino for their extraordinary contribution to the development of lithium ion batteries [3]. The early study by Goodenough in 1970s on $Na_{1+x}Zr_2Si_xP_{3-x}O_{12}$ electrolyte, which was demonstrated to have a framework structure and support fast sodium ion conductivity, was the first representative NASICON (NA Super Ionic CONductor) material [4]. The first rechargeable lithium ion battery, which consisted of a $LiCoO_2$ cathode with a graphitic-carbon anode, was made by Yoshino, then firstly commercialised by Sony to power the portable phone in early 1990s [4]. As shown in Fig 1.1, there are 3 primary components in a lithium battery, including an anode, a cathode and an electrolyte [2].

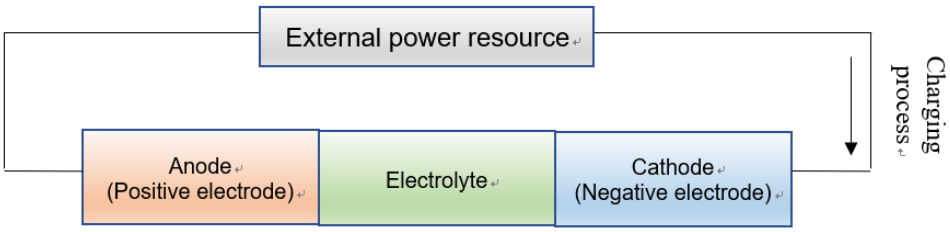

Fig 1.1. The simplified construction of a lithium battery during charging

Adapted from Reference [19].

Anode

Generally, anode materials should simultaneously have a considerable specific capacity and a low electrochemical potential to reach an optimized overall cell voltage. The early anode candidate was lithium metal, but its commercialization was limited by the formation of lithium dendrites during cycling [5]. Carbon-based materials were widely used in commercial lithium batteries with continuous optimisation in recent years. In specific, carbon based materials generally have low cost, easy manufacture and multiple forms. Nanocarbon materials have advantages in conductivity and cycle stability. The 1D carbon materials, such as carbon nanotubes (CNT), carbon nanorods and carbon nanowires, have directional ion transport but

are limited by significant charging loss in early cycles. The 2D carbon nanomaterials, represent by graphene, have a high specific surface area and excellent in-plane electron transport, however, the poor ion transport between adjacent sheets and significant sheet agglomeration limits the overall performance [6]. Transition metal oxides (TMO), such as iron-based oxides: hematite (Fe_2O_3) and magnetite (Fe_3O_4), Co-based oxides, Mn-based oxides and TiO_2, are promising anode candidates because of their promising theoretical specific capacity, wide operating voltage and stable cycle performance [6-7]. The disadvantages of TMO include relatively low capacity compared to silicon and graphite, large volume variation during charging-discharging cycles which may lead to further mechanical failure and degradation of the battery, high costs and environmental concerns in manufacturing [7]. Metal-organic frameworks (MOFs), which are a family of porous materials consisting of metal ions or clusters connected by organic ligands, have drawn a lot of research attention in recent years. MOFs and derivatives have high porosity from the porous structure or single/multi-shell hollow structure. Common MOFs include Materials of Institute Lavoisier series (MIL), Zeolitic Imidazolate Framework series (ZIF) and Prussian Blue analogs series (PB). Some notable features of MOF anodes include high specific surface area, good chemical and thermal stability and tunable pore size and shape. However, MOFs are still in the early stage of research primarily on clarifying the relationship between structure and energy storage performance. There are still challenges including low conductivity, poor lithium-ion diffusion and stability issues [6].

Cathode

Cathode materials generally are intercalation host structures that have empty channels or ordered layers to accept Li ions and mixed-valence species to accept and release electrons during charging and discharging processes. The first materials were layered chalcogenide structures, TiS_2 [8]. Some common cathode materials include layered transition metal oxides such as $LiCoO_2$, $LiNiO_2$ and $LiMnO_2$, spinel cathode materials like lithium manganese oxide ($LiMn_2O_4$) and olivine type material such as lithium iron phosphate ($LiFePO_4$) [9-10]. The layered transition metal oxides are capable of high voltages >4.5 V and have notable specific capacities [9]. There are still challenges for layered transition metals oxides as cathode materials such as large voltage decay and irreversible capacity loss. Specifically, $LiCoO_2$ only exhibits ~50% of its theoretical capacity due to the over-delithiation into $Li_{0.5}CoO_2$, [10]. The environmental concern on the toxicity of Co and its high costs are undesirable for industry [9]. $LiMn_2O_4$ shows better cycle performance and less cost compared to $LiCoO_2$. The main

challenge for $LiMn_2O_4$ is the capacity fading in contact with electrolyte at ~55 °C due to phase transitions. Possible solutions include (a) a protective coating, which reduces its direct contact with electrolyte; doping with Al, Co, Cr, or Ni, which can improve cyclability but reduce the initial capacity [9]. Olivine $LiFePO_4$ has outstanding thermal stability and cycle performance compared to layered oxides. However, its relatively low energy density limits its applications in portable electronic devices [9].

1.2. Electrolyte

The main requirements of an electrolyte in a lithium-ion battery include high ionic conductivity, stability in contact with electrodes materials, wide electrochemical/temperature window and negligible electronic conductivity to avoid potential short circuit.

1.2.1. Non-aqueous electrolytes

Lithium ion batteries in the current commercial marketplace primarily use non-aqueous electrolytes, in which lithium hexafluorophosphate ($LiPF_6$) and electrolyte additives are dissolved in an organic solvent [11]. The ideal solvent should have high dielectric permittivity, which allows complete dissolution of the conducting salt; low viscosity, which facilitates ion transport; reliable stability in contact with the electrodes [11]. The organic carbonate solvents are usually a mixture of both cyclic and non-cyclic solvents. Specifically, the common cyclic solvent is ethylene carbonate (EC) with high dielectric permittivity, while the non-cyclic solvent with low viscosity is acyclic carbonate or carboxylic esters including dimethyl carbonate (DMC), diethyl carbonate (DEC), and ethyl methyl carbonate (EMC) [12]. Small amounts of electrolyte additives are necessary to maintain stable bulk properties of the electrolyte [12]. The commercialised non-aqueous electrolytes have a high ionic conductivity of 10^{-3}-10^{-2} S/cm at ambient temperature, a wide potential window of 0−5 V vs Li/Li^+ and reliability for cell operations normally at -30-60 °C [11]. However, there is severe concern about the poor intrinsic safety of traditional non-aqueous electrolytes, particularly at high operating temperatures. The main challenges include flammable organics in the electrolyte and the formation of lithium dendrites during cycling. Specifically, the volatility and flammability of non-cyclic carbonate solvents in non-aqueous electrolytes can possibly lead to serious accident by improper operations. The conducting salt, $LiPF_6$, may undergo hydrolysis and decomposition during charging-discharging cycles, resulting in toxic organophosphates and

corrosive hydrogen fluoride [12]. Furthermore, the formation of lithium dendrite may continuously consume the electrolyte, ending up with the depletion of available lithium and potential risk of short circuit. Recent research determined that the deposition of dendritic lithium can be attributed to the lack of Li transport on the deposited Li surface [13].

1.2.2. Solid state electrolytes

As a promising alternative to non-aqueous electrolytes, solid state electrolytes have some outstanding features: (a) preventing the formation of lithium dendrites with no hidden risk [13]; (b) better thermal stability and safety by completely avoid the use of flammable organic liquid; (c) simplified battery packaging which offers significantly reduced dead weight and thus increased energy density; (d) better electrochemical stability in compatibility with higher potential cathode materials; and (e) excellent mechanical properties [14]. There are several necessary requirements for solid state electrolytes to be widely commercialised: relevantly high ionic conductivity, $>10^{-3}$ Scm^{-1} at room temperature; negligible electronic conductivity with a high ionic transference number; and wide electrochemical stability windows [14].

1.3. Some representative electrolyte families

There has been extensive research attention on solid state electrolyte materials in recent years. Some electrolyte families, which include LISICON, NASICON, argyrodite, garnet, perovskite, anti-perovskite, LiPON and Li_3N, with representative materials are briefly reviewed primarily in terms of their crystal structure and electronic properties.

1.3.1. LISICON (LIthium Super Ionic CONductors) and thio-LISICON

The family of LISICON materials are based on a crystal structure similar to orthorhombic γ-Li_3PO_4. There is distorted hexagonal close packing (HCP) of O^{2-} with cations, Li^+ and P^{5+}, distributed in different tetrahedral sites. Lithium ions can diffuse between the LiO_4 tetrahedral and interstitial sites in PO_4 network [15], as shown in Fig 1.2.

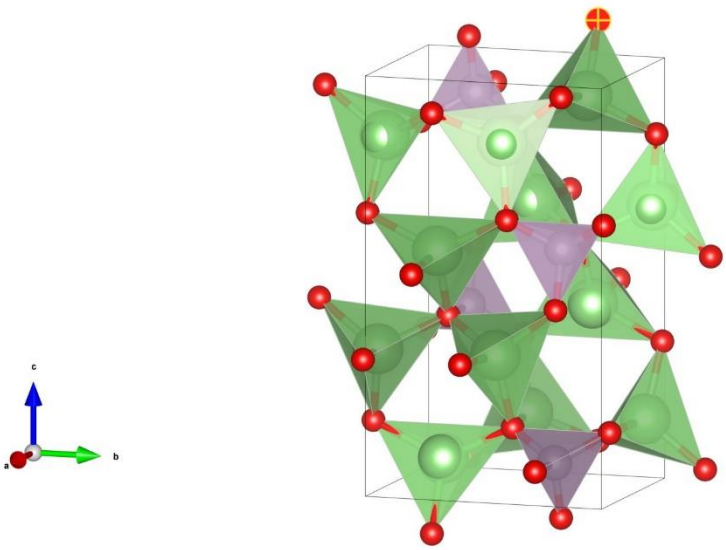

Fig 1.2. Crystal structure of γ-Li_3PO_4, produced by VESTA software [16], Li^+ in green, P^{5+} in purple, O^{2-} in red.

The first material of this kind reported was $Li_{14}Zn(GeO_4)_4$ which is a member of $Li_{2+2x}Zn_{1-x}GeO_4$ solid solution. Its ionic conductivity is highly temperature dependent, with a modest ionic conductivity of ~10^{-7} Scm^{-1} at ambient temperature and 1.25×10^{-1} Scm^{-1} at 573 K. The possible mechanism behind that is the formation of defect complexes at low temperatures which impede the mobile lithium ions [17].

A group of γ-Li_3PO_4 type solid solutions, $Li_{3+x}Y_{1-x}X_xO_4$ (X=Si, Ge, Ti and Y=P, As, V, Cr), show higher ionic conductivities with intermediate compositions rather than the end members. The highest conductivity at room temperature is 4×10^{-5} Scm^{-1} obtained in $Li_{3.6}Ge_{0.6}V_{0.4}O_4$ [17]. The solid solution between Li_3PO_4 and Li_4SiO_4 was well investigated and is discussed in detail in Chapter 5. The aliovalent substitution of P^{5+} by Si^{4+} let the excess lithium ions occupy interstitial sites instead of the tetrahedral sites, resulting in a reduced distance between adjacent lithium ions and a high conductivity of 3×10^{-6} S/cm in $Li_{3.5}Si_{0.5}P_{0.5}O_4$ [15].

More recent research is focused on thio-LISICON materials, in which all O^{2-} ions are substituted by S^{2-}, with a general formula, $Li_{4-x}X_{1-y}Y_yS_4$ (X=Ge, Si and Y=P, Al, Zn, Ga). The ionic conduction of thio-LISICON materials is reported to primarily dependent on the radius

and polarisability of the constituent ions. The substitution of O^{2-} by S^{2-} significantly reduces the interactions between Li^+ in the sublattice resulting in increased concentration of mobile Li^+, which explains the higher conductivity of thio-LISICONs compared to their oxide analogues [18]. The $Li_{10}MP_2S_{12}$ (M=Si, Ge, or Sn) and $Li_{11}Si_2PS_{12}$ family has the highest lithium-ion conductivities in the series. $Li_{10}GeP_2S_{12}$ (LGPS) has an ionic conductivity of ~1.2×10^{-2} Scm^{-1} at ambient temperature. LGPS had a wide potential window of 5 V vs. Li/Li^+ and successfully ran 8 charging-discharging cycles with a capacity of 120 $mAhg^{-1}$ in a battery cell consisting of $LiNbO_3$-coated $LiCoO_2$ cathode, lithium metal anode and LGPS electrolyte [19]. $Li_{10}GeP_2S_{12}$ has a complex 3D structure built of $(Ge_{0.5}P_{0.5})S_4$ tetrahedra, PS_4 tetrahedra, LiS_4 tetrahedra and LiS_6 octahedra, Fig 1.3 (a). The adjacent $(Ge_{0.5}P_{0.5})S_4$ tetrahedra and LiS_6 octahedra form one-dimensional chains along c-axis by sharing a common edge and PS_4 tetrahedra are connected by a common corner with these chains, Fig 1.3 (b). Neutron diffraction research suggested that the thermal vibration of lithium ions inside LiS_4 tetrahedra is extremely anisotropic, while the displacements of these lithium-ions are mainly located either between two 16h sites, or between 16h and 8f sites, indicating the existence of conduction pathways, Fig 1.3 (c),which account for its high conductivity [19]. Main challenges for manufacturing LGPS include: (a) the sensitivity to moisture, thus the synthesis of LGPS in laboratory normally requires an Ar atmosphere in glove boxes to avoid the formation of H_2S [15]; (b) high cost of Ge, for which other research attempted to replace Ge^{4+} with Si^{4+} or Sn^{4+}, or simultaneously replace partial S^{2-} by halogens (Cl^-, Br^-, I^-). The highest conductivity in these doped materials reported with ~2.5×10^{-2} Scm^{-1} in $Li_{9.54}Si_{1.74}P_{1.44}S_{11.7}Cl_{0.3}$ [20] is slightly lower than that of parent LGPS [18]; (c) LGPS is reported to be unstable in contact with some electrodes which limited its application. For instance, when LGPS is in contact with Li, there is reduction by lithium at low voltage and decomposition due to extraction of Li at high voltage [21].

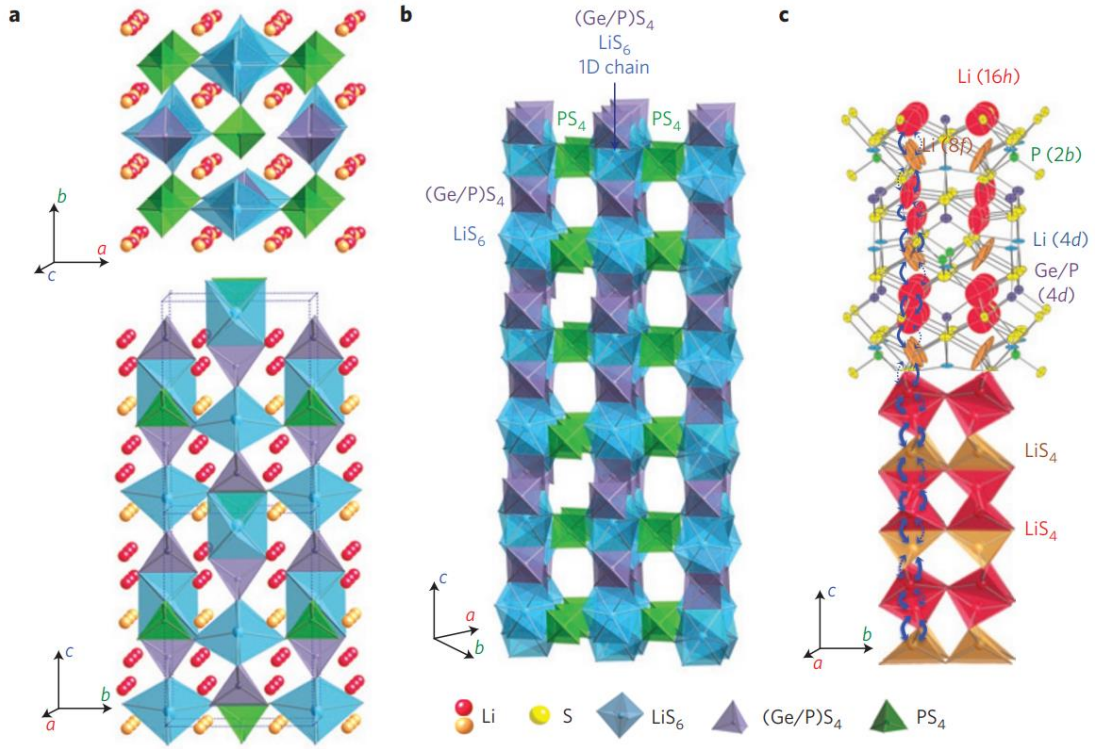

Fig 1.3. (a) Crystal structure of $Li_{10}GeP_2S_{12}$, (b) Framework structure of $Li_{10}GeP_2S_{12}$, (c) Zigzag Conduction pathways of lithium ions along the c axis in $Li_{10}GeP_2S_{12}$. Copied from Reference [19], with permission through Springer Nature and Copyright Clearance Center, the license number is 5700740389023.

1.3.2. NASICON (NA Super Ionic CONductors)

NASICON type material with the general formula, $NaM_2(PO_4)_3$, in which M can be a wide range of cations and P can be partially replaced, had its first material, $Na_{1+x}Zr_2Si_xP_{3-x}O_{12}$, reported in 1976. The end-member $NaZr_2(PO_4)_3$ only has a poor ionic conductivity. Enhancement is achieved by aliovalent doping of P in $Na_{1+x}Zr_2Si_xP_{3-x}O_{12}$. When x=2.0, the overall ionic conductivity increased to 2×10^{-1} Scm^{-1} at 300 °C [22]. NASICON type materials, $(Na/Li)_{1+x}X^{4+}_{2-x}Y^{3+}_x(PO_4)_3$ (X=Ti, Ge, Sn, Hf, or Zr and Y= Cr, Al, Ga, Sc, Y, In, or La), commonly has a rhombohedral unit cell built by corner sharing PO_4 tetrahedra and isolated XO_6 octahedra, as shown in Fig 1.4. Sodium (lithium) ions occupy the 6-fold coordinated sites between two XO_6 octahedra, and/or the 8-fold coordinated sites located between two columns of XO_6 octahedra. The lithium ion conduction depends on the hopping of lithium ions between available sites and occupancies of in-site lithium ions. The size of the lithium pathway and vacancies at the intersection of the pathway are crucial for ionic conductivity. The choice of

X^{4+} cation ion greatly influences the size of the lithium pathway, for example, in $LiXY(PO_4)_3$, replacement of Ge^{4+} (0.53 Å) by Hf^{4+} (0.71 Å) achieved a conductivity that was 4 orders of magnitude higher [15]. The aliovalent doping of X^{4+} by Y^{3+} can also result in an increased ionic conductivity due to higher mobile lithium concentration; for instance, $Li_{1.3}Al_{0.3}Ti_{1.7}(PO_4)_3$ has a conductivity of ~3×10^{-3} Scm^{-1} at room temperature [23].

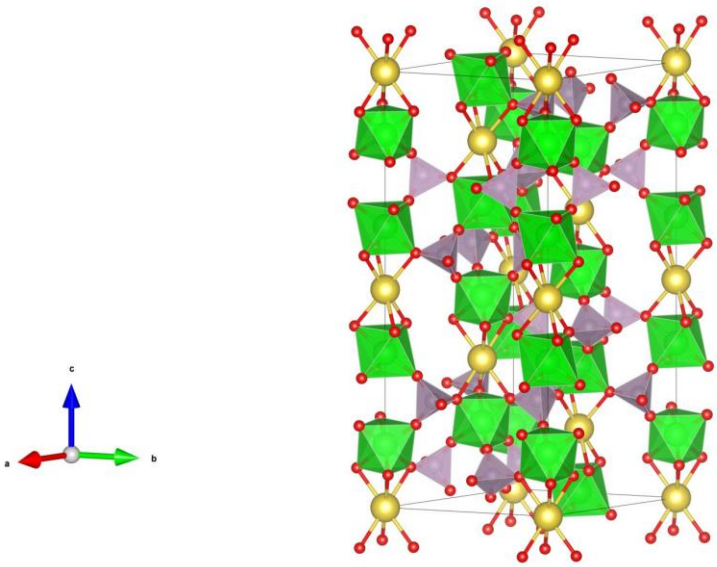

Fig 1.4. Crystal structure of $NaZr_2(PO_4)_3$, produced by VESTA software [16], Na^+ in yellow, Zr^{4+} in green, P^{5+} in purple, O^{2-} in red, there are corner sharing ZrO_6 octahedra (green) and PO_4 tetrahedra (purple)

NASICON type lithium ion electrolytes $LiX_2(PO_4)_3$ (X=Ti, Ge, Sn, Hf, or Zr) are prepared by complete substitution of sodium ions by lithium ions in $NaX_2(PO_4)_3$. For instance, $LiZr_2(PO_4)_3$ has two polymorphs: a high temperature phase prepared at 1200 °C with a modest ionic conductivity of 3.3×10^{-6} S/cm at room temperature; and a low temperature phase prepared at 900°C with a poor ionic conductivity of 10^{-10} S/cm at room temperature [14]. $Li_3Sc_2(PO_4)_3$ prepared by ball-milling followed by high temperature sintering has an ionic conductivity of 3×10^{-6} Scm^{-1} at 25°C, which can be further improved by partial Cr^{3+} or Al^{3+} doping, with 1.5×10^{-4} Scm^{-1} at 25°C in $Li_3Sc_{1.6}Al_{0.4}(PO_4)_3$ [17]. $LiTi_2(PO_4)_3$ has a good conductivity and it can form solid solution with Li_3PO_4, or Li_3BO_3. The highest ionic conductivity, with 3×10^{-4} Scm^{-1} at ambient temperature, is obtained in $LiTi_2(PO_4)_3$- Li_3BO_3 [17].

$LiTi_2(PO_4)_3$ can be doped by a series of trivalent cations, $Li_{1+x}Ti_{2-x}M_x(PO_4)_3$ (M=Al, Cr, Ga, Fe, In, or Sc) [14,15,19]. It shows high ionic conductivity when x<0.3, in which there is a high lithium concentration. Besides the extra ionic conductivity offered by the interstitial lithium ions, its high conductivity is mainly due to the densification of electrolytes with reduced porosity. The highest porosity close to undoped $LiTi_2(PO_4)_3$ is observed in $M=Cr^{3+}$, which was attributed to the formation of glassy secondary phase at grain boundaries [24]. The highest ionic conductivity with ~7×10^{-4} Scm^{-1} is in $M=Al^{3+}$, Sc^{3+}. However, the Ti^{4+} in $Li_{1+x}Ti_{2-x}Al_x(PO_4)_3$ (LATP) is reported to possibly be reduced at low potentials, which make LATP incompatible with some anode materials; or in contact with lithium or C_6Li^+, which may induce electronic conductivity resulting in severe short circuit [25]. The glass-ceramics LAGP electrolyte, $Li_{1.5}Al_{0.5}Ge_{1.5}(PO_4)_3$, prepared by melt-quench and recrystallisation has complex micro-superstructures and a high relative density. Its conductivity value, 4.0×10^{-4} Scm^{-1} at ambient temperature, can be increased further to 1.18×10^{-3} Scm^{-1} in $Li_{1.5}Al_{0.5}Ge_{1.5}(PO_4)_3$-$xLi_2O$ with x=0.05, in which additional Li_2O formed a secondary lithium-containing phase as the nucleating agent during crystallisation [26].

$Li_{1+x}Ti_{2-x}M'_x(PO_4)_3$ can form a glass-ceramic solid solution system of $2[Li_{1+x}Ti_2Si_xP_{3-x}O_{12}]$-$AlPO_4$. There is a continuous variation in its lattice parameters. Specifically, when x<0.1, lattice parameters increased with larger x, mainly due to partial replacement of P^{5+} by Si^{4+}; when 0.1<x<0.4, lattice parameters still increased with larger x, but this was mainly attributed to the substitution of Ti^{4+} by Al^{3+}; when x>0.4, there was no significant variations in the major conductive phase $[Li_{1+x}Ti_2Si_xP_{3-x}O_{12}]$, which may indicate a substitution limit. The highest ionic conductivity with 1.5×10^{-3} Scm^{-1} at ambient temperature is in $2[Li_{1.4}Ti_2Si_{0.4}P_{2.6}O_{12}]$-$AlPO_4$ (x=0.4) [27].

Other research attempted to replace M^{4+} with a higher-valence element $M^{''}$, $Li_{1-x}M_{2-x}M^{''}_x(PO_4)_3$ (M=Ti, Zr and $M^{''}$=Nb, Ta). $Li_{0.1}Ta_{0.9}Zr_{0.1}(PO_4)_3$ has a modest conductivity, 6×10^{-6} Scm^{-1} at room temperature, which is attributed to the massive grain boundaries which may restrict the mobile lithium ions [17]. $LiTiIn_{0.5}Ta_{0.5}(PO_4)_3$ has a conductivity 2.5×10^{-6} Scm^{-1} at room temperature, the variation in its ionic conductivity compared to $LiTi_2(PO_4)_3$ is believed

to be the high unit cell volume due to the larger size of substituted ions (In^{3+} and Ta^{5+}) to Ti^{4+} [28].

1.3.3. Lithium argyrodite

Lithium argyrodite, with general formula Li_6PS_5X (X = Cl, Br, I), shows a structure derived from Ag-argyrodite Ag_8GeS_6 [29]. It has a cubic unit cell with close packing of anions. Lithium ions are randomly located in the interstices between isolated PS_4 tetrahedron, as shown in Li_6PS_5Cl, Fig 1.5. The diffusion of lithium ions among the partially occupied sites constitutes the hexagonal cages, which connect to adjacent cages by the interstitial site around the halide ions in Li_6PS_5Cl and around the sulfur ions in Li_6PS_5I [15].

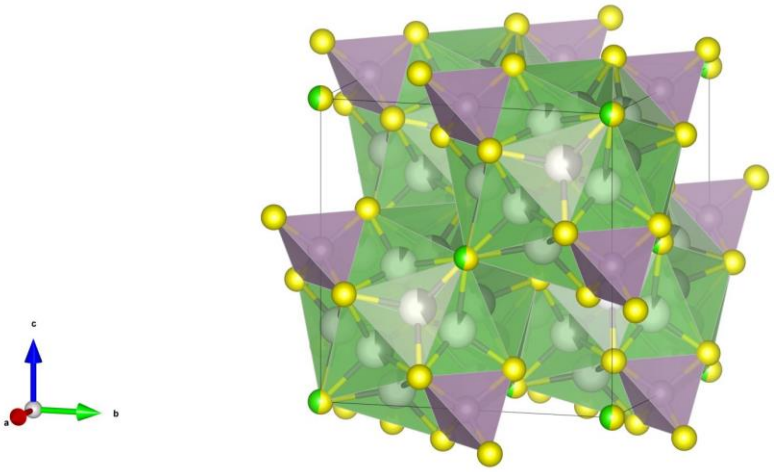

Fig 1.5. Crystal structure of Li_6PS_5Cl with isolated PS_4 tetrahedra (purple), produced by VESTA software [16], Li^+ in grey, P^{5+} in purple, S^{2-} in yellow, Cl^- in green.

The replacement of sulfur with halogen creates vacancies, leading to extra disorder S^{2-}/X^- sublattice which offers local Li-ion diffusion [30]. For instance, Cl^{-1} and Br^{-1} in Li_6PS_5X result in significant disordering of halogen ions, leading to the high ionic conductivity at ambient temperature of Li_6PS_5Cl, with ~1.8×10^{-3} Scm^{-1} and Li_6PS_5Br, with ~1.3×10^{-3} Scm^{-1} [29-30]. The relevantly poor conductivity of Li_6PS_5I, ~10^{-5} Scm^{-1} is attributed to the lack of sublattices inside its crystal structure [29]. Similar to the circumstances in thio-LISICONs, the substitution

of S^{2-} by O^{2-} in lithium argyrodite results in significantly reduced conductivity [15]. Lithium argyrodite Li_6PS_5X is reported to have a very wide electrochemical stability window of 0-7 V vs Li/Li^+ [15]. However, its widespread applications are restricted by exposure to the atmosphere, which is a common challenge for Sulphur-containing electrolytes [14].

1.3.4. Garnet

Garnet electrolytes are derived from the ideal garnet structure, $A_3B_2(SiO_4)_3$ (A=Ca, Mg and B= Al, Cr, Fe), in which cations A^{2+}, B^{3+} and Si^{4+} respectively located at the 8-, 6-, 4-coordinate sites in a cubic structure [15, 29]. Li-containing garnets $Li_xX_2Y_3O_{12}$ are derived from the parent structure of $Ca_3Al_2Si_3O_{12}$, which consists of two AlO_6 octahedra, three SiO_4 tetrahedral and three antiprismatic CaO_8 [31], as shown in Fig 1.6. The analogous Li containing garnet is $Li_3La_3Te_2O_{12}$, in which Li^+ completely replaces the tetrahedral Si^{4+} [31]. The poor conductivity of $Li_3La_3Te_2O_{12}$ was attributed to insufficient Li content. By doping with M^{5+} (M=Ta, Nb) ions, the extra lithium ions in $Li_5La_3M_2O_{12}$ randomly occupy both tetrahedral sites and disordered octahedral sites, resulting in an increased ionic conductivity at room temperature with ~10^{-6} Scm^{-1} in $Li_5La_3Ta_2O_{12}$ compared to 10^{-10} Scm^{-1} in $Li_3La_3Te_2O_{12}$ [32]. $Li_5La_3M_2O_{12}$ showed an activation energy of 0.43 eV in $Li_5La_3Ta_2O_{12}$ and 0.56 eV in $Li_5La_3Nb_2O_{12}$. Ta containing garnet was reported to be stable in contact with Li metal and moisture [18].

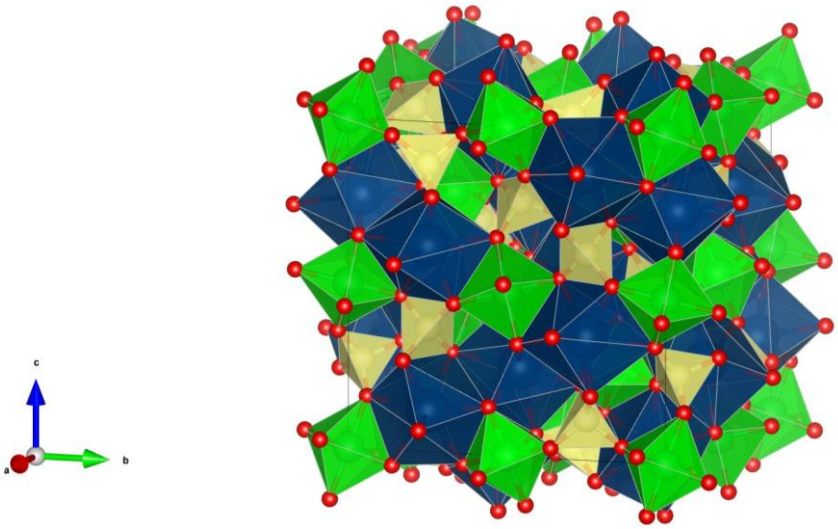

Fig 1.6. Crystal structure of $Ca_3Al_2Si_3O_{12}$ with AlO_6 octahedra (green), three SiO_4 (yellow) tetrahedral and three antiprismatic CaO_8 (navy blue), produced by VESTA software [16], Al^{3+} in green, Ca^{2+} in navy blue, Si^{4+} in yellow, O^{2-} in red.

Further doping attempts on $Li_5La_3M_2O_{12}$ (M=Ta, Nb) suggested two general mechanisms for increased ionic conductivity: (a) higher lithium concentration and/or (b) distribution of lithium ions in both octahedral and tetrahedral sites. Replacing La^{3+} in $Li_5La_3M_2O_{12}$ by divalent ions A^{2+}, $Li_6ALa_2M_2O_{12}$ (A= Mg, Ca, Sr, Ba), lead to increased conductivity of $Li_6BaLa_2Ta_2O_{12}$ with ~4×10^{-5} Scm^{-1} at 25 °C and an activation energy of 0.40 eV [18]. The better ionic conductivity on doping by alkaline earth ions A^{2+} is more due to mechanism (b) [31]. By replacing M^{5+} in $Li_5La_3M_2O_{12}$ by Zr^{4+}, $Li_7La_3Zr_2O_{12}$ (LLZO) was prepared, with a high ionic conductivity of ~3×10^{-4} Scm^{-1} at 25 °C and low activation energy of 0.3 eV in its cubic polymorph [15], as shown in Fig 1.7. The reasons behind its promising ionic conductivity include both mechanisms (a) and (b). Further doping of LLZO includes replacement of Zr^{4+} by aliovalent dopants (Y^{3+}, Sc^{3+}) and replacement of Li^+ by single dopant or co-dopants such as Al^{3+}+Ga^{3+} [14, 15]. The Y^{3+} doping of $Li_5La_3Nb_2O_{12}$ achieved a high ionic conductivity of 2.7×10^{-4} Scm^{-1} at 25 °C in $Li_{6.5}La_3Nb_{1.25}Y_{0.75}O_{12}$ [33], similar to that of LLZO.

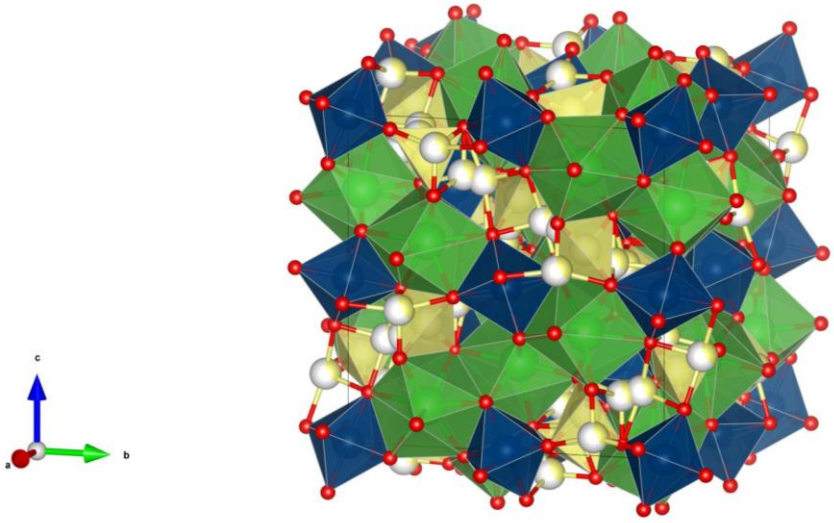

Fig 1.7. Crystal structure of $Li_7La_3Zr_2O_{12}$ with partial lithium as LiO_4 tetrahedra (yellow), 7-cordinated La^{3+} (green) and ZrO_6 octahedra (navy blue), produced by VESTA software [16], Li^+ in yellow, La^{3+} in green, Zr^{4+} in navy blue, O^{2-} in red.

$Li_7La_3Zr_2O_{12}$ (LLZO) has two polymorphs: a cubic structure, which shows random distribution of lithium ions and a tetragonal structure, in which lithium ions have ordered distributions with

fully occupied tetrahedral Li sites [33]. Undoped LLZO undergoes a reversible phase transition from tetragonal to cubic in dry atmosphere at 620 °C to 650 °C [14]. The cubic form has an ionic conductivity of 3×10^{-4} Scm^{-1} which is 2 orders of magnitude higher than that of the tetragonal form [33]. Consequently, it is important to stabilise the cubic phase at the operating temperatures, 0.9 %wt of Al was found to be efficient in stabilising cubic LLZO during solid state reactions [14]. The preparation of cubic LLZO requires completely dry atmosphere. LLZO sample synthesised at ~650 °C in moisture formed a defect cubic phase with decreased ionic conductivity, which may be attributed to either the direct insertion of H_2O into LLZO, or an exchange between H^+ and Li^+ [34]. Similarly, Ga-doped $Li_{7-3x}Ga_xLa_3Zr_2O_{12}$ prepared in the ambient atmosphere has a relative density which is 70 % lower than that of same composition prepared in dry O_2. Composition $Li_{6.4}Ga_{0.2}La_3Zr_2O_{12}$ prepared in ambient atmosphere has an ionic conductivity of 1.5×10^{-6} Scm^{-1} at 25 °C, which is significantly lower than that of same composition prepared in controlled atmosphere with ~3×10^{-3} Scm^{-1} at 25 °C [35].

1.3.5. Perovskite

Perovskite and related materials, with general formula ABO_3, are important soli state materials which have wide applications such as Tc superconductors, cathodes in solid fuel cells and ferroelectrics [17]. The perovskite lithium ion conductors have an ideal structure of a cubic unit cell, in which typically rare earth elements or alkaline earth elements are located in A sites at the corners, typically transition metal elements occupy B sites at the center and O^{2-} settle in the face-centre sites. The oxygen ions together with B-site ions build a corner-sharing BO_6 framework [15]. The first material of this kind reported is $Li_{0.5-3x}La_{0.5+x}TiO_3$ [17]. $Li_{0.5-3x}La_{0.5+x}TiO_3$ (LLTO) system show an increased ionic conductivity and lower activation energy with larger ionic radii of rare-earth element M^{3+} ($Sm^{3+} < Nd^{3+} < Pr^{3+} < La^{3+}$), in which $Li_{0.34}La_{0.56}TiO_3$ has the highest bulk conductivity in the series with ~10^{-3} Scm^{-1} at room temperature and a low activation energy of 0.34 eV [15]. However, the total ionic conductivity of LLTO is significantly lower, ~2×10^{-5} Scm^{-1}, which can be attributed to large grain boundary resistances [17]. The reason for high bulk conductivity of LLTO is believed to be the high concentration of A-site vacancies. The bottlenecks for lithium migration are formed by four TiO_6 octahedra, as shown in Fig 1.8, with simultaneous cation deficiency in A sites [17]. In addition, LLTO is not stable at voltages lower than 1.8 V vs Li/Li^+, by which LLTO is

incompatible with low potential anodes such as lithium metal. The low electrochemical stability was attributed to the reduction of Ti^{4+} at low voltages [14].

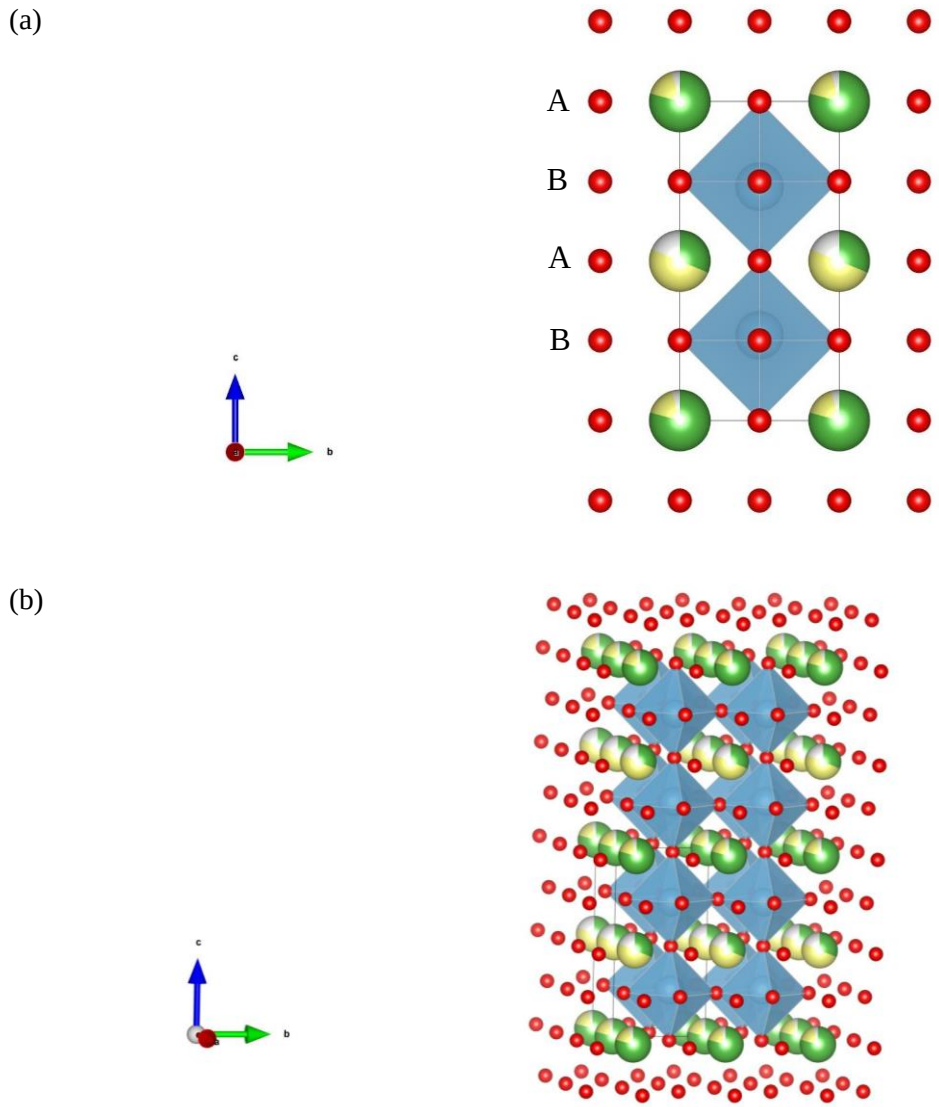

Fig 1.8. Crystal structure of $Li_{0.34}La_{0.56}TiO_3$ (LLTO) with TiO_6 octahedra (blue), produced by VESTA software [16], Li^+ in yellow, La^{3+} in green, Ti^{6+} in blue, O^{2-} in red (a) show the A/B sites alone a-axis while (b) show the lithium pathway formed by TiO_6 octahedra.

To address the incompatibility issue of LLTO, attempts to replace Ti^{4+} by isovalent dopants including Mn^{4+}, Sn^{4+}, Zr^{4+} and Ge^{4+} cannot reach a complete substitution of Ti^{4+}, but gives an increased ionic conductivity [15]. Further investigation reports another perovskite material with a general formula $Li_{2x-y}Sr_{1-x}Ta_yZr_{1-y}O_3$ (LSTZ). Composition $Li_{3/8}Sr_{7/16}Ta_{3/4}Zr_{1/4}O_3$ shows

the highest bulk ionic conductivity of 5×10^{-4} Scm^{-1} at 30 °C with a grain boundary conductivity of 1.33×10^{-4} Scm^{-1} at 30 °C. The bulk conductivity of LSTZ is one order of magnitude lower than that of LLTO, but its grain boundary conductivity is one order of magnitude higher than that of LLTO, resulting in a better total ionic conductivity. LSTZ is stable at voltage higher than 1 V vs Li/Li^+, making it suitable for a wider choice of anode materials [14]. By replacement of Zr by Hf in LSTZ, a similar perovskite structure $Li_{3/8}Sr_{7/16}Ta_{3/4}Hf_{1/4}O_3$ (LSTH) reach an ionic conductivity of 3.8×10^{-4} Scm^{-1} at 25 °C, with a wide stability window of 1.4-4.5 V vs Li/Li^+ [14].

1.3.6. anti-perovskite

Anti-perovskite electrolytes, LiRAPs, are based on a varied perovskite structure, $A^-B^{2-}X^+_3$. A site is located at dodecahedral center and occupied by halogens including F^-, Cl^-, Br^- and I^-, or a mixture of them. B site at the octahedral center is typically occupied by O^{2-}. X site at d vertices is filled by Li^+ [18]. One representative LiRAP is the solid solution system Li_3OCl-Li_3OBr. The two end-members, Li_3OCl and Li_3OBr, have an interstitial dumbbell structure which allows the hopping of lithium ions with low energy barrier, as illustrated in Fig 1.9 [14 36]. Li_3OCl shows a distorted structure and a higher ionic conductivity of 8.5×10^{-4} Scm^{-1} at 25 °C compared to that of Li_3OBr. Li_3OCl sample with high ionic conductivity requires annealing at 250 °C in the vacuum. The Li_3OCl sample synthesised without annealing only show an ionic conductivity of ~10^{-7} Scm^{-1} at 25 °C. The annealing treatment may lead to several changes on Li_3OCl including octahedral tilting, grain boundary variations and vacancy migration [37]. The middle composition, $Li_3OCl_{0.5}Br_{0.5}$, shows an ionic conductivity of 1.94×10^{-3} Scm^{-1} at 25 °C which is higher than those of the two end members. The limited ionic conductivity in Li_3OBr is attributed to the small Li-ion hopping interstitial space, while that in Li_3OCl is attributed to the structural distortion [14]. First principle calculations suggest that a perfect anti-perovskite structure may not show a good ionic conductivity due to the lack of pathways for lithium diffusion, thus introducing defects into the anti-perovskite electrolytes may be important to reach a better ionic conductivity [38].

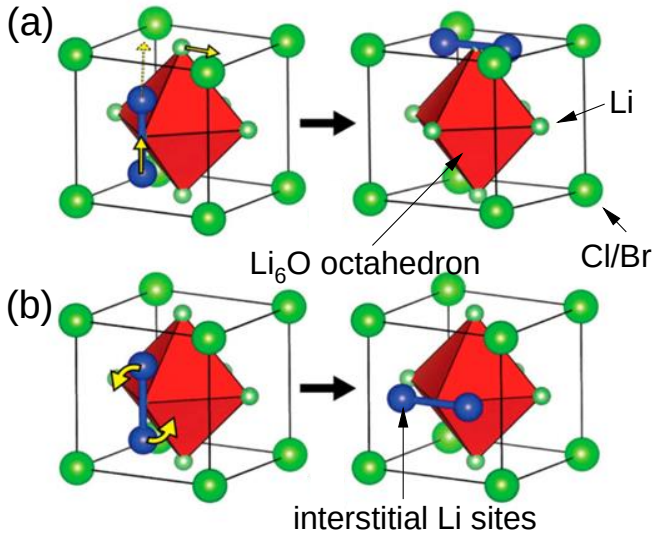

Fig 1.9. The dumbbell motion in Li_3OCl and Li_3OBr: (a) Coordinated perpendicular dumbbell motion, and (b) in-plane dumbbell rotation. Adapted from reference [36]

Doping attempts of anti-perovskite Li_3OCl include partial replacement of Li, or substitution of halogen on the A site. For instance, $Li_{2.9}Ba_{0.05}OCl$ has an increased ionic conductivity of 2.5×10^{-2} Scm^{-1} at 25 °C compared to that of bulk Li_3OCl [18]. $Li_3OCl_{0.5}(BH_4)_{0.5}$ and Li_3OBH_4, in which Cl^- is replaced by cluster anions BH_4, show an ionic conductivity at ambient temperature of 2.1×10^{-4} Scm^{-1} and $\sim10^{-4}$ Scm^{-1}, respectively [14]. Another doping of Li_3OCl by cluster anions, Li_3SBF_4, shows a promising ionic conductivity of 1.9×10^{-2} Scm^{-1} at 25 °C with a low activation energy of 0.176 eV [39].

Li_2OHCl in the LiOH-LiCl solid solution system is reported to have a good conductivity of $\sim10^{-4}$ Scm^{-1} at 100 °C. Li_2OHCl exhibits a phase transition from orthorhombic to cubic at ~50 °C, with an increased ionic conductivity by 2 orders of magnitudes [39]. The protons in Li_2OHCl are important for Li-ion dynamics with increased H contents or at higher temperatures. A sequence of compositions of $Li_{2+x}OH_{1-x}Cl$ show increased ionic conductivities with higher H contents. Molecular dynamics (MD) simulations prove that the fast rotation of O-H bond leads to more facile Frenkel defects and therefore easier Li ion transport [40].

Anti-perovskite electrolytes have many advantages including (a) low melting temperature which simplifies the fabrication of films for applications in layered devices; (b) low densities which are preferred in sintering procedures; and (c) low activation energy. However, the significant hygroscopicity of anti-perovskite commonly requires an inert atmosphere during its synthesis, which is economically unfavoured [37].

1.3.7. LiPON

Lithium phosphorous oxynitride (LiPON) is a class of amorphous Li-ion solid electrolyte which has been applied in small power devices such as smart cards and RFID-tags [41]. LiPON films are commonly fabricated by radio frequency (RF) magnetron sputtering of Li_3PO_4 in N_2 [14, 41, 42]. LiPON has an ionic conductivity of ~2×10^{-6} Scm^{-1} at 25 °C, and a stable contact with lithium [14]. The successful commercialisation of LiPON is due to: (a) the better stability in ambient atmosphere compared to garnet LLZO or thio-LISICONs; (b) the stable and favorable solid electrolyte interfaces (SEI) formed between LiPON without any reduction like that in LATP or sulfides. However, there are limitations on the devices with LiPON films including a limited thicknesses due to the modest ionic conductivity of LiPON and a low current density below 10^{-5} Acm^{-2} [43].

Several parameters including radio frequency (RF) power, N_2 pressure and compositions of target material in the synthesis of LiPON films had a significant influence on the properties of the final product. For instance, replacement of a pure Li_3PO_4 target by a mixture of $2Li_3PO_4$:Li_2O by mole fraction, has a tripled ionic conductivity of ~6.4×10^{-6} Scm^{-1} at 25 °C [43]. The deposition rate of LiPON film increases with higher RF power, reduced N_2 pressure, shorter target-substrate distance and higher target density. By controlling the deposition rate, the product can have an ionic conductivity at room temperature of 5-7×10^{-6} Scm^{-1}. Simultaneously, extra phosphate groups including PO_3^{2-} and PO_2^{-} are observed with verified deposition rate. These disordered structures offer extra lithium ion mobility [14]. Recent attempts to prepare LiPON films by metalorganic-chemical vapour deposition (MOCVD) or atomic layer deposition, reach an ionic conductivity of 5×10^{-6} Scm^{-1} at 25 °C, which is still not good enough for LiPON to be applied in large solid state batteries [44].

The stable potential window of LiPON is below 4.5V vs Li/Li^+, which make it incompatible in advanced 5V batteries [44]. A simulation was based on a sandwich model, in which LiPON film is settled between an Au layer with negative bias and a TiN layer with positive bias. The simulated voltage limit is 4.3-4.5 V vs Li/Li^+. There exhibits the loss of Li^+ under high voltages resulting in a continuous change of secondary phosphate phase in the LiPON layer: $Li_4P_2O_7$, $LiPO_3$, and eventually P_4O_{10}. Simultaneously, there is the release of O_2 gas which is a potential risk in real applications. When the positive bias approaches to the limit (4.3 V), the lithium ions inside the LiPON films can be reduced to metallic lithium filaments, which may cause the short circuit [44].

1.3.8. Li_3N and related phases

Li_3N has a layered crystal structure with alternating layers of Li_2N and Li either parallel to or perpendicular to the *c*-axis, in which there is a higher ionic conductivity of ~10^{-3} Scm^{-1} at 25 °C, as shown in Fig 1.10 [17]. The synthesis of Li_3N is commonly through the reaction of lithium in N_2 atmosphere followed by cold pressing and sintering in N_2 atmosphere. The ionic conductivity of Li_3N is high depend on the final sintering temperature, there is a poor ionic conductivity of 3.7×10^{-8} Scm^{-1} at 25 °C when sintered at 650 °C and a high conductivity of 4×10^{-4} Scm^{-1} at 25 °C when sintered at 800 °C. The increased ionic conductivity in high temperature sintered sample may have an increased Li/N ratio [14].

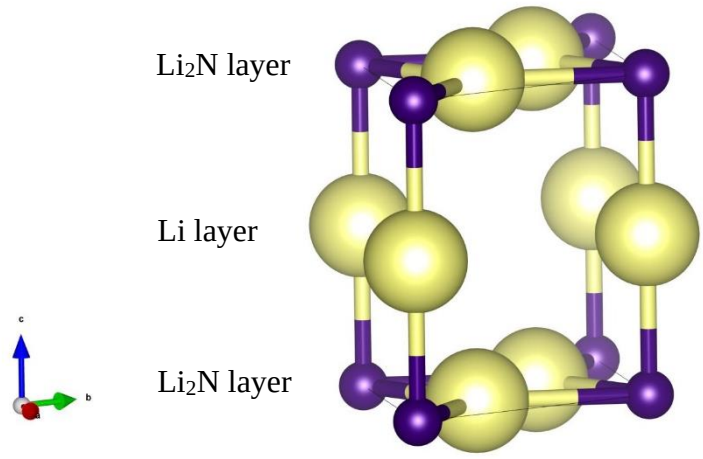

Fig 1.10. Crystal structure of Li_3N with alternative Li_2N and Li layers, produced by VESTA software [16], Li^+ in yellow, N^{3-} in purple.

Although Li_3N has barely satisfactory ionic conductivity, its applications are restricted by its very low decomposition voltage of 0.445 V [17] and poor stability window in contact with many cathode materials below 1.74 V vs Li/Li^+ [14]. The doping of Li_3N created several new phases: Li_3AlN_2 with a cubic anti-fluorite structure has a decomposition voltage of 0.85 V at 104 °C [17]; $LiSi_2N_3$ with an ionic conductivity of 1.2×10^{-3} Scm^{-1} at 327°C [14]. In the Li_3N-LiCl system, compositions between $2Li_3N$-3LiCl and $9Li_3N$-11LiCl have a cubic anti-fluorite structure. The composition, $Li_9N_2Cl_3$, with non-cubic structure has the highest ionic conductivity of 2×10^{-3} Scm^{-1} at 25 °C [14]. The isomorphous system $3Li_3N$-MI (M=Li, Na, K or Rb) with a tetragonal unit cell shows an ionic conductivity range from 7.0×10^{-5} Scm^{-1} at 25 °C to 1.1×10^{-4} Scm^{-1} at 25 °C and a significantly higher decomposition voltage of 2.5-2.8 V [45].

1.3.9. Lithium conduction in solid state electrolyte

Lithium conduction in solid state electrolyte is based on the diffusion of lithium ions in particular lithium pathways. Quantitatively, ionic conductivity can be broken down into a product of three terms: the charge of the carrier (q), the concentration of the carrier (n) and the mobility of the carrier (μ), as shown in equation 1.1.

$$\sigma = nq\mu \quad (1.1)$$

The transport of Li^+ in aprotic liquid electrolytes and solid state electrolytes are different. The mobility of ionic carrier is related to the diffusion coefficient as shown in equation 1.2.

$$D = k_b T\mu \quad (1.2)$$

In which k_b is the Boltzmann constant, T is the temperature in Kelvin,

The diffusion of Li^+ in the solvent medium in liquid electrolyte is further expressed by the Stokes–Einstein equation (1.3):

$$D_{liquid} = \frac{k_b T}{6\pi\vartheta\gamma} \quad (1.3)$$

In which k_b is the Boltzmann constant, T is the temperature in Kelvin, ϑ is the dynamic viscosity while γ the radius of the spherical particle.

Thus, the Li^+ ion conductivity in liquid electrolyte can be improved by higher salt/ion dissociation with greater dielectric constants or using solvents with lower viscosity. Due to the fast ion exchange in liquid, the potential energy profile of mobile lithium ions in liquid electrolytes is regarded to be flat [46].

On the other hand, the ionic conductivity of crystalline solid can be expressed by equation 1.1, in which the mobility of lithium ions (μ) is referred to the lithium diffusion coefficient (D) by the Nernst−Einstein equation (1.4) and equation 1.5 as:

$$\mu = \frac{D}{k_b T} \quad (1.4)$$

$$D = D_0 e^{-\frac{E_A}{k_b T}} \quad (1.5)$$

In which E_A is the the activation energy of ion conductivity (diffusion), D_0 is the pre-exponential constant, k_b is the Boltzmann constant and T is the temperature in Kelvin.

Thus, the ionic conductivity σ can be expressed as:

$$\sigma = A e^{-\frac{E_A}{R \times T}} \quad (1.6)$$

In which A is the exponential pre-factor constant, E_A is the the activation energy, R is the gas constant and T is the temperature in Kelvin.

The activation energy (E_A) is influenced by both migration energy E_m and defect formation energy, E_f, or trapping energy, E_t. In specific, the diffusion of mobile Li^+ in a crystalline solid state electrolyte shows an energetic barrier with two local minima along the lithium pathway, which is commonly referred to as migration energy, E_m. Low migration energy corresponds to higher mobility of lithium ions and better conductivity. In addition, the ionic conductivity in solids is dependent on the interstitials, vacancies and the occupancy on the lattice sites, which is defined as the defect formation energy or the ionic energy gap (E_f). If there is substitution by aliovalent cations, the formation of interstitials and vacancies can be energetically expressed by the trapping energy, E_t [15].

Generally, to achieve a fast ionic conductivity, there should be more available sites for mobile ions to hop into; low migration energy E_m that allows mobile ions to diffuse easily; and these available sites are somehow interconnected to each other to form a reasonable lithium pathway. Elemental substitution (aliovalent doping) has proved to be one of the best strategies for increasing the charge-compensating vacancies and interstitials and forming a non-stoichiometric solid, therefore, to obtain a higher ionic conductivity. However, the real ionic conductivity often shows a maximum and starts to decrease with more dopants were added into the lattice, which can possibly be attributed to a higher migration energy due to the distortion on local structures and extrinsic defects [15].

Previous research compared the bulk ionic conductivity among a selection of representative solid state electrolyte, as shown in Fig 1.11 [15]. The thio-LISICON family and argyrodite have high ionic conductivities with 10^{-2}-10^{-3} S/cm at ambient temperature with the existence of S^{2-} as anions, which can further lead to the issue of water-sensitivity as discussed before. Doped garnet LLZO also shows a promising ionic conductivity. The difference in ionic conductivity in a same family can be ~10^5. Thus, tuning within a given crystal structure by cation doping can possibly control the bottleneck size for lithium-ion diffusion pathway and lattice volume, then change the ionic conductivity significantly [15].

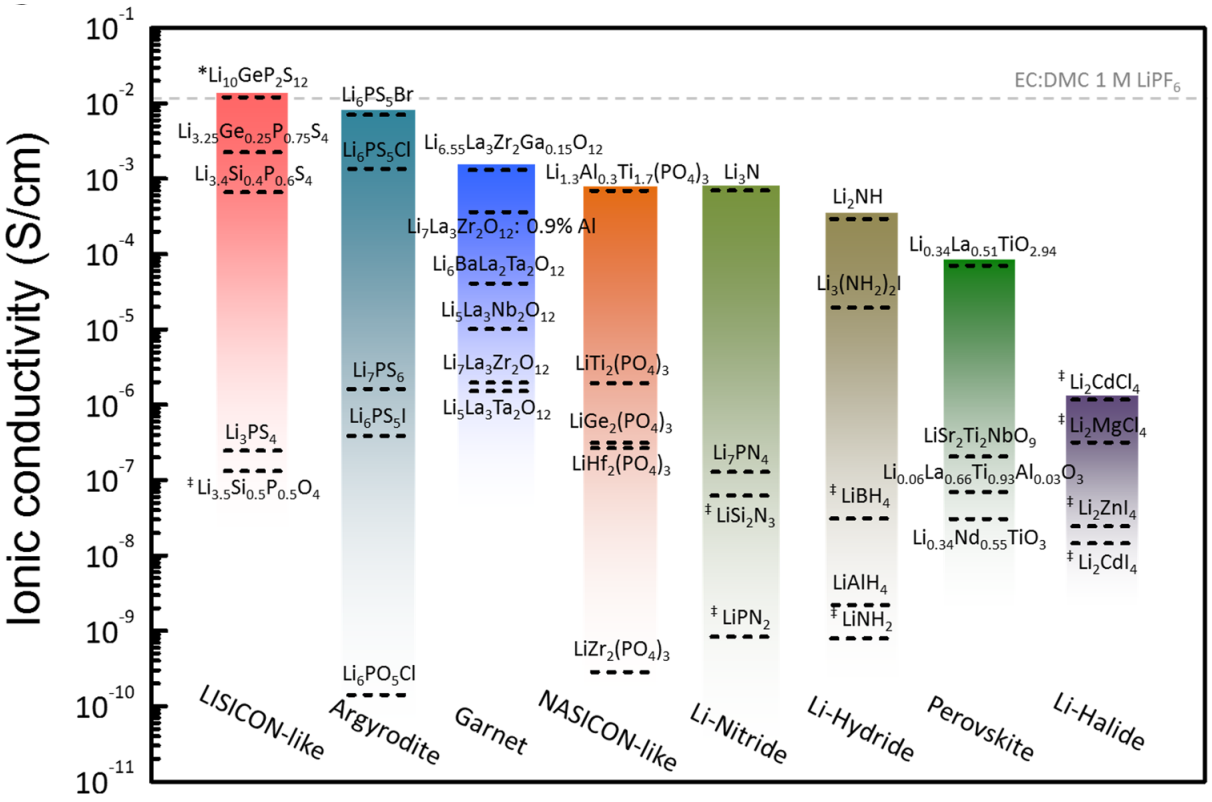

Fig 1.11. Ionic conductivity of different solid-state electrolytes at room temperature

Copied with permission from reference [15], Copyright 2016 American Chemical Society.

1.4. Aim of this study

The primary aim of my PhD research is to find potential candidates for solid-state electrolyte materials. This investigation commences with a follow-on study of Li_5SiO_4F, a new LISICON type electrolyte [48]. This comprehensive study encompasses the synthesis of Li_5SiO_4F, potential cation doping on it, a preliminary analysis of its subcell/supercell structure and a detailed evaluation of its electrical properties. As some possible new phases showed in the doping results, my study subsequently moves to a general survey on related ternary phases systems, trying to determine the composition, synthesis, crystal structure and electrical properties of the possible new oxyfluoride family.

1.5. Layout of this thesis

This thesis has a general introduction in Chapter 1, including the battery components, different types of electrolyte materials and representative solid state electrolyte families with lithium conduction mechanisms.

This study in this thesis primarily focuses on the characterisation of possible new materials. In Chapter 2 and later sections, several techniques were used for material determination: XRD (or STOE), indexing and XRF for composition and crystal structure analysis; impedance measurement and equivalent analysis for electrical properties; gas displacement pycnometer for density measurement; and DSC for melting behaviour.

The comprehensive study on Li_5SiO_4F is discussed in Chapter 3, primarily on its synthesis conditions and impedance responses. The possible cation doping on Li_5SiO_4F is discussed in Chapter 4. Furthermore, Chapter 5 includes an extensive investigation of the Li_2O-SiO_2-LiF system, while Chapter 6 extends the general survey to the Li_4SiO_4-Li_3PO_4-LiF system. Both Chapters 5-6 focus on the exploration of potential new oxyfluoride phases.

References

[1] Y. Wang, B. Liu, Q. Li, S. Cartmell, S. Ferrara, Z. D. Deng, and J. Xiao, "Lithium and lithium ion batteries for applications in Microelectronic Devices: A Review," *Journal of Power Sources*, vol. 286, pp. 330–345, 2015.

[2] A. R. West, "Lithium battery," in *Solid state chemistry and its applications, 2th edition*, Chichester, UK: John Wiley & Sons, 1990, pp. 425–426.

[3] "*The Nobel Prize in chemistry 2019*," NobelPrize.org. [Online]. Available: https://www.nobelprize.org/prizes/chemistry/2019/summary/. [Accessed: 23-Jan-2023].

[4] J. B. Goodenough, "How we made the Li-ion rechargeable battery," *Nature Electronics*, vol. 1, no. 3, pp. 204–204, 2018.

[5] W. Xu, J. Wang, F. Ding, X. Chen, E. Nasybulin, Y. Zhang, and J.-G. Zhang, "Lithium metal anodes for rechargeable batteries," *Energy Environ. Sci.*, vol. 7, no. 2, pp. 513–537, 2014.

[6] J. Chen, "Recent progress in advanced materials for lithium ion batteries," *Materials*, vol. 6, no. 1, pp. 156–183, 2013.

[7] G. Zhang, X. Xiao, B. Li, P. Gu, H. Xue, and H. Pang, "Transition metal oxides with one-dimensional/one-dimensional-analogue nanostructures for advanced supercapacitors," *Journal of Materials Chemistry A*, vol. 5, no. 18, pp. 8155–8186, 2017.

[8] A. R. West, "Cathode materials," in *Solid state chemistry and its applications, 2th edition*, Chichester, UK: John Wiley & Sons, 1990, pp. 426–427.

[9] J. Liu, J. Wang, Y. Ni, K. Zhang, F. Cheng, and J. Chen, "Recent breakthroughs and perspectives of high-energy layered oxide cathode materials for lithium ion batteries," *Materials Today*, vol. 43, pp. 132–165, 2021.

[10] N. Mohamed and N. K. Allam, "Recent advances in the design of cathode materials for Li-Ion Batteries," *RSC Advances*, vol. 10, no. 37, pp. 21662–21685, 2020.

[11] R. Schmuch, R. Wagner, G. Hörpel, T. Placke, and M. Winter, "Performance and cost of materials for lithium-based rechargeable automotive batteries," *Nature Energy*, vol. 3, no. 4, pp. 267–278, 2018.

[12] K. Xu, "Electrolytes and interphases in li-ion batteries and beyond," *Chemical Reviews*, vol. 114, no. 23, pp. 11503–11618, 2014.

[13] Y. He, X. Ren, Y. Xu, M. H. Engelhard, X. Li, J. Xiao, J. Liu, J.-G. Zhang, W. Xu, and C. Wang, "Origin of lithium whisker formation and growth under stress," *Nature Nanotechnology*, vol. 14, no. 11, pp. 1042–1047, 2019.

[14] F. Zheng, M. Kotobuki, S. Song, M. O. Lai, and L. Lu, "Review on solid electrolytes for all-solid-state lithium-ion batteries," *Journal of Power Sources*, vol. 389, pp. 198–213, 2018.

[15] J. C. Bachman, S. Muy, A. Grimaud, H.-H. Chang, N. Pour, S. F. Lux, O. Paschos, F. Maglia, S. Lupart, P. Lamp, L. Giordano, and Y. Shao-Horn, "Inorganic solid-state electrolytes for lithium batteries: Mechanisms and properties governing ion conduction," *Chemical Reviews*, vol. 116, no. 1, pp. 140–162, 2015.

[16] K. Momma and F. Izumi, "vesta 3for three-dimensional visualization of crystal, volumetric and morphology data," *Journal of Applied Crystallography*, vol. 44, no. 6, pp. 1272–1276, 2011.

[17] A. D. Robertson, A. R. West, and A. G. Ritchie, "Review of crystalline lithium-ion conductors suitable for high temperature battery applications," *Solid State Ionics*, vol. 104, no. 1-2, pp. 1–11, 1997.

[18] W. Zhao, J. Yi, P. He, and H. Zhou, "Solid-state electrolytes for lithium-ion batteries: Fundamentals, challenges and Perspectives," *Electrochemical Energy Reviews*, vol. 2, pp.574-605, 2019.

[19] N. Kamaya, K. Homma, Y. Yamakawa, M. Hirayama, R. Kanno, M. Yonemura, T. Kamiyama, Y. Kato, S. Hama, K. Kawamoto, and A. Mitsui, "A lithium superionic conductor," *Nature Materials*, vol. 10, no. 9, pp. 682–686, 2011.

[20] Y. Kato, S. Hori, T. Saito, K. Suzuki, M. Hirayama, A. Mitsui, M. Yonemura, H. Iba, and R. Kanno, "High-power all-solid-state batteries using sulfide superionic conductors," *Nature Energy*, vol. 1, no. 4, 2016.

[21] Y. Mo, S. P. Ong, and G. Ceder, "First Principles Study of the li10gep2S12 lithium super ionic conductor material," *Chemistry of Materials*, vol. 24, no. 1, pp. 15–17, 2011.

[22] H. Y.-P. Hong, "Crystal Structures and crystal chemistry in the system $Na_{1+x}Zr_2Si_xP_{3-x}O_{12}$," *Materials Research Bulletin*, vol. 11, no. 2, pp. 173–182, 1976.

[23] H. Aono, E. Sugimoto, Y. Sadaoka, N. Imanaka, and G. Adachi, "Ionic conductivity of solid electrolytes based on lithium titanium phosphate," *Journal of The Electrochemical Society*, vol. 137, no. 4, pp. 1023–1027, 1990.

[24] H. Aono, E. Sugimoto, Y. Sadaoka, N. Imanaka, and G. Adachi, "Ionic conductivity of the lithium titanium phosphate ($Li_{1+x}M_xTi_{2-x}(PO_4)_3$, M: Al, Sc, Y, and La) systems.," *ChemInform*, vol. 20, no. 29, 1989.

[25] Y. Ren, K. Chen, R. Chen, T. Liu, Y. Zhang, and C.-W. Nan, "Oxide electrolytes for lithium batteries," *Journal of the American Ceramic Society*, vol. 98, no. 12, pp. 3603–3623, 2015.

[26] J. Fu, "Fast Li^+ ion conducting glass-ceramics in the system $Li_2O–Al_2O_3–GeO_2–P_2O_5$," *Solid State Ionics*, vol. 104, no. 3-4, pp. 191–194, 1997.

[27] J. Fu, "Fast Li^+ ion conduction in $Li_2O–Al_2O_3$-TiO_2 -SiO_2-P_2O_5 glass-ceramics," *Journal of the American Ceramic Society*, vol. 80, no. 7, pp. 1901–1903, 2005.

[28] N. B. Abdul Rashid, Y. J. Shan, K. Sugawara, and K. Tezuka, "The effects of lattice volume and carrier concentration on the conductivity of NASICON-type $LiXIn_{0.5}Z_{0.5}(PO_4)_3$ (X = Ti, Zr; Z = Nb, Ta) oxides," *Ionics*, vol. 27, no. 9, pp. 3829–3835, 2021.

[29] R. P. Rao, N. Sharma, V. K. Peterson, and S. Adams, "Formation and conductivity studies of lithium argyrodite solid electrolytes using in-situ neutron diffraction," *Solid State Ionics*, vol. 230, pp. 72–76, 2013.

[30] Z. Zhang, L. Zhang, Y. Liu, C. Yu, X. Yan, B. Xu, and L.-min Wang, "Synthesis and characterization of argyrodite solid electrolytes for all-solid-state Li-ion Batteries," *Journal of Alloys and Compounds*, vol. 747, pp. 227–235, 2018.

[31] C. Wang, K. Fu, S. P. Kammampata, D. W. McOwen, A. J. Samson, L. Zhang, G. T. Hitz, A. M. Nolan, E. D. Wachsman, Y. Mo, V. Thangadurai, and L. Hu, "Garnet-type solid-state electrolytes: Materials, interfaces, and batteries," *Chemical Reviews*, vol. 120, no. 10, pp. 4257–4300, 2020.

[32] V. Thangadurai, S. Narayanan, and D. Pinzaru, "Garnet-type solid-state fast Li ion conductors for Li Batteries: Critical Review," *Chemical Society Reviews*, vol. 43, no. 13, p. 4714, 2014.

[33] S. Narayanan, F. Ramezanipour, and V. Thangadurai, "Enhancing Li ion conductivity of garnet-type $Li_5La_3Nb_2O_{12}$ by Y- and Li-codoping: Synthesis, structure, chemical stability, and transport properties," *The Journal of Physical Chemistry C*, vol. 116, no. 38, pp. 20154–20162, 2012.

[34] G. Larraz, A. Orera, and M. L. Sanjuán, "Cubic phases of garnet-type $Li_7La_3Zr_2O_{12}$: The role of Hydration," *Journal of Materials Chemistry A*, vol. 1, no. 37, p. 11419, 2013.

[35] D. Rettenwander, G. Redhammer, F. Preishuber-Pflügl, L. Cheng, L. Miara, R. Wagner, A. Welzl, E. Suard, M. M. Doeff, M. Wilkening, J. Fleig, and G. Amthauer, "Structural and electrochemical consequences of Al and Ga co-substitution in $Li_7La_3Zr_2O_{12}$ solid electrolytes," *Chemistry of Materials*, vol. 28, no. 7, pp. 2384–2392, 2016.

[36] A. Emly, E. Kioupakis, and A. Van der Ven, "Phase stability and transport mechanisms in anti-perovskite Li_3OCL and Li_3OBR superionic conductors," *Chemistry of Materials*, vol. 25, no. 23, pp. 4663–4670, 2013.

[37] Y. Zhao and L. L. Daemen, "Superionic conductivity in lithium-rich Anti-Perovskites," *Journal of the American Chemical Society*, vol. 134, no. 36, pp. 15042–15047, 2012.

[38] Y. Zhang, Y. Zhao, and C. Chen, "*ab* initio study of the stabilities of and mechanism of superionic transport in lithium-rich anti-perovskites," *Physical Review B*, vol. 87, no. 13, 2013.

[39] Z. Deng, D. Ni, D. Chen, Y. Bian, S. Li, Z. Wang, and Y. Zhao, "anti-perovskite materials for energy storage batteries," *InfoMat*, vol. 4, no. 2, 2021.

[40] A. Y. Song, Y. Xiao, K. Turcheniuk, P. Upadhya, A. Ramanujapuram, J. Benson, A. Magasinski, M. Olguin, L. Meda, O. Borodin, and G. Yushin, "Protons enhance conductivities in lithium halide hydroxide/lithium oxyhalide solid electrolytes by forming rotating hydroxy groups," *Advanced Energy Materials*, vol. 8, no. 3, p. 1700971, 2017.

[41] S. H. Jee, M.-J. Lee, H. S. Ahn, D.-J. Kim, J. W. Choi, S. J. Yoon, S. C. Nam, S. H. Kim, and Y. S. Yoon, "Characteristics of a new type of solid-state electrolyte with a LiPON interlayer for Li-ion thin film batteries," *Solid State Ionics*, vol. 181, no. 19-20, pp. 902–906, 2010.

[42] P. López-Aranguren, M. Reynaud, P. Głuchowski, A. Bustinza, M. Galceran, J. M. López del Amo, M. Armand, and M. Casas-Cabanas, "Crystalline Lipon as a bulk-type solid electrolyte," *ACS Energy Letters*, vol. 6, no. 2, pp. 445–450, 2021.

[43] N. Suzuki, T. Inaba, and T. Shiga, "Electrochemical properties of Lipon Films made from a mixed powder target of Li_3PO_4 and Li_2O," *Thin Solid Films*, vol. 520, no. 6, pp. 1821–1825, 2012.

[44] B. Put, P. M. Vereecken, and A. Stesmans, "On the chemistry and electrochemistry of LiPON breakdown," *Journal of Materials Chemistry A*, vol. 6, no. 11, pp. 4848–4859, 2018.

[45] S. Hatake, J. Kuwano, M. Miyamori, Y. Saito, and S. Koyama, "New lithium-ion conducting compounds $3Li_3N$-MI (M= Li, Na, K, Rb) and their application to solid-state lithium-ion cells," *Journal of Power Sources*, vol. 68, no. 2, pp. 416–420, 1997.

[46] K. Xu, "Nonaqueous liquid electrolytes for lithium-based rechargeable batteries," *Chemical Reviews*, vol. 104, no. 10, pp. 4303–4418, 2004.

[47] R. P. Buck, "Transport properties of ionic conductors," *Sensors and Actuators*, vol. 1, pp. 137–196, 1981.

[48] B. Dong, J. Yan, B. Walkley, K. K. Inglis, F. Blanc, S. Hull, and A. R. West, "Synthesis and characterisation of the new oxyfluoride Li^+ Ion Conductor, Li_5SiO_4F," *Solid State Ionics*, vol. 327, pp. 64–70, 2018.

Chapter 2. Experimental

2.1. Raw materials preparation and solid state synthesis

Samples prepared in this project were mostly synthesised by solid state reactions with a series of raw materials shown in Table 2.1. Raw materials, in powder form, were dried at different temperatures before weighing. Reactants were mixed with acetone using a set of mortar and pestle for ~30 mins. Normally, ~2 g batches of mixed raw materials were prepared. Pellets, for better synthesis, XRF or impedance measurements, were prepared by placing loose powders in 10 mm diameter die and pressed by cold isostatic pressing with 1 ton for 2 minutes. For solid state synthesis, powders and/or pellets were placed in an Au boat, heated at temperatures 600-900 ℃ in a muffle or tube furnace with a heating rate of 5 ℃/min and cooled with 5 ℃/min inside the furnace after maintaining at fixed temperature for 6-10 h. In some circumstances, the samples were slowly cooled to room temperature with a cooling rate of 1 ℃/min. Samples with Li_2CO_3 in the starting material require a pre-heating at 600 ℃ for 6 h to drive off CO_2 and H_2O.

Table 2.1. Details of raw materials

Chemical	Info (Company/purity)	Drying temperature
Li_2CO_3	Sigma Aldrich /99%	180°C
SiO_2	Sigma Aldrich/99.5%	600°C
LiF	Fluka/99%	180°C
ZnO	Sigma Aldrich /99.9%	600°C
MgO	Sigma Aldrich /99%	1000°C
NiO	Alfa Aesar/99.995%	800°C
Ga_2O_3	Sigma Aldrich /99%	600°C
Fe_2O_3	Sigma Aldrich /-	600°C
CoO	Alfa Aesar/99%	600°C
Al_2O_3	Alfa Aesar/99.95%	900°C
GeO_2	Acros/-	800°C
TiO_2	Sigma Aldrich /99%	900°C
$NH_4H_2PO_4$	BDH/-	90°C

2.2. Density measurement

The theoretical density of a material was estimated based the equation shown below:

$$\rho_{theoretical} = \frac{nM}{NV} \quad (2.1)$$

In which n is the number of formula units in a unit cell, M is molar mass, N is the Avogadro constant and V is the volume of unit cell. N=~6.022×10^{23} mol^{-1}. The volume of the unit cell was obtained from the indexing of the XRD data.

The measured density of samples was calculated by the measured diameter and weight of the material pellet:

$$\rho_{measure} = \frac{m}{V} \quad (2.2)$$

In which m is the weight of the pellet and V is the volume of pellet which can be calculated by the diameter of the pellet cylinder.

There do exist some error in measuring, as the pellets can not be standard cylinders, thus an average value of size and mass from 3 different measurements was used.

The density of some powder materials was measured by a ACCUPYC II gas displacement pycnometer, which determines the density and volume of the sample material by measuring the pressure change of helium within calibrated volumes. Each sample was measured for 5 times to gain an average density. The error in this measurement is much less than that in density calculation in pellet cylinder samples.

2.3. XRD/XRF

When a material is exposed to high-energy charged particles, X-rays are created. In a laboratory setting, a tungsten filament is used as the source of high-energy particles, which are electrons. A typical sealed-tube for X-ray production consists of a heated filament that produces electrons, which are then accelerated by a high-voltage electric field and collide with a metal target, commonly made of Cu, Cr, Fe, Co or Mo. When the beam electrons hit the target, they emit a continuous spectrum of X-rays that is typically monotonic and smooth. However, when the energy of the electrons is higher than a certain value, characteristic radiation appears and shows discrete peaks in the X-ray spectrum. This is caused by the collision of electrons with the target material, which ejects a tightly bound electron from the inner shell and leaves a vacancy [1].

The energy difference between two levels gives rise to radiation, which can be observed in the form of Kα and Kβ radiation. To obtain monochromatic X-rays for diffraction experiments, the Kβ radiation is removed by a metal filter, and a channel-cut monochromator is used to remove the Kα2 radiation.

When X-rays interact with atoms in a crystal, they generate scattered X-rays that interfere with each other. In order for constructive interference to occur, the waves must be in phase, meaning their travel paths must differ by nλ, as shown in the Bragg's Law:

$$n\lambda = 2\mathrm{d}\sin\theta \qquad (2.3)$$

In which n is an integer, λ is the wavelength of the X-ray source, θ is the angle of incident X-rays, and d is the d-spacing of the crystal lattice [2].

Typical XRD equipment includes an X-ray generator, goniometer, detector, measuring circuit, recording and analysing system. In this study, a Bruker D2 diffractometer was used for preliminary phase determination and a STOE-STADI Mo PSD Diffractometer was used for high quality XRD data for further indexing and refinements.

Only ~0.1-0.2 g of powder sample was needed for measurement on Bruker D2 diffractometer with Cu Kα radiation (λ= 1.5418 Å). Powder was placed in sample holder with a flat surface. The result pattern commonly covers a 2θ range of 10-80 °/2θ with a step size of ~0.2 ° with a scan rate of 0.5-3 s/step.

A sample paste was needed for XRD measurement on a STOE PSD diffractometer with either Cu $K\alpha_1$ (λ=1.5406 Å) or Mo $K\alpha_1$ (λ=0.7093 Å). A tiny amount of sample powder (and) standard silicon powder was placed on a transparent plastic disc and mixed with 1-2 drops of PVA glue followed by drying. The sample disc was then loaded in the holder, and continuously rotating during the measurement. The common scan range for Mo-STOE is 5-45 °/2θ, with a step size of 0.05° and scan rate of 3-20 s/step. The scan range for Cu-STOE is 10-80 °/2θ with same step size and scan rate. There is no significant difference was observed in short/long scan, thus a scan rate of ~3 s/step is enough for obtaining good XRD data. WinXpow software was used to obtain high-quality diffraction patterns with internal standard Si for peak calibration. Preliminary comparison of experimental and database patterns used standards from ICSD.

Further indexing and preliminary crystal structure investigation also used CIF cards for different materials from the ICSD database. The indexing process by WinXpow software uses the Louer's algorithm, so called DICVOL, which revolves around improving the constrained relationships shown during the comparison between the experimental data and the calculated patterns produced at various stages of the analysis [3]. The indexing results by DICVOL are testified to be reasonable for most of the cases down to monoclinic symmetry but less predictable for triclinic materials [3]. The settings for indexing are as follows: the maximum cell edges are limited to 15 Å while the maximum lattice volume is limited to 2000 $Å^3$; the figure-of-merit (MOF) is set as 5; there is no limitation in peak intensity; the angle in the monoclinic system is limited to 90-125°. As most of cases in this study are new materials with no known compound in them, thus the formular weight and observed density (of any known compound) are set to 0. For a preliminary trail to index the whole diffraction pattern, the first 100 peaks which are determined automatically by WinXpow software will be accepted. Possible crystal systems including cubic, hexagonal, tetragonal and orthorhombic will be firstly tried followed by further trails with monoclinic and triclinic. For most cases, partial peaks are selected for indexing with the window of peak position of 0.05°/2θ for D2 data and 0.03 for STOE data. The indexing result include lattice types and lattice parameters with errors, along with observed and calculated *2θ* values and *d* values, in most cases with XRD patterns from

Bruker D2 diffractometer, the difference between observed and calculated 2θ values less than 0.3 is believed to be reasonable. Generally, many of the XRD data were collected during the Covid shut down period using Bruker D2 diffractometer, which lead to the limited quality and accuracy of the raw XRD data. The indexing attempts on the basic subcell structure, a hexagonal subcell in many cases, were successful. Further trails indexed the first set of partially ordered supercells but most of the patterns were too complex to assign a full supercell using the available XRD data.

A PANalytical Zetium spectrometer (XRF) was used to test the composition of the samples in weight percentages (wt%). Theatrically, when a sample is hit by X-ray, there is emit of fluorescent radiation depending on the Kα reflection of elements. The composition of each possible elements contained in the sample was analysed according to the positions and intensities of the peaks. Any element lighter than oxygen is not able to be detected by XRF and oxygen and fluorine are detectable with significant error. Powder sample was pressed into pellet and reheated at its synthesis temperature for 8-10 h and put into the suitable cup for XRF measurement.

2.4. Impedance measurement and equivalent circuit analysis

Impedance spectroscopy (IS) is an advanced method widely used to analyse the microstructure and electrical properties of electroceramic. By applying an alternating voltage, the impedance of the material can be measured in the frequency domain. One of the main advantages of IS is that it allows for the identification and characterisation of different electrically-active regions, such as the grain, grain boundary, and surface layer, through appropriate data analysis [4].

Impedance is a vector quantity consisting of a real component (Z') and an imaginary component (Z''), which can be expressed as:

$$Z^* = Z' - jZ'' \qquad (2.4)$$

in which j is the square root of -1

Other parameters can be derived from the impedance Z*:

(a) complex admittance:

$$Y^* = (Z^*)^{-1} \quad (2.5)$$

(b) complex electric modulus:

$$M^* = j\omega C_0 Z^* \quad (2.6)$$

in which ω is the angular frequency and C_0 is the vacuum capacitance.

and (c) complex permittivity:

$$\varepsilon^* = (M^*)^{-1} \quad (2.7)\ [5]$$

The electrical properties of materials can be represented by a framework of resistance, R, capacitance, C and inductance, L. Each electrically-distinct region of the sample can ideally characterised by its own time constant, τ:

$$\tau = RC = \rho\varepsilon \quad (2.8)$$

$$\rho = R\frac{A}{d} \quad (2.9)$$

$$\varepsilon = C\frac{d}{A} \quad (2.10)$$

In which ρ is the resistivity and ε is the permittivity of the sample, A is the cross-sectional area of the measured region with its thickness, d.

The geometric factor (GF) is defined as the product of A/d, which will be used in processing the impedance data.

The permittivity of the sample is also expressed by the dielectric constant or so-called relative permittivity, ε':

$$\varepsilon' = \frac{\varepsilon}{e_0} = C\frac{d}{A}e_0^{-1} \quad (2.11)$$

In which e_0 is the permittivity of free space with its value of 8.854×10^{-14} Fcm^{-1}.

The impedance data are collected usually in impedance format, by equations 2.5-2.7, it can be converted to other formalisms. Normally, the impedance data are presented as: firstly, complex plane plot, so called Nyquist plots in which the imaginary component Z'' against the real

component $Z^{'}$, in same scales, linear or logarithmic; and spectroscopic plots, also called Bode plots in which $C^{'}$, $Y^{'}$, $M^{''}$ or $Z^{''}$ are plotted against frequency on a logarithmic scale.

In the case of an ideal electroceramic sample, its response to an AC voltage can be described by a resistance and a capacitance in parallel, thus a RC element. In an impedance complex plane plot, electrical components are separated on a frequency scale according to their different time constants τ [6]. In equivalent circuit analysis, each component, bulk or grain/grain boundary, can be ideally represented by a parallel RC element. However, in reality, most elements are frequency-dependent excepted at high/low frequency limits. At the high frequency end, it represents the limiting frequency permittivity; while at low frequency end, it shows the dielectric constant and *dc* resistance [6]. To achieve a good fit to real impedance data, taking account of the frequency dependence, an additional constant phase element (CPE) is added in parallel to the parallel RC element. The unideal impedance behaviours are represented by Jonscher's Law of universal Dielectric Response (UDR) [6]. In a recent study, the advantages to introduce CPEs in equivalent circuit are summarised as follows: (1) they represent the ubiquitous existence of non- ideality in impedance response of homogeneous bulk materials; (2) their characterisation offers a more insightful bulk conduction mechanisms; (3) the CPE element(a) in equivalent circuits offer better fitting of impedance data of heterogeneous materials [7]. In specific, a R-C-CPE element in equivalent circuit analysis, as shown in Fig 2.1, is believed to be suitable for most of bulk responses. There is a frequency-dependent resistor and capacitor in parallel in a CPE element [7]. The admittance of it is:

$$Y^* = A\omega^n + jB\omega^n \qquad (2.12)$$

Where $j = \sqrt{-1}$ [7]

There is a power law response given by CPE of both conductivity and capacitance [7]. For instance, the R-C-CPE element shows a power law dispersion in conductivity, Y', at high frequencies, which is characterised by the value of n ($0<n<1$), in Fig 2.2 (a). Long range conductivity through bulk dominates the conductivity Y' from which the contribution of CPE is minimal. For capacitance plot, log C'-log f plot, in Fig 2.2 (b), the capacitive component of CPE becomes more significant with lower frequency, which is shown as a dispersion of value (n-1) in capacitance. These power law behaviours are summarised as the UDR Law by Jonscher. The M''/Z'' spectroscopic plots, log $M^{''}/Z^{''}$-log f plots in Fig 2.2 (c), the curves for Z'' and M''

are not ideally Debye-like. In specific, Z'' curve is broadened at low frequency end while M'' curve is broadened at high frequency end. When there is only a parallel R-C element, the Debye peaks show slopes of 1 and -1 at low and high frequencies, respectively. When a CPE is involved in parallel, the slopes of these lines are dependent on the n value [7]. The comparison between different equivalent circuit models to fit impedance responses of different components are discussed in detail in Chapter 3, taking the impedance data of γ-Li_5SiO_4F as a good example.

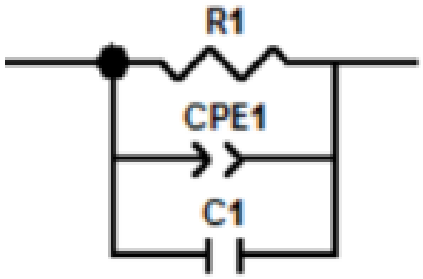

Fig 2.1. A combination of R, C and CPE in parallel, an accurate fit to the bulk response of many materials.

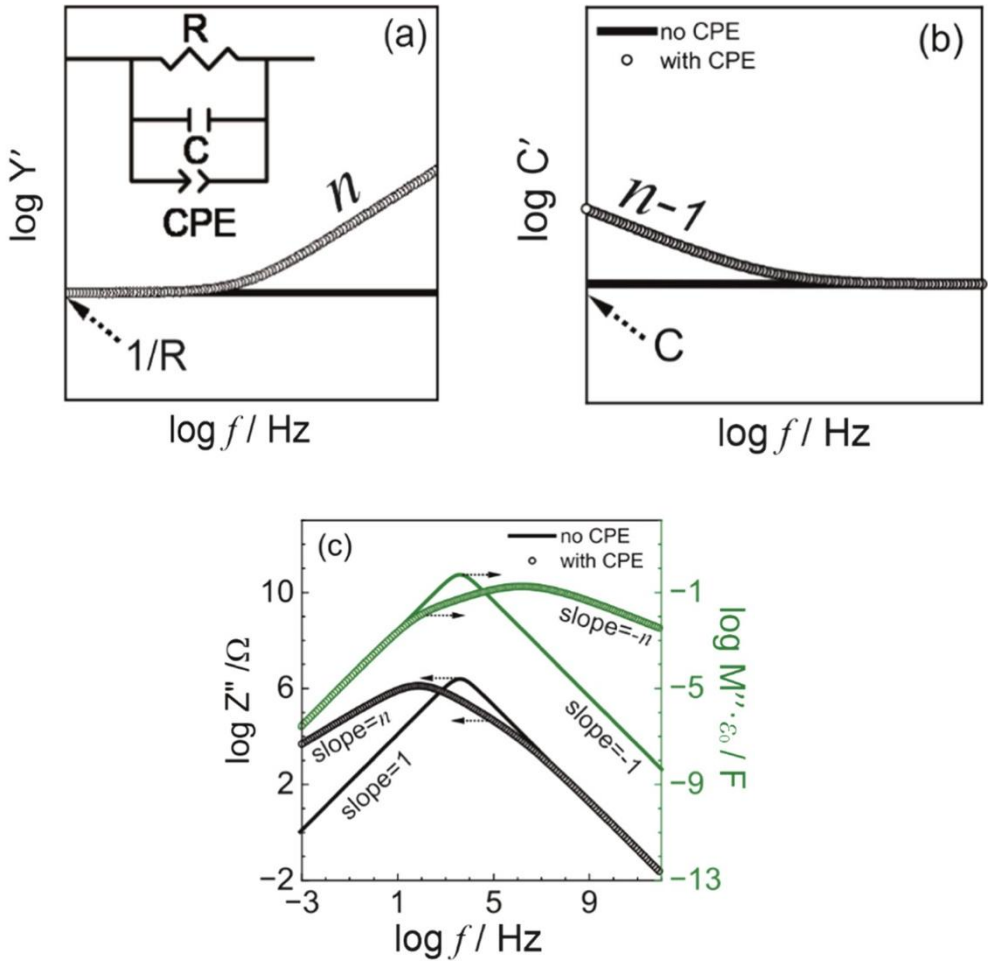

Fig 2.2. Simulations showing the effect of adding a CPE to a parallel RC element on different impedance responses. Copied with permission from [7]. Copyright 2023 FFIOP Publishing, Ltd.

Recent studies show the application of Impedance spectroscopy and equivalent circuit analysis is essential to analyse heterogeneous materials. For instance, a previous case study on CCTO successfully separated a capacitance C_2 values which are several orders of magnitude higher than expected. This referred to a thin region, probably a grain boundary beside the bulk. It also indicated that the giant fixed frequency capacitance is not the intrinsic bulk capacitance value which may be much smaller [7]. Impedance spectroscopy is also used as a non-destructive method to in-situ analysis of the dynamic processes occurring inside a battery. IS analysis with the three-electrode cell configurations offered separate contributions of anodic and cathodic impedances in the battery analysis [8].

The capacitance value can be used to identify different components in the sample. Common capacitance values for possible interpretation are shown in Table 2.2 [6].

Table 2.2. Typical capacitance values for different components

Capacitance (Fcm^{-1})	Possible phenomenon
10^{-12}	Bulk
10^{-11}	Minor, second phase
10^{-11}-10^{-8}	Grain boundary
10^{-10}-10^{-9}	Bulk ferroelectric
10^{-9}-10^{-7}	Surface layer
10^{-7}-10^{-5}	Sample-electrode interface
10^{-4}	Electrochemical reaction

Impedance pellets were prepared by either cold press or hot press: (a) Powder was pressed by either an uniaxial press or a cold isostatic press at 1 ton for 2 mins; (b) Powder was heated to 300°C and pressed at 1 ton for roughly 15 mins, then air cooled to room temperature). Green pellets were sintered at synthesis temperature for 8-10 h and coated with Au electrode paste on opposite sides. Coated pellets were placed in a crucible and heated at the synthesis temperature of the sample material for 8 h and then programmed cooling to room temperature. Pellets with electrodes were loaded into a jig facility, which was placed in a tube furnace for impedance measurements.

A new Solartron analyser (Analytical Ltd, Farnborough, UK) was used for impedance measurements in ambient atmosphere with a frequency range of 10^{-2}-10^{6} Hz. A Solartron SI 1260 impedance analyser (Analytical Ltd, Farnborough, UK) was used for impedance measurements in N_2 with a frequency range of 10^{-2}-10^{6} Hz. The analysis of impedance data used Zview software. The geometric correction of the data used the geometric factor (GF) calculated based on measured size of the sample pellet. The jig correction of the data used the short circuit / open circuit jig impedance data without loading any sample. IS data was used to

draw the Arrhenius plots with conductivity against reciprocal temperature. The slope of these plots was then used to calculate the activation energy.

2.5. DSC

Differential scanning calorimeter (DSC) is a popular calorimetry to test the thermal properties of materials. DSC tracks the temperature and heat flow related with material transitions as a function of time and temperature. DSC quantifies the amount of heat released or absorbed by the sample on the basis of the temperature difference between the sample and a reference material [9]. Commonly, there are two types of DSCs: heat-flux DSC and power-compensated DSC.

In a heat flux DSC, a sample material enclosed within a pan with another empty reference container are positioned on a thermoelectric disc in a heating furnace. The furnace gradually heats up at a set constant rate, and the heat is transferred to both the sample and reference pans through the thermoelectric disc. Due to the different heat capacity (*Cp*) of the sample, there arises a temperature difference between the sample and reference pans, which is measured by the area thermocouples. The heat flow is then determined according to the thermal equivalent of Ohm's law:

$$q = \frac{\Delta T}{R} \qquad (2.12)$$

In which q is the measured heat flow, ΔT is the temperature difference between sample and reference pans, and R is the resistance of thermoelectric disk [9]

In a power-compensated DSC, the sample and reference pans are placed in separate furnaces, each with its own heating element. The sample and reference are maintained at the same temperature, and the difference in thermal power required to maintain them at the same temperature is measured and plotted as a function of temperature or time [10].

In the experiment, powder samples were dried at 200°C to drive off H_2O and weighed by balance, placed in pans made of alumina which is suitable for high-temperature measurements. Then sample pan and reference pan were placed in to a Netzsch DSC facility. The measuring

temperature range is room temperature to 750°C, which is slightly lower than the possible melting temperature of the Li-Si-O-F samples. The heating and cooling rate are set as 1°C/min.

References

[1] ScienceDirect, "X ray diffraction," *X Ray Diffraction - an overview* [Online]. Available: https://www.sciencedirect.com/topics/nursing-and-health-professions/x-ray-diffraction. [Accessed: 02-Mar-2023].

[2] A.R. West, "X-Ray diffraction" in *Solid State Chemistry and Its Applications*, 2th edition'. John Wiley & Sons. West Sussex, pp.232-265.

[3] A. Boultif and D. Louër, "Indexing of powder diffraction patterns for low-symmetry lattices by the successive dichotomy method," *Journal of Applied Crystallography*, vol. 24, no. 6, pp. 987–993, 1991.

[4] D. C. Sinclair "Electroceramic: Characterization by impedance spectroscopy," *Bol Soc Esp Ceram Vidrio*, vol. 34, pp. 55–65, 1995.

[5] J. T. Irvine, D. C. Sinclair, and A. R. West, "Electroceramics: Characterization by impedance spectroscopy," *Advanced Materials*, vol. 2, no. 3, pp. 132–138, 1990.

[6] A. R. West, "Chapter 11," in *Solid state chemistry and its applications*, Chichester: John Wiley & Sons, 2022

[7] J. Ramírez-González, D. C. Sinclair, and A. R. West, "Impedance and dielectric spectroscopy of functional materials: A critical evaluation of the two techniques," Journal of The Electrochemical Society, vol. 170, no. 11, p. 116504, 2023.

[8] L. A. Middlemiss, A. J. R. Rennie, R. Sayers, and A. R. West, "Characterisation of batteries by electrochemical impedance spectroscopy," *Energy Reports*, vol. 6, pp. 232–241, 2020.

[9] M. E. Brown and P. K. Gallagher, "Differential thermal analysis and differential scanning calorimetry," in *Handbook of thermal analysis and Calorimetry*, Oxford, UK: Elsevier, 2008, pp. 279–361

[10] O. Koshy, L. Subramanian, and S. Thomas, "Differential scanning calorimetry in Nanoscience and nanotechnology," *Thermal and Rheological Measurement Techniques for Nanomaterials Characterization*, pp. 109–122, 2017.

Chapter 3. Electrical properties of Li_5SiO_4F

Summary

As an extended study on the previously reported phase, Li_5SiO_4F, its two polymorphs, α-Li_5SiO_4F and γ-Li_5SiO_4F, were synthesised at 650-700 °C and at 750-775 °C, respectively. The possible incongruent melting of γ-Li_5SiO_4F at ~800 °C was observed. During the investigation of their electrical properties, by impedance measurement and equivalent circuit analysis, we found that (a) the long-time heat treatment on γ-Li_5SiO_4F lead to loss of LiF by volatilisation, which leave a thin layer of Li_4SiO_4 in the sample; (b) there is clear dipole effect in the bulk of γ-Li_5SiO_4F; (c) the Ag coating γ-Li_5SiO_4F pellet showed possible ion exchange of Ag^+-Li^+ near sample-electrodes interface and electrochemical redox reaction at high temperatures.

3.1. Introduction

Since the first commercialisation of lithium batteries by Sony in the early 1990s, it has played an indispensable role in many applications including as the power source for portable devices and other micro instruments, power systems for electric vehicles and stationary energy storage systems in grids, etc. [1]. All lithium-ion batteries consist of three main components: an anode, a cathode and an electrolyte[2]. Anode materials require both a high specific capacity and a low electrochemical potential to reach an optimised overall cell voltage [3]. Cathode materials require an intercalation host structure to accept and release electrons during charging and discharging processes. [4] The main requirement for electrolytes is their ionic conductivity, which should be as high as possible in order to reduce the internal resistance of a cell during battery operations. [5]. Simultaneously, to avoid a possible short circuit, the electronic conductivity of an electrolyte should be negligible [4].

Compared to the commercialised non-aqueous electrolytes, solid state electrolytes have advantages including (a) preventing the growth of lithium dendrites and associated risks [6]; (b) avoiding the usage of non-cyclic carbonate solvents which are volatile and flammable

especially at high operating temperatures or under improper operations and (c) better mechanical properties and a simple battery package [4].

Li_4SiO_4 has two polymorphs: a monoclinic α-phase and a triclinic γ-phase, with an α- to γ-phase transition in several successive steps over a wide temperature range 600-725 °C [7]. Monoclinic Li_4SiO_4 is built of SiO_4 tetrahedra with lithium ions partially occupying the interstitial sites [8]. Li_4SiO_4 is a promising parent material for LISICON type electrolytes [9]. Stoichiometric Li_4SiO_4 has a modest ionic conductivity with ~2.5×10^{-6} Scm^{-1} at 573 K, a promising thermal stability and wide compatibility with common electrodes including lithium metal and graphite [10].

Previous attempts at anion doping attempt of Li_4SiO_4 with LiF found a new phase: Li_5SiO_4F, which has two polymorphs: low temperature α-Li_5SiO_4F and high temperature γ-Li_5SiO_4F. γ-Li_5SiO_4F has ionic conductivity ~10^{-7}-10^{-6} S/cm at ambient temperature, which is ~3 orders of magnitude higher than that of Li_4SiO_4 [11]. This study followed the reported synthesis process of Li_5SiO_4F [11], but there are extended attempts with different synthesis conditions. Based on the measured electrical properties of Li_5SiO_4F and equivalent circuit analysis, there are some unreported new findings.

3.2. Synthesis of α-/γ-Li_5SiO_4F

(a)

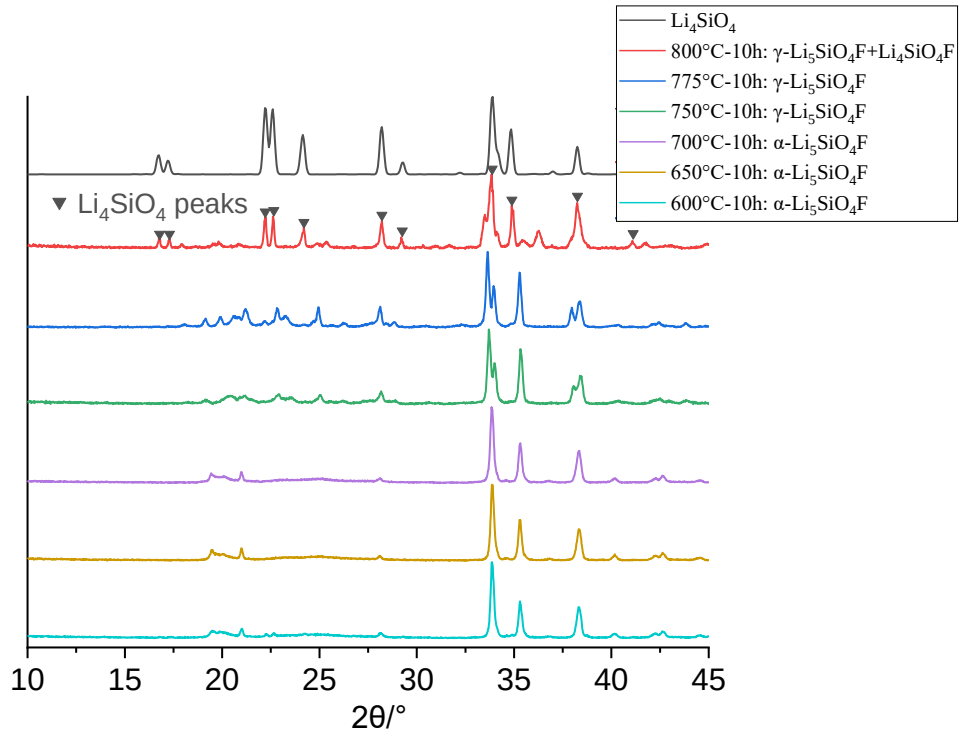

(b)

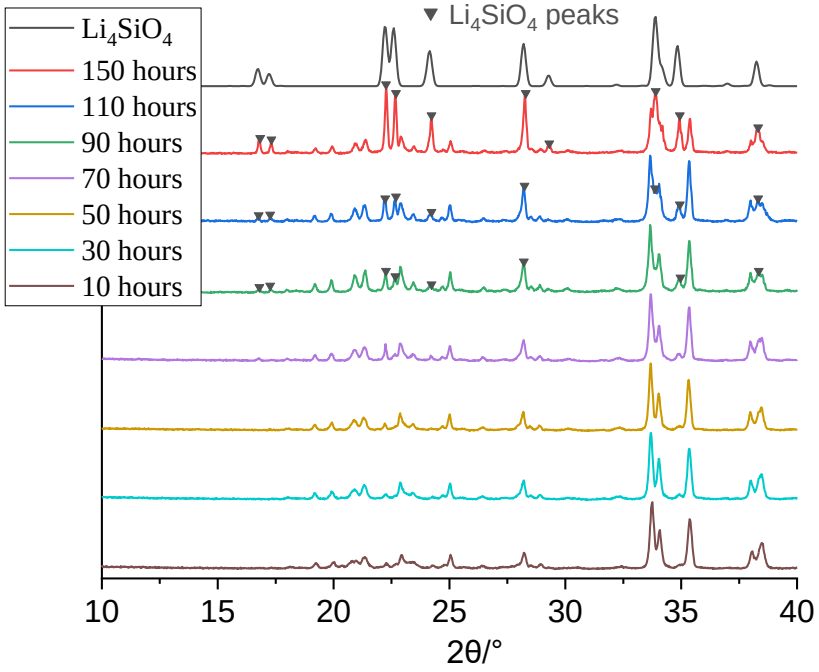

Fig 3.1 (a) Li_5SiO_4F synthesised at different temperatures,

(b) γ-Li_5SiO_4F synthesised at 775 °C for different times.

According to the previous study by Dong et al. [11], α-Li_5SiO_4F and γ-Li_5SiO_4F can be prepared at ~650 °C and ~750 °C by solid state reaction. In order to clarify the influence of synthesis temperature and time, different samples were prepared with XRD results shown in Fig 3.1 (a-b). α-Li_5SiO_4F was synthesised at 650-700 °C while γ-Li_5SiO_4F was synthesised at 750-775 °C. γ-Li_5SiO_4F had higher crystallinity with slightly higher temperature. Li_4SiO_4 was observed as a secondary phase at 800 °C and there is an unidentified peak marked in red, which indicates a possible incongruent melting of Li_5SiO_4F at ~800 °C, Fig 3.1 (a). Li_4SiO_4 was also observed on heating for > 70 hours at 775 °C, Fig 3.1 (b), which may indicate the volatilisation of LiF.

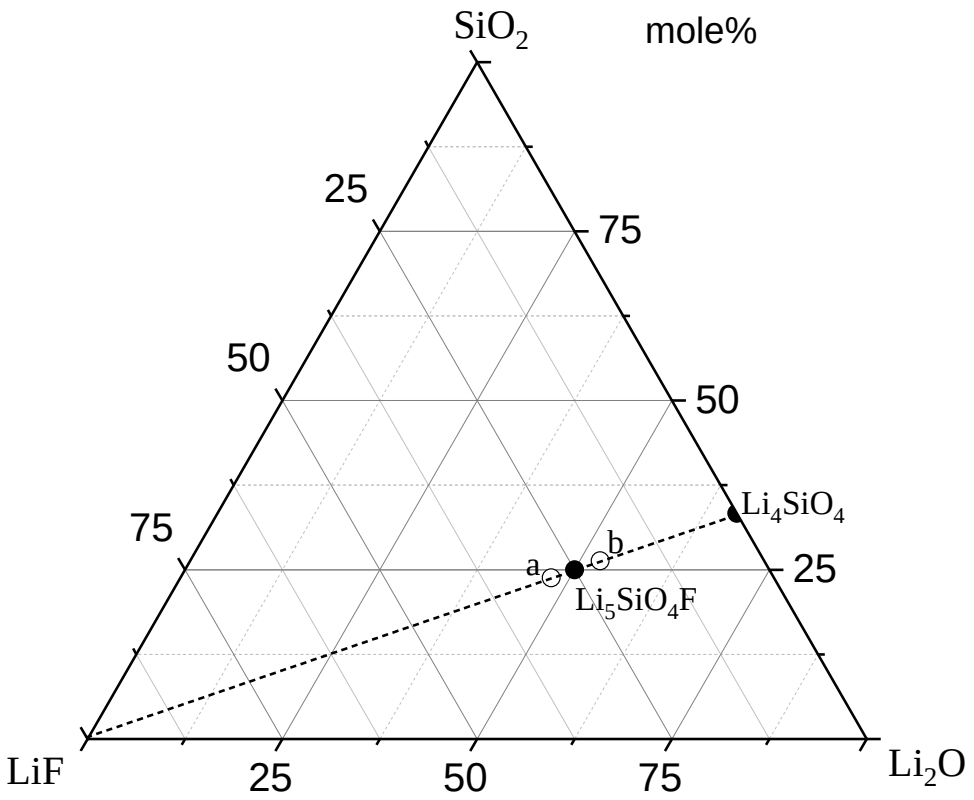

Fig 3.2. Li_5SiO_4F and two adjacent compositions in ternary system Li_2O-SiO_2-LiF

(a)

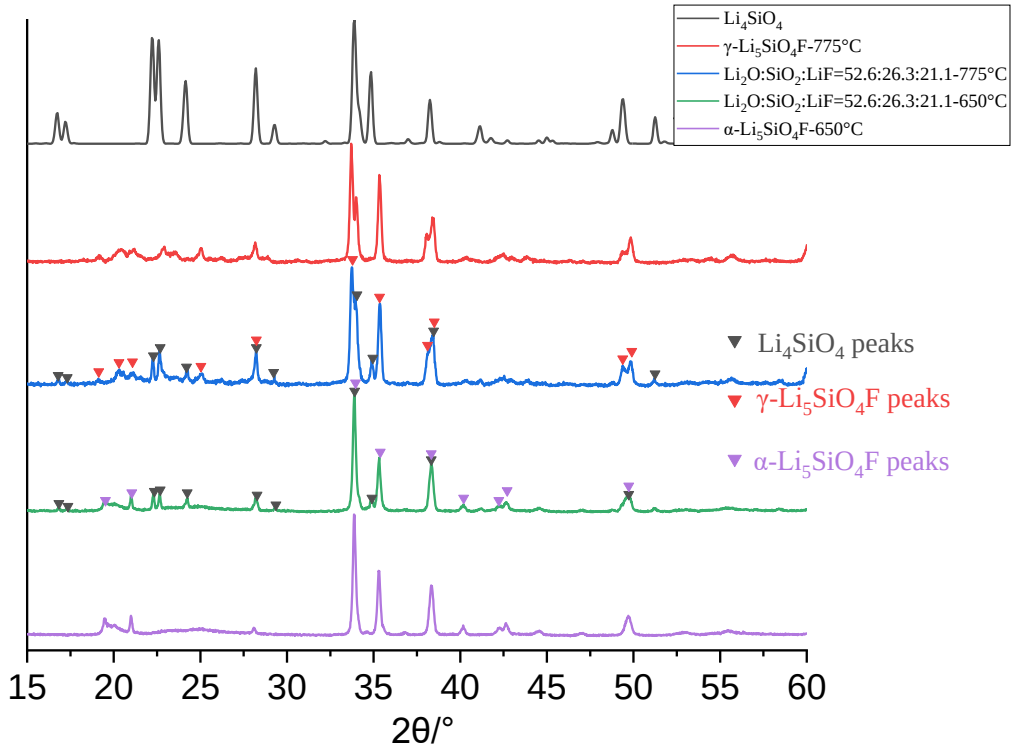

(b)

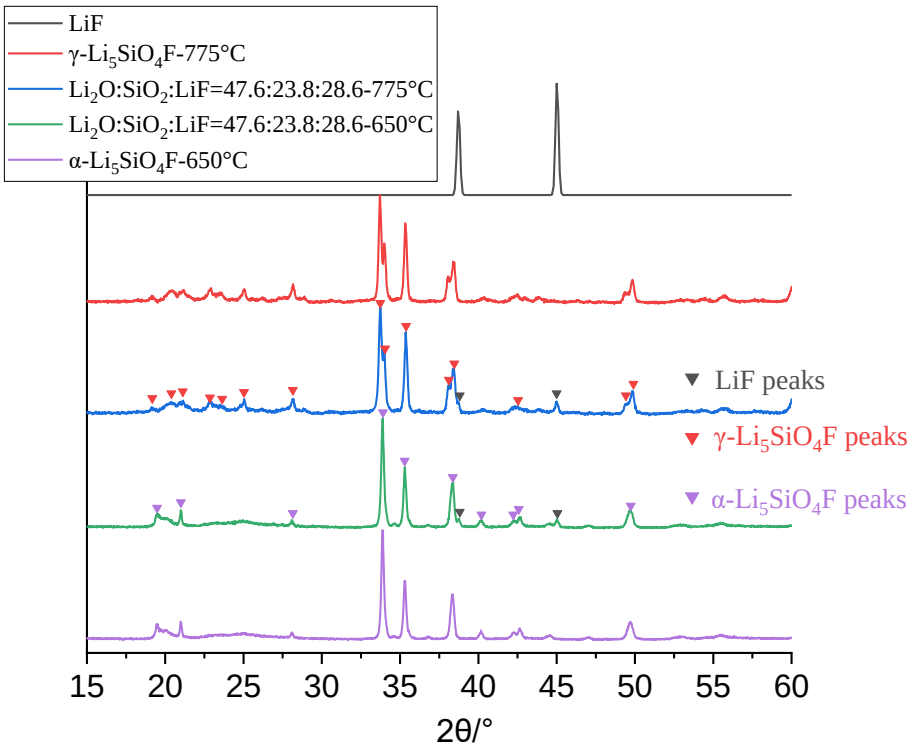

Fig 3.3. (a) $Li_2O:SiO_2:LiF=52.6:26.3:21.1$ and (b) $Li_2O:SiO_2:LiF=47.6:23.8:28.6$ prepared at 650/750°C

Li_5SiO_4F is reported to be the only single phase between Li_4SiO_4 and LiF [11], Fig 3.2. Two compositions with slightly less or more LiF than Li_5SiO_4F, Li_2O:SiO_2:LiF=47.6:23.8:28.6 (a) and Li_2O:SiO_2:LiF=52.6:26.3:21.1 (b), were prepared under the same conditions. Composition B made at either 650 °C or 775 °C showed a mixture of α-/γ-Li_5SiO_4F and Li_4SiO_4, Fig 3.3 (a), whereas composition A prepared at different temperature shows unreacted LiF, Fig 3.3 (b). Compared to standard γ-Li_5SiO_4F, the diffraction patterns of these two compositions at 775 °C showed slight differences in peak splitting of the pair of lines around 33.5 °2θ. This indicates two possibilities, either: (a) an intermediate phase between α-Li_5SiO_4F and γ-Li_5SiO_4F, or (b) a limited solid solution of Li_5SiO_4F with either excess or deficiency of F^-.

3.3. Electrical properties of Li_5SiO_4F

3.3.1. Impedance plots for γ-Li_5SiO_4F, coated with Au or Ag electrodes.

3.3.1.1. Impedance plots for Au coated γ-Li_5SiO_4F

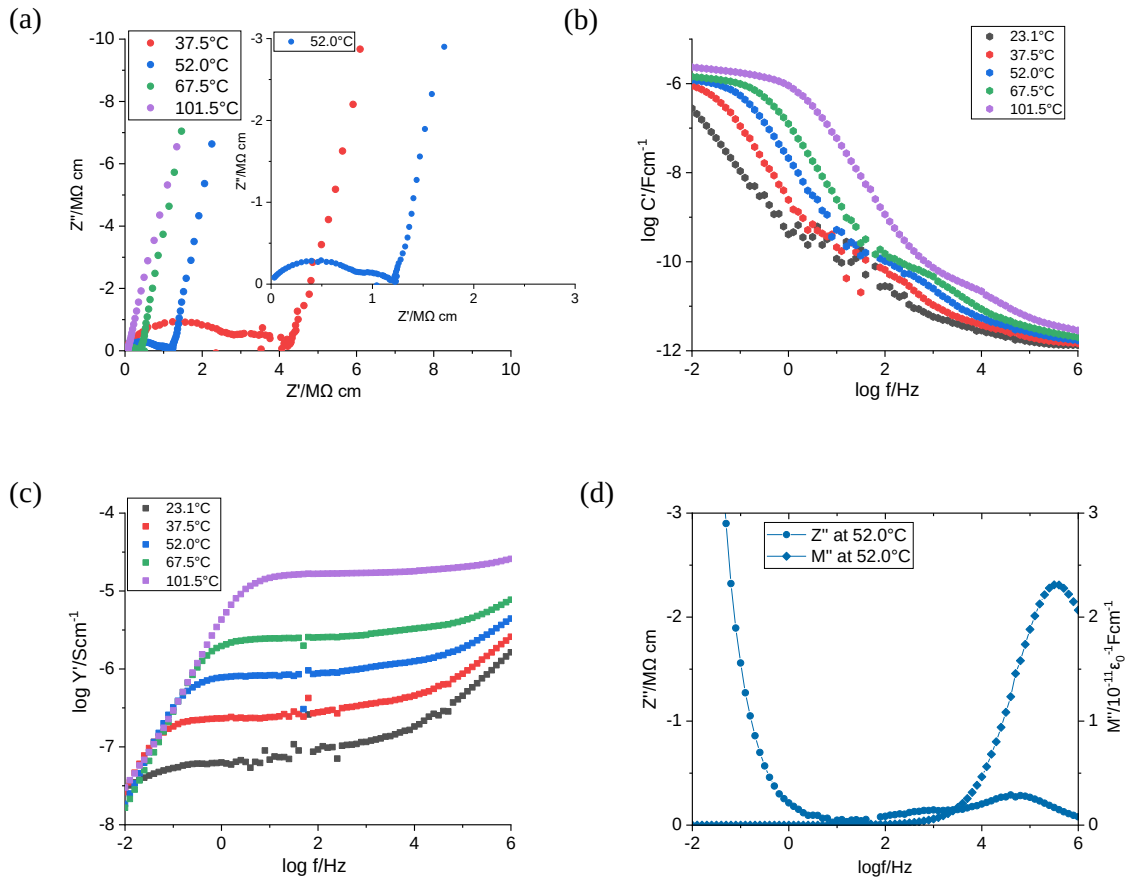

Fig 3.4. Impedance results for γ-Li_5SiO_4F (sintered at 775°C for 50 hours, Au electrodes)

(a) impedance complex plane plot at 52.0°C.

Spectroscopic plots of (b) C', (c) Y', and (d) Z''/M'' at 52.0°C

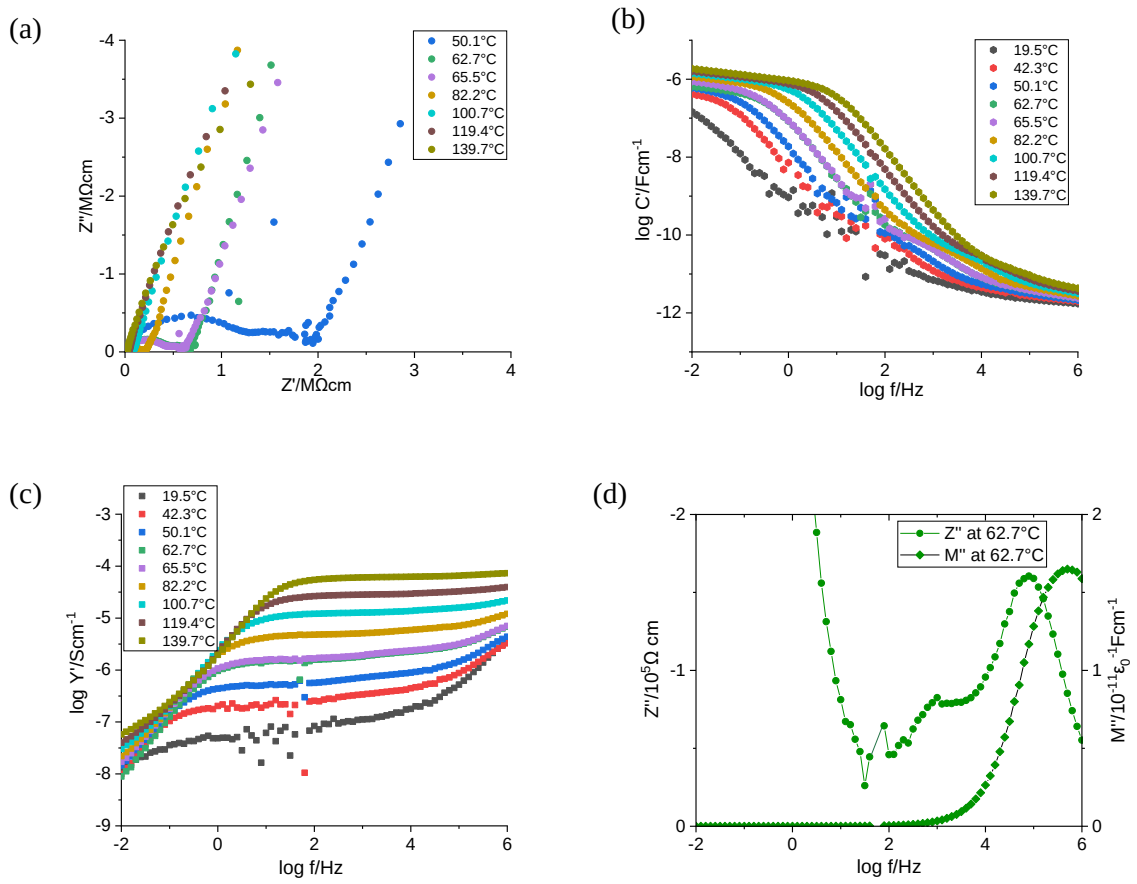

Fig 3.5. Impedance results for γ-Li_5SiO_4F (sintered at 775°C for 10 hours, Au electrodes)

(a) impedance complex plane plot

Spectroscopic plots of (b) C', (c) Y', and (d) Z''/M'' at 62.7°C

Some impedance datasets for γ-Li_5SiO_4F are shown in 4 different complementary formats in Figs 3.4 and 3.5. Typically, the impedance complex plane plots, Fig 3.4 (a), consist of two semicircles and a large spike with a total resistance of 1.21 MΩ cm at 52.0 °C. Spectroscopic plots of capacitance, (b), show 2 clear plateaux at ~10^{-6} F/cm, and ~10^{-12} F/cm, with a partially resolved intermediate plateau at ~10^{-10} F/cm. From the high frequency capacitance, ~1.2×10^{-12} F/cm, the bulk permittivity of the sample, given by $\varepsilon' = C/e_0$ is around 13.6 and is lower than the reported value of 45.2 [11]. The spike in (a) and high values of the low frequency capacitance of ~10^{-6} F/cm in (b) indicate a significant sample-electrode capacitance and therefore ionic conduction in the sample. The log Y'-log f plot in (c) shows a distorted total

conductivity plateau over the range ~10^1-10^6 Hz with dispersions at both low and high frequency ends. The sample-electrode interface is responsible for the low frequency dispersion, while the small high frequency dispersion can be attributed to Jonscher Law behaviour. The Z'' plot in (d) consists of a shoulder peak followed by the main peak at higher frequency. The intermediate frequency peak shoulder is probably associated with a grain boundary response, which is also supported by the intermediate plateau in (b) and the poorly-resolved semicircle at intermediate frequencies in (a). As the high frequency Z'' M'' peaks in (d) are nearly coincident on the frequency scale, the high frequency semicircle in (a) and the high frequency capacitance plateau at ~10^{-12} F/cm in Fig 3.4 (b) can be attributed to the bulk response. Similar impedance results are observed on γ-Li_5SiO_4F synthesised for 10 h, Fig 3.5.

3.3.1.2. Impedance plots for Ag coated γ-Li_5SiO_4F

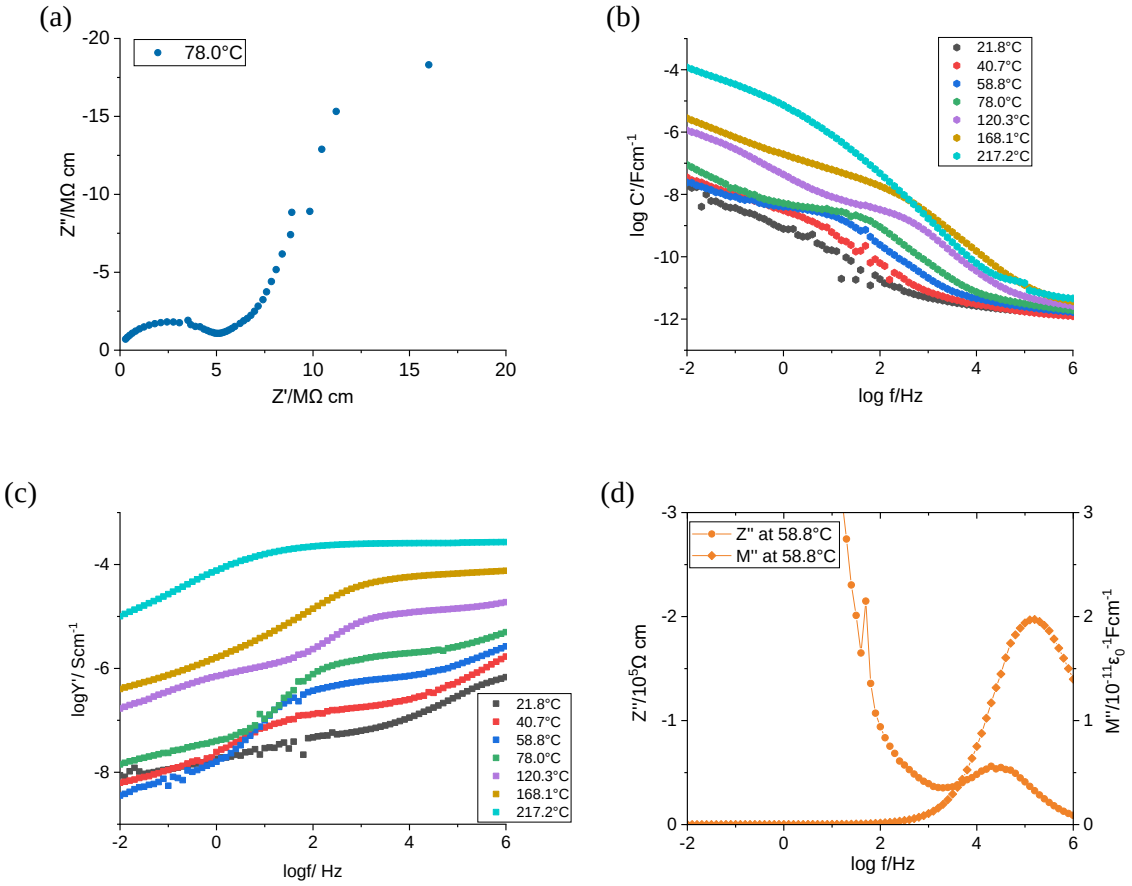

Fig 3.6. Some impedance datasets for Li_5SiO_4F (sintered at 750°C, 10 hours, coated with Ag at ambient temperature) (a) Z''-Z' complex plane plot at 78.0°C,Spectroscopic plots of (b) C', (c) Y', and (d) Z''/M'' at 58.8°C.

Impedance data were also collected on a γ-Li_5SiO_4F pellet coated with Ag electrodes, Fig 3.6, which is clearly different to that of Au coated sample. In specific, the impedance complex plane plot, (a), consists of a depressed semicircle which is more likely to be two partially overlapped semicircles and a non-linear spike. The capacitance, (b), shows a similar value to Au-coated Li_5SiO_4F around 10^{-12} F/cm, but a clear plateau seen at ~10^{-8} F/cm is 2-3 orders of magnitude higher than a typical grain boundary value. It is possible that Li^+/Ag^+ exchange at the sample surface gave a more resistive, thin surface layer containing immobile Ag^+ ions, represented by the capacitance plateaux at 10^{-8} F/cm at 21.8-78.0 °C. With increasing temperature, at 120-

217 °C, C' increased to 10^{-4} F/cm at 10^{-2} Hz which indicates that, instead of a double layer capacitance with value 1-10 μF forming at the sample-electrode interfaces, an electrochemical redox reaction occurred, especially at high temperatures. At 217 °C, the capacitance value of 100 μF can be attributed to both resistive Ag^+ layer and the redox reactions which may possibly increase further at still lower frequencies.

3.3.2. Equivalent circuit analysis

3.3.2.1. Fitting to Bulk γ-Li_5SiO_4F and possible dipole effect

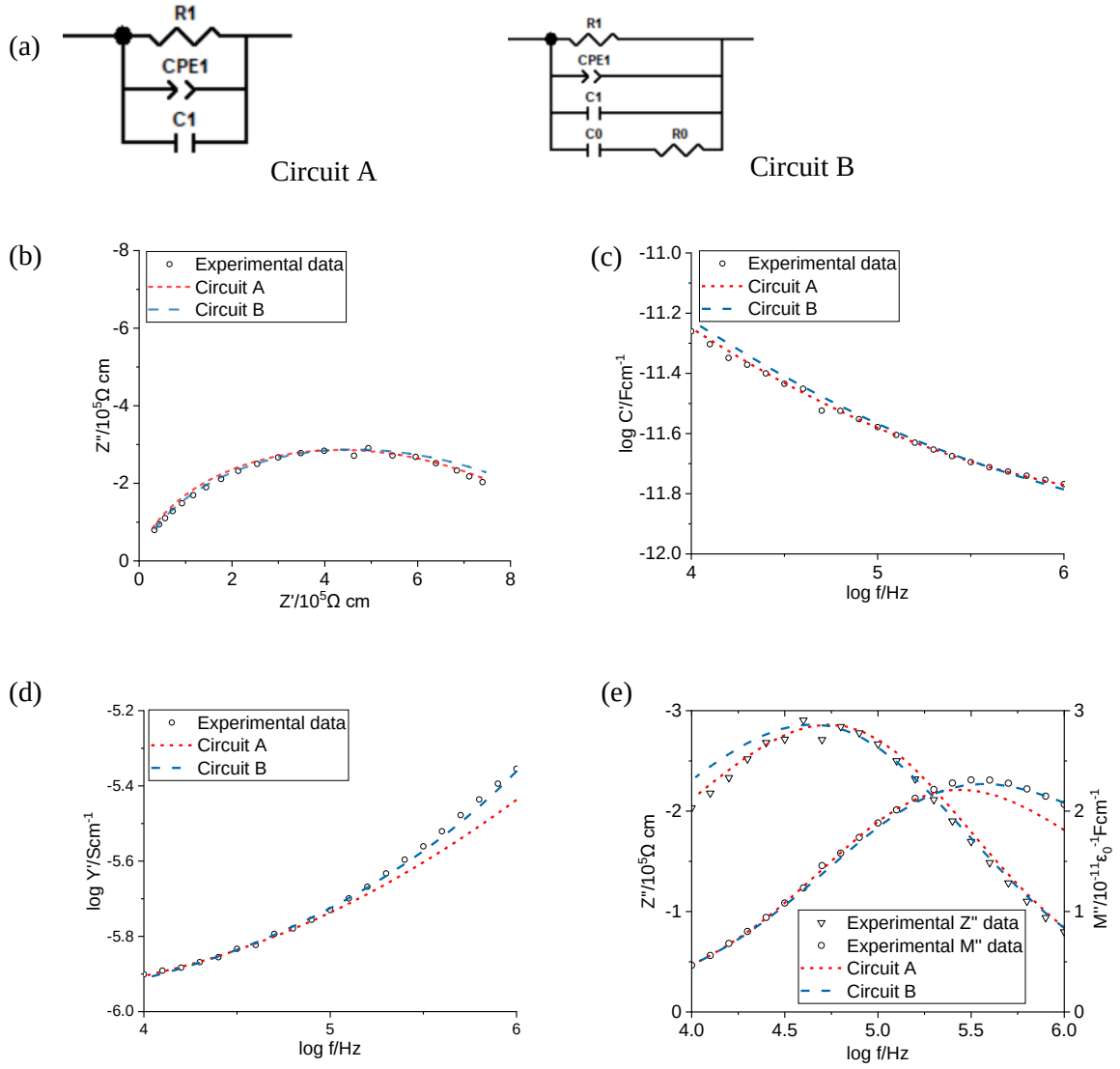

Fig 3.7. Different equivalent circuits fitted to the bulk response in γ-Li_5SiO_4F at 52.0°C (sintered at 775°C for 50 hours) coated by Au electrodes.

Table 3.1. Fitted values by Circuit B of the dipole elements, R_0 and C_0, and bulk capacitance, C_1, for γ-Li_5SiO_4F (sintered at 775°C for 50 hours) coated by Au electrode at different temperatures

Temperature	R_0 / kΩ	C_0 / pFcm^{-1}	C_1 / pFcm^{-1}	R_1 / kΩ	CPE_1-T /nFcm^{-1}	CPE_1-P
52.0°C	210(50)	0.37(9)	1.3(4)	1030(68)	1.6(8)	0.50(9)
67.5°C	369(2)	0.5(2)	1.1(2)	370(3)	8(2)	0.40(2)
101.5°C	98(5)	1.6(4)	1.3(4)	55.7(1)	3.6(4)	0.515(8)

Since the impedance data in Fig 3.4 (a) for γ-Li_5SiO_4F (heated for 50 h) showed evidence for two overlapping components, equivalent circuit analysis was carried out to characterise the two components.

First, two possible circuits that may fit the bulk response as shown in Fig 3.7 (a) were fitted to the experimental data at 52.0 °C, with results shown in (b-e). Circuit A is a common circuit used to fit a bulk response and consists of a parallel RC element and a constant phase element CPE in parallel. R represents the sample resistance and C represents the capacitance or polarisability. The additional CPE element, CPE_1, represents the frequency-dependent response of a real bulk, simultaneously taking the frequency-independent permittivity into account, especially at high frequencies and low temperatures. As dielectric losses are ubiquitous in real bulk samples, which are associated with short range, charge displacement processes [12-13], Circuit B has an additional dipole element, R_0C_0, which has been suggested to represent a dipole component in addition to the long range conductivity in samples of yttria-stabilised zirconia, where R_0 depends on the difficulty of the corresponding atomic displacement, and C_0 represents the charge stored by the process of dipole reorientation and subsequent alignment [13].

The fit results, in Fig 3.7, show that Circuit A gives a poor fit to the high frequency admittance in (d) and to the M'' peak shoulder at high frequencies in (e). The fit results for Circuit B in (b-e) show good fit to the high frequency Y' data especially for the high frequency admittance data in (d). Circuit A represents the Jonscher Law dispersion, whereas Circuit B would represent both the high frequency dispersion and the dipole effect. As summarised in Table 3.1,

C_0 increases with higher temperatures, but its value is very small; R_0 decreases with increasing temperature, as expected for a thermally activated process. C_1 seems to be temperature independent. The value of R_1 decreases with higher temperature. Circuit B shows poor fitting to $C^{'}$, (c) and $Z^{''}$, (e), at lower frequencies, 10^4-5×10^4 Hz. The possible reason for that is the grain boundary contribution affected the impedance data over the entire frequency range and therefore needed to be considered to achieve a better fitting. However, fitting results using Circuits A and B offer an example of the dipole behaviour in γ-Li_5SiO_4F, how it can be represented by R_0C_0 and how it can affect the impedance results especially at the high frequency end.

3.3.2.2. Fitting to Bulk and possible 'grain-boundary' in γ-Li_5SiO_4F

(a)

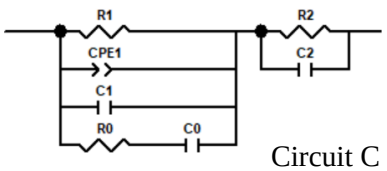

Circuit C

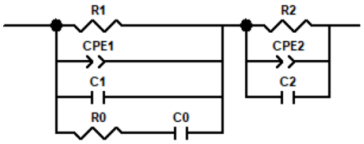

Circuit D

(b)

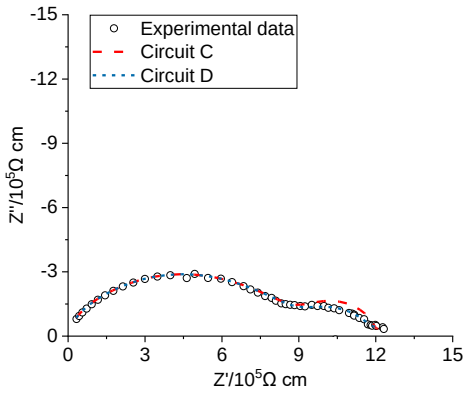

(c)

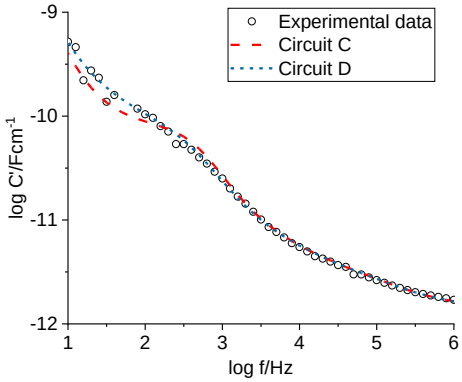

(d)

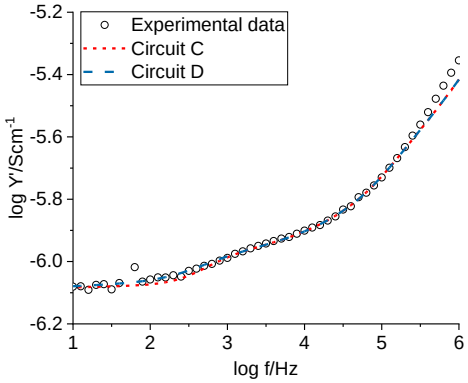

(e)

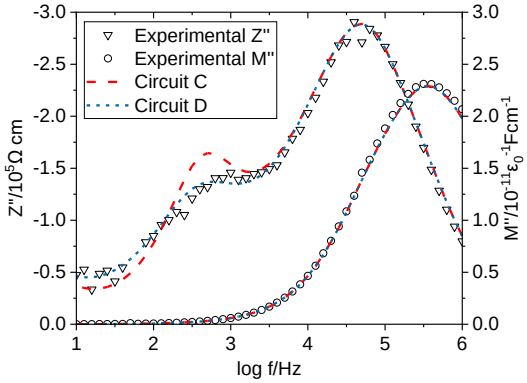

Fig 3.8. Different equivalent circuits fitted to both bulk and grain boundary components in γ-Li_5SiO_4F at 52.0°C (sintered at 775°C for 50 hours) coated by Au electrode

In order to determine the possible influence of possible 'grain boundary' impedance on the overall impedance results, Circuits C and D, in Fig 3.8 (a), were tested. The results, (b-e), show that a grain boundary element with additional CPE_2 (Circuit D) gives a better fit to the

experimental data. However, fitting to the highest frequency admittance in (d) is not improved by introducing the grain boundary element.

3.3.2.3. Fitting to overall impedance responses in γ-Li_5SiO_4F

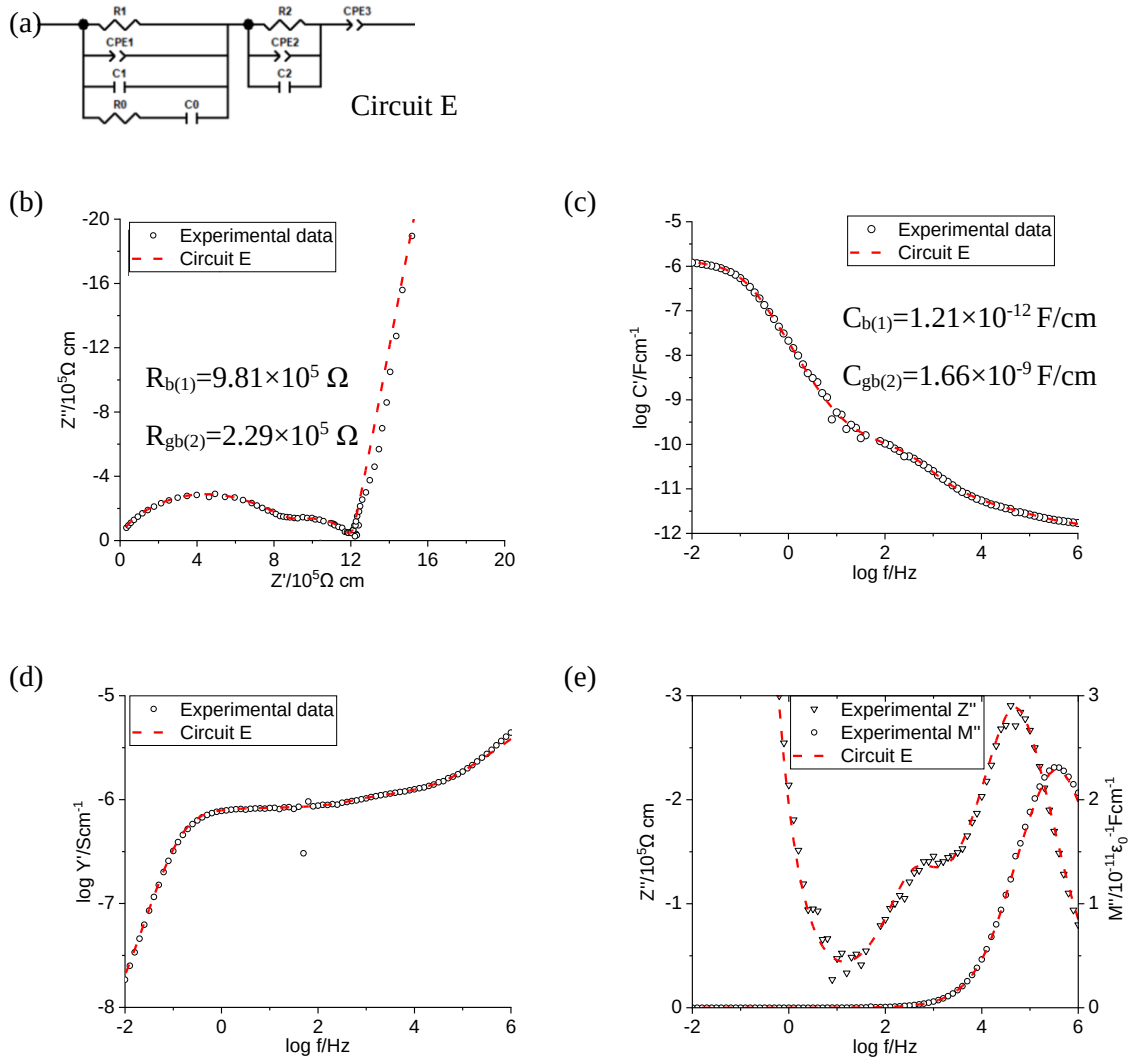

Fig 3.9. Experimental and fitted impedance datasets for γ-Li_5SiO_4F at 52.0°C (sintered at 775°C, 10 hours, coated with Au)

(b) Z''-Z' complex plane plot, spectroscopic plots of (c) capacitance C', (d) admittance Y', and (e) Z'', M''

Equivalent circuit analysis of the data set at 52°C, shown in Fig 3.4, was carried out using the circuit shown in Fig 3.9 (a), which consists of 3 elements in series, corresponding to the responses from bulk, grain boundary and sample-electrode interface. Fitting results at 52 °C are shown in Fig 3.9 (b-e). Compared with circuit D in (a), CPE_3 is used to fit the sample-electrode interface response. The impedance plots in (b) give $R_1=9.81\times10^5$ Ω and $R_2=2.29\times10^5$ Ω. The poorly fitted part of the spike may indicate a rough sample-electrode interface [14]. Capacitance data fit well to the equivalent circuit in (c), with C_1 (bulk)$=1.21\times10^{-12}$ F/cm and C_2 (grain boundary)$=1.66\times10^{-9}$ F/cm. C_2 is higher than expected compared with the literature value around 8×10^{-12} F/cm [15], indicating a very thin grain boundary. The low frequency capacitance data are well fitted, presumably because the Au-sample interface acts as a blocking double layer capacitor (CDL). $Y^{'}$ data fit well in (d) with a plateau over 10^0-10^4 Hz, followed by a high frequency power law dispersion. The $M^{''}$ peak fits well to the equivalent circuit in (e). The fitting results for impedance data at 65.5 °C are shown in Fig 3.S1 in Appendix.

Fitting results for γ-Li_5SiO_4F heated for 50 h with impedance data in Fig 3.5 are shown in Fig 3.S2 (67.5 °C) and Fig 3.S3 (101.5 °C) in Appendix, while the fitting results for γ-Li_5SiO_4F heated for 110 h at 40.6 °C are shown in Fig 3.S4 in Appendix. These results indicate a universally good fitting to overall impedance response by Circuit E, as shown in Fig 3.9(a).

These equivalent circuit studies show that Circuit E is suitable for ionically conducting γ-Li_5SiO_4F with clear bulk, grain boundary and sample-electrode interface responses. The bulk response data consist of the usual parallel combination of R_1-C_1-CPE_1, but with addition of a dipolar element R_0C_0.

3.3.2.4. The Arrhenius plot for different Li_5SiO_4F samples, Li_4SiO_4 thin layer in Li_5SiO_4F

Table 3.2. Fitted capacitance value for bulk, grain boundary and sample-electrode interphase response in different γ-Li_5SiO_4F samples sintered at 775°C for different time.

γ-Li_5SiO_4F	Temperature/K	Bulk cpacitance $C_b(C_1)$/pFcm^{-1}	Grain boundary capacitance C_{gb} (C_2)/nFcm^{-1}	Sample-electrode capacitance C_{dl}/Fcm^{-1}
Synthesised for 10 hours	323.3	1.30	4.00	4.00×10^{-7}
	338.7	1.26	2.02	6.00×10^{-7}
	355.4	1.20	2.80	1.10×10^{-6}
Synthesised for 50 hours	310.6	1.00	6.00	8.40×10^{-7}
	325.1	1.01	3.80	1.02×10^{-7}
	340.7	1.11	3.80	1.09×10^{-7}
	374.7	1.33	4.85	1.77×10^{-7}
Synthesised for 110 hours	313.8	1.03	11.03	3.60×10^{-7}
	331.7	1.01	9.00	4.41×10^{-7}
	350.8	1.01	8.00	5.30×10^{-7}
	393.3	1.51	18.05	7.60×10^{-7}

Based on the fitting results, shown in Figures 3.9 and 3.S1-S4, capacitance data of each component, bulk, grain boundary, or sample-electrode interface, in different γ-Li_5SiO_4F samples are summarised in Table 3.2. The average bulk capacitance C_1 of different Li_5SiO_4F samples is ~1pF/cm, and shows no obvious variation with sintering time. The grain boundary capacitance C_2 fluctuated around 1-10 nF/cm. A typical grain boundary capacitance is expected to be 1-2 orders of magnitude higher than C_1, especially in poorly-sintered materials, but the values shown in (c) are 3-4 orders of magnitude larger, especially after longer synthesis times. This indicates that the grain boundary becomes thinner with time and may be due to either reduced porosity associated with increased sintering of the grain-grain contacts, or due to formation of a very thin layer of Li_4SiO_4 formed by volatilisation of LiF. The capacitance of the sample-electrode interface, (d), increased with measuring temperature, giving an average capacitance of 10^{-6} F/cm.

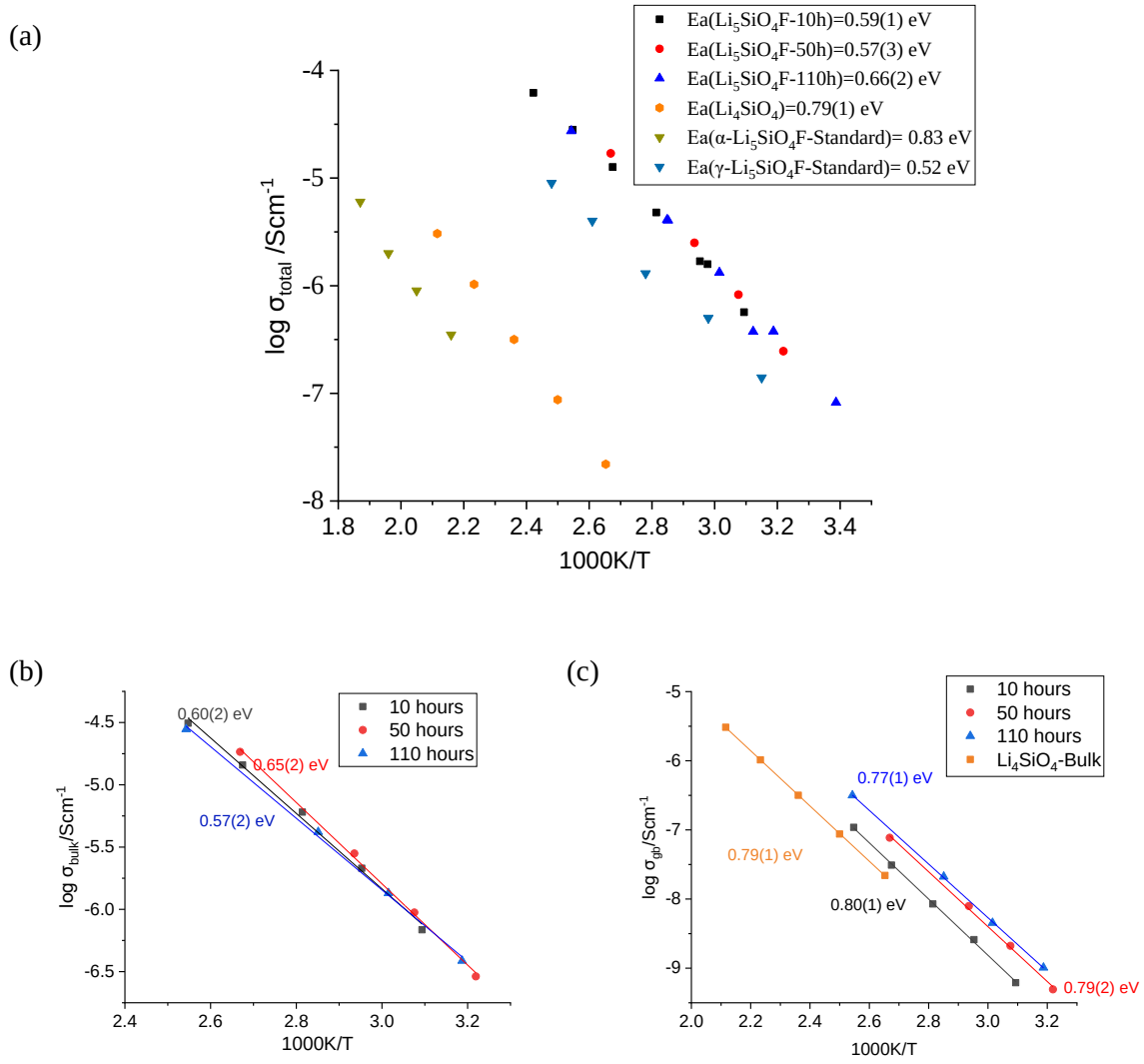

Fig 3.10. (a) The Arrhenius plot for total ionic conductivity for different Li_5SiO_4F samples

The Arrhenius plot for (b) bulk, (c) grain boundary (geometry corrected) for different Li_5SiO_4F samples (sintered at 775°C, for 10, 50, and 110 hours)

Based on the impedance results and fitting results with Circuit E, Arrhenius plots for different Au-coated γ-Li_5SiO_4F samples are shown in Fig 3.10 (a) , giving an average total ionic conductivity of ~2×10^{-7} S/cm at 25 °C, which is 2-3 orders of magnitude higher than that of Li_4SiO_4. There is no significant difference in total ionic conductivity with sintering time. The fitted bulk and grain boundary conductivities are shown in (b-c). The bulk Arrhenius plot, (b),

shows similar ionic conductivity for samples heated for different times at 775 °C, with smallest activation energy of 0.57(2) eV, which is still slightly higher than the previously reported value of 0.51 eV [11].

Table 3.3. The activation energy of bulk and grain boundary in different γ-Li_5SiO_4F

Sample	Activation energy -bulk/eV	Activation energy - grain boundary/eV	Relative density
γ-Li_5SiO_4F-10 hours	0.60(2)	0.80(1)	0.76(1)
γ-Li_5SiO_4F-50 hours	0.65(2)	0.79(2)	0.77(1)
γ-Li_5SiO_4F-110 hours	0.57(2)	0.77(1)	0.82(1)

The geometry corrected grain boundary conductivities were calculated by correcting for the difference between the fitted bulk and grain boundary capacitances, as shown in Table 3.3, ~3.5×10^3. Although this gives only a rough estimation of the real grain boundary conductivities, the Arrhenius plots in (c), show almost the same conductivity and activation energy as that of bulk Li_4SiO_4. This strongly indicates that the apparent grain boundary response represents a very thin layer of Li_4SiO_4 formed either at the grain boundary or at the pellet surface. This explanation is supported by the capacitance values for C_2, in Table 3.2, which are 1-2 orders of magnitude higher than expected for a typical grain boundary. The porosity, given by the relative density, decreases with increasing synthesis time. However, there is no evidence of change in either of the activation energies with heating time even though there was a gradual increase in pellet density. The similarity in conductivities, Fig 3.10 (b) indicates that the γ-Li_5SiO_4F main phase was fully formed after 10 h and the effect of longer heating time was to improve slightly sintering and pellet density, but the pellets probably gradually lost LiF by volatilisation, leaving a thin layer of Li_4SiO_4.

3.3.2.5. Fitting to impedance responses of Ag coated γ-Li_5SiO_4F, possible Li^+/Ag^+ exchange

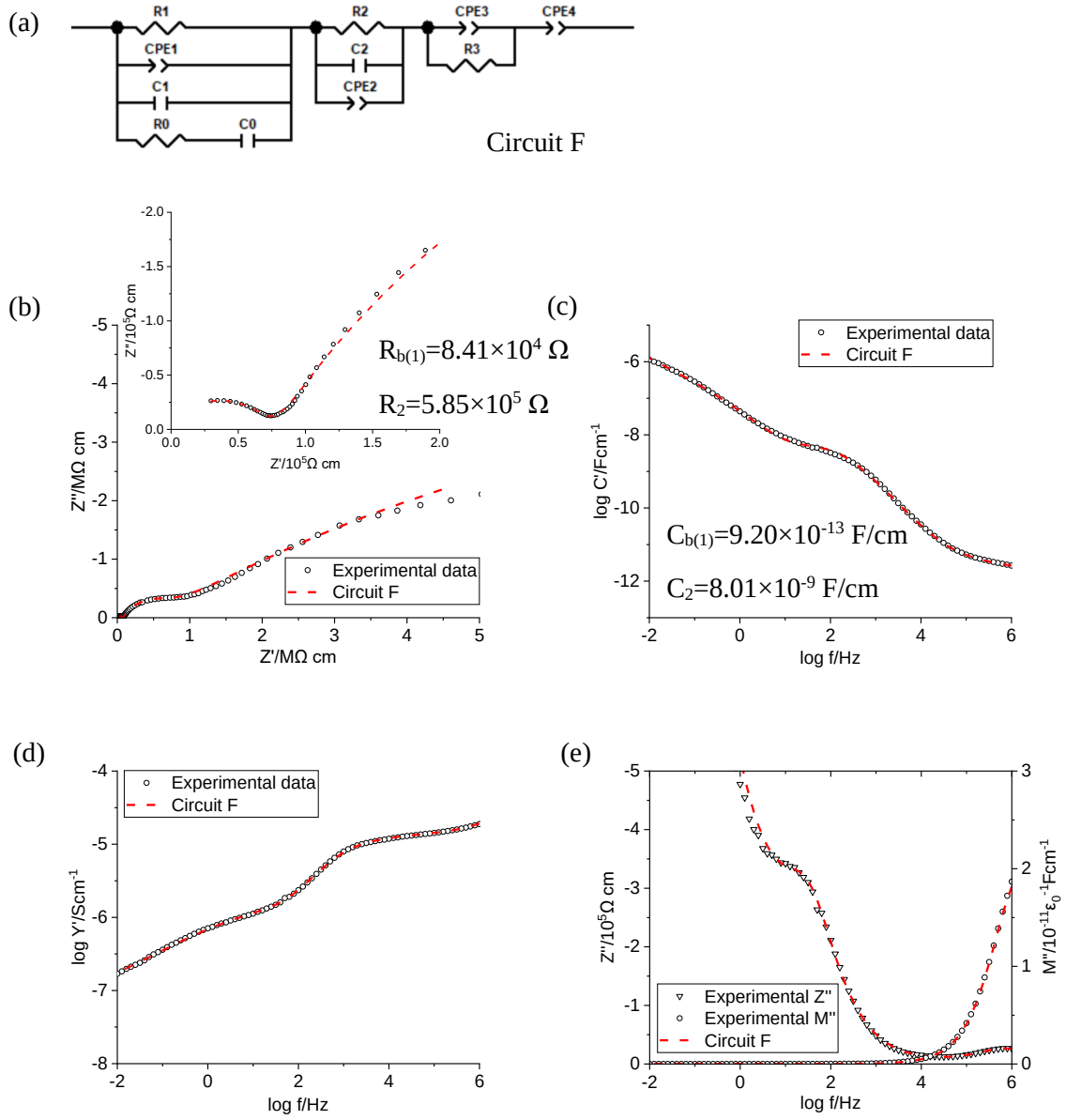

Fig 3.11. Experimental and fitted impedance dataset for γ-Li_5SiO_4F (sintered at 775°C, 10 hours, coated with Ag) at 120.3°C.

(b) $Z^{''}$-$Z^{'}$ complex plane plot, spectroscopic plots of (c) capacitance C', (d) admittance Y', and (e) $Z^{''}M^{''}$.

Equivalent circuit analysis has been carried out for γ-Li_5SiO_4F coated with Ag electrode, with impedance data in Fig 3.6, to investigate the effect of Ag electrode and possible LiF loss. Fitting results by Circuit F, (a) are shown in Fig 3.11. Circuit F is similar to Circuit E, in Fig 3.9, but with an additional element R_3-CPE_3. The Ag-coated samples had a more complicated sample-electrolyte interface response than Au-coated samples as curved spike in Figs 3.11 (b). As well as possible volatilisation of LiF, referred to above, an additional complication appears to arise from Ag/Li exchange at sample surfaces. The spectroscopic plots of Z'' and M'' for γ-Li_5SiO_4F, in Fig 3.11 (e), fit well apart from a range of intermediate frequencies at ~1 Hz that correspond to an intermediate region between element 2 and element 3, which is possibly due to the Ag layer formed near the sample-electrode interphase.

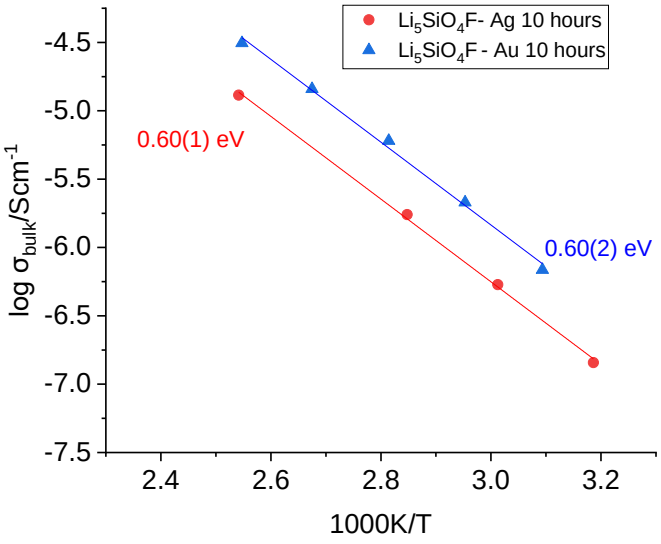

Fig 3.12. The Arrhenius plots for bulk ionic conductivity of γLi_5SiO_4F coated with either Au, or Ag electrode.

The Arrhenius plot in Fig 3.12 used the fitted values of bulk resistance R_1. The bulk ionic conductivity of γ-Li_5SiO_4F with Au coated sample is 4-5 times higher than the Ag coated sample. Both samples have a similar activation energy. The reason for that is more likely to be

a reduction of mobile Li^+ ion concentration possibly due to Li^+/Ag^+ exchange near the sample surface, rather than to a mixed alkali effect involving Li^+/Ag^+ mixed conductivity which usually results in a reduced ionic conductivity but increased activation energy [16].

3.3.2.6. General considerations in Ag coated samples, with fitting to two compositions adjacent to γ-Li_5SiO_4F

(a)

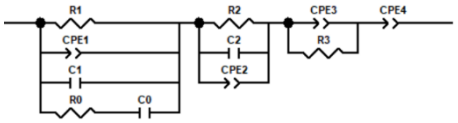

Circuit F

(b)

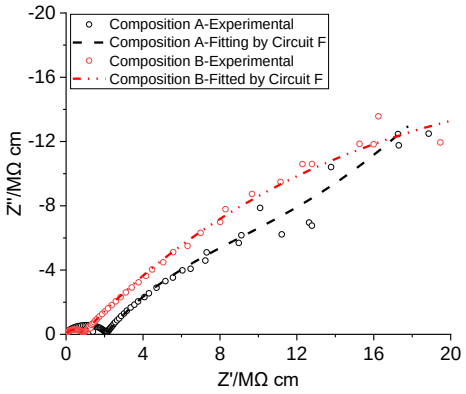

(c)

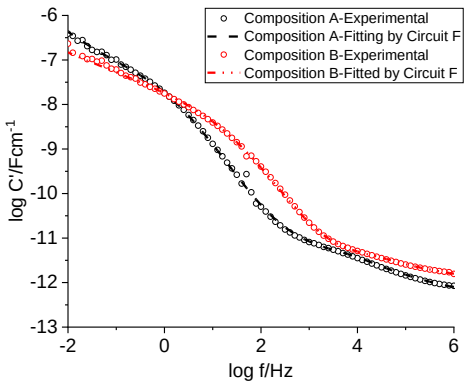

(d)

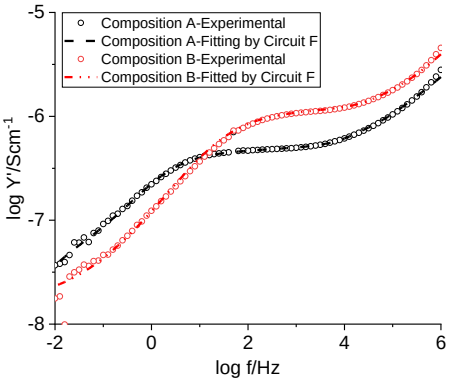

(e)

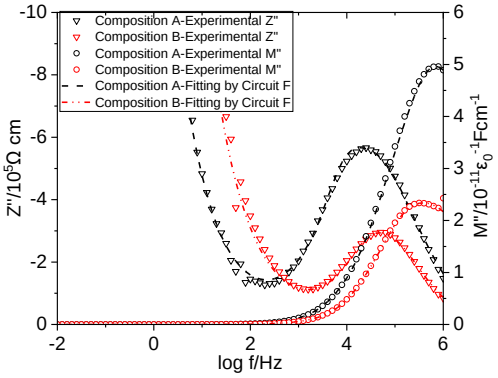

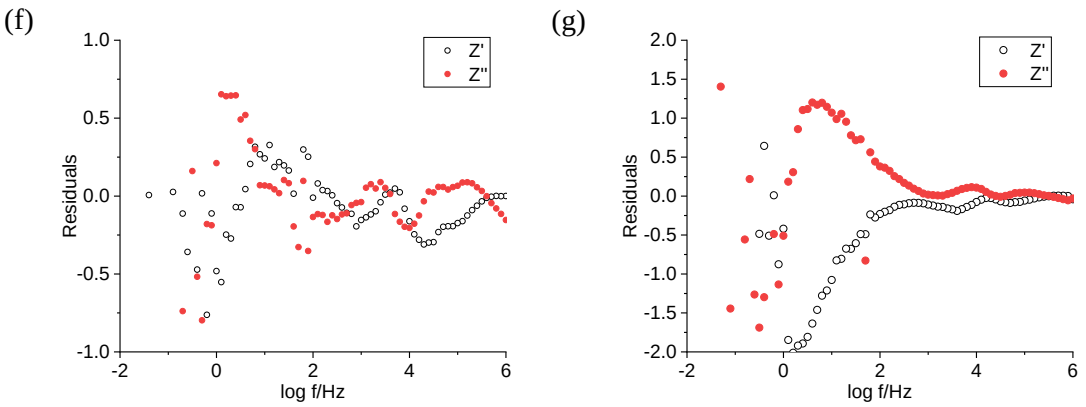

Fig 3.13. Test and fitted impedance dataset for composition A: Li_2O:SiO_2:LiF=47.6:23.8:28.6 at 104.8°C and composition B: Li_2O:SiO_2:LiF=52.6:26.3:21.1 at 124.2°C (sintered at 775°C, 10 hours, coated with Ag) (b) Z''-Z' complex plane plot, spectroscopic plots of (c) C, (d) Y, and (e) $Z''M''$

Residuals plots (Z'-Z'') for (f) composition A and (g) composition B

Impedance data for compositions with slightly less or more LiF than Li_5SiO_4F were collected followed the same procedures with that of pure Li_5SiO_4F, with Li_2O:SiO_2:LiF=47.6:23.8:28.6 (a) and Li_2O:SiO_2:LiF=52.6:26.3:21.1 (b) with fitting results shown in Figs 3.13. Impedance pellets were coated with Ag. Compared to Ag coated Li_5SiO_4F, with fitting result in Fig 3.11, the main difference for them is the nature of C' at intermediate and low frequencies, in which C' increases more gradually from ~10^{-9}-10^{-8} F, Fig 3.13 (c), to 10^{-6} F, Fig 3.11 (c). Compositions A and B, have a bulk capacitance with ~5×10^{-13}-10^{-12} F/cm, which is slightly lower than that of γ-Li_5SiO_4F with ~10^{-12} F/cm. The fitting to Z''-M'' for Compositions A and B, shown in Fig 3.13 (e), show more separated peaks in Composition A, indicating a more inhomogeneous bulk, which may be attributed to deficiency of Li^+ or/and F^-. The residual in Figures 3.13 (f-g) show an average value ~≤0.5, which is higher than the targeted value of ≤0.1. It could perhaps be improved with better quality impedance data or shows a larger error in fitting of a non-single phase sample.

In general, several possible influences should be taken into account when analysing the impedance datasets of Ag coated sample: (a) an electrochemical reaction between Li^+ ions near the pellet surface and Ag in the metal electrode, (b) diffusion of Ag^+ towards the surface of Li_5SiO_4F, and (c) some remaining double layer capacitor with ionic conductivity. The R_1-C_1-CPE_1-R_0C_0 element represents the bulk response taking dipole effect into account. The R_2-C_2-CPE_2 element possibly represents the response of a very thin Ag^+ layer formed near the sample surface during Li^+/Ag^+ exchange in γ-Li_5SiO_4F; while the simple R_2-C_2 element represents a typical grain boundary in Compositions A and B. The R_3-CPE_3 element in parallel is used to show the mixed ionic and electronic conductivity. Specifically, a charge transfer resistance (R_{CT}) is commonly used to quantify the redox reaction at sample-electrode interface. The redox reaction always occurs in two directions including lithium reduction reaction and lithium evolution reaction, which are separately represented by two different R_{CT} elements with one dominating the sample-electrode interface [15]. Then, a Warburg impedance, CPE_3, with ideal n value of 0.5, which appears as a spike with an inclined angle of 45° to the Z' axis in complex plane plots, is suggested to be used to represent the diffusion-controlled impedance [15]. The CPE_4 element is suggested to be used when there is a rough sample surface in contact with electrode [14].

3.4. Conclusion

α-Li_5SiO_4F and γ-Li_5SiO_4F were synthesised at 650°C and 775°C, similar to that previously reported by Dong (2019) [11] and a detailed study on its impedance of γ-Li_5SiO_4F has been made. γ-Li_5SiO_4F decomposes gradually due to volatilisation of LiF during prolonged heating as shown by both XRD results and impedance data: Li_4SiO_4 is observed to appear gradually in the XRD patterns of samples given prolonged heating. A thin layer of Li_4SiO_4 at pellet surfaces of interfaces is detected by impedance measurements. γ-Li_5SiO_4F shows an average bulk ionic conductivity of ~2×10^{-7} S/cm at ambient temperature, which is 2-3 orders of magnitude higher than that of Li_4SiO_4. There is no evidence of bulk conductivity variation with longer synthesis time and increased pellet density. The activation energy for the bulk conductivity of γ-Li_5SiO_4F is 0.57(2) eV, which is slightly higher than the value, 0.51 eV reported in the literature [11]. There is clear dipole effect in the bulk of γ-Li_5SiO_4F, given by better fitting circuit with R_0C_0 element. The possible existence of dipole effect should be considered when looking into the

bulk behaviours of other materials. Impedance measurements on Li_5SiO_4F with Ag electrodes gave a significantly higher and less well-defined sample-electrode interface capacitance, which is attributed to Ag^+-Li^+ ion exchange between sample and electrodes and, at higher temperatures, an electrochemical redox reaction across the sample-electrode interface, which offers a good example for further investigations on Ag coated impedance pellets. A reduced ionic conductivity of Li_5SiO_4F is observed with Ag electrodes and may possibly be attributed to the reduced concentration of mobile Li^+ carriers by Li^+/Ag^+ exchange. Although XRD results suggest Li_5SiO_4F possibly forms a very limited solid solution with excess and/or deficiency of LiF, two compositions A and B adjacent to Li_5SiO_4F show a reduced bulk ionic conductivity.

References

[1] Y. Wang, B. Liu, Q. Li, S. Cartmell, S. Ferrara, Z. D. Deng, and J. Xiao, "Lithium and lithium ion batteries for applications in Microelectronic Devices: A Review," *Journal of Power Sources*, vol. 286, pp. 330–345, 2015.

[2] A.R. West Lithium ion conductors in 'Solid State Chemistry and Its Applications, 2th edition'. John Wiley & Sons. West Sussex, pp. 418-419.

[3] X. Duan, Y. Ren, and L. Chen, "Lithium metal anodes for high-performance rechargeable batteries," *Metal Electrodes for Battery Technologies*, 2021.

[4] A.R. West Lithium battery in 'Solid State Chemistry and Its Applications, 2th edition'. John Wiley & Sons. West Sussex, pp.425-427.

[5] K. Xu, "Electrolytes and interphases in li-ion batteries and beyond," *Chemical Reviews*, vol. 114, no. 23, pp. 11503–11618, 2014.

[6] Y. Gong, L. Liu, J. Qi, M. Yang, J. Li, H. Wang, H. Guo, G. Zhang, and T. Lu, "A comprehensive study on $Li_4Si_{1-x}Ti_xO_4$ ceramics for advanced tritium breeders," *Journal of Advanced Ceramics*, vol. 9, no. 5, pp. 629–640, 2020.

[7] A. R. West, "Ionic conductivity of oxides based on Li_4SiO_4," *Journal of Applied Electrochemistry*, vol. 3, no. 4, pp. 327–335, 1973.

[8] Y. Deng, C. Eames, J.-N. Chotard, F. Lalère, V. Seznec, S. Emge, O. Pecher, C. P. Grey, C. Masquelier, and M. S. Islam, "Structural and mechanistic insights into fast lithium-ion

conduction in Li_4SiO_4–Li_3PO_4 solid electrolytes," *Journal of the American Chemical Society*, vol. 137, no. 28, pp. 9136–9145, 2015.

[9] A.R. West Li_4SiO_4 in 'Solid State Chemistry and Its Applications, 2th edition'. John Wiley & Sons. West Sussex, pp. 193.

[10] A. D. Robertson, A. R. West, and A. G. Ritchie, "Review of crystalline lithium-ion conductors suitable for high temperature battery applications," *Solid State Ionics*, vol. 104, no. 1-2, pp. 1–11, 1997.

[11] B. Dong, J. Yan, B. Walkley, K. K. Inglis, F. Blanc, S. Hull, and A. R. West, "Synthesis and characterisation of the new oxyfluoride Li+ Ion Conductor, Li_5SiO_4F," *Solid State Ionics*, vol. 327, pp. 64–70, 2018.

[12] N. Masó and A. R. West, "Electronic conductivity in yttria-stabilized zirconia under a small dc bias," *Chemistry of Materials*, vol. 27, no. 5, pp. 1552–1558, 2015.

[13] M. A. Hernandez and A. R. West, "Dipolar relaxation and impedance of an yttria-stabilised zirconia ceramic electrolyte," *Journal of Materials Chemistry A*, vol. 4, no. 4, pp. 1298–1305, 2016.

[14] D. C. Sinclair, "Characterization of Electro-materials using ac Impedance Spectroscopy," *Boletín de la Sociedad Española de Cerámica y Vidrio*, vol. 34, no. 2, pp. 55–65, 1995.

[15] A.R. West Lithium battery in '*Solid State Chemistry and Its Applications, 2th edition*'. John Wiley & Sons. West Sussex, pp.619-634.

[16] J. E. Tsuchida, F. A. Ferri, P. S. Pizani, A. C. Martins Rodrigues, S. Kundu, J. F. Schneider, and E. D. Zanotto, "Ionic conductivity and mixed-ion effect in mixed alkali metaphosphate glasses," *Physical Chemistry Chemical Physics*, vol. 19, no. 9, pp. 6594–6600, 2017.

Appendix

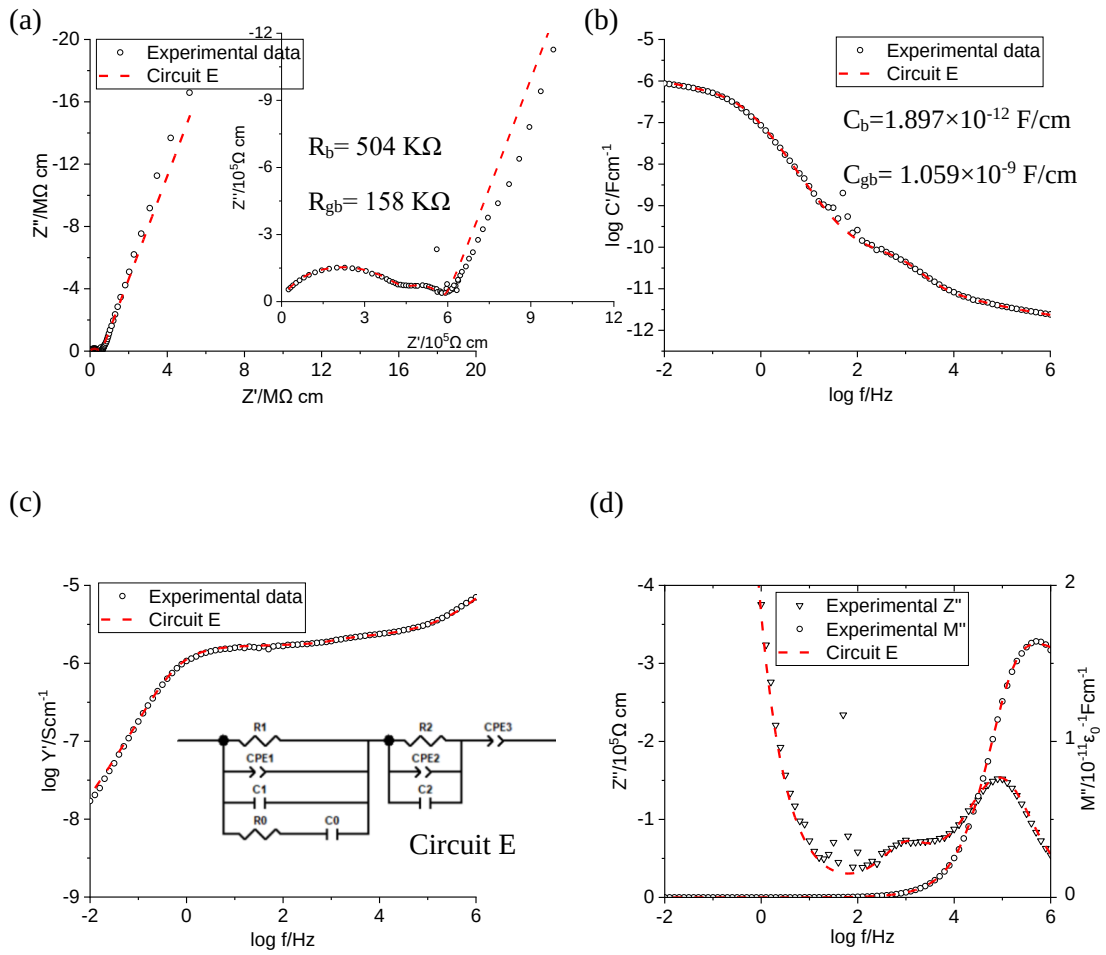

Fig 3.S1. Test and fitted impedance dataset for Li_5SiO_4F (sintered at 775°C, 10 hours) at 65.5°C

(a) $Z^{''}$-$Z^{'}$ complex plane plot, spectroscopic plots of (b) capacitance C', (c) admittance Y', and (d) $Z^{''}M^{''}$

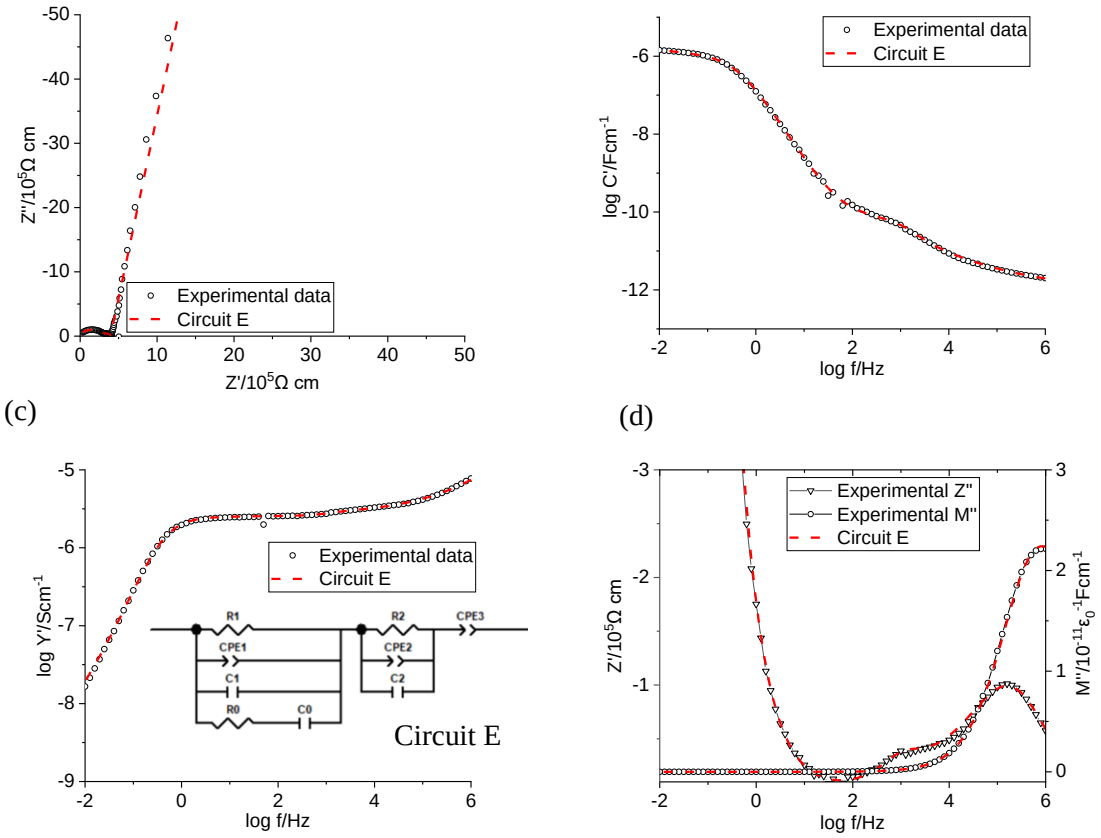

Fig 3.S2. Test and simulated impedance dataset for Li_5SiO_4F (sintered at 775°C, 50 hours) at 67.2°C

(a) Z''-Z' complex plane plot, spectroscopic plots of (b) capacitance C', (c) admittance Y', and (d) $Z''M''$

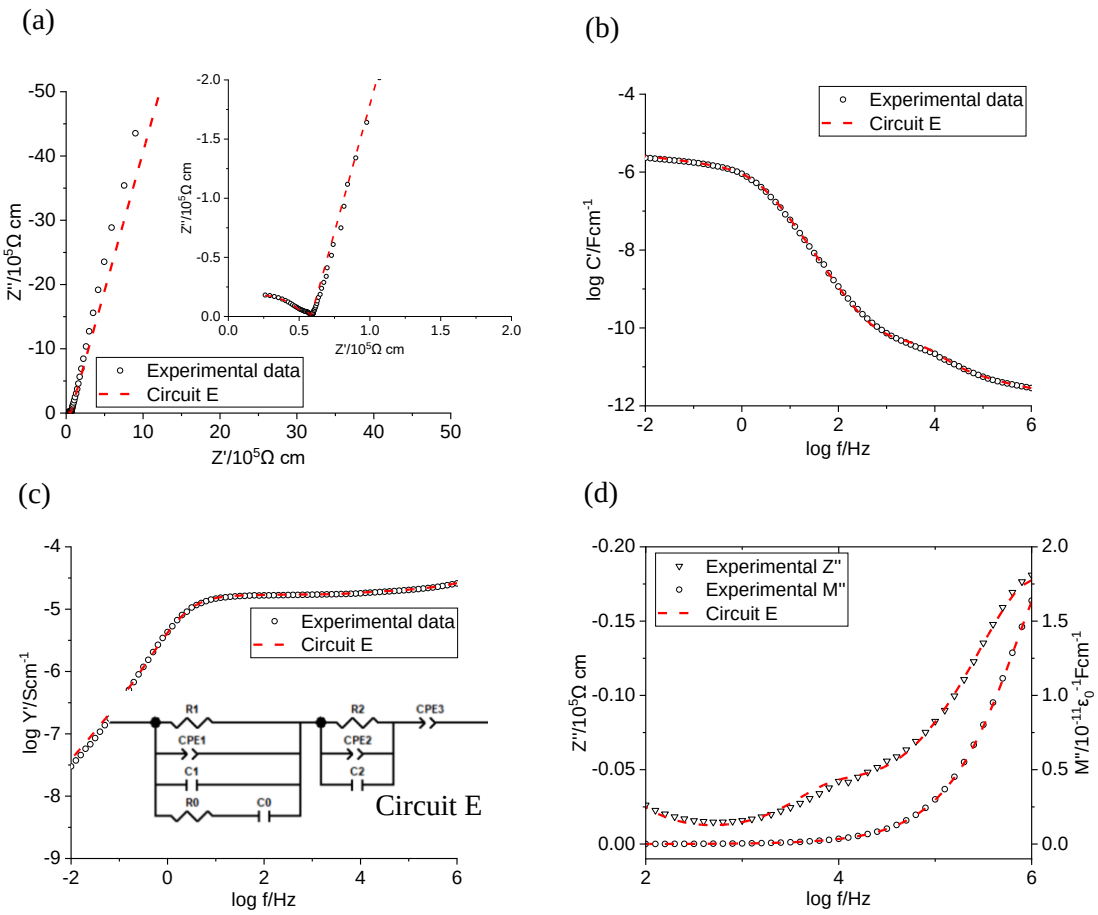

Fig 3.S3. Test and simulated impedance dataset for Li_5SiO_4F (sintered at 775°C, 50 hours) at 101.5°C

(a) $Z^{''}$-$Z^{'}$ complex plane plot, spectroscopic plots of (b) capacitance C', (c) admittance Y', and (d) $Z^{''}M^{''}$

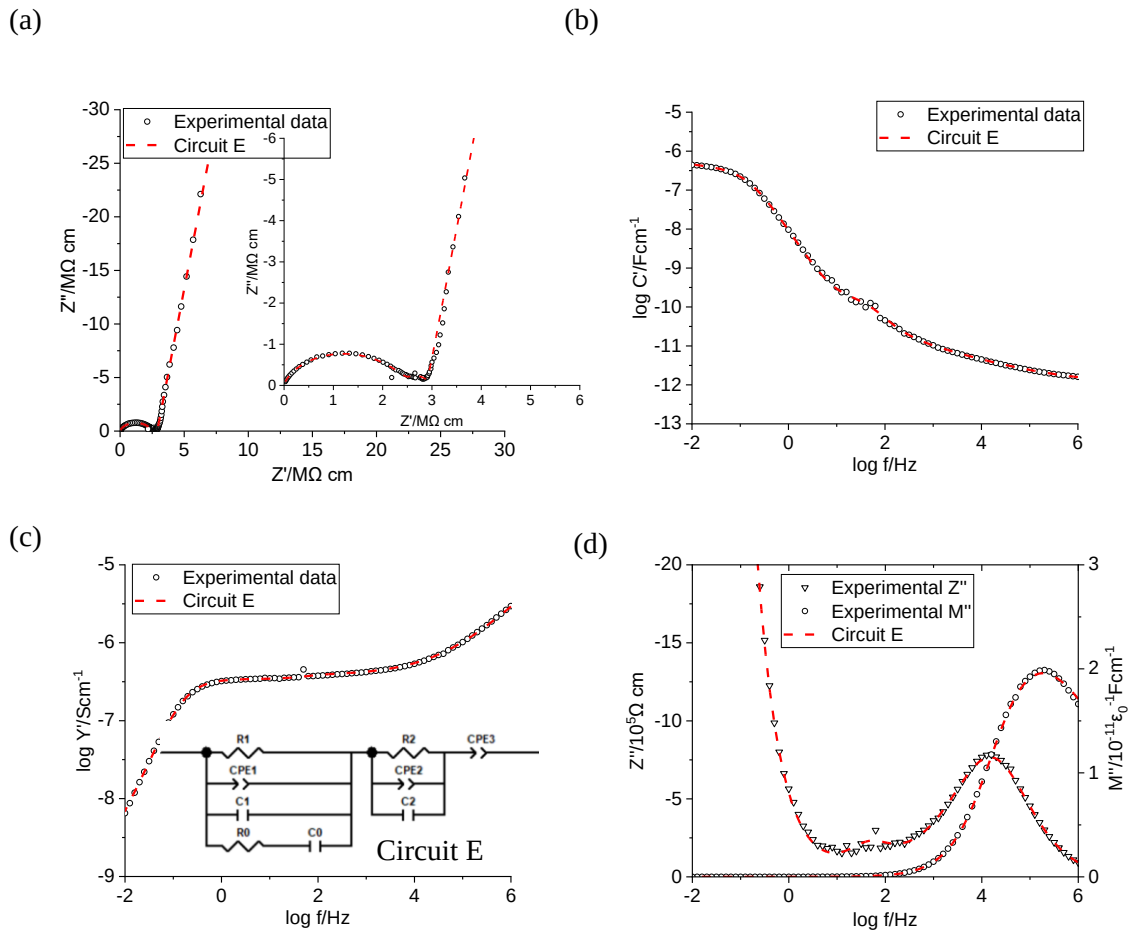

Fig 3.S4. Test and fitted impedance dataset for Li_5SiO_4F (sintered at 775°C, 110 hours) at 40.6°C

(a) $Z^{''}$-$Z^{'}$ complex plane plot, spectroscopic plots of (b) capacitance C', (c) admittance Y', and (d) $Z^{''}M^{''}$.

Chapter 4. Possible cation doping of Li_5SiO_4F and its electrical properties.

Summary

As the electrical properties of Li_5SiO_4F has been discussed in Chapter 3, further doping attempts on γ-Li_5SiO_4F with cation candidates with valence from +2 to +5 have been tried, in order to achieve a higher ionic conductivity. There are three sets of outcomes. Firstly, cation candidates including Al^{3+} and Ga^{3+} are successfully doped into γ-Li_5SiO_4F according to their XRD results. However, their ionic conductivity decreased. The mechanism behind that is unknown. Secondly, when some dopants participate in the solid-state synthesis of γ-Li_5SiO_4F, a significant number of secondary phases are shown in the product. Thirdly, in the preparations with some other dopants, possible new phases have been observed, which leads to further investigations in different ternary phases systems. Li_2O-SiO_2-LiF system was studied in Chapter 5, while Li_4SiO_4-$LiPO_4$-LiF system was studied in Chapter 6.

4.1. Introduction

Li_5SiO_4F is a possible new LISICON type solid electrolyte material reported recently, it was found in attempt of anion doping on Li_4SiO_4 [1]. In Chapter 3, with impedance measurement and equivalent circuit analysis, it shows that bulk γ-Li_5SiO_4F has an ionic conductivity of ~2×10^{-7} S/cm at ambient temperature. Starting materials for synthesis Li_5SiO_4F with less or more LiF had already showed Li_5SiO_4F is the only composition on Li_4SiO_4-LiF join. Further doping on Li_5SiO_4F can possibly reach a better ionic conductivity.

As there is no report on doping of Li_5SiO_4F, it can possibly follow the doping research on Li_4SiO_4 which has been well investigated. For instance, $Li_{4+x}Si_{1-x}Al_xO_4$ solid solutions with x=0.1-0.3 were prepared at ~850 °C for 10 h as a tritium breeder. The sample with x=0.3 was indexed on a monoclinic cell similar to bulk Li_4SiO_4 with a=11.58753 Å, b=6.19179 Å, c=16.81925 Å and β=99.27601 °. The electronic properties of $Li_{4+x}Si_{1-x}Al_xO_4$ were not well investigated in this study [2]. Another study of Li_4GeO_4-$LiAlO_2$ solid solution with general

formula, $Li_{2+x}Ge_xAl_{2-2x}O_4$, x=0.82-0.93, reported an ionic conductivity of ~10^{-6} S/cm at room temperature which decreased slightly with increasing Al content [3].

Ga^{3+} doped Li_4SiO_4 was investigated in 3 different solid solution systems: (a) $Li_{4+x}Si_{1-x}Ga_xO_4$, (b) $Li_{1+2x}Si_xGa_{1-2x}O_2$ and (c) $Li_{4-3x}GaSiO_4$ [4]. For (a), samples were prepared at 700-900 °C. The loss of lithia by evaporation was observed on successive heating at 800-900 °C given by the increasing amount of $LiGaO_2$ in the products. The ionic conductivity reached a maximum of ~10^{-5} S/cm at ambient temperature with x=0.15. For (b), samples with x=0-0.2 were prepared at 1000-1250 °C by solid state reaction. The solid solution had a $LiGaO_2$-like diffraction pattern. A sample with x=0.09 had ionic conductivity of only ~10^{-9} S/cm at 25 °C which is several orders of magnitude lower than that of other γ-type materials related to Li_3PO_4. For (c), samples with x=0-0.25 were heated at 1100 °C. The impedance results suggest a pronounced maximum ionic conductivity of ~10^{-6} S/cm when x=0.20-0.25 [4].

Isovalent doping of Li_4SiO_4 by Sn^{4+}, $Li_4Si_{1-x}Sn_xO_4$, gave an ionic conductivity of 3.07×10^{-5} S/cm at ambient temperature with x=0.02. Sn-doped samples showed a better thermal stability, suggesting better mobility of available lithium ions during charging and discharging process [5].

A previous study on Li_4XO_4 (x=Si^{4+}, Ti^{4+}, and Ge^{4+}) suggested difficulty to prepare $Li_4Si_{1-x}Ti_xO_4$ solid solution by solid state reaction, because of easy absorption of CO_2 from the atmosphere [8]. A more recent study successfully prepared $Li_4Si_{1-x}Ti_xO_4$ with x=0-0.25 ceramic pebbles by hydrothermal processing and multistage reactive sintering [7]. The ionic conductivity of x=0.05-0.25 samples was similar to that of bulk Li_4SiO_4. A value of 1.69×10^{-5} S/cm at 25 °C for x=0.1 was observed, which is roughly 1 order of magnitude higher than that of bulk Li_4SiO_4 [7].

Li_4SiO_4-Li_3PO_4 solid solution is reported to have a range of ~12-60 mole% of Li_4SiO_4 [8]. With 50 mole% Li_4SiO_4, the highest ionic conductivity within the solid solution system of 3×10^{-6} S cm^{-1} at ambient temperature was observed [9].

Although the supercell structure of Li_5SiO_4F is not yet know, and there is no evidence of the relationship on crystal structure between Li_4SiO_4 and Li_5SiO_4F. However, the cation doping on Li_5SiO_4F may follow the same compensation mechanisms to that of Li_4SiO_4. In specific, if Li^+ is partially replaced by an element A with higher valence n, there will be lithium vacancies in $Li_{5-nx}A_xSiO_4F$; if Si^{4+} is partially replaced by element A with higher valence n, there will be also some lithium vacancies in $Li_{5-nx}Si_{1-x}A_{nx}O_4F$; if Si^{4+} is partially replaced by element B with lower valence m, there will be more interstitial Li^+ in $Li_{5+mx}Si_{1-x}B_xO_4F$ for charge compensation. Generally, lithium vacancies can offer more available sites for the hopping of lithium ions; and additional interstitial lithium can act as additional mobile Li^+ during lithium migration. Thus, a series of candidates including Ni^{2+} , Zn^{2+} , Mg^{2+}, Ga^{3+}, Al^{3+}, Fe^{3+}, Co^{3+}, Ge^{4+}, Ti^{4+} and P^{5+} were studied with results reported here.

The anion doping on Li_4SiO_4 has also been tried. The attempt to dope Li_4SiO_4 by LiF showed no success on doping but found Li_5SiO_4F as a possible LISICON type electrolyte [1]. The attempt to dope Li_4SiO_4 by Cl^- was also unsuccessful, but found a new anti-perovskite stacking material, $Li_6SiO_4Cl_2$ [10]. Due to the limited time of this study, further anion doping on Li_5SiO_4F has not been tried, but possible candidates with similar radius size to partially replace F^- (119 pm) include N^{3-} (132 pm), Cl^- (167 pm) and S^{2-} (170 pm) [11].

4.2. Synthesis and electrical properties of cation-doped Li_5SiO_4F

Successful dopants

4.2.1. Al^{3+} doped Li_5SiO_4F

Table 4.1. Brief experimental procedures for different Al-doped Li_5SiO_4F samples

Compensation mechanism	Synthesis method	Experimental procedures
1.Creating Li^+ vacancy	1A	Step 1: Li_2CO_3, SiO_2, and Al_2O_3 with desired composition were heated at 850°C for 10 hours to get $Li_{4-3x}Al_xSiO_4$, x=0.1, and 0.2; Step 2: $Li_{4-3x}Al_xSiO_4$ precursors and LiF were reacted at 750°C for 10 hours to get $Li_{5-3x}Al_xSiO_4F$, x=0.1, and 0.2.
	1B	Step 1: $Li_{5-3x}Al_xSiO_4F$ was directly synthesised from Li_2CO_3, SiO_2, Al_2O_3, and LiF heating at 750°C for 10 hours, x=0.1.
2. Introducing interstitial Li^+	2A	Step 1: Li_2CO_3, SiO_2, and Al_2O_3 with desired composition were heated at 850°C for 10 hours to get $Li_{4+y}Al_ySi_{1-y}O_4$, y=0.05, 0.1, 0.2, and 0.3; Step 2: $Li_{4+y}Al_ySi_{1-y}O_4$ and LiF were heated at 750°C for 10 hours for $Li_{5+y}Al_ySi_{1-y}O_4F$, y=0.05, 0.1, 0.2.
	2B	Step 1: $Li_{5+x}Al_xSi_{1-x}O_4F$ was prepared from Li_2CO_3, SiO_2, Al_2O_3, and LiF heating at 750°C for 10 hours, y=0.05, 0.1, 0.15 and 0.2.

Li_5SiO_4F can, in principle, be doped by Al^{3+} according to two different compensation mechanisms. In mechanism 1, $Li_{5-3x}Al_xSiO_4F$, three Li^+ could be replaced by one Al^{3+} leaving 2 vacant sites. In mechanism 2, $Li_{5+y}Al_ySi_{1-y}O_4F$, Si^{4+} could be partially replaced by Al^{3+} with additional Li^+ in interstitial sites to maintain charge neutrality. Both mechanisms could possibly give high Li^+ ionic conductivity by either Li vacancy or Li interstitial migration. Samples based on each mechanism were prepared in two ways, either in two steps, A, or as a single step, B, as summarised in Table 4.1. In reaction 1A, $Li_{4-3x}Al_xSiO_4$ was prepared first and then reacted with LiF. In 2A, $Li_{4+y}Al_ySi_{1-y}O_4$ was prepared first and then reacted with LiF. In reactions 1B and 2B, samples were synthesised directly from Li_2CO_3, SiO_2, Al_2O_3 and LiF.

Mechanism 1: $Li_{5-3x}Al_xSiO_4F$: x=0.1, 0.2

Reaction 1A:

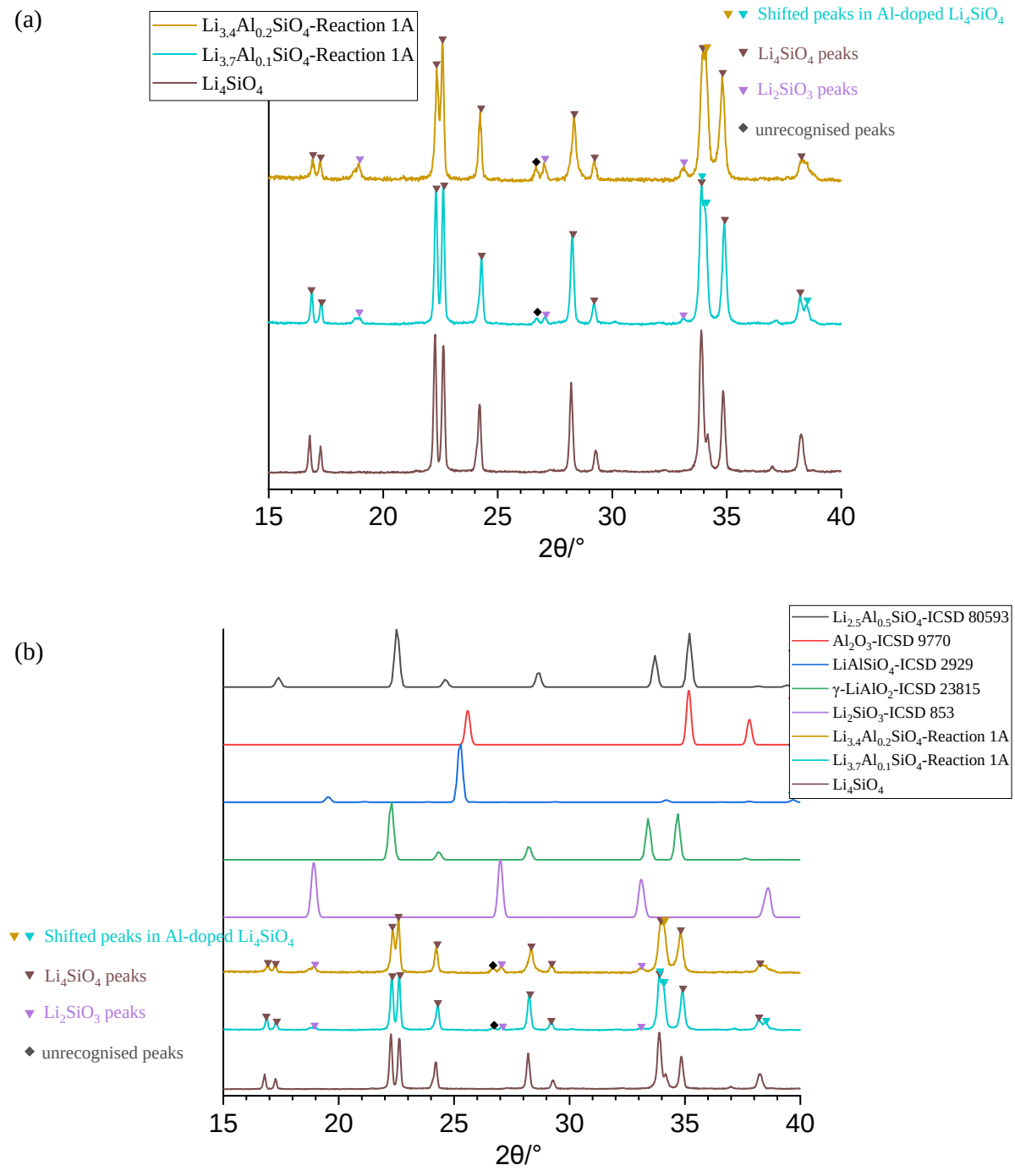

Fig 4.1 (a). XRD results of $Li_{4-3x}Al_xSiO_4$ (x=0.1 and 0.2), the precursor in step 1 of reaction 1A with Li_2SiO_3 lines; (b) compared with standard patterns.

In reaction 1A, oxide and carbonate reagents were mixed and reacted at 850°C for 10 h to produce $Li_{4-3x}Al_xSiO_4$ precursor. XRD results of the products are shown in Fig 4.1 (a). Both compositions show similar pattern to Li_4SiO_4, marked by brown triangles, with some shifted peaks marked by blue triangles. The tiny peaks at ~19 °/2θ, ~26-27 °/2θ and ~33.2 °/2θ,whose intensity increased with higher Al content, do not belong to $LiAlO_2$, $LiAlSiO_4$, Al_2O_3, nor $Li_{2.5}Al_{0.5}SiO_4$, as shown in Fig 4.1 (b). Most extra peaks belong to Li_2SiO_3, marked by purple triangles, except for the first line in the doublet peaks at ~26-27 °/2θ, marked by black rhombus, which probably belongs to Al-doped Li_4SiO_4 solid solution. Thus, the XRD results possibly indicate a successful doping of Li_4SiO_4 by Al^{3+} with small amount of Li_2SiO_3 as a secondary phase, whose content may increase with higher Al^{3+} content.

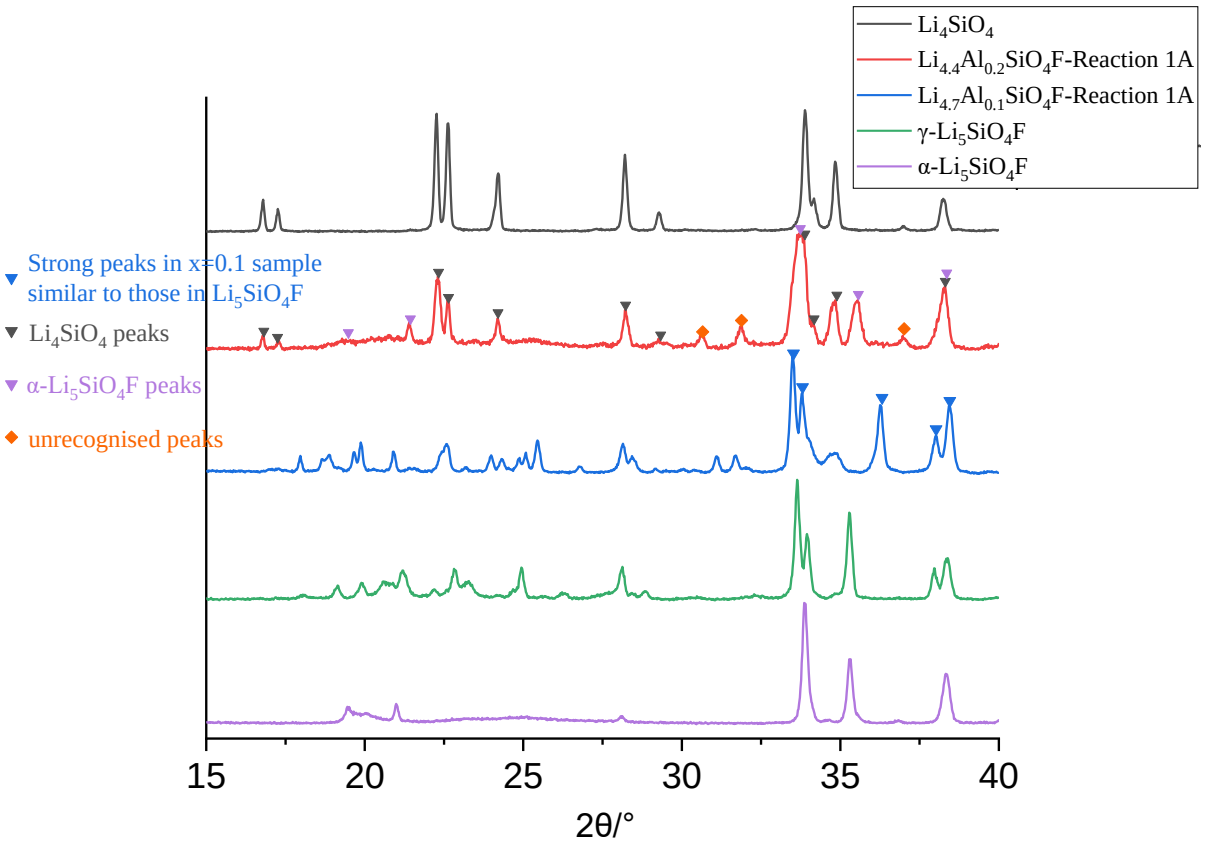

Fig 4.2. XRD results of $Li_{5-3x}Al_xSiO_4F$(x=0.1 and 0.2) prepared in step 2 of reaction 1A, with Li_4SiO_4 lines. When x=0.1, the product is a γ-type phases similar to γ-Li_5SiO_4F; when x=0.2, the main phases include Li_4SiO_4 and α-Li_5SiO_4F with some unknown lines.

The $Li_{4-3x}Al_xSiO_4$ precursor and LiF were then reacted at 750°C, with XRD results shown in Fig 4.2. When x=0.1, the pattern is similar to γ-Li_5SiO_4F with doublet peaks at 33.5-34°/2θ and 38-38.5°/2θ, but a clear shift of the middle peak, from ~35°/2θ in γ-Li_5SiO_4F to ~36°/2θ, as marked by blue triangles. The tiny peaks at low 2θ angles, ~17 to 28 °/2θ, are different from those in γ-Li_5SiO_4F. The tentative conclusion is that, instead of doping Li_5SiO_4F, a new phase is formed, that probably belongs to the β family, discussed later in the thesis and in the discussion, Chapter 7. When x=0.20, the XRD pattern shows a clear mixture of Li_4SiO_{4ss} and an α-Li_5SiO_4F-like phase. The Li_4SiO_{4ss} is probably a double-doped Li_4SiO_4, which may be worth further investigation. The broad peaks suggest a poor crystallinity which may be improved by heating at slightly higher temperature. These results indicate that a solid solution may form in composition x=0.1, but composition x=0.2 is beyond the solid solution limit.

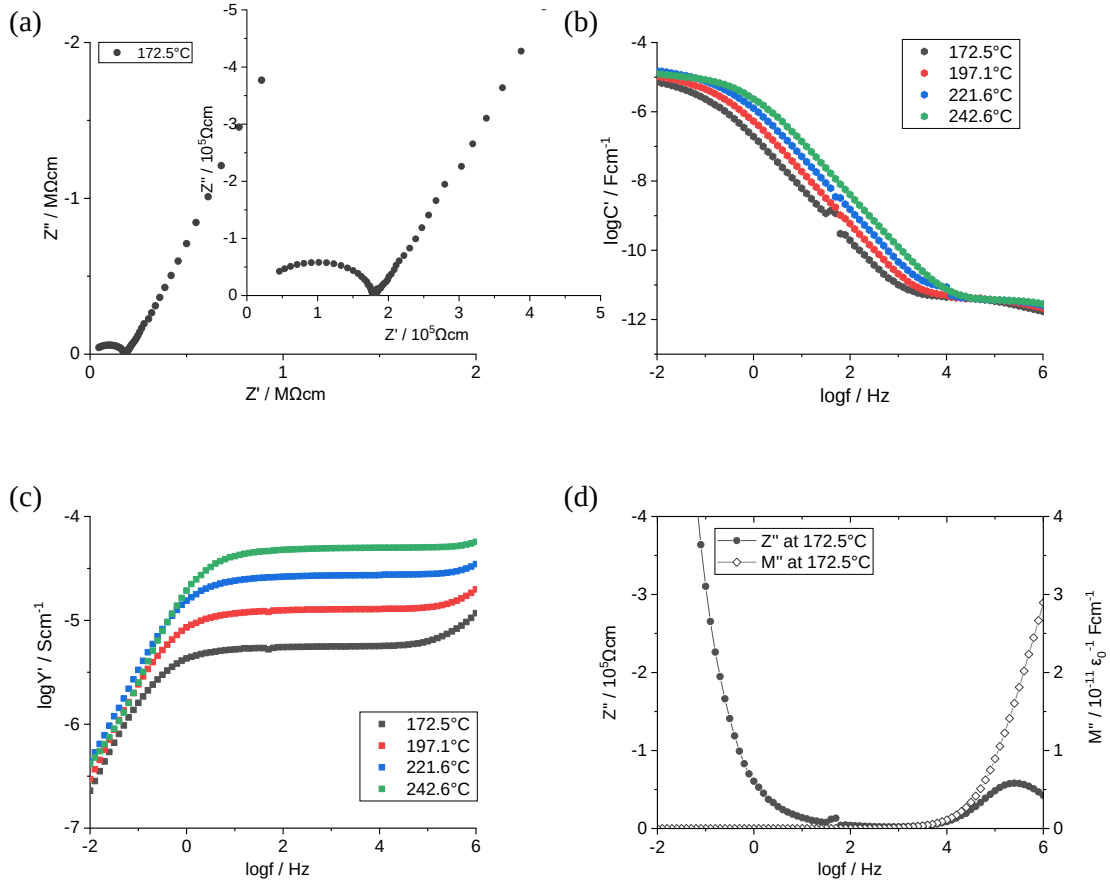

Fig 4.3. The impedance dataset for $Li_{4.7}Al_{0.1}SiO_4F$ prepared by reaction 1A (sintered at 750°C, 10 hours), (a) impedance complex plane plot, spectroscopic plots of (b) capacitance C', (c) admittance Y', and (d) Z''-M'' at 172.5°C.

A pellet of sample with x=0.1, prepared by reaction 1A, was coated by Au electrodes and sintered at 750°C for 4 hours for impedance measurement. The results in Fig 4.3 show typical impedance data for an ionic conductor with a bulk response and a sample-electrode response. The total resistance in (a) at 172.5°C is ~1.77×10^5 Ω. However, the attempts to fit the impedance data in Fig 4.3 with (a) the circuit consisting of R_1-C_1-CPE_1 and CPE_3, or (b) R_1-C_1-CPE_1, R_2-C_2-CPE_2, and CPE_3 in series were not successful. This may arise the concern that there is more than one bulk component in $Li_{4.7}Al_{0.1}SiO_4F$ by reaction 1A, thus there may be a mixture of a β-family phase and other phase in it.

Reaction 1B:

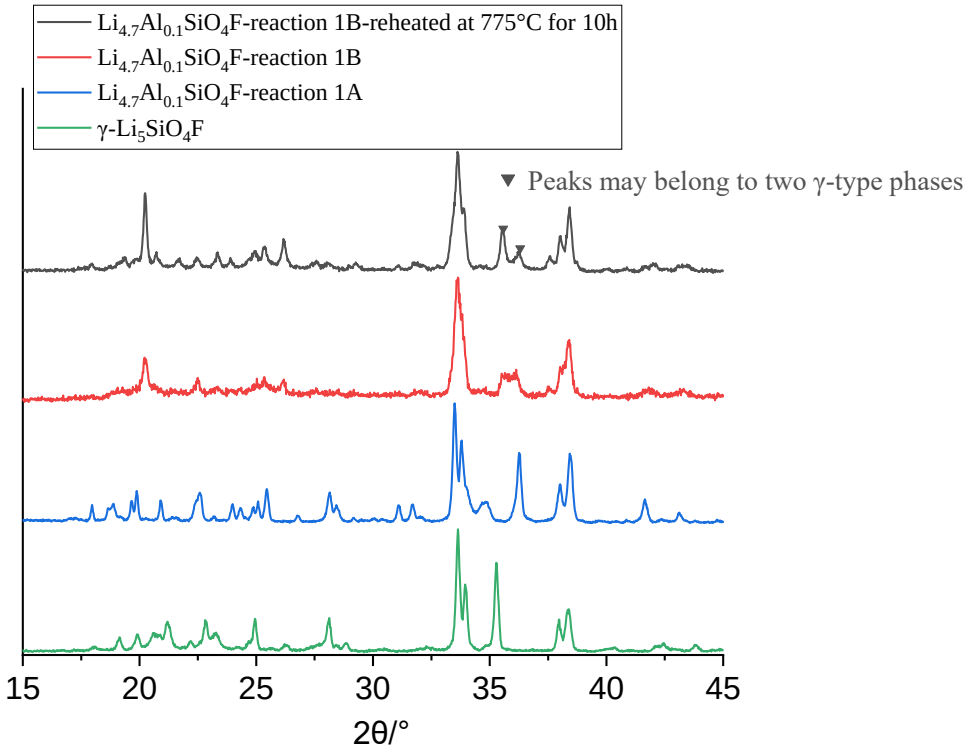

Fig 4.4. XRD results of $Li_{5-3x}Al_xSiO_4F$ (x=0.1) prepared by reactions 1A and 1B. Sample prepared by reaction 1B shows probably a mixture of two γ-type phases, which is different to that of the sample prepared by reaction 1A.

Reaction 1B with x=0.1 at 750°C for 10 h gave a diffraction pattern clearly different to that of the product with the same composition prepared by reaction 1A, Fig 4.4. It shows several peaks overlapped at 35.5-36°/2θ and some tiny broad peaks at low 2θ region, which indicates probably an incomplete reaction or a poor crystallinity. Thus, the sample was reheated at 775°C for another 10 hours. The XRD result of reheated sample shows more clear and sharper peaks. The doublet peaks in reheated sample, at 35-37°/2θ, marked by black triangles, are probably an indication of a mixture of two different γ-type phases in the product. The reason for the clear differences between the samples with same composition, when x=0.1, prepared by different method, reaction 1A and 1B, is unknown so far. The sample with x=0.2 was not prepared as the lower Al content sample, x=0.1, already showed an unidentified new phase.

Mechanism 2: $Li_{5+y}Al_ySi_{1-y}O_4F$, y=0.05-0.30

Reaction 2A:

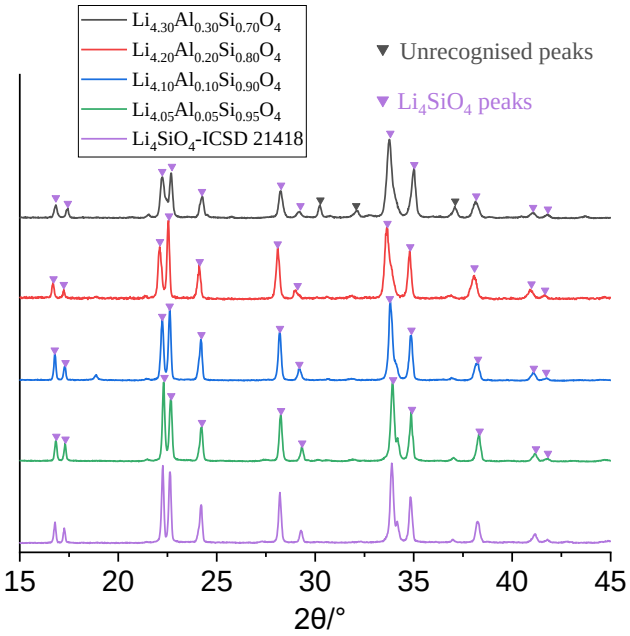

Fig 4.5. XRD results of $Li_{4+y}Al_ySi_{1-y}O_4$ (y=0.05-0.3) precursors in reaction 2A compared to standard Li_4SiO_4. Extra peaks beyond Li_4SiO_4 lines start to show in x=0.3 sample.

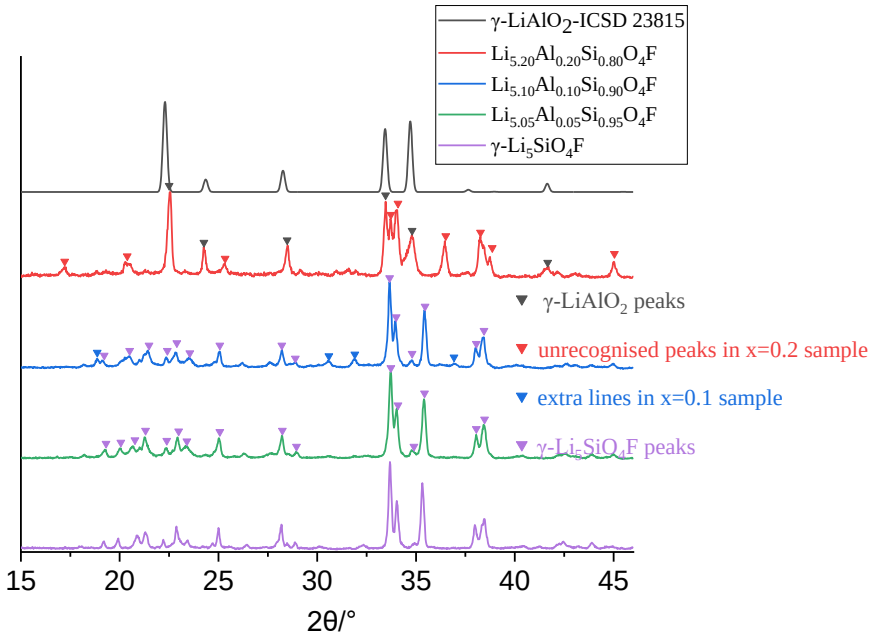

Fig 4.6. XRD results of $Li_{5+y}Al_ySi_{1-y}O_4F$ (x=0.05-0.2) prepared by reaction 2A compared to standard patterns. when x=0.5, there is a γ-Li_5SiO_4F pattern indicating possible successful doping; when x=0.10, there is a mixture of the main phase of γ-Li_5SiO_4F with some extra lines, marked by blue triangles; when x=0.20, there is no clear trace of γ-Li_5SiO_4F but clearly γ-$LiAlO_2$ lines.

$Li_{4+y}Al_ySi_{1-y}O_4$ precursors was prepared at 850°C, method 2A in Table 4.1. XRD results, Fig 4.5 show a Li_4SiO_4 solid solution pattern when $0.05 \leq x < 0.30$, consistent with previous research [5]. When x=0.30, there are several unrecognised peaks, mark with black triangles, which may belong to secondary phase(s). XRD results for step 2 are shown in Fig 4.6: when $0.05 \leq x \leq 0.10$, there is a γ-Li_5SiO_4F-like phase; when x=0.20, a mixture of another γ-type phase with a strong peak at ~36.4°/2θ and $LiAlO_2$ can be seen. It is concluded that Al may partially doped into Li_5SiO_4F as limited solid solution forms by mechanism 2A, two steps synthesis of $Li_{5+y}Al_ySi_{1-y}O_4F$.

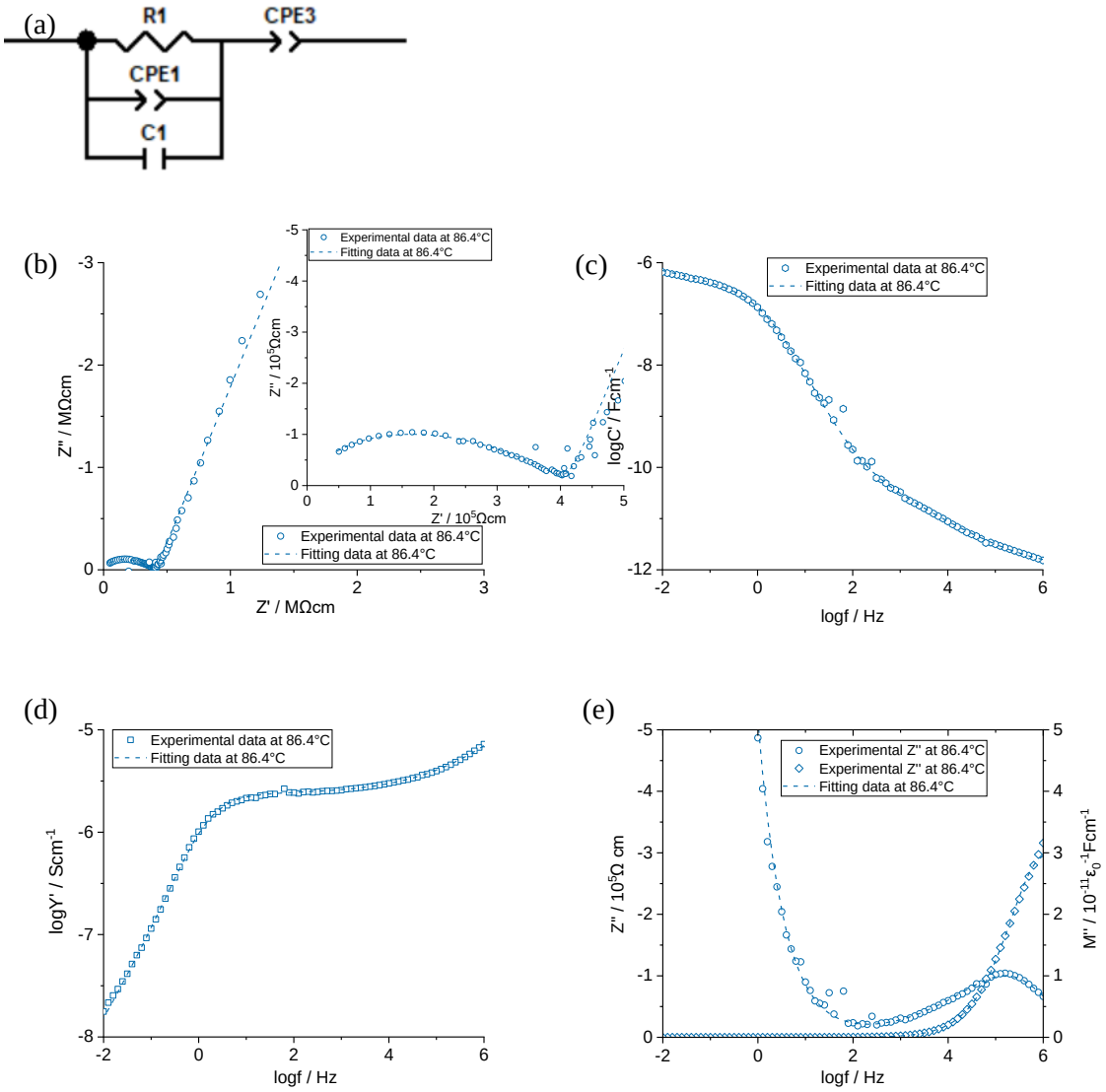

Fig 4.7. Experimental and fitted impedance datasets for $Li_{5.05}Al_{0.05}Si_{0.95}O_4F$ prepared by mechanism 2A, at 86.4°C by circuit in (a), (b) $Z^{''}$-$Z^{'}$ complex plane plot, spectroscopic plots of (c) capacitance $C^{'}$, (d) admittance $Y^{'}$, and (e) $Z^{''}$, $M^{''}$.

Table 4.2. the bulk resistance and bulk capacitance for $Li_{5.05}Al_{0.05}Si_{0.95}O_4F$ prepared reaction 2A, at different temperatures

Sample	R_b / kΩ	CPE1-T / $nFcm^{-1}$	CPE1-P	C_b / $pFcm^{-1}$	CPE3-T / μFcm^{-1}	CPE3-P
86.4°C	416(6)	5(2)	0.45(2)	0.97(9)	0.427(5)	0.798(5)
104.3°C	166(1)	5(2)	0.48(3)	0.9(1)	0.557(4)	0.796(3)
126.8°C	66(1)	10(10)	0.42(6)	1.3(4)	0.783(9)	0.801(5)
147.2°C	30(5)	30(30)	0.40(8)	1.6(5)	1.24(1)	0.776(4)

Pellets of samples with y=0.05, 0.10, and 0.20, prepared by reaction 2A, with similar results are shown in Fig 4.7 (y=0.05) and Figs 4.S1 (y=0.10)-S2 (y=0.20), respectively. All compositions show typical impedance results of an ionic conductor with bulk and sample-electrode responses. The equivalent circuit, Fig 4.7 (a), was used to fit the impedance results at 86.4°C, with results shown in Figs 4.7(b-e). The overall fitting results are good but do not suggest any secondary bulk nor grain boundary response should be included, which consistent with the previous conclusion that Al^{3+} is successfully doped in Li_5SiO_4F in form of an Al containing Li_5SiO_4F solid solution. The fitted bulk resistance $R_b = 4.16\times10^5$ Ω and the bulk capacitance $C_b = 9.73\times10^{-13}$ Fcm^{-1}, which gives the permittivity of the bulk is ~10.99. Parameters obtained by equivalent circuit analysis at other temperatures are summarised in Table 4.2.

Reaction 2B:

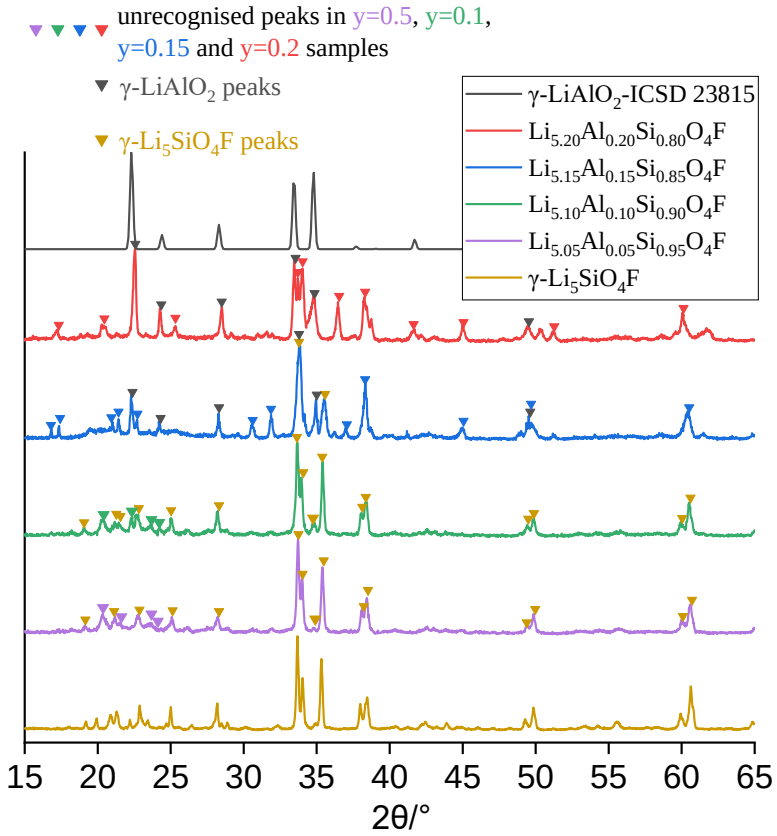

Fig 4.8. XRD results of $Li_{5+y}Al_ySi_{1-y}O_4F$ (y=0.05-0.2) prepared by reaction 2B, compared to standard patterns. When y=0.05-0.10, there is a main phase of γ-Li_5SiO_4F with some extra lines; when y=0.15, there is a mixture of γ-Li_5SiO_4F-like phase, γ-$LiAlO_2$ and extra unknown lines; when y=0.2, the γ-$LiAlO_2$ lines are more significant.

In reaction 2B, Table 4.1 and Fig 4.8, when x=0.05, the XRD pattern of the product looks like a γ-Li_5SiO_4F solid solution; when y=0.10-0.15, there is a mixture of the γ-Li_5SiO_4F-like phase and some tiny secondary peaks; when y=0.20, there is significant amount of $LiAlO_2$. It seems the limit of doping on γ-Li_5SiO_4F by Al on Si^{4+} site, $Li_{5+y}Al_ySi_{1-y}O_4F$, by reaction 2B is y < 0.1.

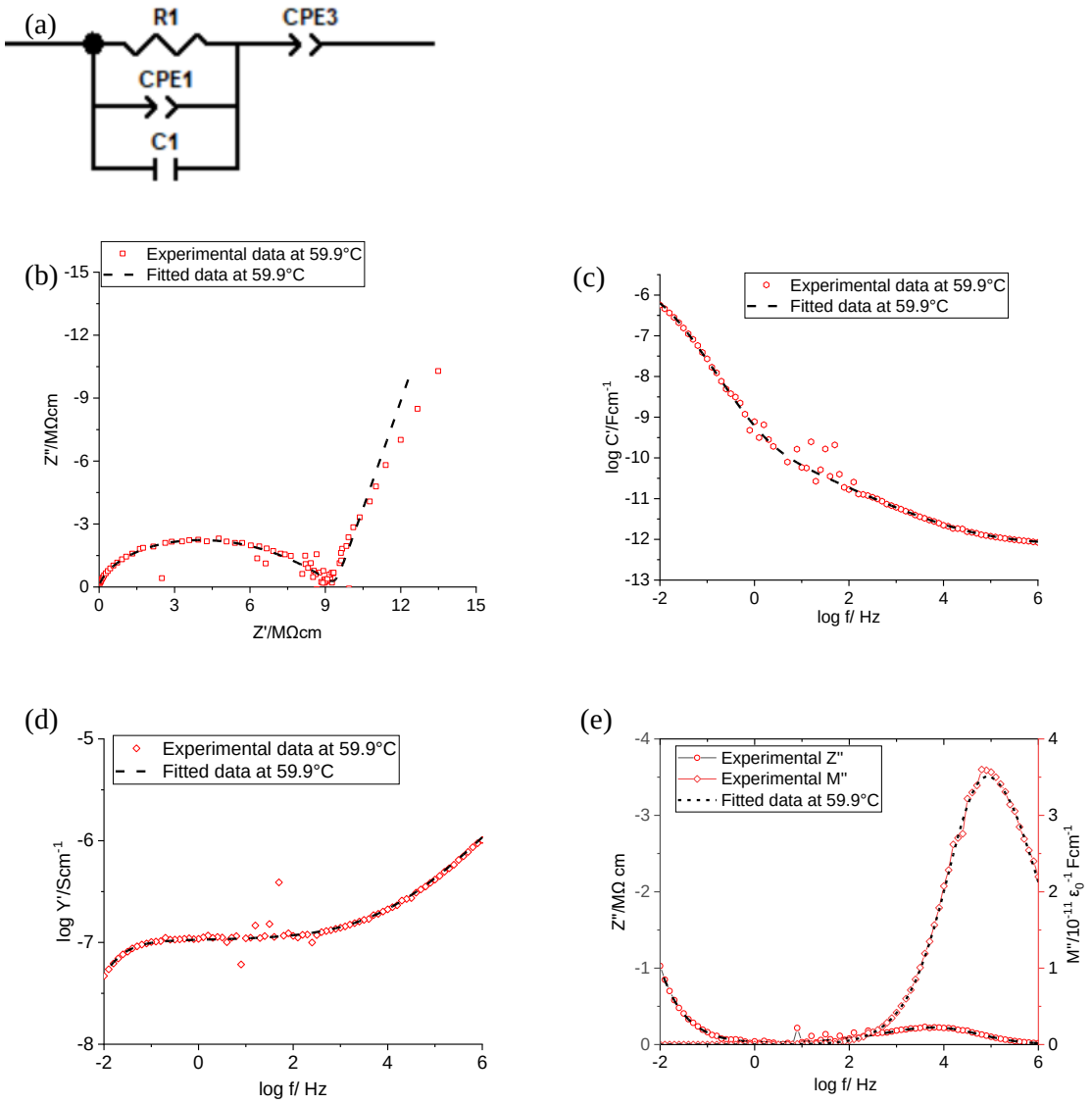

Fig 4.9. Experimental and fitted impedance datasets for $Li_{5.05}Al_{0.05}Si_{0.95}O_4F$ prepared by reaction 2B at 59.9°C by circuit in (a), (b) Z''-Z' complex plane plot, spectroscopic plots of (c) capacitance C', (d) admittance Y', and (e) Z'', M''.

Table 4.3. the bulk resistance and bulk capacitance for $Li_{5.05}Al_{0.05}Si_{0.95}O_4F$ prepared by reaction 2B, at different temperatures.

Sample	R_b / Ω	CPE1-T / F	CPE1-P	C_b / F	CPE3-T / F	CPE3-P
59.9°C	9.4(2) $\times10^6$	7(2)$\times10^{-10}$	0.48(2)	7.3(5) $\times10^{-13}$	9(1)$\times10^{-7}$	0.82(5)
81.1°C	2.48(3)$\times10^6$	7(2)$\times10^{-10}$	0.52(2)	6.0(6)$\times10^{-13}$	9.3(3)$\times10^{-7}$	0.82(1)
102.9°C	7.42(3)$\times10^5$	7.4(1)$\times10^{-10}$	0.55(2)	5.9(4) $\times10^{-13}$	1.041(7) $\times10^{-6}$	0.842(4)
126.1°C	2.41(1)$\times10^5$	5(1)$\times10^{-10}$	0.62(2)	3(1)$\times10^{-13}$	1.188(7)$\times10^{-6}$	0.804(3)

Impedance data for y=0.05, reaction 2B, also show a typical bulk and sample-electrode interphase impedance, Fig 4.9, similar to that of same composition prepared by reaction 2A with results in Fig 4.7. The equivalent circuit analysis gives R_b=9.44$\times10^6$ Ω, C_b = 7.3$\times10^{-13}$ F and ε'=8.24 at 59.9°C. However, the spike is not well fitted in (b), probably due to a rough sample-electrode surface. The fitted R and C data at other temperatures are summarised in Table 4.3.

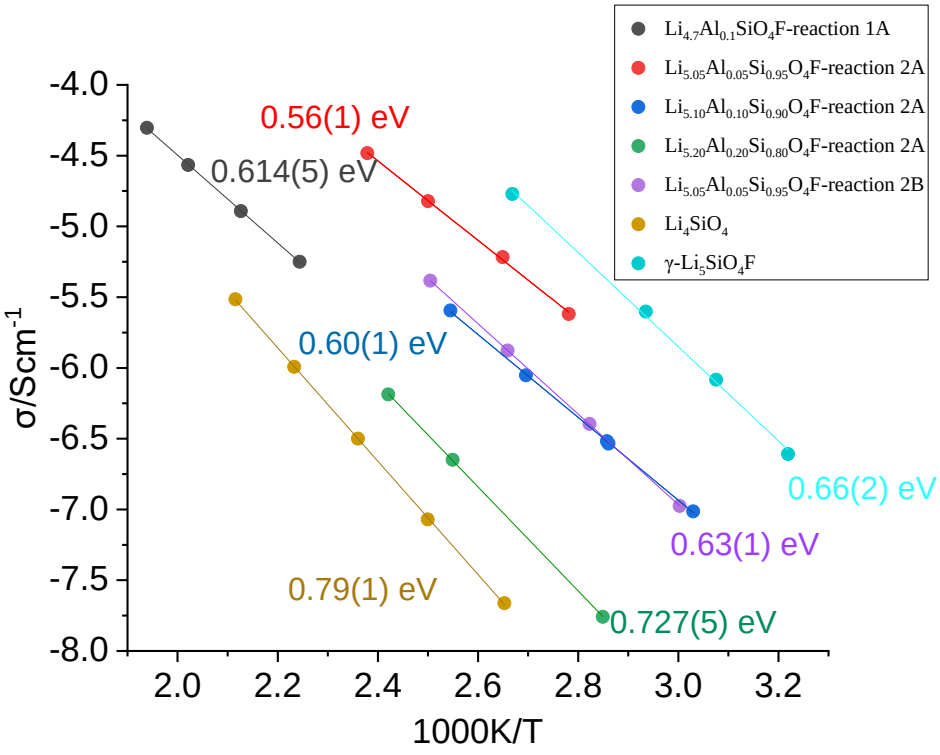

Fig 4.10. Arrhenius plot for Al doped Li_5SiO_4F samples compared to Li_5SiO_4F and Li_4SiO_4

The Arrhenius plots in Fig 4.10 compares the total conductivity of Al-doped Li_5SiO_4F and γ-Li_5SiO_4F. The Li^+ vacancy sample, $Li_{5-3x}Al_xSiO_4F$, by reaction 1A, shows an ionic conductivity higher than that of bulk Li_4SiO_4, but still significantly lower than that of γ-Li_5SiO_4F. The Li^+ interstitial samples, $Li_{5+y}Al_ySi_{1-y}O_4F$, by reactions 2A or 2B, have an average ionic conductivity roughly ~1-2 orders of magnitudes lower than that of γ-Li_5SiO_4F, which reduces with higher Al content. The highest total conductivity is observed in y=0.05 sample, which is still several times lower than that of pure γ-Li_5SiO_4F. The activation energy of the Li^+ interstitial samples also increased with higher Al composition, possibly indicate the reduced mobile ions carriers due to the addition Al^{3+}.

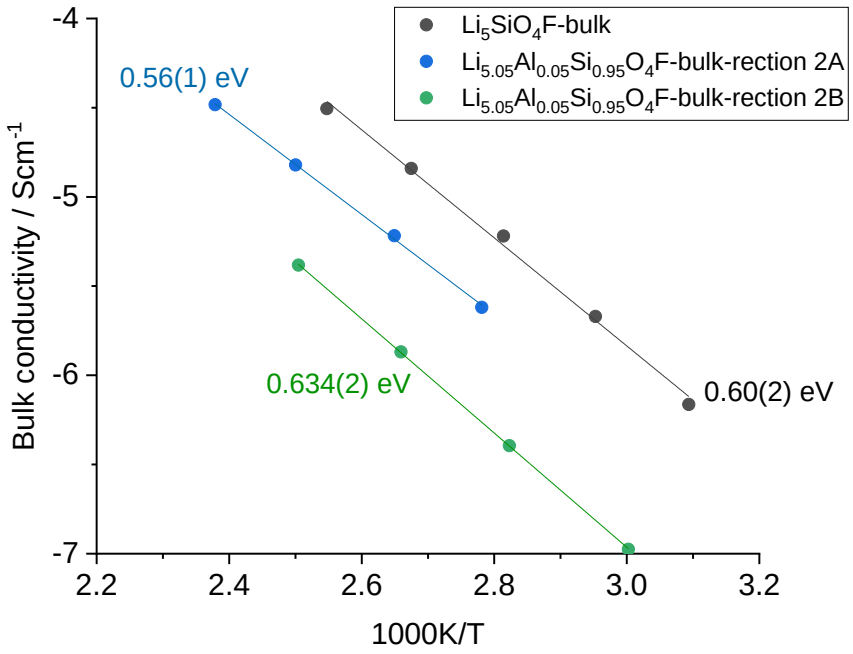

Fig 4.11. Arrhenius plot for bulk $Li_{5.05}Al_{0.05}Si_{0.95}O_4F$ samples and bulk γ-Li_5SiO_4F.

Based on previously mentioned equivalent circuit analysis, the bulk conductivity of two interstitial Li^+ samples with y=0.05, prepared by 2A or 2B, were compared to bulk γ-Li_5SiO_4F in Fig 4.11. The bulk capacitance of both doped samples, in (a), is similar to that of bulk γ-

Li_5SiO_4F, while a clear grain boundary response is not observed in Al doped samples. It shows that: (a) the doped sample prepared by 2A shows the lowest activation energy, with 0.56 eV; and a bulk ionic conductivity several times lower compared to bulk γ-Li_5SiO_4F. The same composition prepared by 2B has a lower ionic conductivity and higher activation energy, with 0.63 eV, compared to bulk γ-Li_5SiO_4F, with 0.60 eV.

In conclusion, doping by mechanism 1, $Li_{5-3x}Al_xSiO_4F$, was not successful, but there is a possibility of a new γ-type phase in reactions 1A and 1B, with x=0.1. Doping study by mechanism 2, $Li_{5+y}Al_ySi_{1-y}O_4F$, was successful when $y<0.1$. Composition $Li_{5+y}Al_ySi_{1-y}O_4F$ showed reduced ionic conductivity with increasing Al content and sample y=0.05, 2A, had a better ionic conductivity and lower activation energy than y=0.05, 2B.

4.2.2. Ga^{3+} doped Li_5SiO_4F

Following the successful attempt to dope Li_5SiO_4F with Al, with $y<0.1$ in $Li_{5+y}Al_ySi_{1-y}O_4F$, another trivalent candidate, Ga^{3+}, has been tried. The Pauling ionic radii of Ga^{3+}, 76 pm, and Al^{3+}, 67.5 pm, are similar [2]. The Ga^{3+} doped samples were also prepared using the same two compensation mechanisms: (1) $Li_{5-3x}Ga_xSiO_4F$ and (2) $Li_{5+y}Ga_ySi_{1-y}O_4F$.

Mechanism 1: $Li_{5-3x}Ga_xSiO_4F$

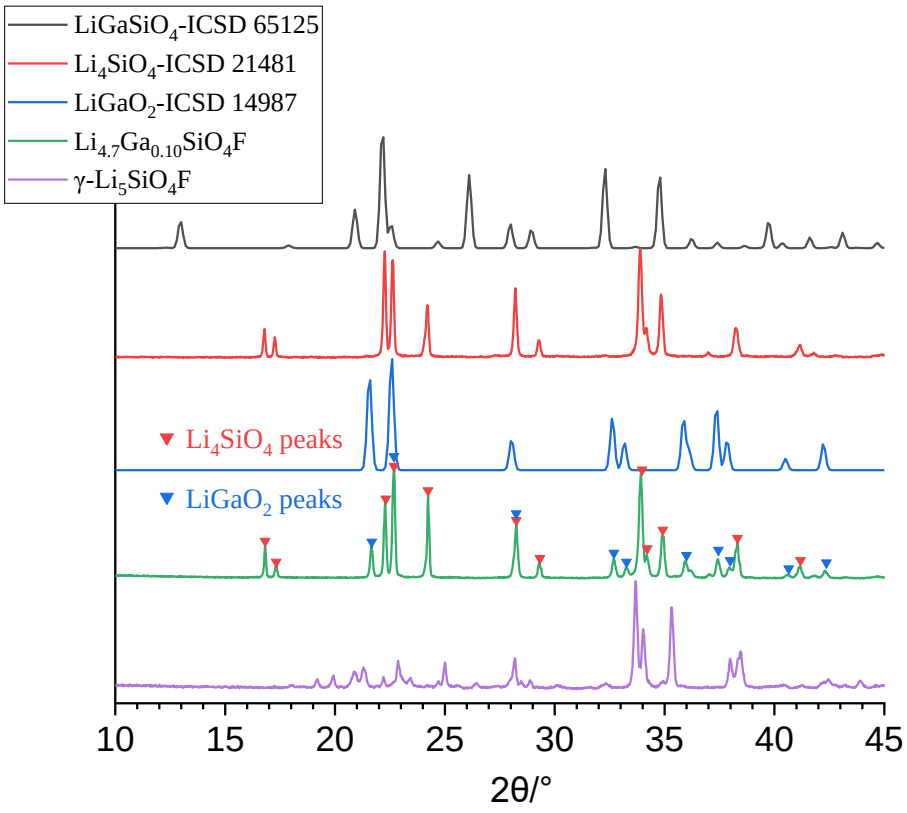

Fig 4.12. XRD result of $Li_{5-3x}Ga_xSiO_4F$, x=0.1, by mechanism 1, compared with standard patterns. Ga^{3+} doped sample with x=0.1 by mechanism 1 shows a mixture of Li_4SiO_4 and $LiGaO_2$.

A sample with x=0.1 was synthesised using Li_2CO_3, SiO_2, Ga_2O_3 and LiF by solid state reaction at 750°C for 20 hours. The XRD result, Fig 4.12, shows a mixture of Li_4SiO_4 and $LiGaO_2$. There is no sign of Li_5SiO_4F in the products, thus either the doping by Ga^{3+} with mechanism 1 may require a different synthesis method or it is not possible to prepare thermodynamically stable solid solutions with this general formula.

Mechanism 2: $Li_{5+y}Ga_ySi_{1-y}O_4F$

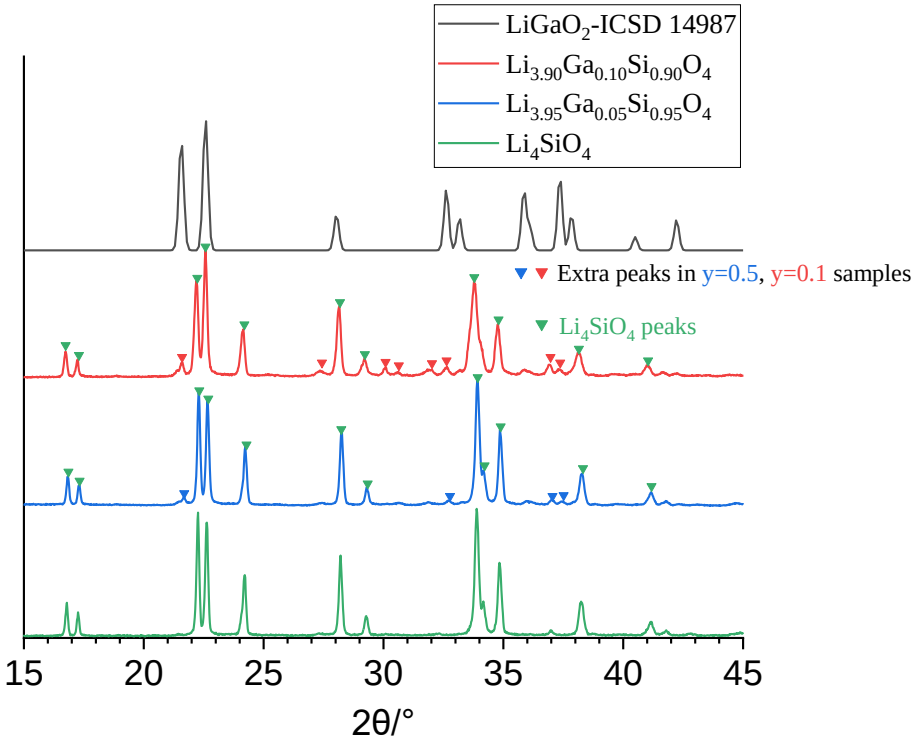

Fig 4.13. XRD result of $Li_{4+y}Ga_ySi_{1-y}O_4$ precursors, in step 1 of mechanism 2, y=0.05 and 0.1, compared with standard patterns.

In step 1, $Li_{4+y}Ga_ySi_{1-y}O_4$ (y=0.05, 0.10) precursors were prepared using Li_2CO_3, Ga_2O_3, and SiO_2 at 900°C for 10 h, as a previous study on $Li_{3.4}Ga_{0.2}SiO_4$ suggested a doping temperature of 890-975°C [12]. The XRD results, Fig 4.13, show unrecognised tiny peaks, marked by red/blue triangles which is not belong to $LiGaO_2$. The intensity of these peaks increased with higher Ga content. These peaks may belong to secondary phase(s), or indicate a Ga contained Li_4SiO_4 solid solution.

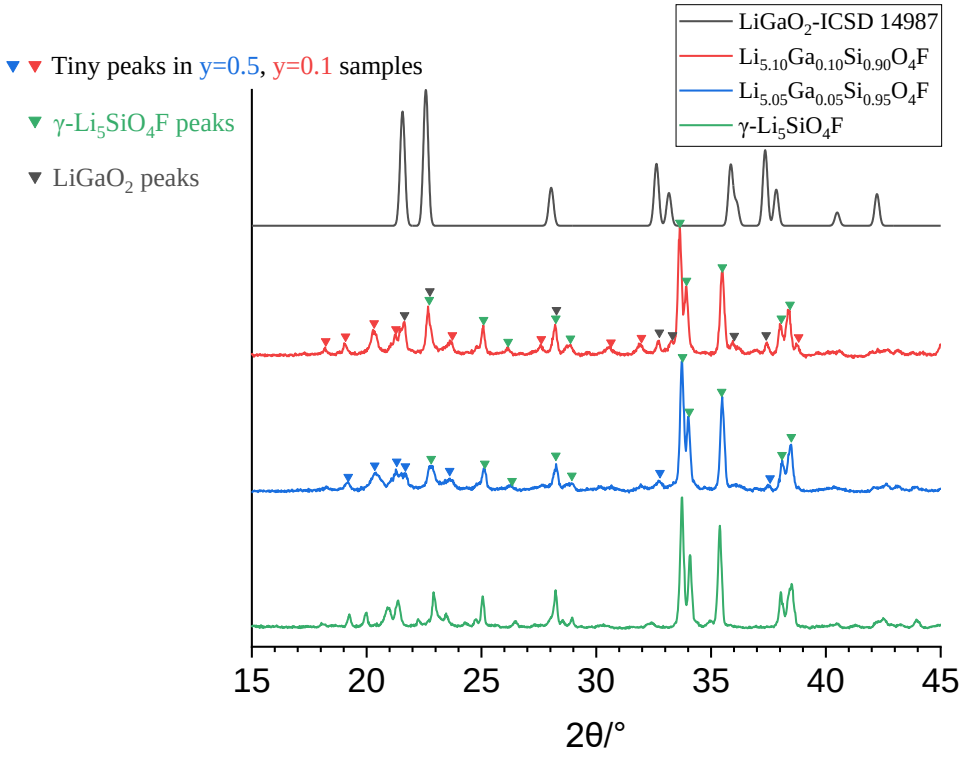

Fig 4.14. XRD result of $Li_{5+y}Ga_ySi_{1-y}O_4F$, y=0.05 and 0.1, in step 2 of mechanism 2, compared with standard patterns. When y=0.05, the pattern is similar to that of γ-Li_5SiO_4F with some different tiny peaks; when y=0.10, there is clear $LiGaO_2$ in the product.

In step 2, Ga doped Li_4SiO_4 precursors were reacted with LiF at 750°C for 10 h. Results, Fig 4.14, show a similar pattern to Li_5SiO_4F and possibly a small amount of $LiGaO_2$. It appears that there may be some successful doping of Ga into Li_5SiO_4F, especially for y=0.05.

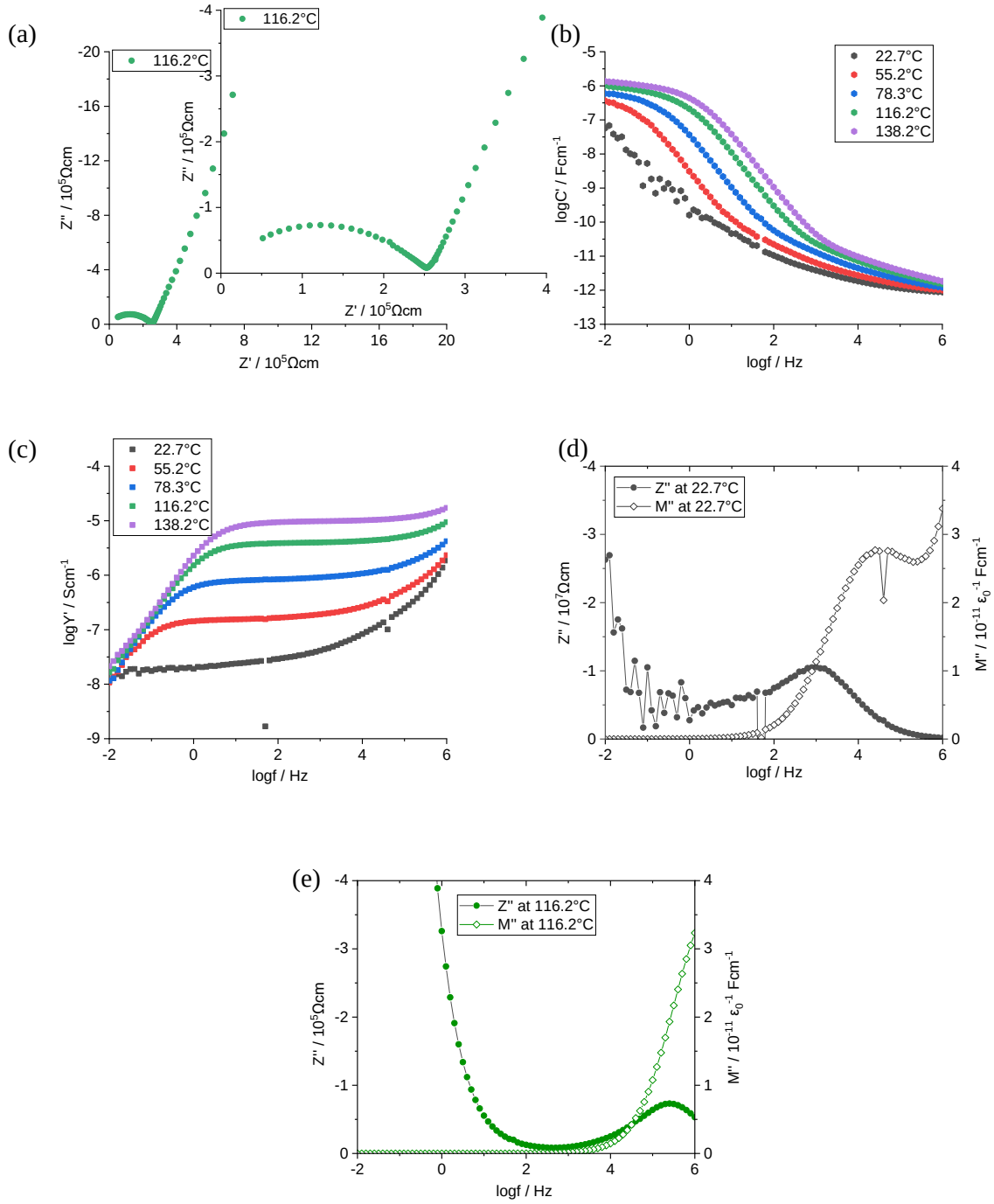

Fig 4.15. The impedance datasets for $Li_{5.05}Ga_{0.05}Si_{0.95}O_4F$, pellet sintered at 750°C, 10 hours, (a) impedance complex plane plot, spectroscopic plots of (b) capacitance C', (c) admittance Y', and (d) Z''-M'' at 22.7°C (e) Z''-M'' at 116.2°C.

Pellets made by mechanism 2 were sintered at 750°C for 10 h, coated with Au electrode paste and reheated at 750°C for 4 h. The impedance results of y=0.05 show an asymmetric semicircle followed by a low frequency spike in the impedance complex plane plot, Fig 4.15 (a). The semicircle shows the total resistance, ~2.5×10^5 Ωcm^{-1} at 116.2°. Two plateaux at ~10^{-12} and 10^{-7}-10^{-6} Fcm^{-1} in $C^{'}$ plots, (b), correspond to bulk and sample-electrode interphase responses. $Y^{'}$, (c), shows a wide plateau over 1-10^4 Hz with dispersions at both low and high frequency ends. Two $M^{''}$ peaks can be seen in data at ambient temperature, (d). It can possibly be due to a secondary phase in the sample, which lead to the other bulk response. If so, it will be a very conductive element. The only possible secondary phase given by XRD result, Fig 4.14, is $LiGaO_2$ which is relatively a poor ionic conductor with 10^{-6} Ωcm^{-1} at ~500°C [13]. Thus, the possible second bulk response cannot be $LiGaO_2$ due to its low ionic conductivity value. Impedance results for the y=0.10, Fig 4.S3, show no high frequency $M^{''}$ peak in (d), thus the unexpected $M^{''}$ peak in y=0.05 is possibly due to unknown instrument issues.

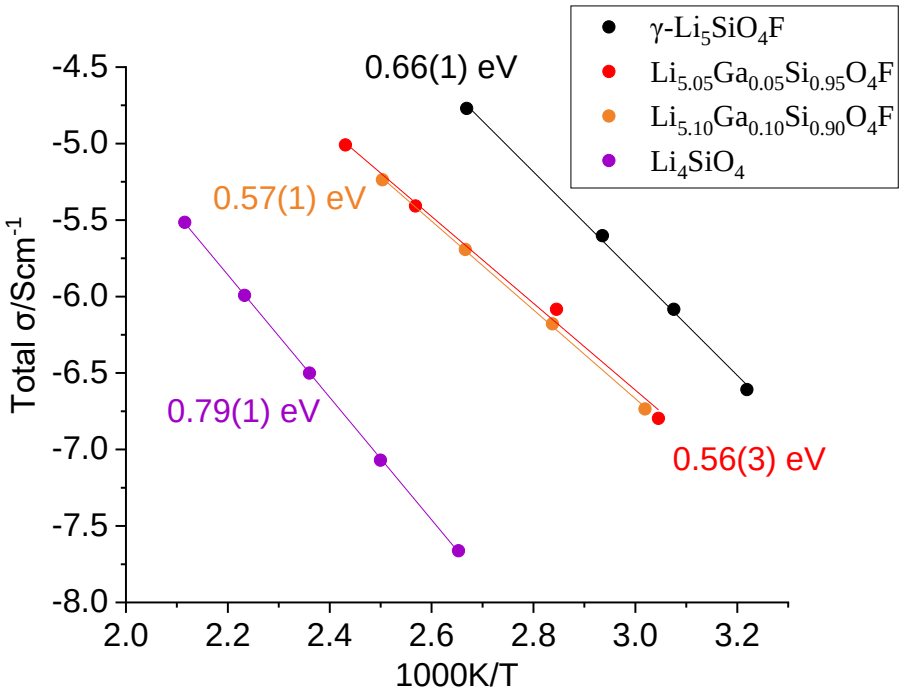

Fig 4.16. Arrhenius plot for Ga doped Li_5SiO_4F samples

The Arrhenius plots, Fig 4.16, show a total ionic conductivity which is ~1 order of magnitude lower than that of undoped γ-Li_5SiO_4F. No significant difference was observed in samples with y=0.05 or 0.10, which probably indicates a common doped γ-Li_5SiO_4F bulk component in them. Both Ga-doped samples have a lower activation energy compared to that of undoped Li_5SiO_4F.

Unsuccessful dopants

4.2.3. Ni^{2+} doped Li_5SiO_4F

In doping γ-Li_5SiO_4F by divalent dopants, A^{2+}, every A^{2+} is likely to replace 2 Li^+ leaving one lithium vacant site. The first divalent dopant tried was Ni^{2+}. $Li_{5-2x}Ni_xSiO_4F$, x=0.1, was prepared by solid state reaction at 750°C for 10 h with starting materials Li_2CO_3, SiO_2, NiO and LiF.

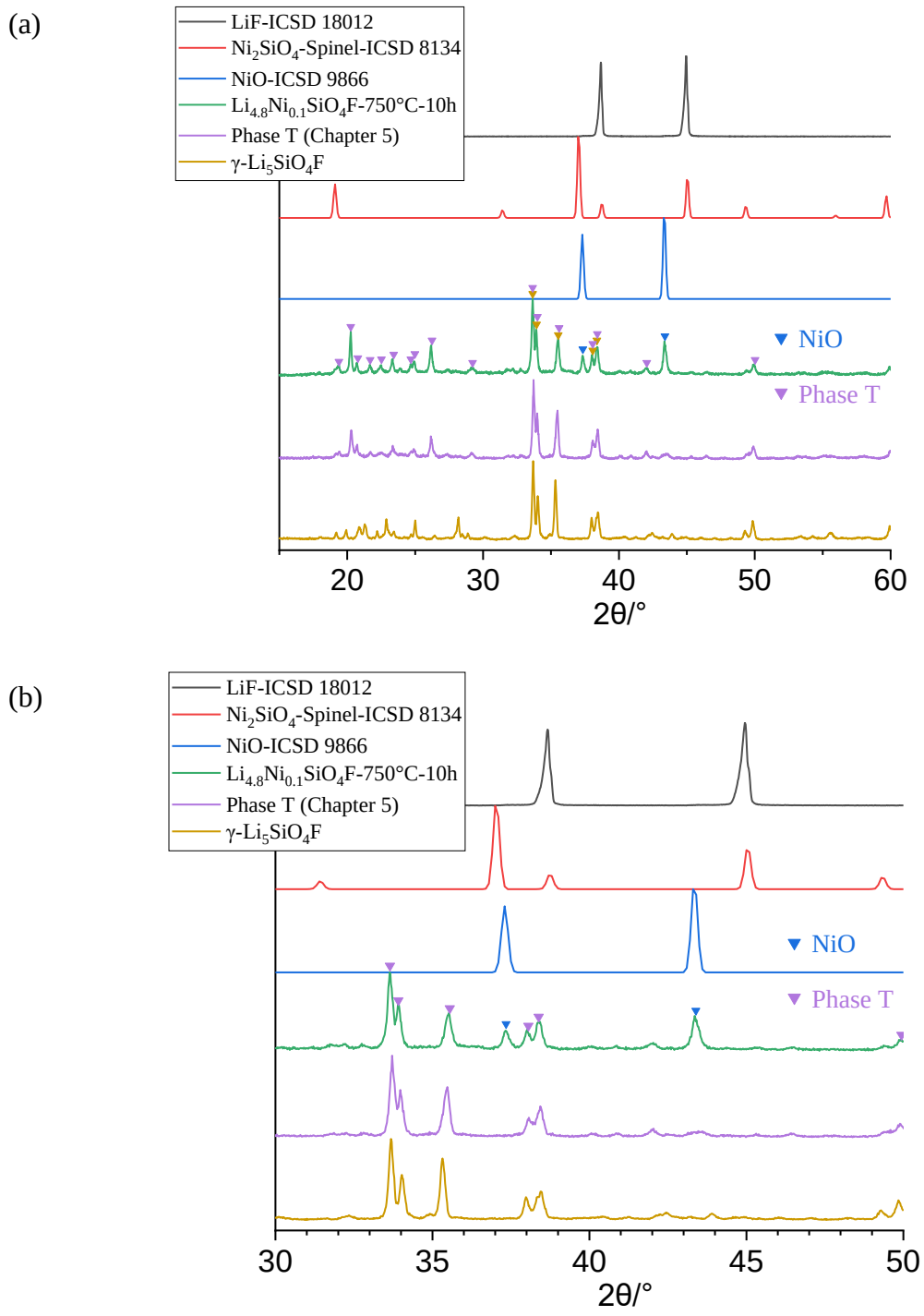

Fig 4.17. (a) XRD result of $Li_{5-2x}Ni_xSiO_4F$, x=0.1 prepared at 750°C for 10 hours (b) on an expanded scale. The product is a mixture of Phase T and NiO.

The XRD result , Fig 4.17, shows a mixture of two possible phases: (1) a new γ-type phase, named as Phase T, which is discussed in detail in Chapter 5; (2) NiO, which indicates that little

or no Ni^{2+} can be doped in γ-Li_5SiO_4F under current experimental conditions. Possibly, some Ni^{3+} may form as defects in NiO, in which two Ni^{2+} are replaced by Ni^{3+} and Li^+ [14].

To conclude, this work was not successful as a doping study as there is no evidence that γ-Li_5SiO_4F can be doped by Ni^{2+} at 750°C, but it shows there may exist other γ-type phase, undoped or Ni-doped, similar to γ-Li_5SiO_4F in the ternary system Li_2O-SiO_2-LiF.

4.2.4. Mg^{2+} doped Li_5SiO_4F

Doping of Mg^{2+} was tried with composition $Li_{5-2x}Mg_xSiO_4F$, x=0.10. Li_2CO_3, SiO_2, MgO and LiF were heated at 750°C for 30 h for solid state reaction.

(a)

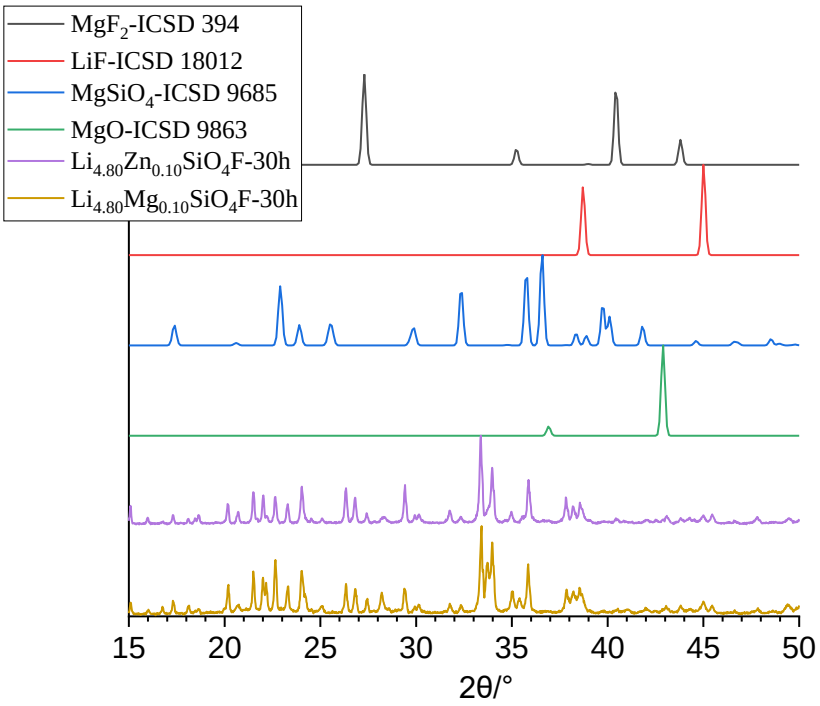

(b)

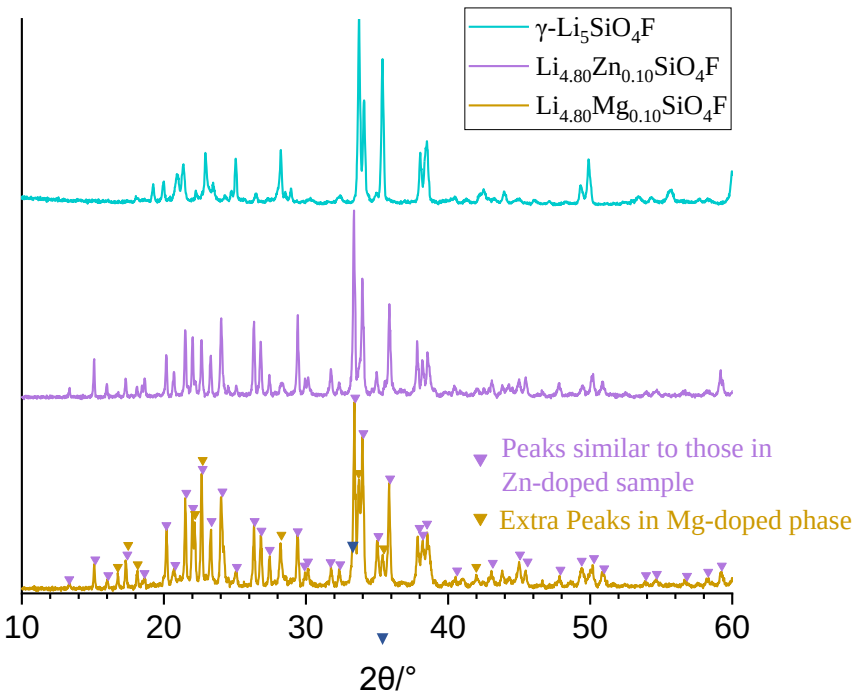

Fig 4.18. (a)x=0.1 sample, $Li_{4.8}Mg_{0.1}SiO_4F$ prepared at 750°C for 30 hours and a similar Zn-doped sample, clearly different to the γ-Li_5SiO_4F pattern. (b) extra peaks can be seen in Mg-doped phase compared to Zn-doped phase.

The XRD results of $Li_{5-2x}Mg_xSiO_4F$, with x=0.10, in Fig 4.18, show a mixture of at least 2 phases. The main phase has a similar diffraction pattern to $Li_{4.8}Zn_{0.1}SiO_4F$, in purple, which was named as Phase L, in section 4.2.9. The Mg doped sample has at least 7 extra peaks compared to Phase L as marked by yellow triangles in (b), which do not belong to any known compound. The additional peaks at 33.5°/2θ and 35.5°/2θ possibly indicate a secondary γ-type phase closely related to γ-Li_5SiO_4F.

In conclusion, the attempt to dope γ-Li_5SiO_4F by Mg^{2+} was unsuccessful. Phase L was prepared in two dopant studies: Zn^{2+} and Mg^{2+}. However, attempts to index Phase L have not been successful; the large numbers of peaks at low 2θ angles indicate a large or complex supercell.

4.2.5. $Co^{2+/3+}$ doped Li_5SiO_4F

Common oxidation states of Co include +2 and +3. There are, again, two possible mechanisms for doping Li_5SiO_4F by Co: (1).$Li_{5-2x(3x)}Co_xSiO_4F$, in which every 2 (or 3) Li^+ ions could be replaced by Co^{2+} or Co^{3+} leaving 2 (or 1) vacant sites; (2).$Li_{5+y(2y)}Co_ySi_{1-y}O_4F$, in which Si^{4+} ions could be replaced by Co^{2+} or Co^{3+} introducing interstitial Li^+ for charge compensation. Starting materials Li_2CO_3, SiO_2, Co_3O_4 and LiF were heated at 750°C for 10 h. Co_3O_4 can be heated in oxygen at 900 °C to give monoxide CoO [15]. The formulae of the final products are presented assuming Co was trivalent Co^{3+}.

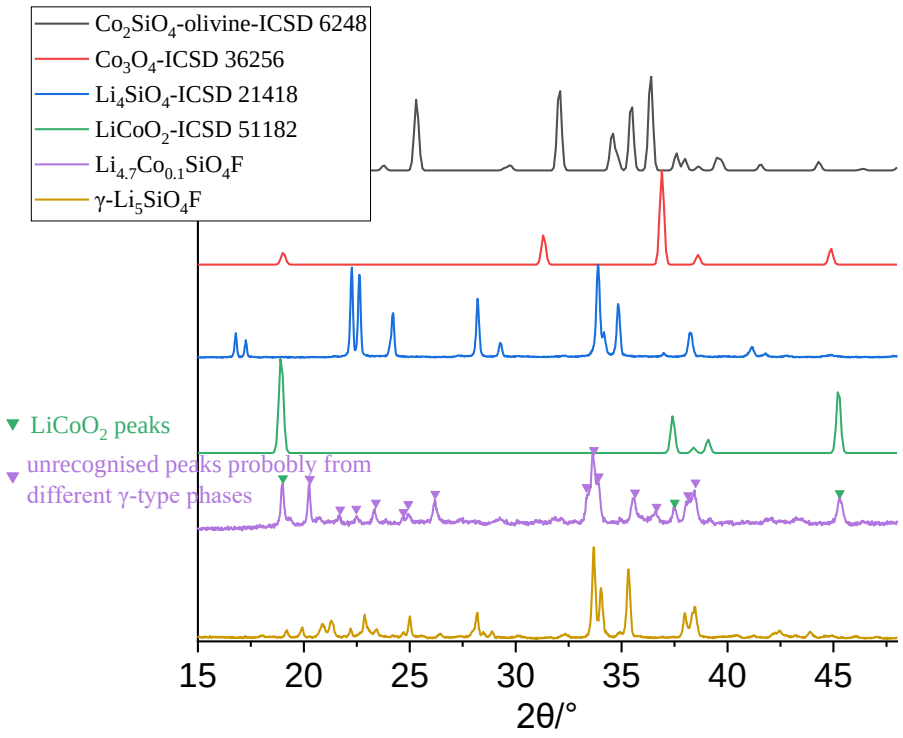

Fig 4.19. XRD result of $Li_{5-3x}Co_xSiO_4F$, x=0.1, by mechanism 1, prepared at 750°C for 10 hours shows a mixture of unknown peaks, which probably belong to at least two different γ-type phase, with $LiCoO_2$ lines.

In mechanism 1, the XRD result for x=0.1, Fig 4.19, show a mixture of (1) $LiCoO_2$, labelled by green triangles, (2) a possible mixture of at least two different γ-type phase labelled by purple triangles. The partially overlapped strong peaks at 33-40 °/2θ offer strong evidence of mixture of phases. These γ-type phase(s) may be closely related to γ-Li_5SiO_4F, from the shift of peak at ~35.3°/2θ in γ-Li_5SiO_4F, to slightly higher 2θ angles.

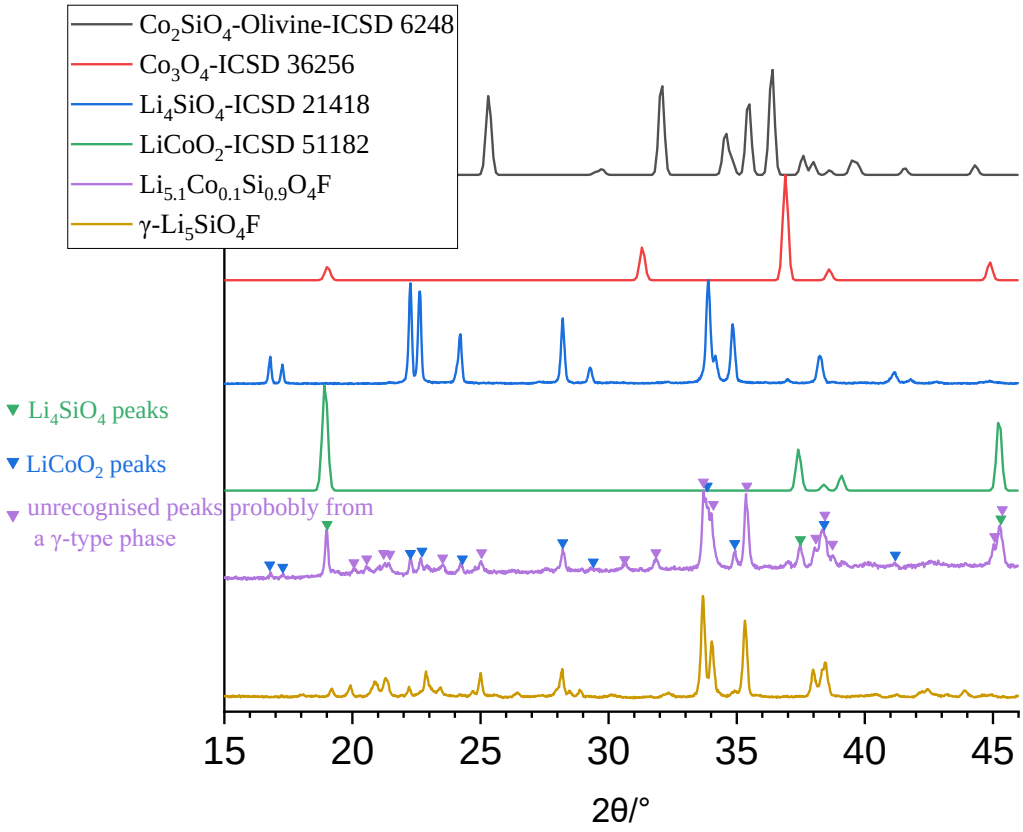

Fig 4.20. XRD result of $Li_{5-y}Co_ySi_{1-y}O_4F$, y=0.1, the product by mechanism 1 shows a mixture of $LiCoO_2$, Li_4SiO_4 and some unknown lines probably belong to a γ-type phase.

In mechanism 2, the product with y=0.1, Fig 4.20, consists of at least three different phases: a γ-Li_5SiO_4F-like phase (purple triangles), Li_4SiO_4 (blue triangles), and $LiCoO_2$ (green triangles). The amount of $LiCoO_2$ is large, which suggests a doping limit much less than y=0.1, or more likely, indicates no Co doped γ-Li_5SiO_4F can be formed under these experimental conditions.

To conclude, there is no sign of successful doping of γ-Li_5SiO_4F by Co^{3+} by solid state reactions at 750°C, either by mechanism 1 or 2, but other γ-related phase of unknown composition may form.

4.2.6. Fe^{3+} doped Li_5SiO_4F

The ionic radii of Fe^{3+}, 78.5 pm, and Ga^{3+}, 76 pm, are quite similar [2]. Thus, the trivalent dopant, Fe^{3+}, has been tried by the same two mechanisms as Ga^{3+}: (1). $Li_{5-3x}Fe_xSiO_4F$; (2). $Li_{5+y}Fe_ySi_{1-y}O_4F$. Compositions based on mechanisms, 1 and 2, were prepared in two steps: Firstly, Fe-doped Li_4SiO_4 precursors were prepared using Li_2CO_3, SiO_2, and Fe_2O_3 by solid state reaction at 900°C for 20 h; then, the precursors were reacted with LiF at 750°C for 10 hours. Results are as follows:

Mechanism 1: $Li_{5-3x}Fe_xSiO_4F$ (x=0.1)

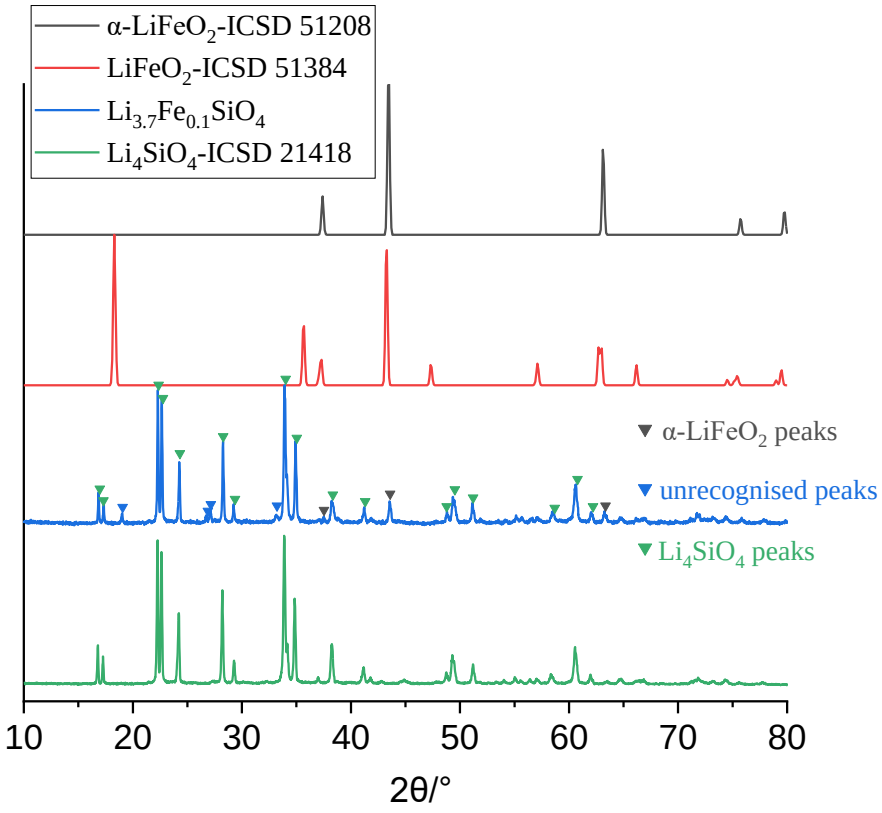

Fig 4.21. (a) XRD result of $Li_{4-3x}Fe_xSiO_4$, x=0.1, the precursor in mechanism 1 show main phase of Li_4SiO_4 (green) with α-$LiFeO_2$ (black) and extra lines (blue).

In step 1, the precursor, Fig 4.21, shows a main phase Li_4SiO_4 with several extra tiny peaks. The peaks at ~37.5°/2θ, ~43.5°/2θ and ~64.5°/2θ may correspond to α-$LiFeO_2$, marked by

black triangles. Other peaks, marked by blue triangles may indicate a Fe contained Li_4SiO_4. At this stage, it is difficult to determine whether Fe is doped in Li_4SiO_4.

(a)

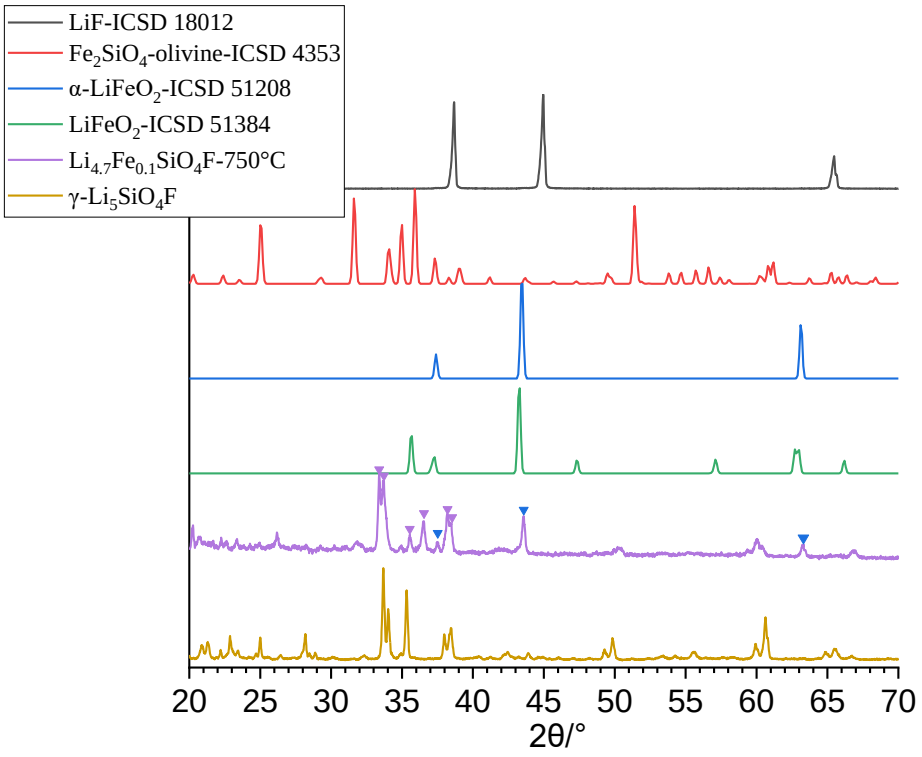

(b)

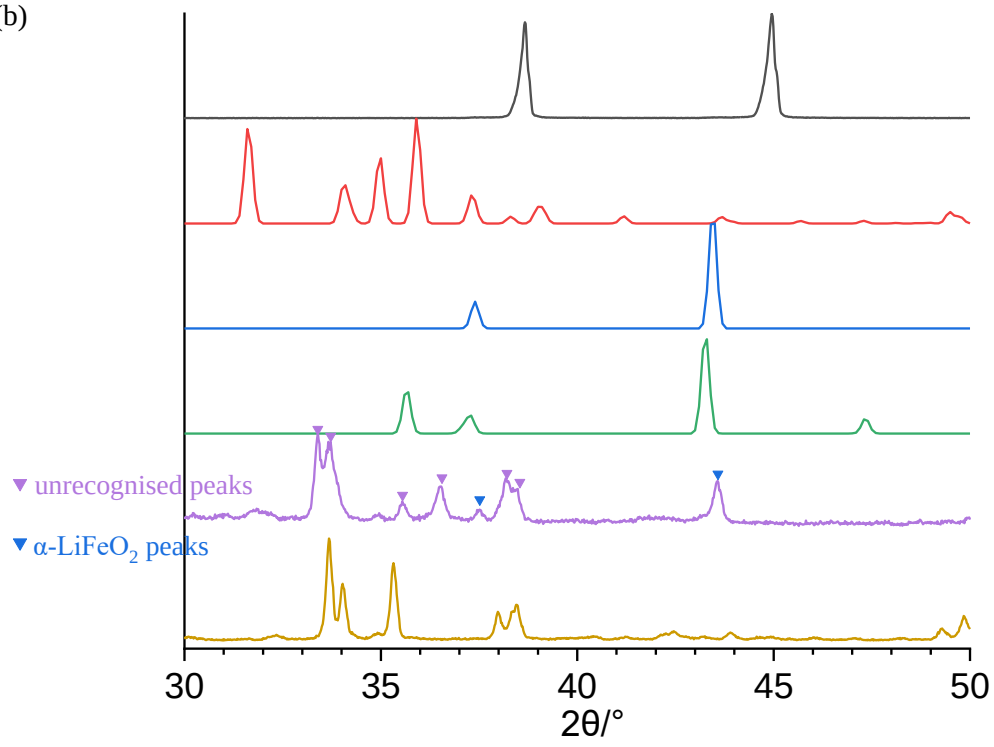

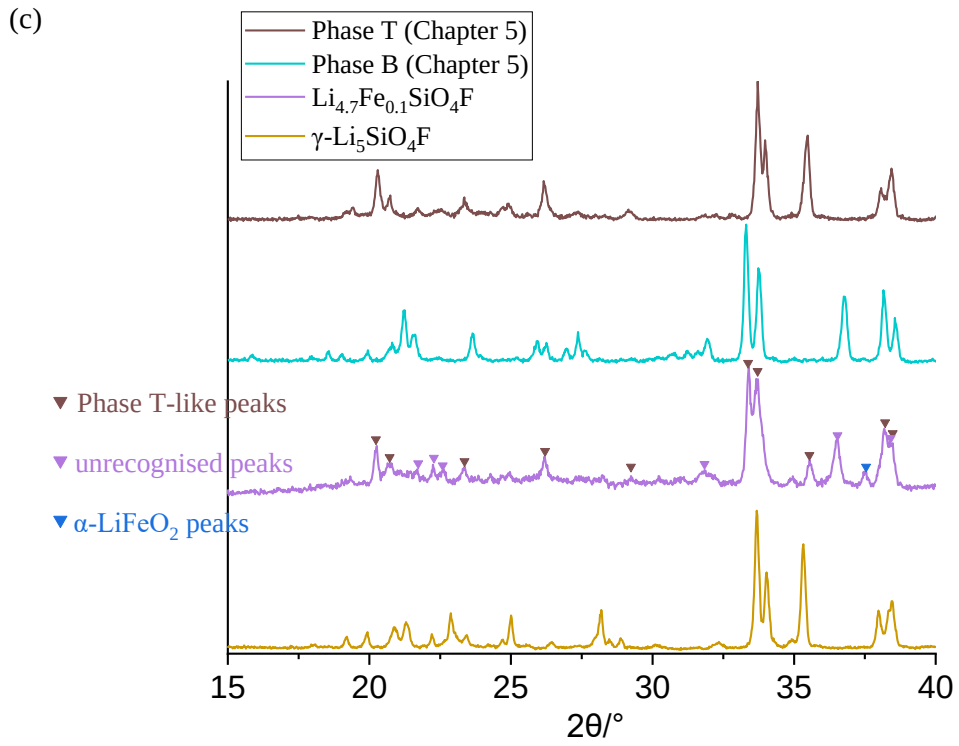

Fig 4.22. (a) XRD result of $Li_{5-3x}Fe_xSiO_4F$, x=0.1, final product in mechanism 1, which contains a mixture of α-$LiFeO_2$ (marked by blue triangles in (b) and (c)) and some unrecognised peaks, some of which may belong to Phase T-like phase (marked by brown triangles in (c), discussed in detail in Chapter 5)

In step 2, the final product, Fig 4.22, consists of several phases. There appears to be γ-type phase(s), given by characteristic peaks at 35.5°/2θ and 36.5°/2θ marked with purple triangles in (b). One may belong to Phase T or Phase B, new phases in the Li_2O-SiO_2-LiF system discussed in Chapter 5, as shown in (c). Two strong peaks at 43.5°/2θ and 63.3°/2θ, marked by blue triangles in (b), confirm the existence of cubic rock salt α-$LiFeO_2$ with disordered cations. This work may not be recognised as a successful doping study, but it gives a hint to further study on different γ-type phases with similar composition to Li_5SiO_4F that may contain less Li^+ content due to partial replacement by Fe^{3+}.

Mechanism 2: $Li_{5+y}Fe_ySi_{1-y}O_4F$(y=0.1)

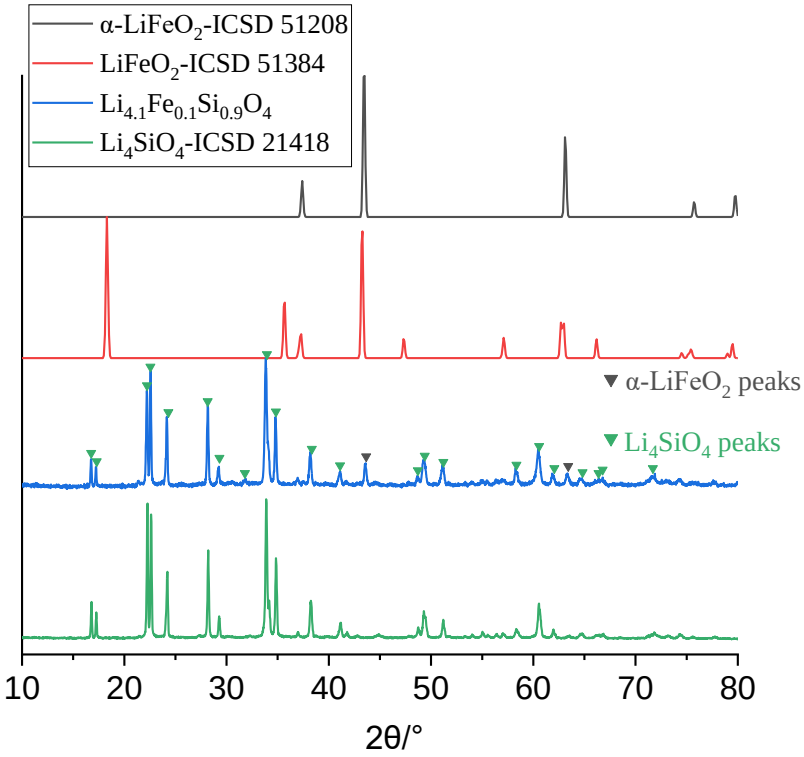

Fig 4.23. XRD result of $Li_{4+y}Fe_ySi_{1-y}O_4$, y=0.1, the precursor in mechanism 2 with Li_4SiO_4 lines (green) and α-$LiFeO_2$ lines (black).

The precursor in step 1, Fig 4.23, is similar to undoped Li_4SiO_4 with a small amount of α-$LiFeO_2$, given by extra peaks at 43.5°/2θ and 63.3°/2θ, marked by black triangles. Similar to the precursor in mechanism 1, it is hard to determine whether partial Fe^{3+} ions were partially doped into Li_4SiO_4.

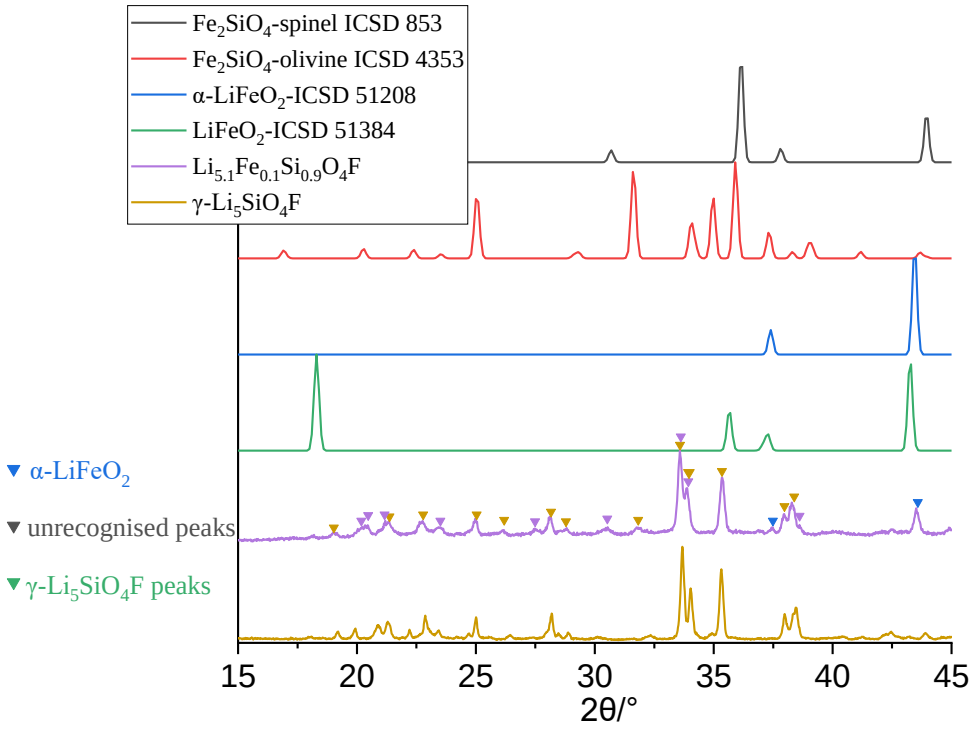

Fig 4.24. XRD result of $Li_{5+y}Fe_ySi_{1-y}O_4F$, y=0.1, the product of mechanism 2, shows a mixture of γ-Li_5SiO_4F-like phase (green) and α-$LiFeO_2$ (blue) with some unknown lines (purple).

Step 2, Fig 4.24, shows a mixture of γ-type phase and α-$LiFeO_2$, marked by blue triangles. There are many similarities between the γ-type phase and γ-Li_5SiO_4F, as marked by yellow triangles, but with small differences in some line position and peak splitting. There are two possibilities: (a) Fe doping of Li_5SiO_4F possibly occurred but the solid solution limit is less than y=0.1; (b) Fe is completely in α-$LiFeO_2$, the γ-type phase is closely related to γ-Li_5SiO_4F but with different Li:Si:O:F ratio due to different starting materials.

(a)

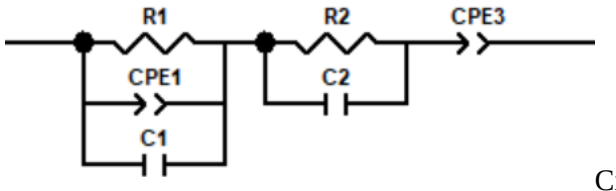

Circuit A

(b)

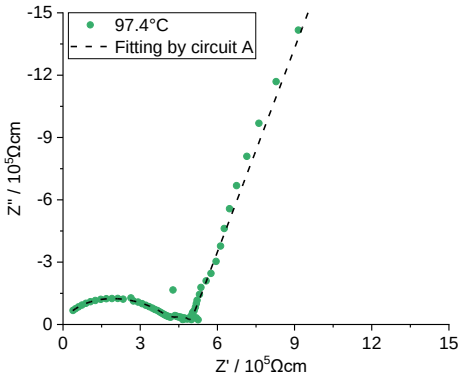

(c)

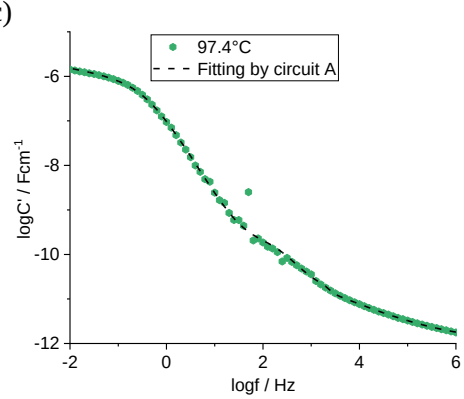

(d)

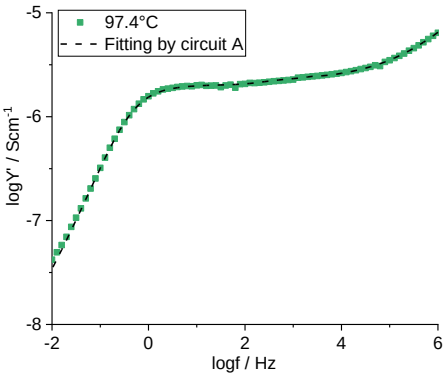

(e)

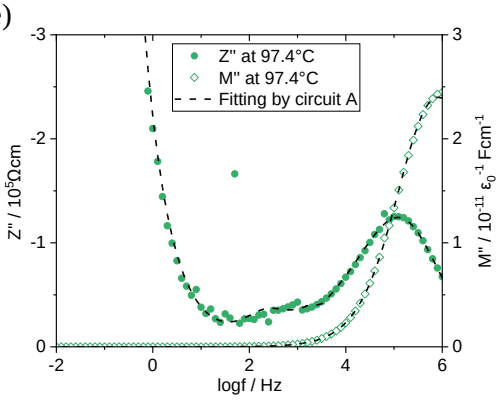

Fig 4.25. Experimental and fitted impedance datasets for $Li_{5.1}Fe_{0.1}Si_{0.9}O_4F$ at 97.4°C by circuit A in (a), (b) $Z^{''}$-$Z^{'}$ complex plane plot, spectroscopic plots of (c) capacitance $C^{'}$, (d) admittance $Y^{'}$, and (e) $Z^{''}$-$M^{''}$.

Table 4.4. The parameters in elements 1-3 for $Li_{5.1}Fe_{0.1}Si_{0.9}O_4F$ at different temperatures

Sample	97.4°C	116.1°C	141.9°C
R_1/ Ω	$4.44(8)\times10^{5}$	$1.61(3)\times10^{5}$	$6.1(2)\times10^{4}$
CPE1-T / F	$1.6(6)\times10^{-9}$	$1.7(9)\times10^{-9}$	$1(1)\times10^{-9}$
CPE1-P	0.53(3)	0.55(4)	0.6(1)
C_1 / F	$1.1(1)\times10^{-12}$	$10(2)\times10^{-13}$	$9(5)\times10^{-13}$
R_2/ Ω	$4.9(8)\times10^{4}$	$1.4(3)\times10^{4}$	$6(1)\times10^{3}$
C_2 / F	$1.3(4)\times10^{-8}$	$1.3(5)\times10^{-8}$	$1.0(5)\times10^{-8}$
CPE3-T / F	$9.75(9)\times10^{-7}$	$1.263(8)\times10^{-6}$	$1.70(1)\times10^{-6}$
CPE3-P	0.811(5)	0.795(3)	0.786(3)

A pellet of y=0.1, mechanism 2, sintered at 750°C for 10 h with Au electrodes and reheated at 750°C for 6 h gave typical impedance datasets for an ionic conductor, as shown in Fig 4.25 with equivalent circuit fitting by the circuit in (a). The data at 97.4°C are well fitted as shown in (b-e). The parameters in the equivalent circuit are summarised in Table 4.4. The capacitance of element 2, C_2, show an average value of 10^{-8} F, which is ~4 orders magnitude larger than C_1. As the typical grain boundary value is 2-3 orders of magnitude higher than the bulk [16], element 2 may regarded as another bulk element formed as a very thin layer.

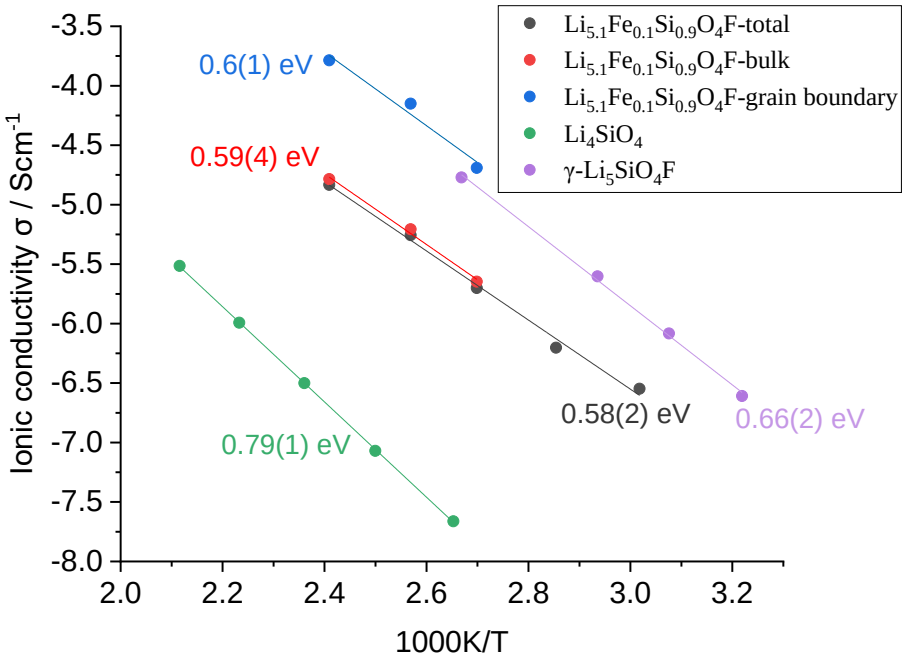

Fig 4.26. Arrhenius plot for Fe-doped Li_5SiO_4F by mechanism 2, y=0.1

The high conductivity of the grain boundary element, element 2, in the Arrhenius plot in Fig 4.26, does not indicate a highly conductive material. As there is a large difference by ~4 orders magnitude in fitted C_1 and C_2, Table 4.4, element 2 may be regarded as a very thin layer bulk material with its geometrically corrected ionic conductivity roughly 3 orders of magnitude lower than the total or bulk conductivity. The total conductivity of the sample by mechanism 2 is ~1 order of magnitude lower than that of undoped Li_5SiO_4F. The activation energy of the Fe doped sample, with 0.58(2) eV is lower than that of γ-Li_5SiO_4F, with 0.66(2) eV.

To conclude, Fe^{3+} doping of γ-Phase B by mechanism 1 was not successful as a doping study but shows possible existence of other γ-type phases. Based on the XRD result in Fig 4.24 and Arrhenius plot in Fig 4.26, whether there is partial Fe^{3+} is doped into γ-Li_5SiO_4F by mechanism 2 cannot be confirmed, but there is a secondary phase, α-$LiFeO_2$, in the final product by XRD and secondary element in impedance, thus probably Fe^{3+} can be doped in γ-Li_5SiO_4F but with a much less limit, or more likely, Fe^{3+} may not be doped in γ-Li_5SiO_4F by this method.

4.2.7. Ti^{4+} doped Li_5SiO_4F

One tetravalent dopant of γ-Li_5SiO_4F, Ti^{4+}, has been tried with a general formula, $Li_5Si_{1-x}Ti_xO_4F$. Starting materials, Li_2CO_3, SiO_2, TiO_2 and LiF, were reacted at 750°C for 20 h.

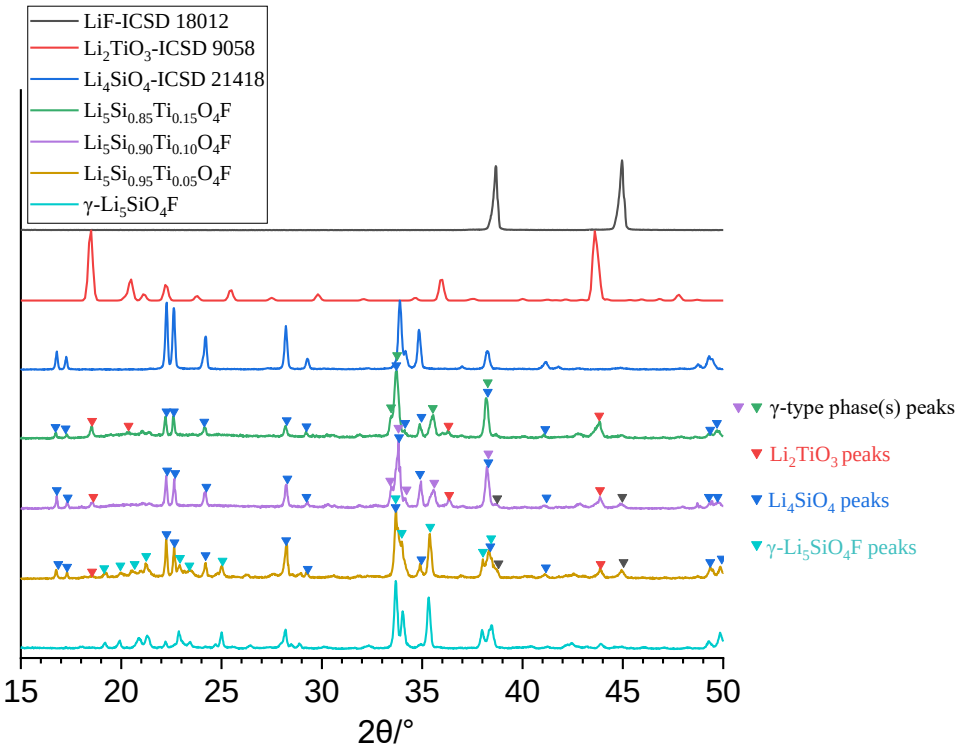

Fig 4.27. XRD results of Ti^{4+} doped γ-Li_5SiO_4F sample, with x=0.05, 0.10 and 0.15, mixture of γ-Li_5SiO_4F (light blue triangles in x=0.05 sample) or other γ-type peaks (purple triangles in x=0.10 sample or green peaks in 0.15 sample), Li_4SiO_4 (blue triangles) and Li_2TiO_3 (red triangles).

The XRD results, Fig 4.27, show a mixture of at least 3 phases: Li_4SiO_4 (blue triangles), Li_2TiO_3 (red triangles) and an unknown phase (yellow/purple/green triangles). With higher x value, the content of Li_2TiO_3 seems to increase; simultaneously, the content of Li_4SiO_4 is lower. Li_2TiO_3 in products is likely to be the monoclinic polymorph, β-form, as the transition from monoclinic β-Li_2TiO_3 to cubic γ-Li_2TiO_3 requires a higher temperature of 1150-1250°C [17].

Under current experimental conditions, there is no evidence of Ti-doped γ-Li_5SiO_4F. However, it raised possible existence of Li_5TiO_4F, similar to γ-Li_5SiO_4F, which may deserve further investigation.

4.2.8. Ge^{4+} doped Li_5SiO_4F

The other tetravalent dopant Ge^{4+} was tried, with a general formula, $Li_5Si_{1-x}Ge_xO_4F$. Samples were also prepared by two different methods: (1) directly by reaction of Li_2CO_3, SiO_2, GeO_2 and LiF at 750°C for 20 hours; or (2) in two steps, by first preparing Ge-doped Li_4SiO_4 at 900°C for 20 h, which was then reacted with LiF at 750°C for 10 h.

Method 1* (direct synthesis)*:

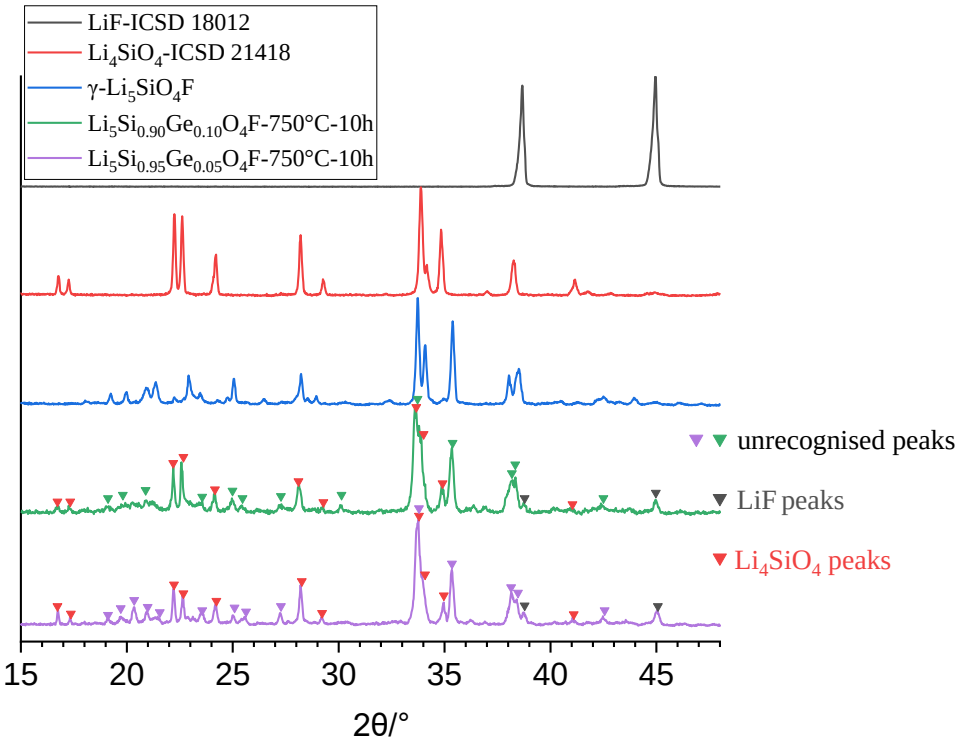

Fig 4.28. Ge doped γ-Li_5SiO_4F sample prepared by method 1, with x=0.05 and 0.10, with clear Li_4SiO_4 lines (marked by red triangles) and small LiF lines (marked by black triangles).

XRD results of x=0.05 and 0.10, method 1, are shown in Fig 4.28. When x=0.05, the product consists of a γ-type phase, Li_4SiO_4 and a small amount of LiF. Compared to γ-Li_5SiO_4F, the γ-type phase shows differences in two groups of doublet peaks at 33.5-34.5°/2θ and 38-39°/2θ

and peaks at low 2θ angles region. When x=0.10, same 3 phases are shown in the products with higher content of Li_4SiO_4. So far, it is hard to say whether Ge^{4+} has been doped in this γ-type phase, as there is no trace of other Ge contained compounds by XRD results.

Method 2 (2 steps synthesis):

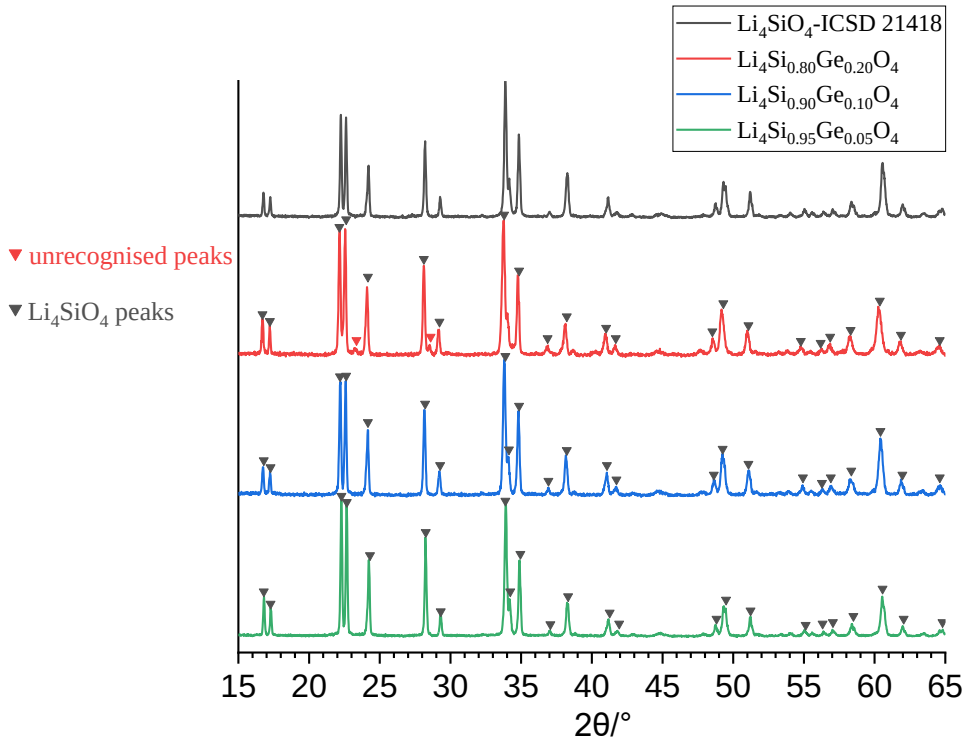

Fig 4.29. Ge doped Li_4SiO_4 samples, with x=0.05, 0.10 and 0.20, the precursors in step 1 of method 2, showing main phase of Li_4SiO_{4SS}.

Table 4.5. Compositions, synthesis conditions and products of Ge-doped samples

Composition	Synthesis temperature	Synthesis time	Products
$Li_4Si_{1-x}Ge_xO_4$			
x=0.05	900°C	20 hours	$Li_4SiO_{4\ ss}$
x=0.10	900°C	20 hours	$Li_4SiO_{4\ ss}$
x=0.20	900°C	20 hours	$Li_4SiO_{4\ ss}$
$Li_5Si_{1-x}Ge_xO_4F$ (Method 2)			
x=0.05	750°C	10 hours	Li_4SiO_4 and γ-type phase 2
x=0.10	750°C	10 hours	Li_4SiO_4 and γ-type phase 2
$Li_5Si_{1-x}Ge_xO_4F$ (Method 1)			
x=0.05	750°C	10 hours	Li_4SiO_4, γ-type phase 1 and LiF
x=0.10	750°C	10 hours	Li_4SiO_4, γ-type phase 1 and LiF

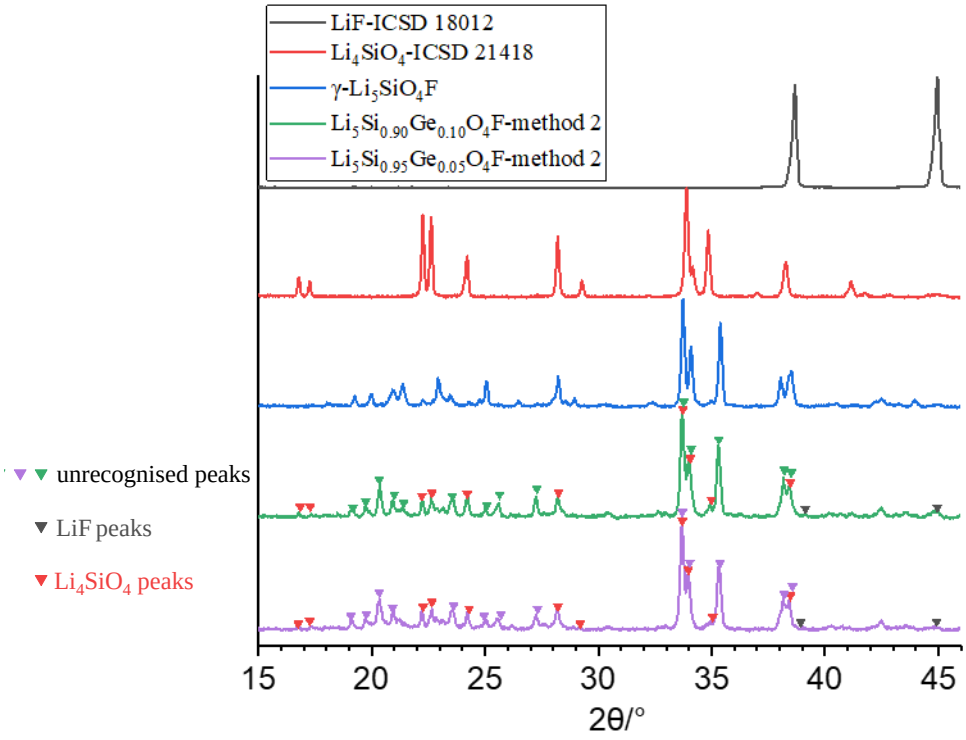

Fig 4.30. XRD results of $Li_5Si_{4-x}Ge_xO_4F$ samples, with x=0.05 and 0.10, products in step 2 of method 2, showing γ-type phase (marked by purple triangles in x=0.05 sample and green triangles in x=0.10 sample), Li_4SiO_4 (red triangles) and LiF (black triangles) mixture.

In step 1 of method 2, the XRD results of Ge doped Li_4SiO_4 precursors are shown in Fig 4.29. When x=0.05 and 0.10, the products show a Li_4SiO_4 solid solution pattern indicating a successful doping by Ge^{4+}; when x=0.20, extra peaks show as mark by red triangles. It indicates a limit of Ge^{4+} form a Li_4SiO_4-type solid solution, x<0.20, which is lower than the literature value, with x<0.33 [18]. In step 2, products with x=0.05 and 0.10 show a mixture of γ-type phase, Li_4SiO_4 and probably a small amount of LiF, Fig 4.30. There is no trace of other Ge-contained compound. Possibly, Ge^{4+} is successfully doped into the γ-type phase. However, Li_4SiO_4 in the final products indicate a varied compositions of starting materials to reach the single phase. XRD results of all samples are summarised in Table 4.5.

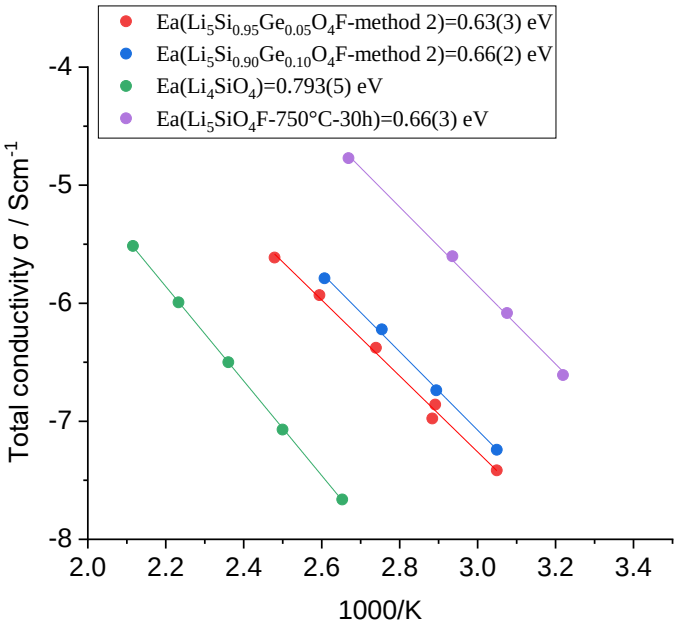

Fig 4.31. Arrhenius plot for Ge-doped Li_5SiO_4F by mechanism 2, x=0.05 and 0.10, compared with Li_4SiO_4 and γ-Li_5SiO_4F

The impedance results of x=0.05 and x=0.10, by method 2, are shown in Fig 4.S4-S5. Both samples show a typical ionic conductor behaviour. The total ionic conductivity of Ge-doped Li_5SiO_4F by method 2, are shown in Arrhenius plot in Fig 4.31. Both samples show a total ionic conductivity of ~8×10^{-7} S/cm at ~100 °C, which is higher than that of stochiometric Li_4SiO_4 but lower than that γ-Li_5SiO_4F.

In conclusion, by current XRD results, it seems that Ge^{4+} is successfully doped into Li_4SiO_4 with a doping limit x<0.2 and may be successfully doped into γ-Li_5SiO_4F by method 2. When x=0.05 and 0.10, both products show a mixture of γ-type phase and small amount of Li_4SiO_4. The γ-type phase may share a similar subcell structure with γ-Li_5SiO_4F, but a different supercell as possible. It may worth trying to determine a better synthesis method to obtain single phase for further crystal structure studies.

4.2.9. Zn^{2+} doped Li_5SiO_4F: $Li_{5-2x}Zn_xSiO_4F$ and aLi_2ZnSiO_4-bLiF system

$Li_{5-2x}Zn_xSiO_4F$:

Zn doping of γ-Li_5SiO_4F has been tried with general formula, $Li_{5-2x}Zn_xSiO_4F$. Samples were prepared from Li_2CO_3, SiO_2, ZnO and LiF, heating at 775 °C for 30 h (or longer).

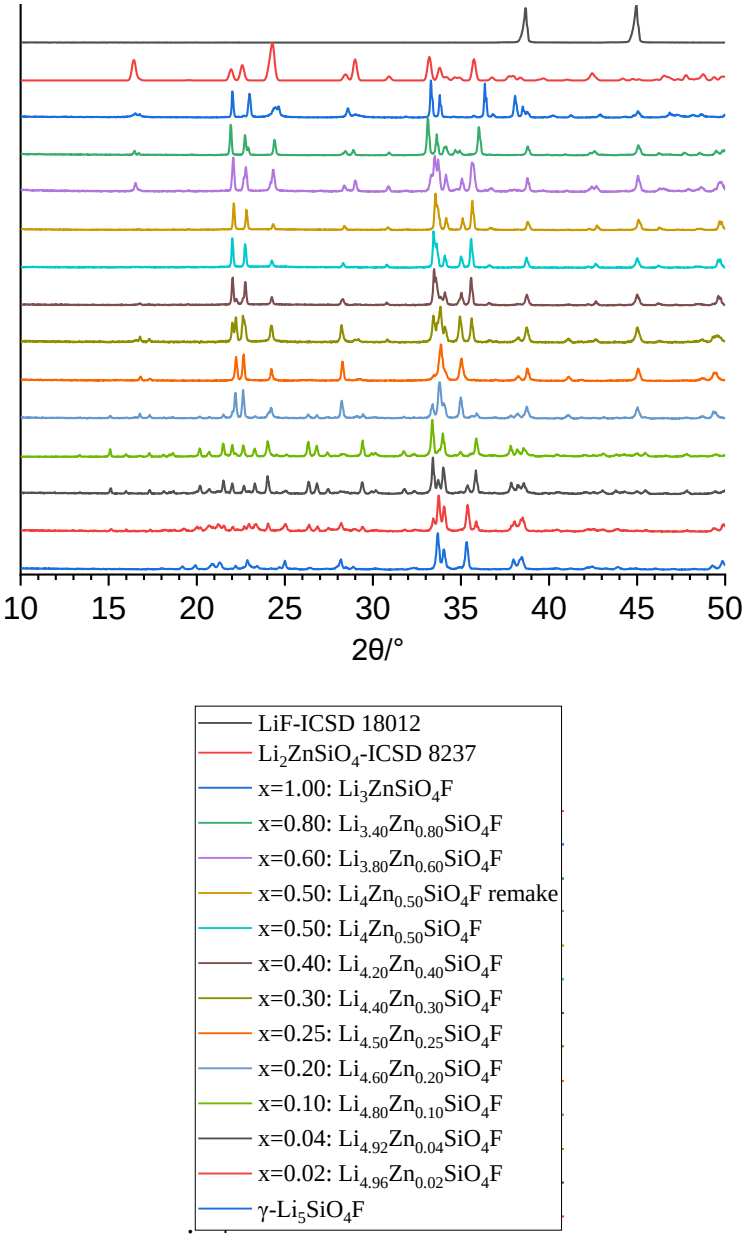

Fig 4.32. XRD results of $Li_{5-2x}Zn_xSiO_4F$ samples prepared at 750 °C for 30 h.

The XRD results with x=0-1 are shown in Fig 4.32. Sample x=0 corresponds to γ-Li_5SiO_4F. Zn substitution appears to give four new phases with compositions: x=0.10 (Phase L), x=0.25 (Phase M), x=0.50 (Phase H) and x=1 (Phase HH). LiF shows in compositions x>0.20, thus the true composition of Phase M, Phase H and Phase HH may contain less F^- than expected. At other compositions, mixtures of at least 3 phases were obtained.

Phase L (0.04<x<0.20):

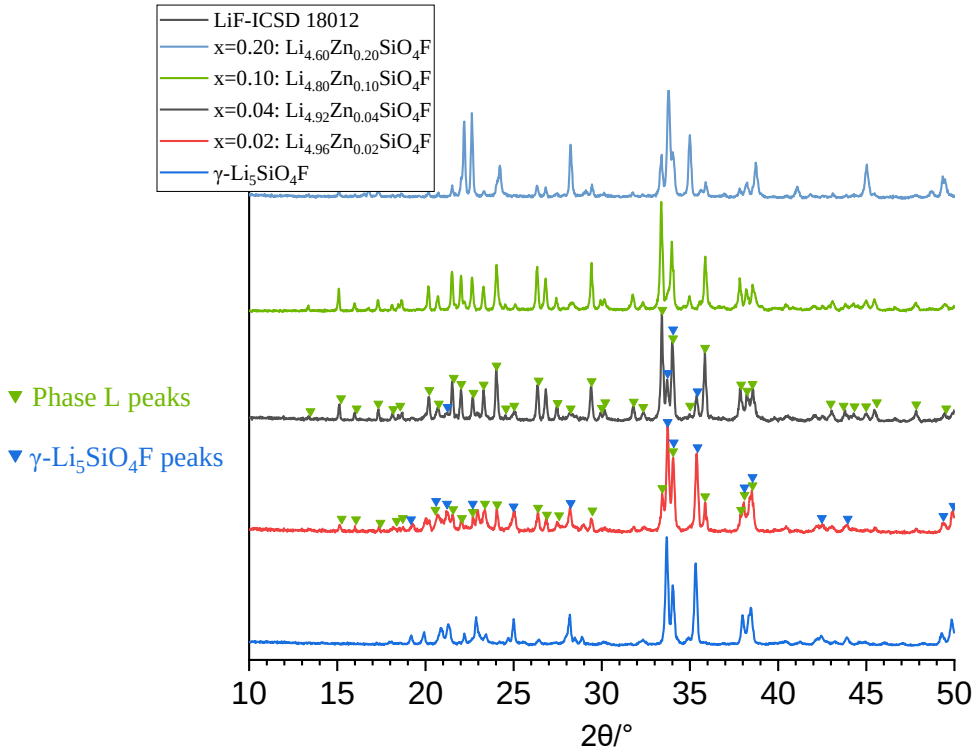

Fig 4.33. XRD results of $Li_{5-2x}Zn_xSiO_4F$ system with x=0-0.20, possible new Phase L shown in x=0.10 sample, marked by light green peaks.

When 0.04<x<0.20, the first possible new phase named as Phase L is obtained. Peaks in x=0.10 sample are not belonged to any known compound. At this stage, x=0.10 sample is regarded as a possible new phase, named Phase L. x=0.02 and x=0.04 samples show a mixture of γ-Li_5SiO_4F similar phase and Phase L. The composition of γ-Phase decreases with higher Zn content, while the composition of Phase L increases simultaneously.

Phase M (0.10<x<0.30):

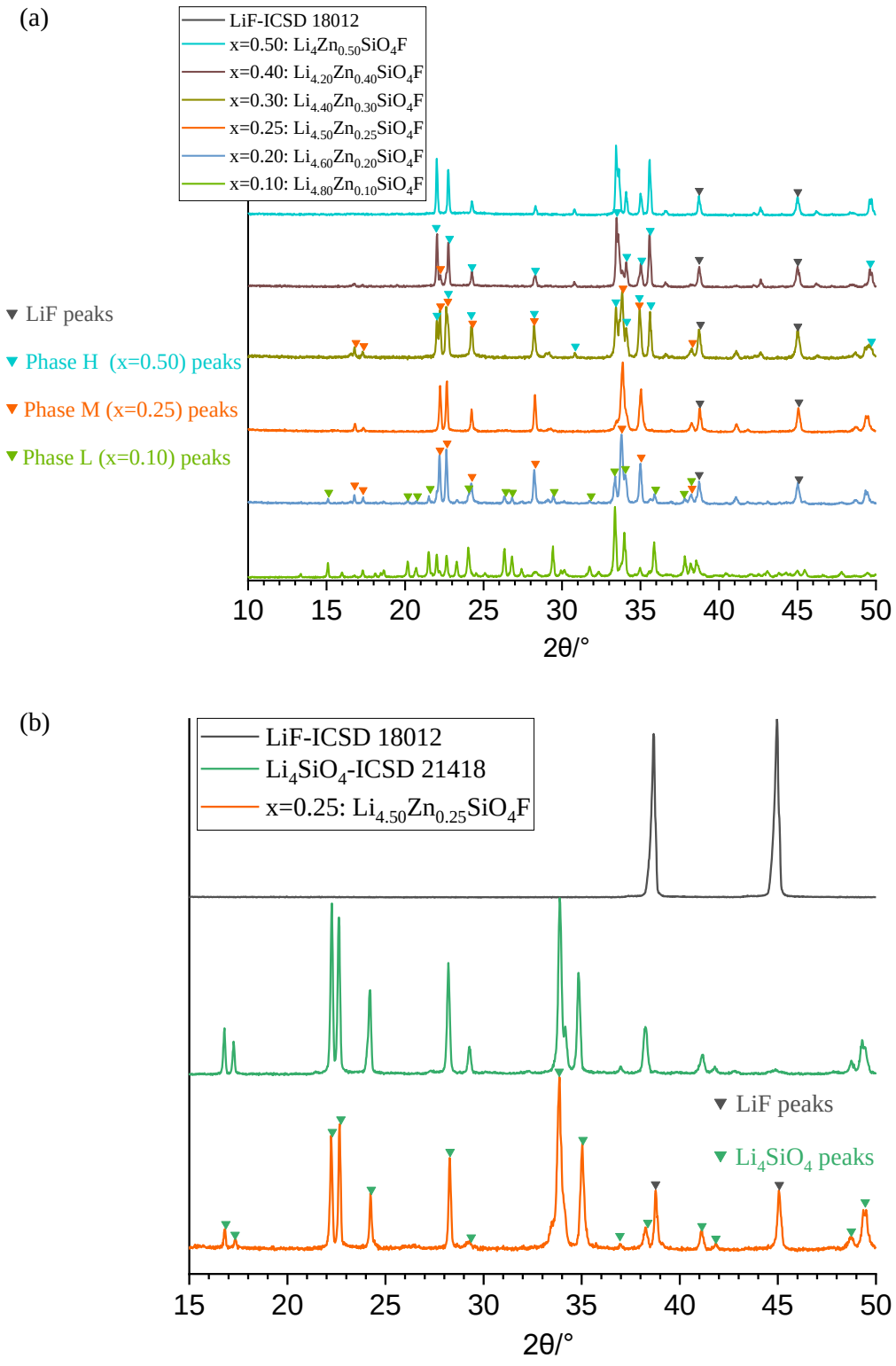

Fig 4.34. (a) XRD results of $Li_{5-2x}Zn_xSiO_4F$ system with x=0.10-0.50, possible new Phase M shown in x=0.25 sample (b) Phase M appears to be a mixture of Li_4SiO_4 solid solution and LiF.

Phase M appears to show with LiF when x=0.25 and coexists with other phases in x=0.20-0.30 samples, with peaks marked with orange triangles in Fig 4.34 (a). Phase M may be a Zn+F co-doped Li_4SiO_4 solid solution, Fig 4.34 (b), with a lower limit of F^- in its single phase as there is unreacted LiF left when x=0.25 but not x=0.10.

Phase H (0.30<x<0.60):

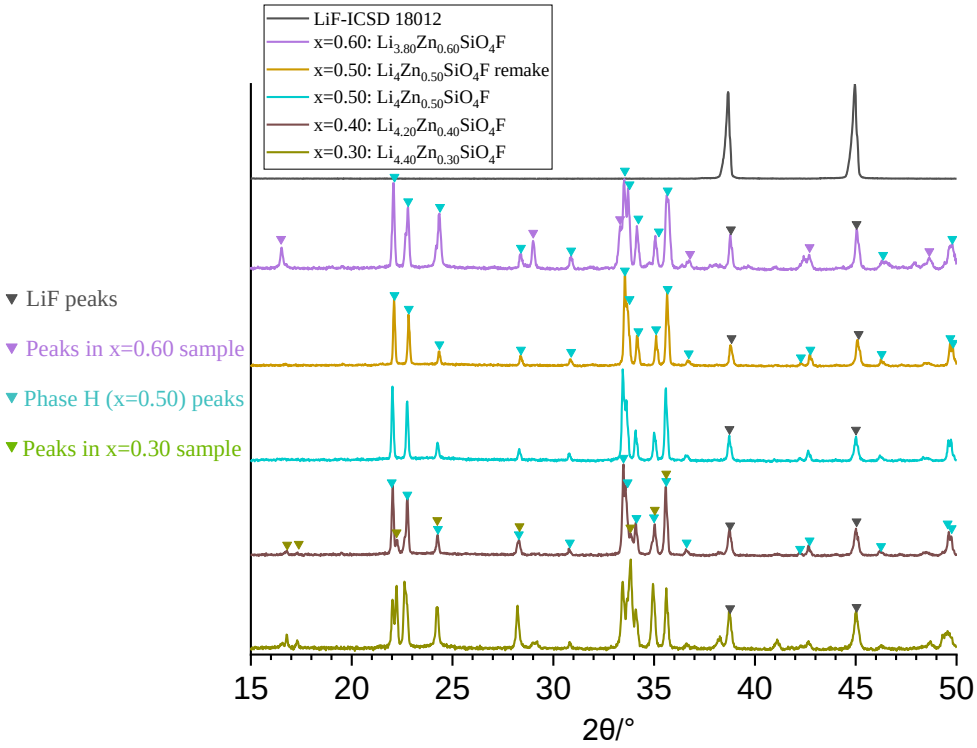

Fig 4.35. XRD results of $Li_{5-2x}Zn_xSiO_4F$ system with x=0.30-0.60, possible new Phase H shown in x=0.50 sample

Phase H shows in higher Zn-content samples with x=~0.50, Fig 4.35. At this stage, it should be noticed that there are some overlapped peaks between Phase M and Phase H, marked by red triangles, it cannot be confirmed whether these peaks are in similar positions, or they are mixtures in samples with x=0.3-0.6.

Phase HH and (0.60<x≤1.00):

(a)

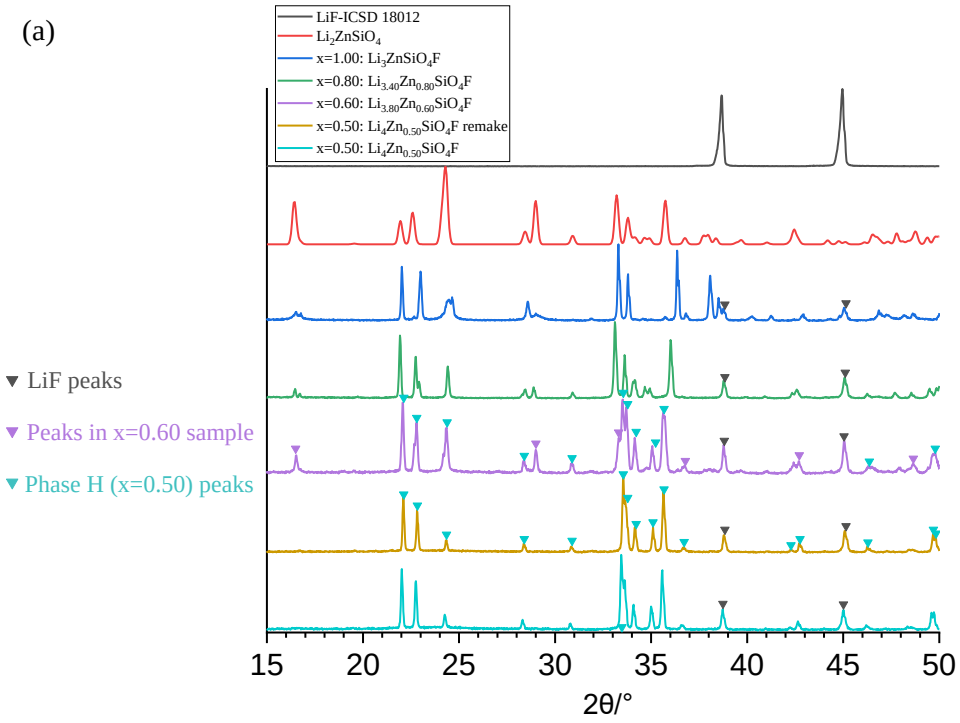

(b)

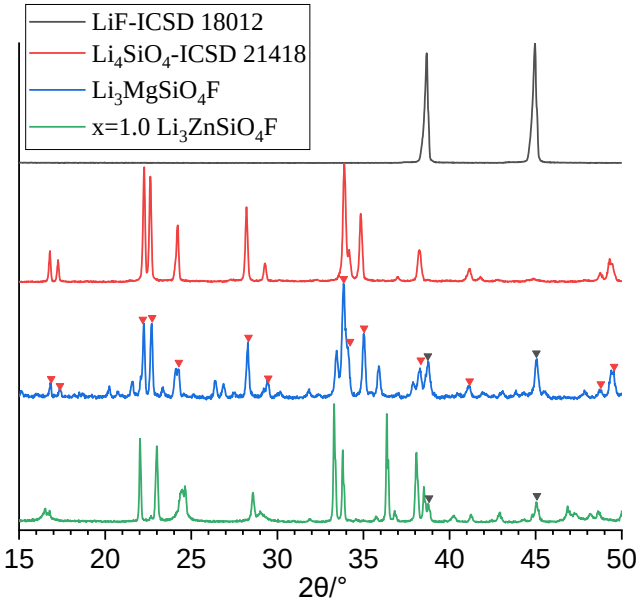

Fig 4.36. XRD results of $Li_{5-2x}Zn_xSiO_4F$ system with x=0.5-1.0, another possible new Phase HH shown in x=1.00 sample while some other phases possibly coexist in x=0.60-0.80 samples (b) Li_3ZnSiO_4F (x=1) and Li_3MgSiO_4F compared to standard patterns: $MgSiO_4F$ is clearly a mixture of Li_4SiO_4, LiF and extra lines while Li_3ZnSiO_4F appears to be a mixture of Phase HH and LiF.

Based on Fig 4.36. At least three different phases coexist in the samples with x=0.60-0.8, given by the peaks at 33-36°/2θ. Phase HH, appears to have a fixed composition with x=1.00, Li_3ZnSiO_4F. Similarly, Li_3MgSiO_4F was also prepared with same synthesis conditions, with comparison shown in Fig 4.36 (b). The product 'Li_3MgSiO_4F' consists of at least three phases: Li_4SiO_4, LiF and some unknown peaks. Thus, the sequence of new phases in Zn doping system seems to be different from those in Mg doping system.

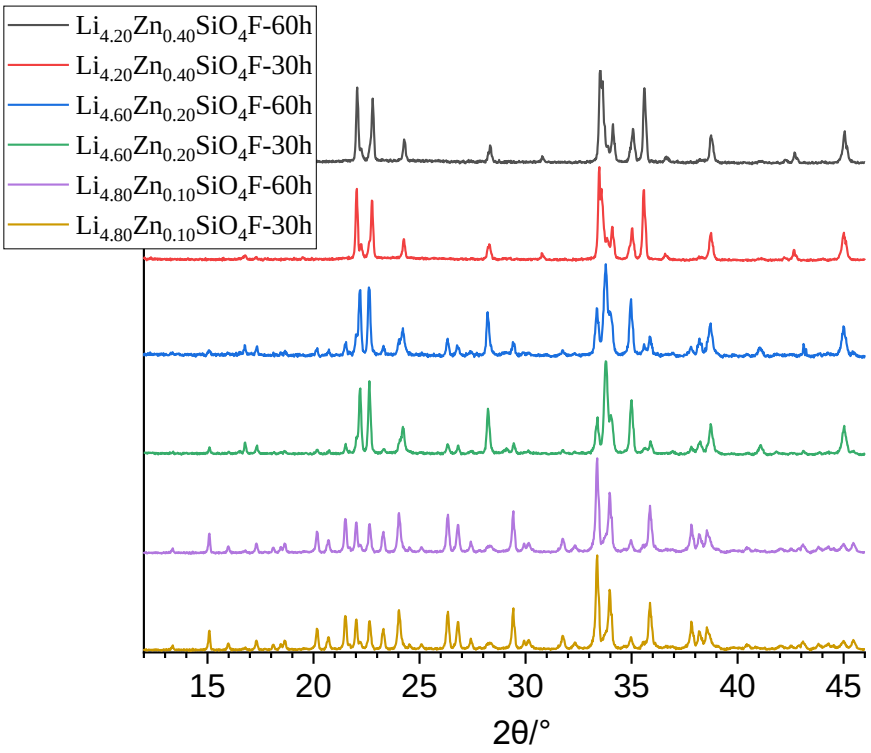

Fig 4.37. XRD results of some $Li_{5-2x}Zn_xSiO_4F$ samples reheated at 775°C.

Further heat treatment at 775 °C on some compositions, Fig 4.37, caused no further changes. As there is unreacted LiF remained in the product, the stoichiometric compositions of these new phases require further work, followed by structural and electrical property studies.

Arrhenius plot for $Li_{5-2x}Zn_xSiO_4F$ system:

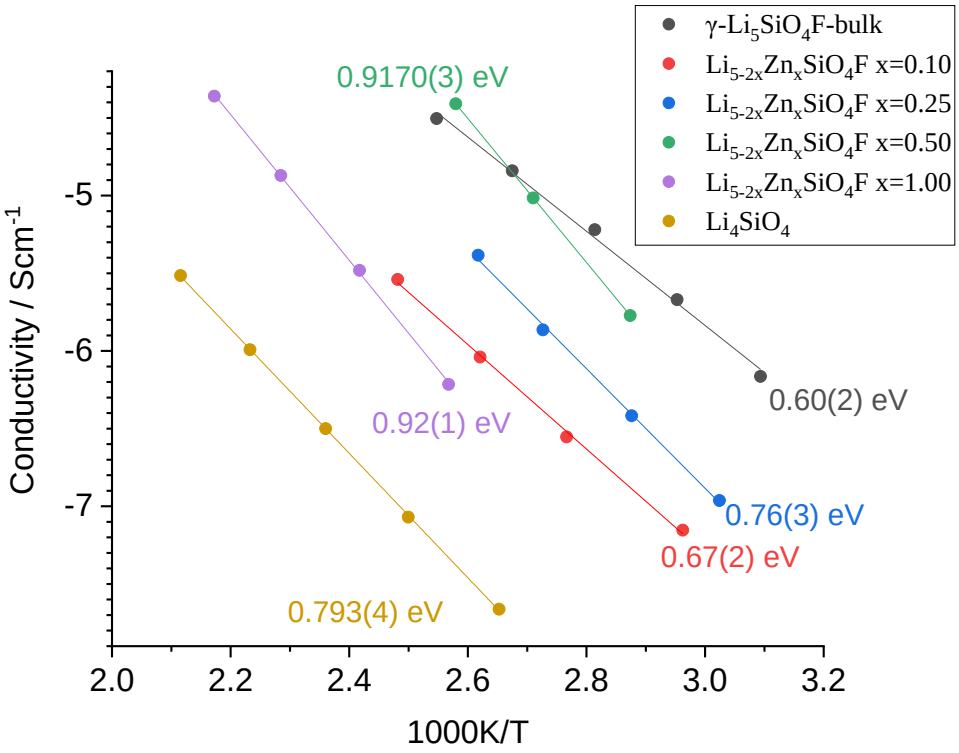

Fig 4.38. Arrhenius plot for Zn-doped Li_5SiO_4F, $Li_{5-2x}Zn_xSiO_4F$, x=0.10, 0.25, 0.50 and 1.00, compared to Li_4SiO_4 and γ-Li_5SiO_4F

The impedance results for samples with x=0.10, 0.25, 0.50 and 1.00 are shown in Figs 4.S6-S9. Samples with x=0.25 and x=0.50 exhibit the common response of a Li^+ ion conductor with bulk and sample-electrode interphase. Clear grain boundary response can be seen only in samples with x=0.10 and 1.00. The Arrhenius plots, Fig 4.38, show the total conductivity of Zn-doped samples. When x=0.1-0.5, the ionic conductivity of the sample increased with higher Zn content while its activation energy also increased. X=0.50 sample, Phase H, has the highest total ionic conductivity in this series similar to that of γ-Li_5SiO_4F but much higher activation energy, 0.92 eV and 0.60 eV, respectively. Further increase in Zn content, x=1.00, leads to reduced ionic conductivity which is still roughly 1 order of magnitude higher than that of bulk Li_4SiO_4. The activation energy of x=0.50, Phase H, and x=1.00, Phase HH, is close, ~0.92 eV, probably indicates a similar ion migration mechanism.

***a*Li_2ZnSiO_4-*b*LiF:**

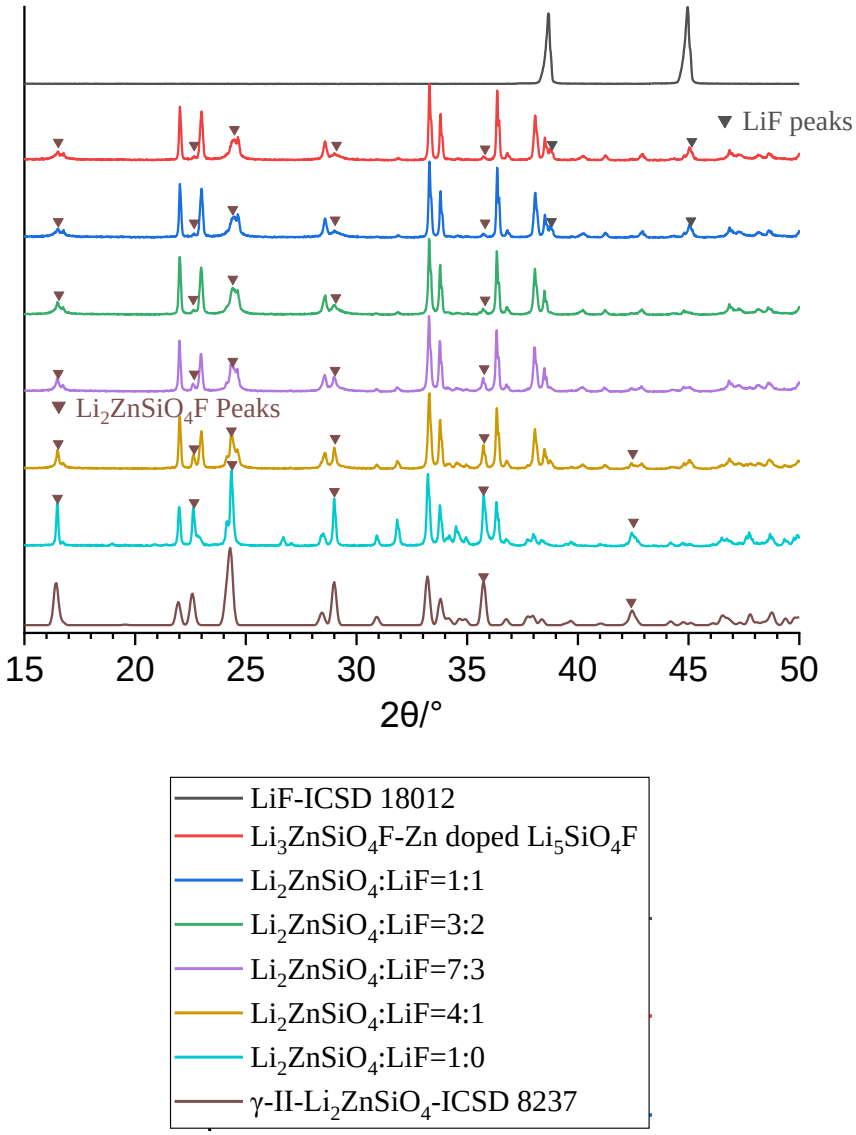

Fig 4.39. Compositions *a*Li_2ZnSiO_4-*b*LiF prepared at 750°C for 30 hours: the intensities of Li_2ZnSiO_4 lines decrease with higher F content while LiF start to show as a secondary phase when Li_2ZnSiO_4:LiF=1:1.

Composition x=1.00, Li_3ZnSiO_4F, with XRD shown in Fig 4.36, may be related to Li_2ZnSiO_4. A series of compositions with different Li_2ZnSiO_4:LiF ratio were prepared at 775 °C for 30 h, Fig 4.39. The main phase in different LiF-containing samples is similar. Several peaks have reduced intensity with higher composition of LiF, as marked by brown triangles, which belong to the monoclinic γ-Li_2ZnSiO_4; some other peaks have increased intensity with more

composition of LiF in starting material, probably belong to the orthorhombic β-Li_2ZnSiO_4. As LiF only presents in *a*:*b*=1:1 sample, a Li_2ZnSiO_4-LiF solid solution may exist between Li_2ZnSiO_4 (*a*:*b*=1:0) and Li_3ZnSiO_4F (*a*:*b*=1:1).

Table 4.6. The designed & real compositions of Zn, F, O, Si in some samples

x=0.10 $Li_{5-2x}Zn_xSiO_4F$ (Phase L)	Si /weight %	O /weight %	Zn /weight %	F /weight %
Test 1	26.01	62.42	4.68	6.89
Test 2	28.01	59.24	4.49	8.26
Test 3	23.43	67.27	4.37	4.92
Desired	23.88	54.41	5.56	16.15
x=0.30 $Li_{5-2x}Zn_xSiO_4F$ (Phase H+Phase M)	Si /weight %	O /weight %	Zn /weight %	F /weight %
Test 1	20.10	41.05	9.99	28.85
Test 2	17.64	44.55	7.93	29.88
Test 3	17.39	45.22	7.37	30.02
Desired	21.49	48.96	15.01	14.54
x=0.50 $Li_{5-2x}Zn_xSiO_4F$ (Phase H)	Si /weight %	O /weight %	Zn /weight %	F /weight %
Test 1	19.84	40.53	17.32	22.31
Test 2	15.96	43.79	13.94	26.31
Test 3	18.26	40.77	15.25	25.72
Desired	19.54	44.51	22.74	13.21
x=1 $Li_{5-2x}Zn_xSiO_4F$ ($LiF:Li_2ZnSiO_4$=1:1 Phase HH)	Si /weight %	O /weight %	Zn /weight %	F /weight %
Test 1	15.05	39.89	30.08	14.98
Test 2	15.09	45.45	25.76	13.69
Test 3	14.48	40.93	34.31	10.29
Desired	15.92	36.26	18.53	10.77

XRF tests were used as a preliminary determination of the composition of possible new phases (or solid solutions), with results shown in Table 4.6. The F content in Phase L was significantly lower than expected. The F^- content in Phase H samples was approximately double that expected, which may be attributed to the presence of LiF as second phase, Fig 4.35. The XRF results suggest that the true compositions of these possible new phases may vary from the design; however, there is still some F^- in these phases.

Products of all compositions prepared in the ternary system Li_4SiO_4-Zn_2SiO_4-LiF are summarised in Table 4.S1. In conclusion, this attempt to dope Li_5SiO_4F by Zn is not successful as a doping study, but it leads to potential further research on the Li_4SiO_4-Zn_2SiO_4-LiF system. Several possible new phases including Phase L, Phase M, Phase H, Li_3ZnSiO_4F and $a$$Li_2ZnSiO_4$-$b$LiF solid solutions have been observed. Their true composition, synthesis method, detailed crystal structures and electrical properties require further investigation.

4.3. Possible anion doping of Li_4GeO_4 / Li_4TiO_4 by LiF

As γ-Li_5SiO_4F has been found in previous research into F^- doping of Li_4SiO_4 [1], a preliminary attempt at anion doping of Li_4XO_4 (X=Ge^{4+} and Ti^{4+}) by LiF, with a general formula $Li_{4-x}XO_{4-x}F_x$, has been tried.

4.3.1. Li_4GeO_4+LiF

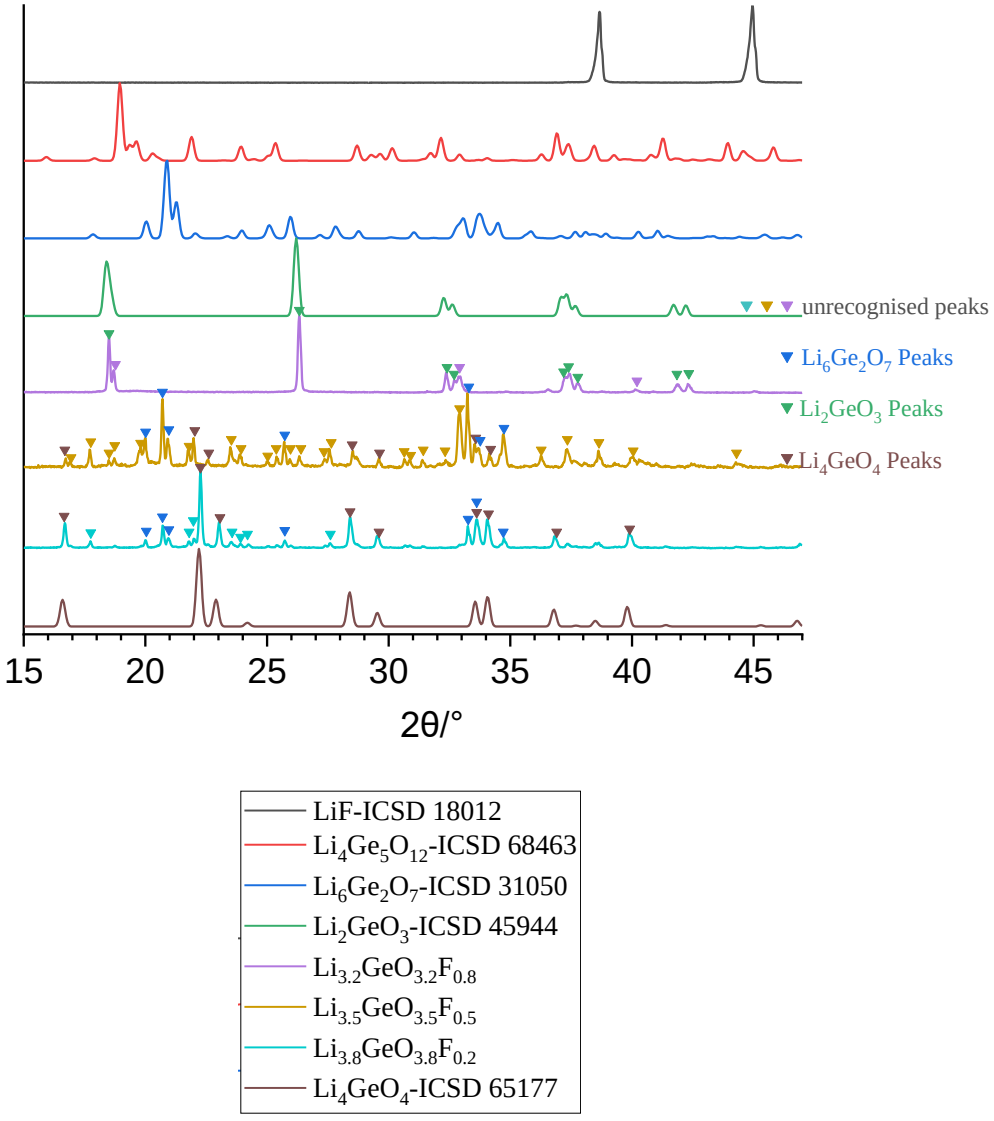

Fig 4.40. Possible F^- doped Li_4GeO_4 samples compared to standard patterns: when x=0.20 and 0.50, there is a mixture of different Ge contained oxides with extra lines; when x=0.8, the main phase is Li_2GeO_3 (in green) with some extra lines (in purple).

Starting materials Li_2CO_3, Ge_2O and LiF were heated at 750°C for 20 h. The XRD results are shown in Fig 4.40. In all samples, there is no evidence of LiF in the final products. Previous synthesis of γ-Li_5SiO_4F at the same temperature did not show any loss of LiF, thus it appears that F^- is somehow doped in Ge-contained compounds. When x=0.2, the product seems to be a mixture of Li_4GeO_4 and $Li_6Ge_2O_7$. As there is no trace of LiF, Li_4GeO_4 in x=0.2 sample may be a F^- containing solid solution with some extra lines marked by light blue triangles. When x=0.5, the unknown diffraction pattern may indicate a mixture of several different Li-Ge-O compounds. When x=0.8, the product shows a diffraction pattern similar to Li_2GeO_3 but several extra peaks are marked with purple triangles.

Although it is only a very preliminary attempt, the results indicate some promising possible further studies. Firstly, there appears to be F^--containing Li_4GeO_4 solid solution, or other F^- contained Li-Ge-O compound, their single phases may exhibit similar crystal structure but varied properties. Secondly, Li_2GeO_3 is a good anode material [19]. $Li_{3.2}GeO_{3.2}F_{0.8}$ shows a possible Li_2GeO_3 solid solution pattern, therefore a good possibility to dope Li_2GeO_3 with LiF.

4.3.2. Li_4TiO_4+LiF

As Li_4TiO_4 can easily react with CO_2 in the atmosphere, the preparation of Li_5TiO_4F was tried in two steps. In step 1, Li_4TiO_4 precursor was synthesised using Li_2CO_3 and TiO_2. Samples were firstly heated in N_2 at 600°C for 6 h for the decomposition of Li_2CO_3, then at 750 °C and 800 °C for 20 h also in N_2. In step 2, Li_4TiO_4 was reacted with LiF at 750 °C for 20 h.

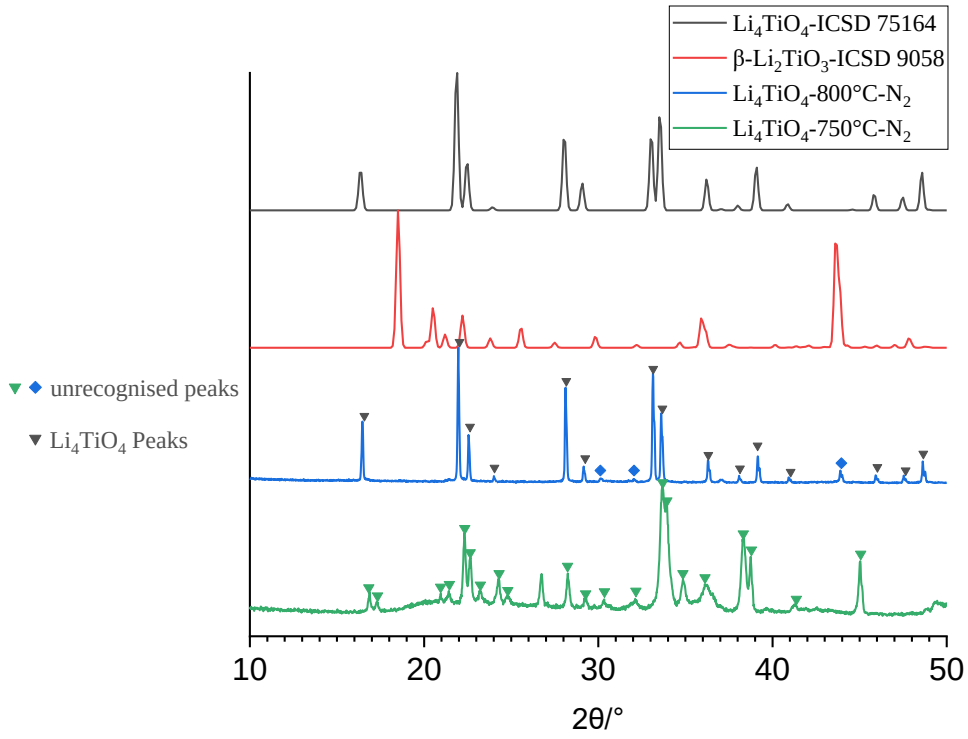

Fig 4.41. XRD results of Li_4TiO_4 prepared in N_2 at different temperatures in step 1 of method 1, compared to standard patterns, showing a possible doped Li_4TiO_4 in 800°C sample.

In step 1, the precursor, Fig 4.41, at 750 °C, is a mixture of some unknown lines and Li_4TiO_4, compared it with product at 800 °C, it seems that the reaction at 750 °C is incomplete with some broad peaks; at 800 °C, there is a main phase of Li_4TiO_4 with varied intensity ratio of the peaks at 34-35°/2θ and several extra lines.

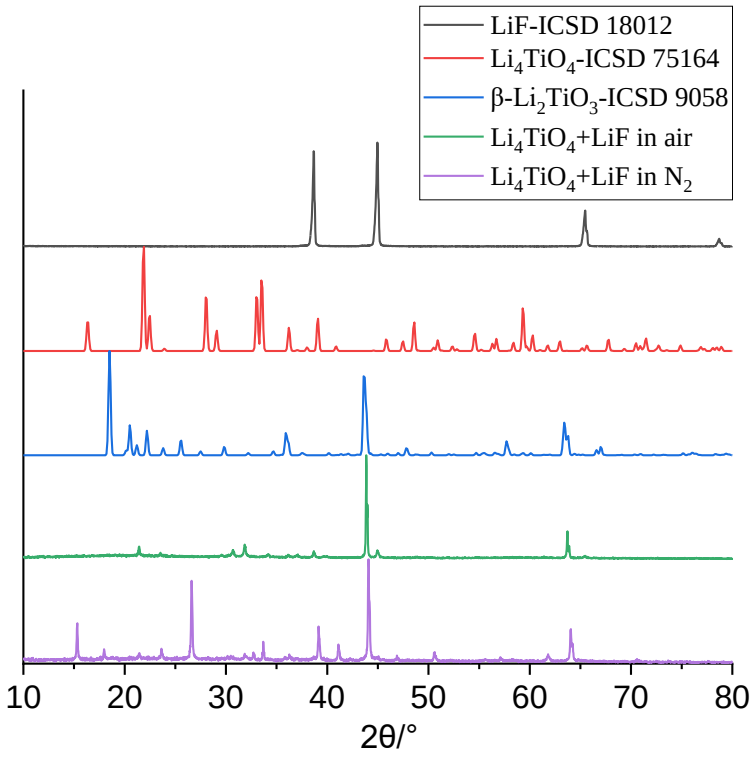

Fig 4.42. XRD results of Li_4TiO_4+LiF prepared in air and N_2 at 750°C for 20 hours, products in step 2 of method 1, compared to standard patterns.

Table 4.7. Index result for Li_4TiO_4+LiF heated in N_2

h	k	l	2θ-obs	2θ-cal	2θ-dif	d-obs	d-cal	d-dif
1	**0**	**0**	15.333	15.339	**-0.006**	5.77392	5.77170	0.00222
1	**1**	**0**	17.993	17.979	**0.014**	4.92598	4.92994	-0.00396
0	**1**	**1**	23.650	23.616	**0.034**	3.75903	3.76426	-0.00523
1	**2**	**-1**	26.633	26.623	**0.010**	3.34432	3.34560	-0.00128
1	**0**	**1**	32.758	32.768	**-0.010**	2.73169	2.73082	0.00087
1	**1**	**-2**	39.190	39.203	**-0.013**	2.29689	2.29613	0.00076
1	**4**	**0**	41.142	41.139	**0.003**	2.19228	2.19244	-0.00016
0	**0**	**2**	44.112	44.126	**-0.014**	2.05132	2.05071	0.00061
0	**4**	**1**	-	44.095	**0.017**	-	2.05210	-0.00078
1	**5**	**0**	50.625	50.633	**-0.008**	1.80165	1.80136	0.00029
1	**6**	**-1**	61.833	61.871	**-0.038**	1.49925	1.49842	0.00083
3	**1**	**1**	64.101	64.104	**-0.003**	1.45157	1.45152	0.00005
Monoclinic: *a*=6.80(1) Å, *b*=9.480(4) Å, *c*=4.830(3) Å, *β*=121.89(8)°, V=264.31 Å^3								

Table 4.8. (a) Index result for Li_4TiO_4+LiF heated in air (b) lattice parameters compared to standard β-Li_2TiO_3

(a)

h	k	l	2θ-obs	2θ-cal	2θ-dif	d-obs	d-cal	d-dif
1	**0**	**0**	21.426	21.417	**0.009**	4.14386	4.14553	-0.00167
1	**0**	**-1**	30.690	30.689	**0.001**	2.91090	2.91095	-0.00005
0	**2**	**0**	31.861	31.847	**0.014**	2.80645	2.80773	-0.00128
1	**2**	**0**	38.686	38.702	**-0.016**	2.32565	2.32471	0.00094
0	**2**	**1**	43.856	43.858	**-0.002**	2.06270	2.06263	0.00007
1	**1**	**1**	44.969	44.968	**0.001**	2.01422	2.01426	-0.00004
2	**1**	**1**	63.716	63.709	**0.007**	1.45942	1.45956	-0.00014
2	**0**	**-2**	63.888	63.909	**-0.021**	1.45590	1.45547	0.00043
Monoclinic: *a*=4.353(3) Å, *b*=5.616(2) Å, *c*=3.192(2) Å, *β*=107.75(4)°, V=74.31 Å^3								

(b)

	Type	***a***	***b***	***c***	***β***
Li_4TiO_4+LiF heated in air	Monoclinic	4.353(3)Å	5.616(2)Å	3.192(2)Å	107.75(4)°
β-Li_2TiO_3 (icsd-9058)	Monoclinic	5.06661(2)Å	8.78583(3)Å	9.74892(2) Å	100.1045(3)°

In step 2, Li_4TiO_4 prepared at 800°C was reacted with LiF, respectively in air and N_2, Fig 4.42. No remaining LiF is found in both samples.

The product in N_2 is a possible new phase, which can be indexed in a monoclinic structure, with lattice parameters: *a*=6.80(1) Å, *b*=9.480(4) Å, *c*=4.830(3) Å and *β*=121.89(8)°, Table 4.7. Another possibility is a mixture of cubic, F^- doped Li_2TiO_3 and another unknown phase.

The product in air appears to show a disordered Li_2TiO_3 pattern, which can be indexed in a smaller monoclinic cell as shown in Table 4.8 (a), which is compared to the ordered β-Li_2TiO_3 in (b). The attempt to index it on a cubic structure, a typical α-Li_2TiO_3 structure, is unsuccessful. β-Li_2TiO_3 commonly has a stable ordered rock salt superstructure. There are several possibilities for its ordered-disordered transition: (a) when forming Li_2TiO_3-MgO solid solution [20]; (b) or during high-energy ball-milling [21]. In this study, the absence of peaks in Li_4TiO_4+LiF sample prepared in air probably indicates a disordered Li_2TiO_3 structure, thus a

possible new method to achieve a disordered rock salt Li_2TiO_3, which deserves some further investigations.

4.4. Conclusion

Attempts to dope γ-Li_5SiO_4F by series of cations have some findings: (a) Al^{3+} and Ga^{3+} can possibly doped in γ-Li_5SiO_4F based on their single phase XRD results and typical single bulk impedance results, but with a decreased ionic conductivity compared to undoped sample; (2) in the doping study by Fe^{3+} and Ge^{4+}, there are trace of other possible γ-type phases; (3) as there is indication of other γ-type phases which has similar composition to γ-Li_5SiO_4F, a more general survey on different ternary phases systems, Li_2O-SiO_2-LiF and Li_3PO_4-Li_4SiO_4-LiF, were discussed in later Chapters 5 and 6, respectively. It seems that trivalent elements may be most promising candidates to dope γ-Li_5SiO_4F, different synthesis method and more insightful study on them deserve further investigation.

The preliminary study on the possible anion doping on Li_4GeO_4 and Li_4TiO_4 found good possibility to dope Li_4GeO_4, Li_2GeO_3 and disordered Li_2TiO_3 by LiF, their single phase, crystal structure and electrical properties deserve further investigations.

References

[1] B. Dong, J. Yan, B. Walkley, K. K. Inglis, F. Blanc, S. Hull, and A. R. West, "Synthesis and characterisation of the new oxyfluoride Li^+ Ion Conductor, Li_5SiO_4F," *Solid State Ionics*, vol. 327, pp. 64–70, 2018.

[2] L. Zhao, X. Long, X. Chen, C. Xiao, Y. Gong, Q. Guan, J. Li, L. Xie, X. Chen, and S. Peng, "Design, synthesis and characterization of the advanced tritium breeder: $Li_{4+x}Si_{1-x}O_4$ Ceramics," *Journal of Nuclear Materials*, vol. 467, pp. 911–916, 2015.

[3] A. Rodger, J. Kuwano , and A. R. West, "Li+ ion conducting γ solid solutions in the systems Li_4XO_4-Li_3YO_4: X=Si, Ge, Ti; Y=P, As, V; Li_4XO_4-$LiZO_2$: Z=Al, Ga, Cr and Li_4GeO_4-Li_2CaGeO_4," *Solid State Ionics*, vol. 15, no. 3, pp. 185–198, 1985.

[4] P. Quintana and A. R. WEST, "Lithium ion conducting solid solutions in the system Li_2O-Ga_2O_3-SiO_2," *Solid State Ionics*, vol. 34, no. 3, pp. 149–155, 1989.

[5] S. B. R. S. Adnan and N. S. Mohamed, "Effects of SN substitution on the properties of Li_4SiO_4 ceramic electrolyte," *Solid State Ionics*, vol. 262, pp. 559–562, 2014.

[6] B. L. Dubey and A. R. West, "Crystal Chemistry of Li_4XO_4 phases: X = Si, Ge, Ti," *Journal of Inorganic and Nuclear Chemistry*, vol. 35, no. 11, pp. 3713–3717, 1973.

[7] Y. Gong, L. Liu, J. Qi, M. Yang, J. Li, H. Wang, H. Guo, G. Zhang, and T. Lu, "A comprehensive study on $Li_4Si_{1-x}Ti_xO_4$ ceramics for advanced tritium breeders," *Journal of Advanced Ceramics*, vol. 9, no. 5, pp. 629–640, 2020.

[8] A. Khorassani, G. Izquierdo, and A. R. West, "The solid electrolyte system, Li_3PO_4-Li_4SiO_4," *Materials Research Bulletin*, vol. 16, no. 12, pp. 1561–1567, 1981.

[9] J. Bates, "Electrical properties of amorphous lithium electrolyte thin films," *Solid State Ionics*, vol. 53-56, pp. 647–654, 1992.

[10] A. Morscher et al., "$Li_6SiO_4Cl_2$: A hexagonal argyrodite based on anti-perovskite layer stacking," *Chemistry of Materials*, vol. 33, no. 6, pp. 2206–2217, 2021.

[11] R. D. Shannon, "Revised effective Ionic radii and systematic studies of interatomic distances in halides and chalcogenides," *Acta Crystallographica Section A*, vol. 32, no. 5, pp. 751–767, 1976.

[12] R. I. Smith and A. R. West, "Crystal structure of the lithium ion conductor, $Li_{3.4}Ga_{0.2}SiO_4$," *Journal of Solid State Chemistry*, vol. 88, no. 2, pp. 564–570, 1990.

[13] R. Grant, I. M. Hodge, M. D. Ingram, and A.R. West, "Migration losses in single-crystal ionic conductors: Sodium beta alumina and," *Journal of the American Ceramic Society*, vol. 60, no. 5-6, pp. 226–229, 1977.

[14] S. Moghe, A. D. Acharya, R. Panda, S. B. Shrivastava, M. Gangrade, and V. Ganesan, "Electrical properties of Fe doped Nio thin films," *AIP Conference Proceedings*, 2012.

[15] A. F. Holleman, E. Wiberg, and N. Wiberg, "Cobalt," *Lehrbuch der Anorganischen Chemie (in German) (102nd ed.)*, pp. 1146–1152, 2007.

[16] A.R. West Lithium battery in 'Solid State Chemistry and Its Applications, 2th edition'. John Wiley & Sons. West Sussex, pp.425-427.

[17] D. Becker, R. Haberkorn, and G. Kickelbick, "Mechanochemical induced structure transformations in lithium titanates: A detailed PXRD and 6LI MAS NMR study," *Inorganics*, vol. 6, no. 4, p. 117, 2018.

[18] M. Hodge, M. D. Ingram, and A.R. West, "Ionic conductivity of Li_4SiO_4, Li_4GeO_4, and their solid solutions," *Journal of the American Ceramic Society*, vol. 59, no. 7-8, pp. 360–366, 1976.

[19] M. M. Rahman, I. Sultana, T. Yang, Z. Chen, N. Sharma, A. M. Glushenkov, and Y. Chen, "Lithium germanate (Li_2GeO_3): A high-performance anode material for lithium-ion batteries," *Angewandte Chemie International Edition*, vol. 55, no. 52, pp. 16059–16063, 2016.

[20] M. Castellanos and A. R. West, "Order-disorder phenomena in oxides with rock salt structures: The system Li_2TiO_3-MgO," *Journal of Materials Science*, vol. 14, no. 2, pp. 450–454, 1979.

[21] H. Brandstätter, D. Wohlmuth, P. Bottke, V. Pregartner, and M. Wilkening, "Li+ ion dynamics in nanocrystalline and structurally disordered Li2TiO3," *Zeitschrift für Physikalische Chemie*, vol. 229, no. 9, pp. 1363–1374, 2015.

Appendix

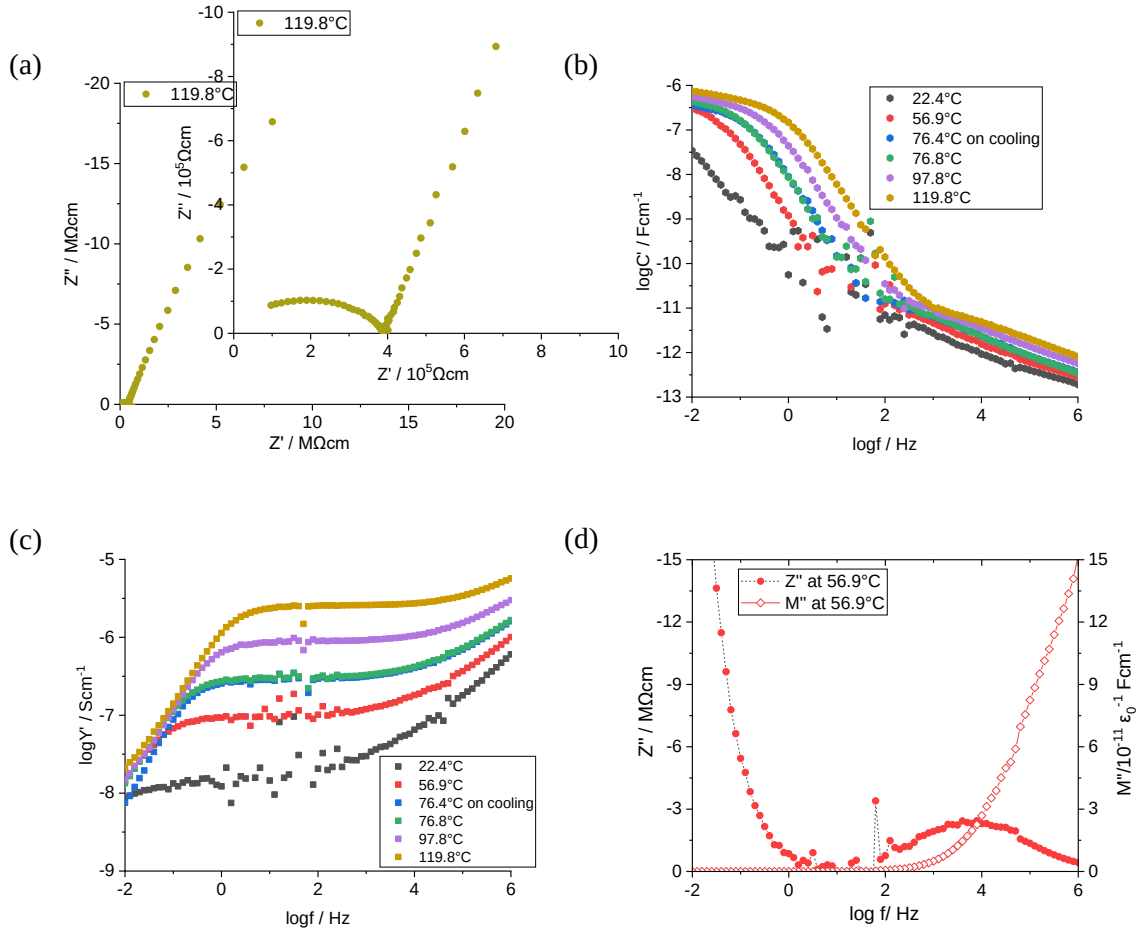

Fig 4.S1. Some impedance datasets for $Li_{5.10}Al_{0.10}Si_{0.90}O_4F$ prepared by reaction 2A

(a) Z''-Z' complex plane plot at 119.8°C,

Spectroscopic plots of (b) C', (c) Y', and (d) Z''/M'' at 56.9°C

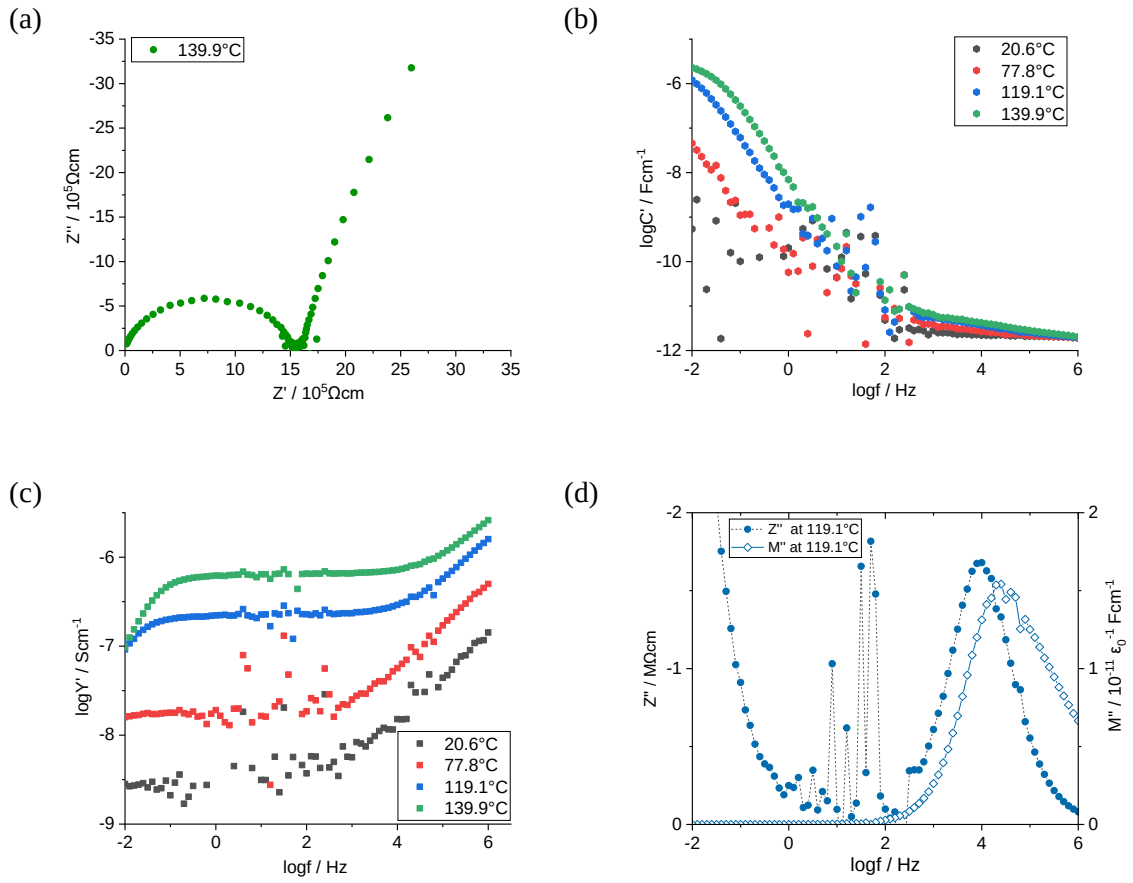

Fig 4.S2. Some impedance datasets for $Li_{5.20}Al_{0.20}Si_{0.80}O_4F$ prepared by reaction 2A

(a) Z''-Z' complex plane plot at 139.9°C,

Spectroscopic plots of (b) C', (c) Y', and (d) Z''/M'' at 119.1°C

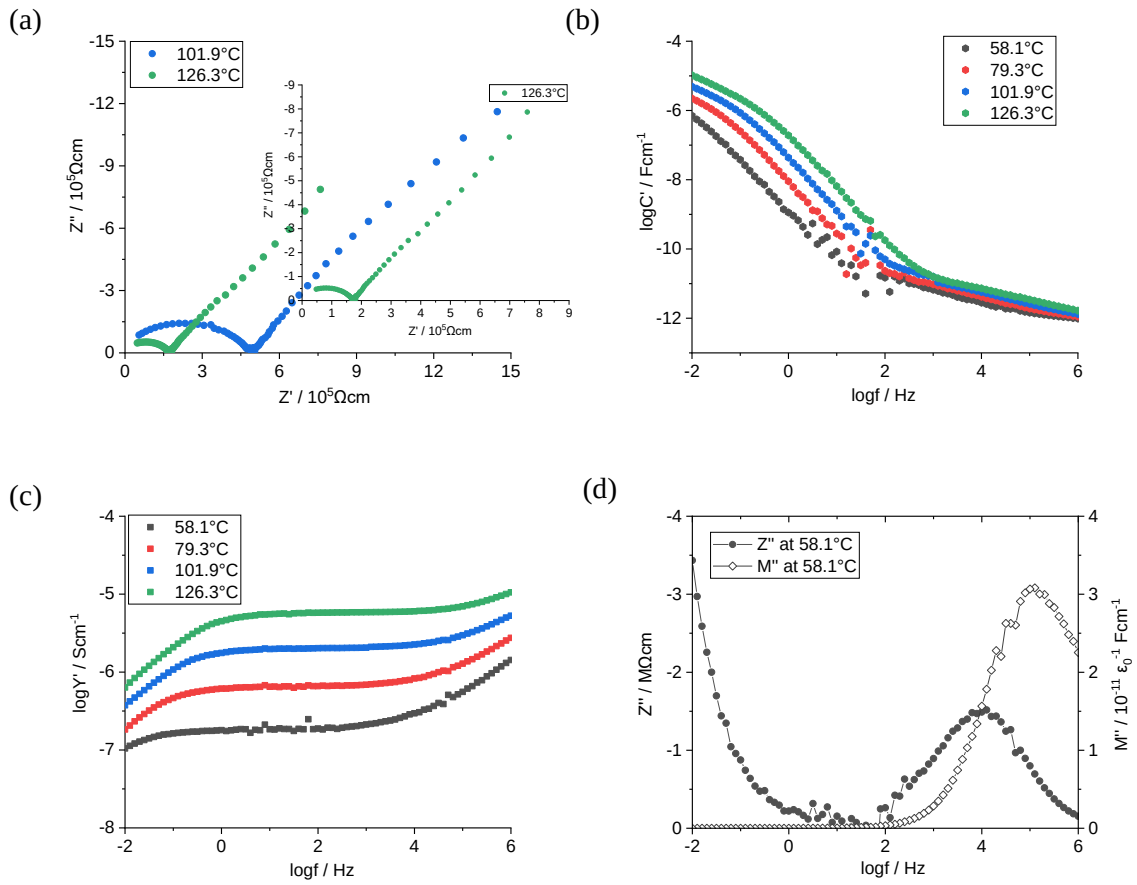

Fig 4.S3. The impedance dataset for $Li_{5.10}Ga_{0.10}Si_{0.90}O_4F$, pellet sintered at 750°C, 10 hours, (a) impedance complex plane plot, spectroscopic plots of (b) capacitance C', (c) admittance Y', and (d) $Z^{''}$-$M^{''}$ at 58.1°C

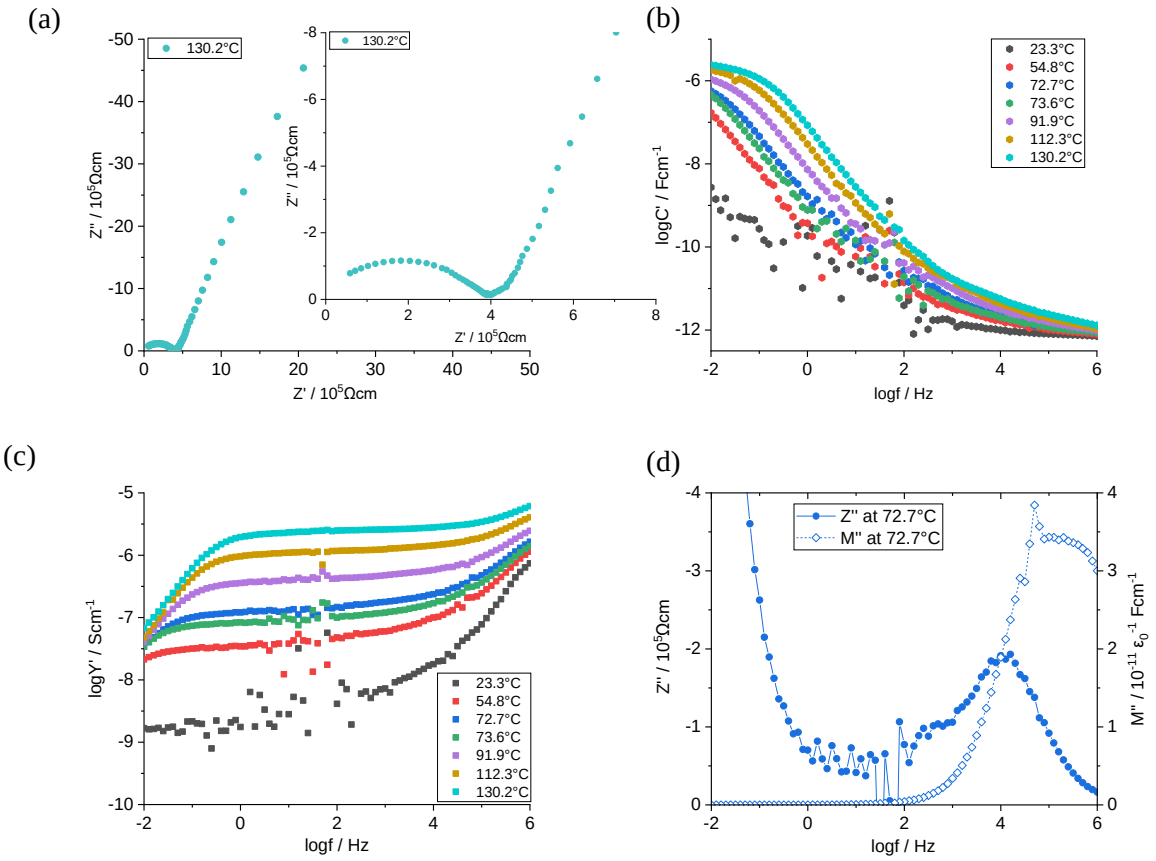

Fig 4.S4. The impedance dataset for $Li_5Si_{0.95}Ge_{0.05}O_4F$, prepared by method 2, pellet sintered at 750°C, 10 hours, (a) impedance complex plane plot, spectroscopic plots of (b) capacitance C', (c) admittance Y', and (d) Z''-M'' at 72.7°C.

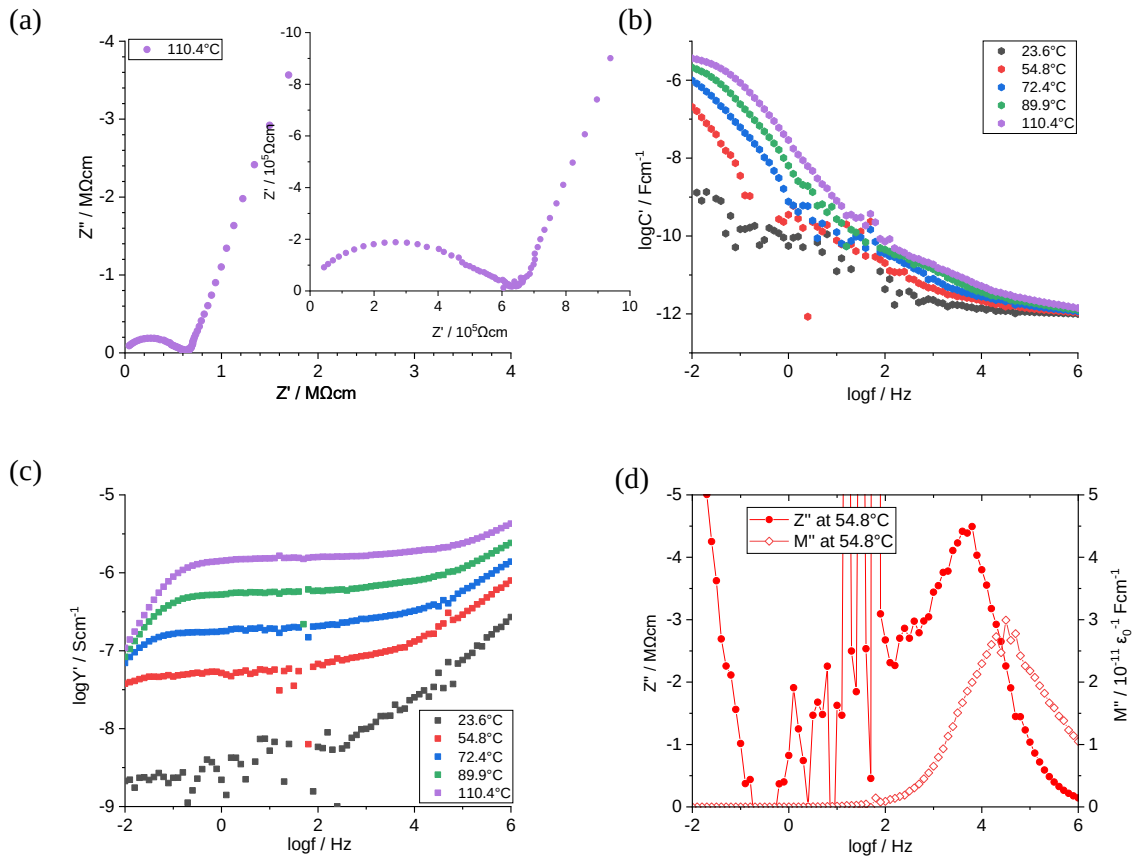

Fig 4.S5. The impedance dataset for $Li_5Si_{0.90}Ge_{0.10}O_4F$, prepared by method 2, pellet sintered at 750°C, 10 hours, (a) impedance complex plane plot, spectroscopic plots of (b) capacitance C', (c) admittance Y', and (d) Z''-M'' at 54.8°C.

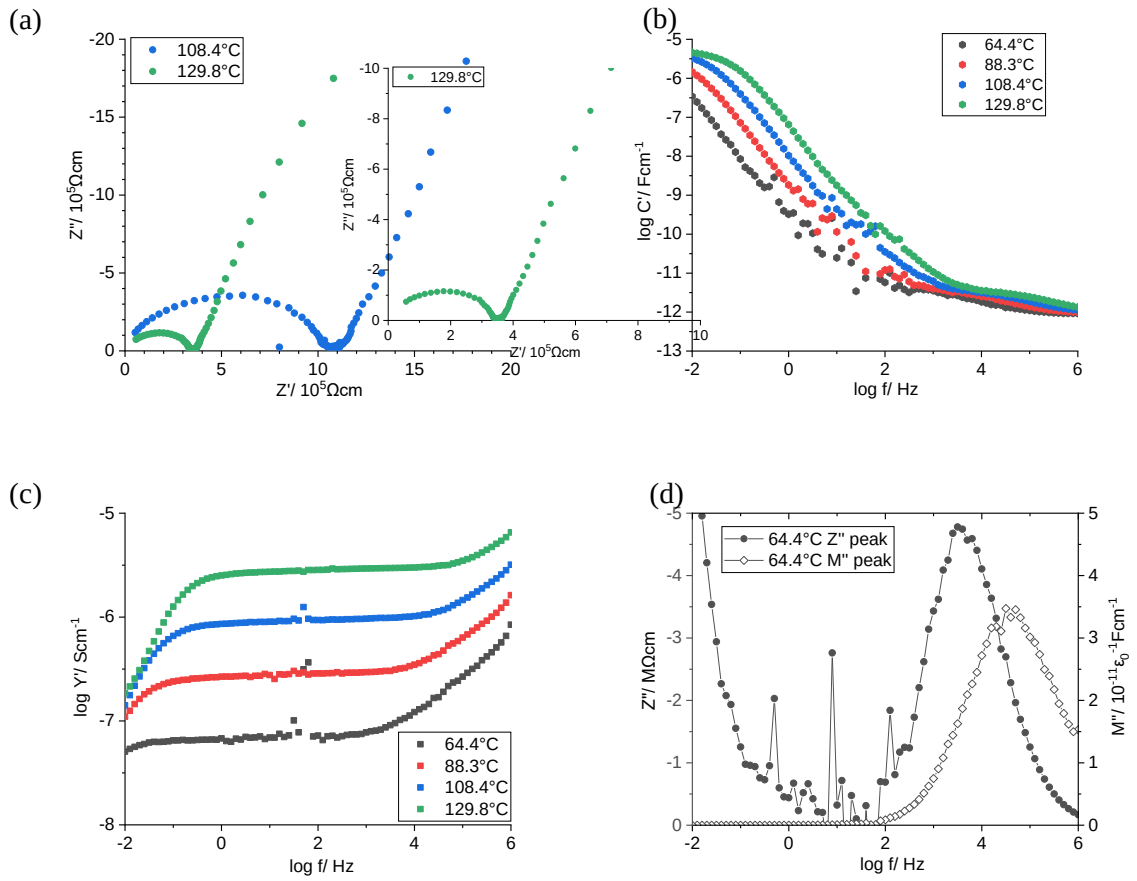

Fig 4.S6. Some impedance datasets for $Li_{5-2x}Zn_xSiO_4F$, x=0.1, heated at 775°C

(a) Z''-Z' complex plane plot at 108.4°C and 129.8°C,

Spectroscopic plots of (b) C', (c) Y', and (d) Z''/M'' at 64.4°C

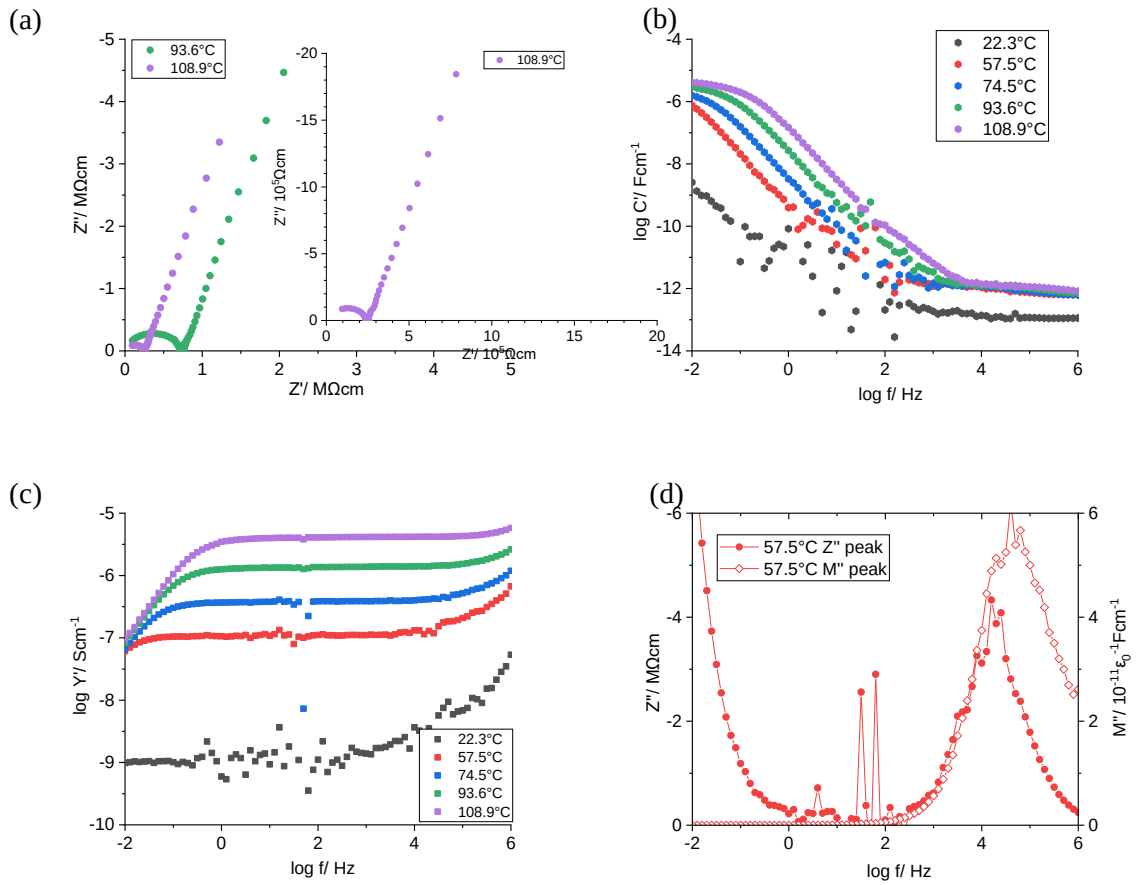

Fig 4.S7. Some impedance datasets for $Li_{5-2x}Zn_xSiO_4F$, x=0.25, heated at 775°C

(a) Z''-Z' complex plane plot at 93.6°C and 108.9°C,

Spectroscopic plots of (b) C', (c) Y', and (d) Z''/M'' at 57.5°C

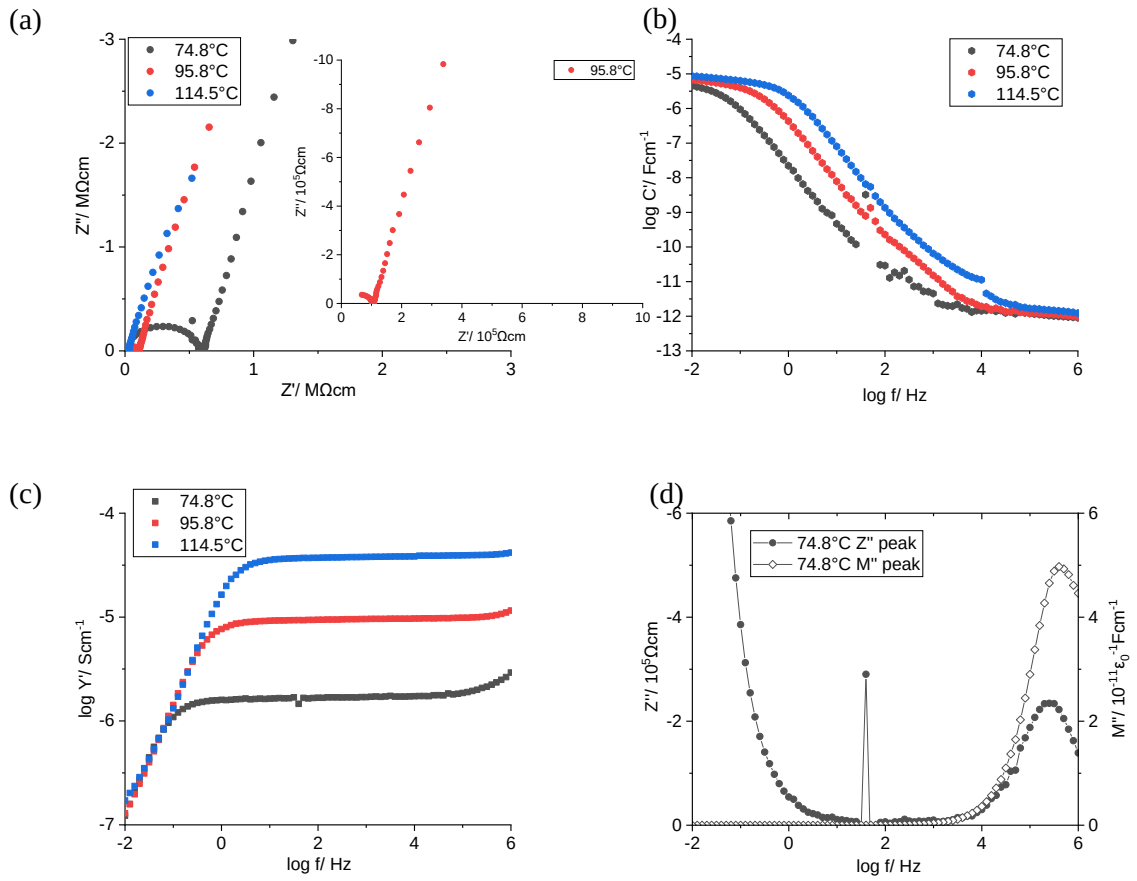

Fig 4.S8. Some impedance datasets for $Li_{5-2x}Zn_xSiO_4F$, x=0.50, heated at 775°C

(a) Z''-Z' complex plane plot at 74.8°C, 95.8°C and 114.5°C,

Spectroscopic plots of (b) C', (c) Y', and (d) Z''/M'' at 74.8°C

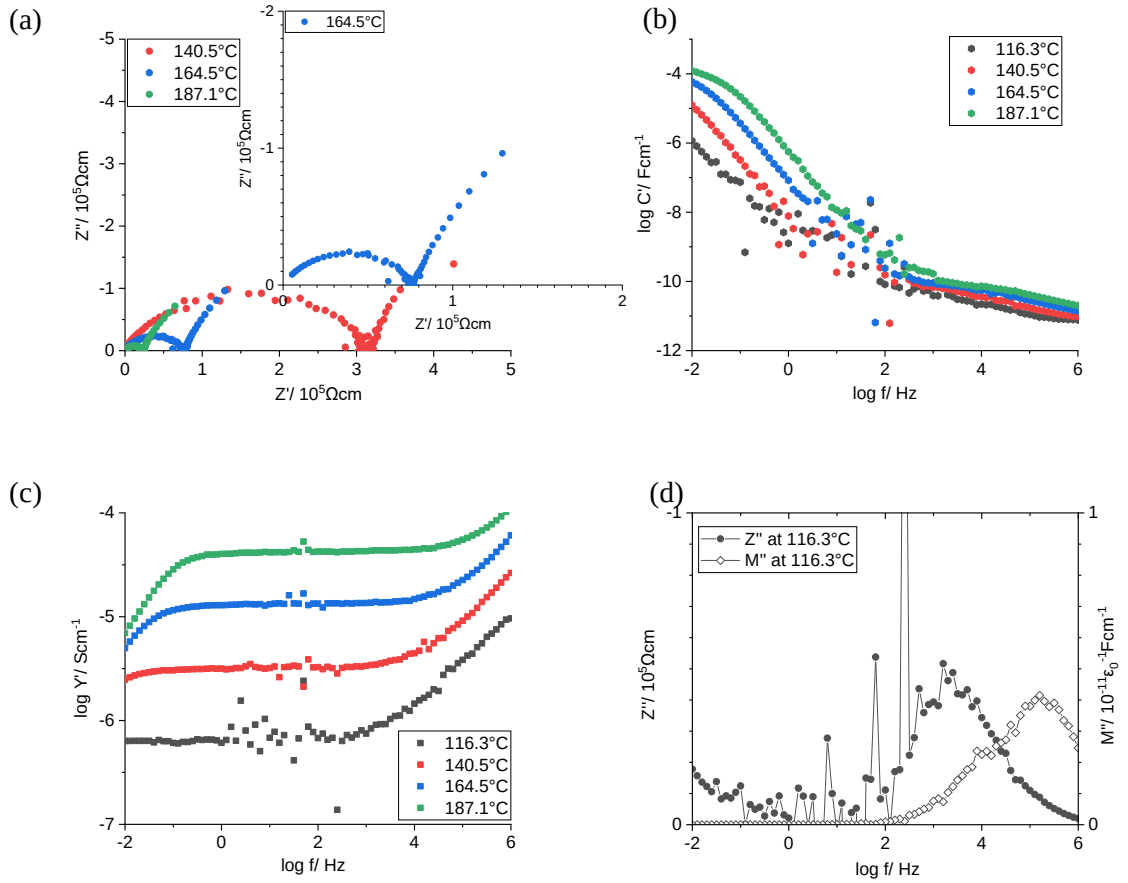

Fig 4.S9. Some impedance datasets for $Li_{5-2x}Zn_xSiO_4F$, x=1.00, heated at 775°C

(a) Z''-Z' complex plane plot at 140.5°C, 164.5°C and 187.1°C,

Spectroscopic plots of (b) C', (c) Y', and (d) Z''/M'' at 116.3°C

Table 4.S1. Products of all compositions prepared in $Li_{5-2x}Zn_xSiO_4F$ system and aLi_2ZnSiO_4-$bLiF$ system.

Desired composition	Synthesis temperature	Synthesis time	products
$Li_{5-2x}Zn_xSiO_4F$ system			
x=0: Li_5SiO_4F	770°C	30 hours	γ- Li_5SiO_4F
x=0.02: $Li_{4.96}Zn_{0.02}SiO_4F$	770°C	30 hours	(d) γ- Li_5SiO_4F, and (i) Phase L
x=0.04: $Li_{4.92}Zn_{0.04}SiO_4F$	770°C	30 hours	(d) γ- Li_5SiO_4F, and (i) Phase L
x=0.10: $Li_{4.8}Zn_{0.1}SiO_4F$	770°C	30 hours	Phase L
		60 hours	Phase L
x=0.20: $Li_{4.6}Zn_{0.2}SiO_4F$	770°C	30 hours	(d) Phase L, Phase M and LiF
		60 hours	(d) Phase L, Phase M and LiF
x=0.25: $Li_{4.5}Zn_{0.25}SiO_4F$	770°C	30 hours	Phase M and LiF
x=0.30: $Li_{4.4}Zn_{0.3}SiO_4F$	770°C	30 hours	(d) Phase M, Phase H and LiF
x=0.40: $Li_{4.2}Zn_{0.4}SiO_4F$	770°C	30 hours	(d) Phase M, (i) Phase H and LiF
x=0.50: $Li_4Zn_{0.5}SiO_4F$	770°C	30 hours	Phase H and LiF
		60 hours	Phase H and LiF
x=0.60: $Li_4Zn_{0.5}SiO_4F$	770°C	30 hours	Phase H, LiF and extra peaks
x=0.80: $Li_4Zn_{0.5}SiO_4F$	770°C	30 hours	Phase H, LiF and extra peaks
x=1.00: Li_3ZnSiO_4F	770°C	30 hours	Phase HH and LiF
aLi_2ZnSiO_4: $bLiF$			
a:b=1:0 Li_2ZnSiO_4	770°C	30 hours	Li_2ZnSiO_4 solid solution
a:b=4:1	770°C	30 hours	'Doped Li_2ZnSiO_4 ss'
a:b=7:3	770°C	30 hours	'Doped Li_2ZnSiO_4 ss'
a:b=3:2	770°C	30 hours	'Doped Li_2ZnSiO_4 ss'
a:b=1:1: Li_3ZnSiO_4F	770°C	30 hours	'Doped Li_2ZnSiO_4 ss' and LiF

(d): possibly decreased composition (i): possibly increased composition

Chapter 5. Synthesis of new oxyfluoride phases in the ternary system Li_2O-SiO_2-LiF

Summary

Four new phases have been synthesised and characterised in the ternary system: Li_2O-SiO_2-LiF.

Phase B was prepared at the stoichiometry Li_2O:SiO_2:LiF=47:28:25 by solid state reaction at ~750 °C. It shows a ZnO-type hexagonal subcell, and has a modest ionic conductivity of ~5.6×10^{-8} Scm^{-1} at 100 °C.

γ-Phase B appears to be a more ordered polymorph related to Phase B, that forms over a wide solid solution range. The crystal structure of γ-Phase B appears to have an orthorhombic subcell derived from that of hexagonal ZnO type cell. Its structure probably involves an ordered arrangement of the cations. Its ionic conductivity is ~1.1×10^{-6} Scm^{-1} at 100 °C.

Phase T and Phase N have similar composition to previously reported Li_5SiO_4F but significantly different crystal structures and electrical properties. Phase T forms a solid solution within a narrow area in the Li_2O-SiO_2-LiF system but shows a poor ionic conductivity, similar to that of Li_4SiO_4. As yet, no composition giving single phase N has been found.

5.1 Introduction

As promising parent materials for solid state electrolytes, Li_4SiO_4 and related LISICON materials have become one of the important electrolyte families [1]. Although cation doping of silicate materials like Li_4SiO_4 has been widely reported [1-3], aliovalent anion doping of Li_4SiO_4 has been little studied. It is theoretically feasible to replace some of the O^{2-} ions in SiO_4 tetrahedra because of the similar sizes of the O^{2-}, N^{3-} and F^- ions [4]. Previous attempts by Dong to dope Li_4SiO_4 with F^- were unsuccessful as a doping study but were successful in the synthesis of a new Li^+ ion conducting phase, Li_5SiO_4F [5]. Chapter 3 discusses the attempts to dope Li_5SiO_4F by a series of cations. 3 sets of results were obtained. Some candidates were successfully doped into Li_5SiO_4F by forming a solid solution. Other dopants showed phase mixtures in the products with no

evidence of successful doping of Li_5SiO_4F. A third category of results indicated the existence of new phases, some of which appeared to be related to Li_5SiO_4F, which raised our interest to make a more detailed study of them. Preliminary studies in the systems Li_4SiO_4-LiF and Li_2O-P_2O_5-LiF indicated the possible existence of several previously unreported new phases. This Chapter 5 presents the synthesis and characterisation of some new oxyfluorides in the ternary system of Li_2O-SiO_2-LiF.

The composition triangle Li_2O-SiO_2-LiF, with known phases is shown in Fig 5.1. Two binary joins reported in [5] are shown dashed. The edge Li_2O-SiO_2 shown in Fig 5.1, has been well investigated for many years. There are four different thermodynamically stable stoichiometric lithium silicates, Li_8SiO_6, Li_4SiO_4, Li_2SiO_3 and $Li_2Si_2O_5$ together with one metastable phase, $Li_2Si_3O_7$ [6].

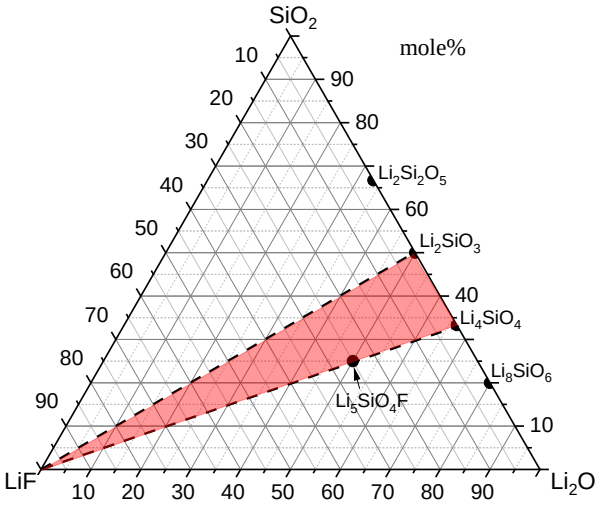

Fig 5.1. Known phases in the ternary system Li_2O-SiO_2-LiF with two compatibility lines reported in [5] (shown dashed): Li_2SiO_3-LiF and Li_4SiO_4-LiF; (b) The main region investigated in this study is shown in red

Li_8SiO_6 can be prepared via solid state reaction of Li_2O and SiO_2, and doped by Co [7], but its electrical properties were not investigated. Li_8SiO_6 is reported to have a better capability to absorb CO_2 compared to other silicates like Li_4SiO_4, and has potential application as a material for absorbing CO_2, and therefore reducing CO_2 emissions [8].

Li_4SiO_4 is a promising candidate for wide applications as the parent material for solid electrolytes [9], CO_2 capture material [10] and tritium breeding material [11]. Li_4SiO_4 can be

prepared by solid state reaction of Li_2O and SiO_2 at ~850°C [12]. The characterisation and electrical properties of Li_4SiO_4 have been well studied. Li_4SiO_4 has two polymorphs: α-Li_4SiO_4 with a monoclinic structure, and γ-Li_4SiO_4 with a triclinic structure [13]. For possible lithium battery applications, Li_4SiO_4 is compatible with a wide range of electrodes including lithium metal and graphite [14].

The ionic conductivity of stoichiometric Li_4SiO_4 is modest, ~10^{-7} Scm^{-1} at 300 °C. Li_4SiO_4 can be doped with the tetravalent cations, Ge^{4+} and Ti^{4+}, to form series of isovalent solid solutions with Li_4GeO_4 and Li_4TiO_4. $Li_4Ti_{0.4}Si_{0.6}O_4$ has an ionic conductivity of 5×10^{-4} Scm^{-1} at ~300 °C [14]. Sn can also be doped into Li_4SiO_4 and has an ionic conductivity of ~3.07×10^{-5} Scm^{-1} at room temperature [15]. Li_4SiO_4 can be doped with several aliovalent cations leading to much higher conductivity. These aliovalent dopants can create either Li^+ vacancies or interstitial Li^+ ions, such as $Li_{4-x}Si_{1-x}V_xO_4$ and $Li_{4+x}Si_{1-x}Al_xO_4$, respectively. $Li_{3.4}Si_{0.4}V_{0.6}O_4$ has an ionic conductivity of ~10^{-5} Scm^{-1} at ~20 °C. [16] $Li_{4.2}Si_{0.8}Al_{0.2}O_4$ has an ionic conductivity of 1.6×10^{-3} Scm^{-1} at ~300 °C [17].

Li_2SiO_3 is a possible candidate as an electrolyte due to its low cost synthesis and stability, but it has a lower conductivity, ~2×10^{-8} Scm^{-1}, at ambient temperature than that of Li_4SiO_4 [18]. Although there are wide possibilities for an improved conductivity for Li_2SiO_3, so far, no success has been reported. Li_2SiO_3 can be used as a coating material in Li-Mn-Co-Ni-O cathodes for better rate capacity and cycling performance [19] and as surface modification on graphite anodes to relieve the swelling of the graphite during cycles [20]. Porous particles of Li_2SiO_3 prepared by the facile one-step hydrothermal route using $LiOH\cdot H_2O$ and TEOS (tetraethyl orthosilicate) are a promising adsorbent to capture CO_2 and heavy metals over a wide temperature range [21].

$Li_2Si_2O_5$ was the first glass-ceramic material to be made in the 1950s [22]. The microstructure of Li_2SiO_5 glass-ceramics can be optimised by attention to the nucleation and crystallisation processes [23], leading to a wide range of microstructures for different specialised applications. The most common applications of $Li_2Si_2O_5$ glass ceramics are for hard disk substrates and sealing materials for SOFCs [24].

In the other two limiting binary edges of the ternary system Li_2O-SiO_2-LiF, there are no reports of any compound or solid solution. In the ternary system Li_2O-SiO_2-LiF, one new ternary phase Li_5SiO_4F has been reported as shown in Fig 5.1a. This phase, Li_5SiO_4F, formed on the join Li_4SiO_4-LiF. Li_5SiO_4F has two polymorphs α and γ prepared below and above ~750 °C. XRD data were reported but their crystal structures were not known. Above 800 °C, Li_5SiO_4F showed partial melting which is believed to be incongruent. The ionic conductivity of γ-Li_5SiO_4F is ~1.2×10^{-7} S/cm at 25 °C, which is ~3 orders of magnitude higher than that of Li_4SiO_4, as shown in Fig 5.2 [5]. The conductivity of α-Li_5SiO_4F is also shown in Fig 5.2, its conductivity is lower than that of Li_4SiO_4 and especially, that of γ-Li_5SiO_4F.

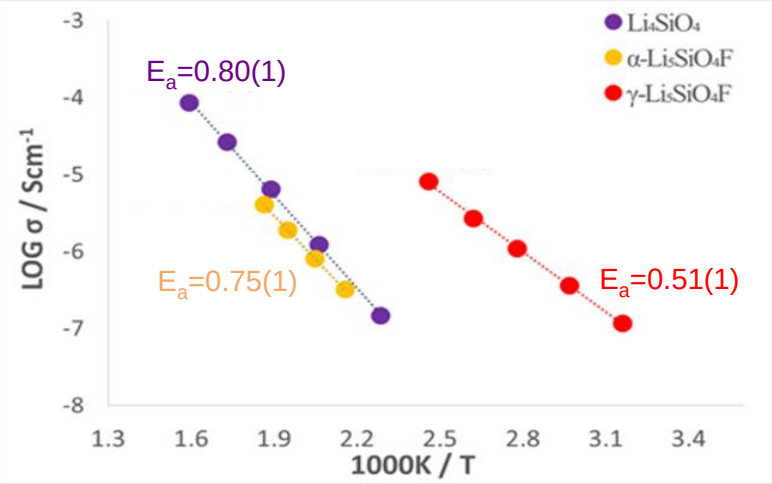

Fig 5.2. Arrhenius plots for Li_4SiO_4 and Li_5SiO_4F, reproduced from Dong, et al[5].

Results from Dong's study [5] showed that the join Li_2SiO_3-LiF is compatible at 700-800 °C, as shown in Fig 5.1, since compositions reacted on this join showed a mixture of Li_2SiO_3 and LiF.

The region of the ternary Li_2O-SiO_2-LiF system bounded by Li_2SiO_3, SiO_2 and LiF was briefly investigated from the results of heating samples in air at 700-800 °C. Results indicated that the products could not be rationalised in terms of the phase diagram. For example, attempts to react '$LiSiO_2F$' gave a mixture of Li_2SiO_3, SiO_2, LiF at 700 °C; a mixture of four phases: Li_2SiO_3, SiO_2, LiF and $Li_2Si_2O_5$ were obtained at 800 °C [5]. In both cases, the presence of Li_2SiO_3 and $Li_2Si_2O_5$ in reaction mixtures on the join LiF-SiO_2 indicated a possible loss of F during reaction;

alternatively, consideration of the quaternary phase diagram Li-Si-O-F is needed to explain the results. No further studies in this region of the phase diagram have been made.

Common silicate structures are built of SiO_4 tetrahedra. With more condensed silicate units, there are between 2 and 4 bridging oxygens per Si, each of which connects two SiO_4 tetrahedra. The structure of the silicate units can be simply deduced by the Si:O ratio. When the Si:O ratio is 1:4, all silicate anions are isolated SiO_4 tetrahedra; when the Si:O ratio is 1:3.5, adjacent SiO_4 tetrahedra share a common corner by a bridging oxygen to form dimers $Si_2O_7^{6-}$; when the Si:O ratio is 1:3, more tetrahedra are connecting to each other to form either rings or chains; further condensed silicate units are also able to form sheets and 3D structures [25]. Previously reported Li_5SiO_4F [5] is located on the Li_4SiO_4-LiF join and possibly has isolated SiO_4 tetrahedra. So far, the location of F^- anion has not been reported. Although no compound build of $Si_2O_7^{6-}$ dimers has been reported in the ternary system Li_2O-SiO_2-LiF, it is, for instance, in principle, still possible to have both $Si_2O_7^{6-}$and F^- anions in a complex structure.

In this Chapter, compositions around Li_5SiO_4F, especially those located in the triangle bounded by Li_2SiO_3, Li_4SiO_4 and LiF, shown in Fig 5.1, were prepared as a continuation of studies in the system Li_2O-SiO_2-LiF [5]. Results presented here show the existence of four new phases which have been labelled as Phase B, γ-Phase B, Phase N, and Phase T. Their synthesis, stability, XRD characterisation and electrical properties are reported.

5.2. Results and discussion

5.2.1. Synthesis and characterisation of four new phases in the system Li_2O-SiO_2-LiF

In the ternary system Li_2O-SiO_2-LiF, 51 compositions in the triangle bounded by Li_2SiO_3, Li_4SiO_4 and LiF have been prepared and reacted at different temperatures. It was found that, heating to at least 750°C is required to achieve complete reaction, but the nature of the products varied somewhat on heating at either 750 °C or 775-800 °C. At 750 °C, one new phase labelled as Phase B was identified, and the results on this are presented first.

5.2.1.1. Phase B

5.2.1.1.1. Synthesis

(a)

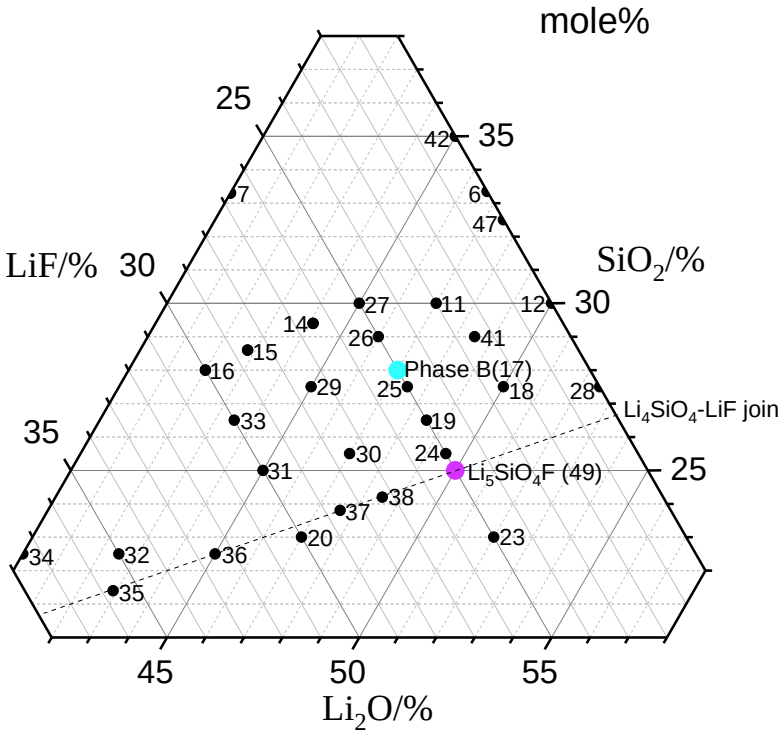

(b)

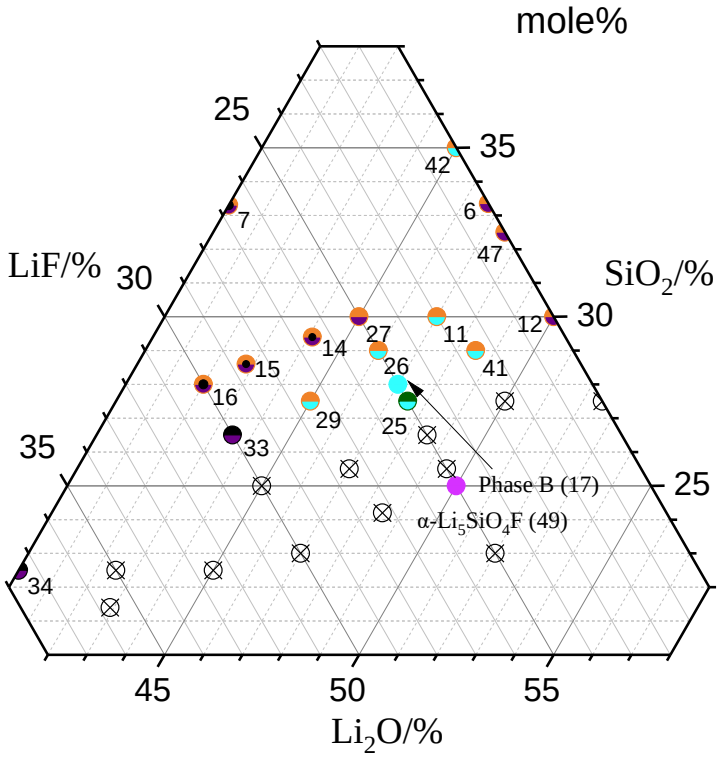

* (γ)-Phase B refers to a phase(s) related to γ-Phase B, which is a more ordered phase that is not clearly defined at 750°C. γ-Phase B is discussed in section 5.2.1.2.

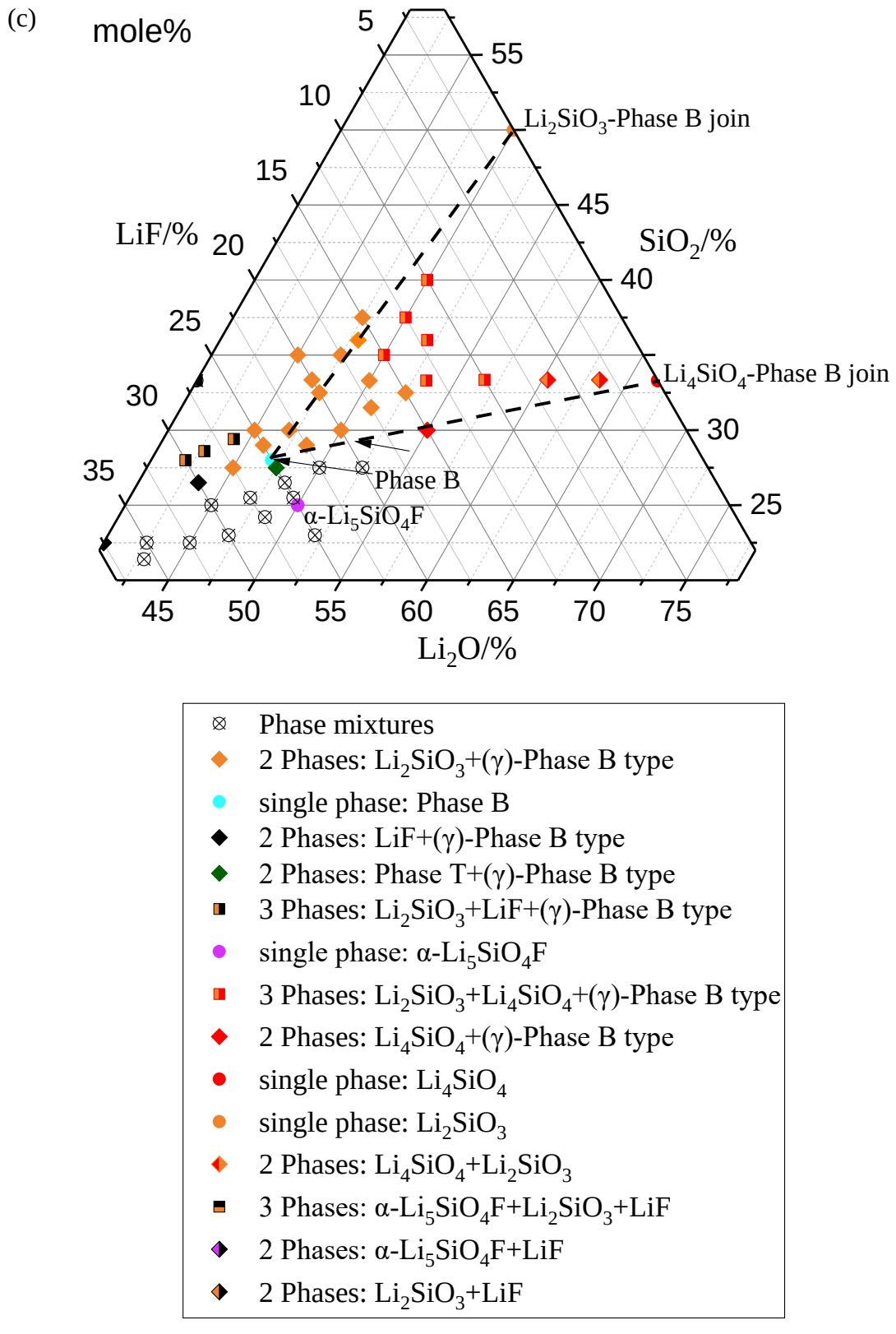

Fig 5.3. (a) Compositions studied in the ternary system Li_2O-SiO_2-LiF; (b) phase(s) present at 750 °C; (c) Phase(s) present summary at 750 °C with possible compatibility lines.

Figure 5.3 (a) and Table 5.S1 show the compositions studied and results obtained after reaction at 750°C for typically 10-20 h. Phase B forms as a single phase at only the composition Li_2O:SiO_2:LiF=47:28:25 (composition 17). There was no evidence for Phase B forming a solid solution. As discussed later, we believe that Phase B is metastable, therefore the results shown in Fig 5.3 do not represent the thermodynamic equilibrium. In some compositions, a phase (or phases) related to Phase B were sometimes present in phase mixtures. As this study is a general survey for possible new phase(s) with no known XRD pattern in different ternary phases systems, a pattern may appear to be single phase if there are no known second phases present while some of the new phases appear to be solid solutions as they contain the same sets of lines but with small systematic line shifts.

The results become clearer after reactions at 775°C-800 °C, discussed later. Using the results shown in Table 5.S1 and Fig 5.3, phase compatibility triangles were identified in which Phase B is one of the phases presents. These compatibility triangles are shown in Fig 5.3 (c). The following 2-phase joins are present: Phase B+LiF; Phase B +Li_2SiO_3; and Phase B+Li_4SiO_4. These joins enclose two 3-phase compatibility triangles: LiF+Li_2SiO_3+Phase B; and Li_2SiO_3+Li_4SiO_4+ Phase B. XRD patterns of some representative compositions in each possible compatibility region, either 2 phases or 3 phases, are shown in Fig 5.S1. The compositions between Phase B and Li_5SiO_4F show more complex behaviour, as discussed in results of heating at higher temperature.

5.2.1.1.2. Indexed subcell of Phase B, compared to hexagonal ZnO

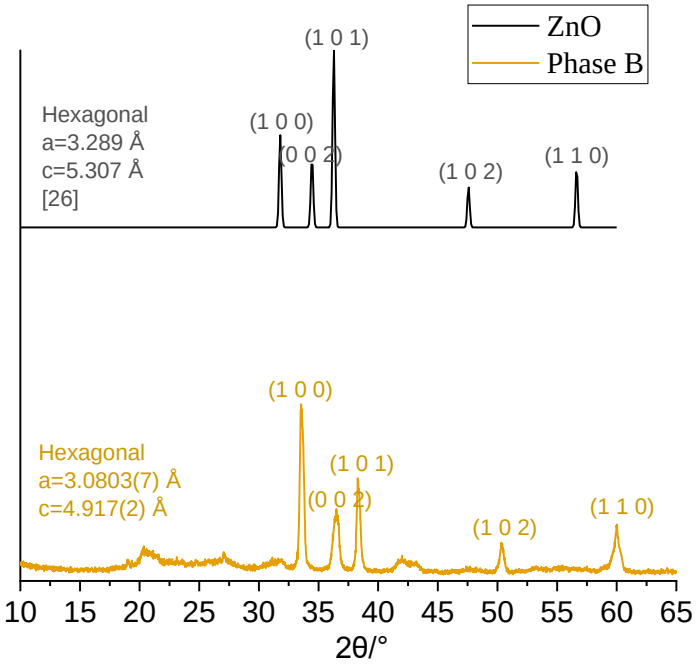

Figure 5.4. Comparison between Phase B, and ZnO [26].

The XRD of Phase B, by Bruker D2, Fig 5.4, shows several sharp peaks in the range 10-65 °2θ and a number of broad peaks. The sharp peaks have a similar general appearance to the XRD pattern of ZnO [26], but with somewhat different d-spacings. By analogy with ZnO, the sharp peaks were indexed on a hexagonal unit cell with lattice parameters of a=3.08 Å and c= 4.92 Å, as shown in Fig 5.4. The Mo-STOE results show a corrected high quality diffraction pattern which can also be indexed on a hexagonal unit cell with lattice parameters of a=3.088(2) Å and c= 4.917 (4) Å, as shown in Table 5.1. It appears therefore that Phase B may have a subcell closely related to ZnO, but with a supercell attributed to a more ordered structure whose details are unknown at present. ZnO, has space group $P6_3mc$ and only show the reflection of (0 0 l) planes with l=2n. The unit cell volume of the hexagonal subcell in Phase B, with ~40 $Å^3$, corresponds to the expected volume of the unit cell containing two anions: O^{2-}, and/or F^-. Further attempts to index both sharp peaks and the broad peaks, especially at low 2θ angles as shown in Fig 5.4, were unsuccessful. These broad peaks probably indicate the long-distance disorder [27], probably for both cations and anions in this case. A preliminary hypothesis is polyhedral with central Si connected to O and F, which is derived from basic SiO_4 tetrahedra. Similar patterns can be seen in amorphous silica glass with randomly jointed individual SiO_4 tetrahedra [28]. Clearly, the true structure of Phase B is much more complex, because of the complex formula of two cations and two anions. The existence of the broad peaks indicates a more complex supercell structure based on the hexagonal subcell which has not been identified

so far; since the extra peaks are all broad, the supercell is unlikely to be well defined in Phase B.

Table 5.1. Indexed data for Phase B with Mo-STOE data

h	k	l	2θ-obs	2θ-cal	2θ-dif	d-obs	d-cal	d-dif
1	0	0	15.217	15.242	-0.024	2.67847	2.67423	0.00424
0	0	2	16.591	16.588	0.004	2.45803	2.45857	-0.00054
1	0	1	17.343	17.365	-0.022	2.35229	2.34927	-0.00302
1	0	2	22.583	22.600	-0.017	1.81130	1.80992	0.00138
1	1	0	26.587	26.559	0.028	1.54235	1.54397	-0.00162
1	0	3	29.414	29.403	0.011	1.39693	1.39745	-0.00052
Hexagonal: *a*=3.0803(7) Å, *c*=4.917(2) Å, V=40.40 Å^3								

5.2.1.1.3. Indexed subcell of α-Li_5SiO_4F, compared with the hexagonal subcell of Phase B

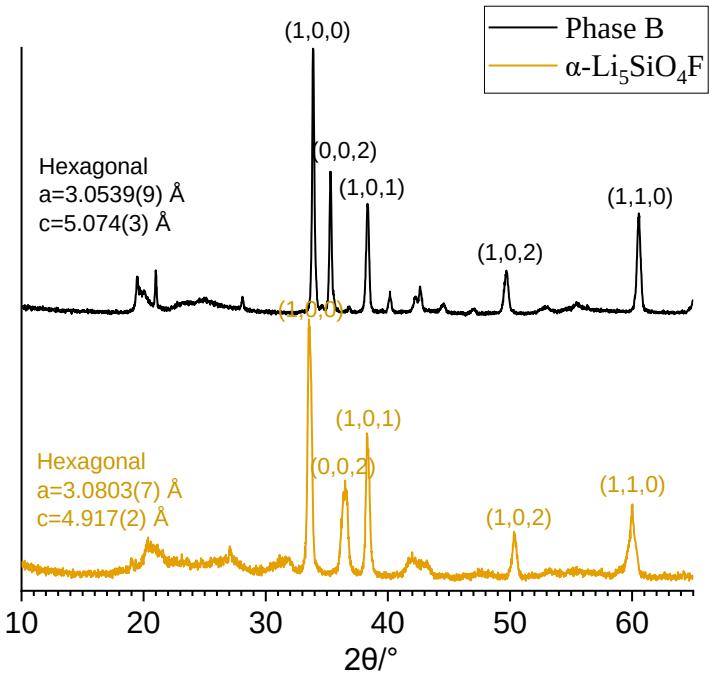

Fig 5.5. Comparison between Phase B, and α-Li_5SiO_4F

Table 5.2. Indexed data for α-Li_5SiO_4F with partial peaks.

h	k	l	2θ-obs	2θ-cal	2θ-dif	d-obs	d-cal	d-dif
1	0	0	33.895	33.866	-0.029	2.64260	2.64479	0.00219
0	0	2	35.350	35.349	-0.001	2.53704	2.53713	0.00009
1	0	1	38.368	38.348	-0.020	2.34415	2.34533	0.00118
1	0	2	49.753	49.760	0.007	1.83117	1.83090	-0.00027
1	1	0	60.591	60.592	0.001	1.52746	1.52697	-0.00049
Hexagonal: *a*=3.0539(9) Å, *c*=5.074(3) Å, V=40.98 Å^3								

Table 5.3. Lattice parameters of hexagonal subcell for Phase B and α-Li_5SiO_4F compared to hexagonal ZnO.

3 hexagonal unit cell	*a* (Å)	*c* (Å)
ZnO [25]	3.289 Å	5.307 Å
α-Li_5SiO_4F	3.0539(9) Å	5.074(3) Å
Phase B	3.0803(7) Å	4.917(2) Å

The diffraction pattern of Phase B is compared to that of α-Li_5SiO_4F in Fig 5.5. α-Li_5SiO_4F can be indexed on a similar hexagonal subcell to that of Phase B and ZnO, as shown in Table 5.2. This similarity to ZnO was not recognised in the original report of α-Li_5SiO_4F [5]. The additional supercell reflections in α-Li_5SiO_4F are different to those in Phase B and therefore, their superstructures are likely to be different. On comparing the hexagonal subcell parameters for Phase B and α-Li_5SiO_4F, *a* is slightly larger and *c* is significantly small in B, as shown in Table 5.3.

5.2.1.2. γ-Phase B

5.2.1.2.1. Synthesis of γ-Phase B at different temperatures

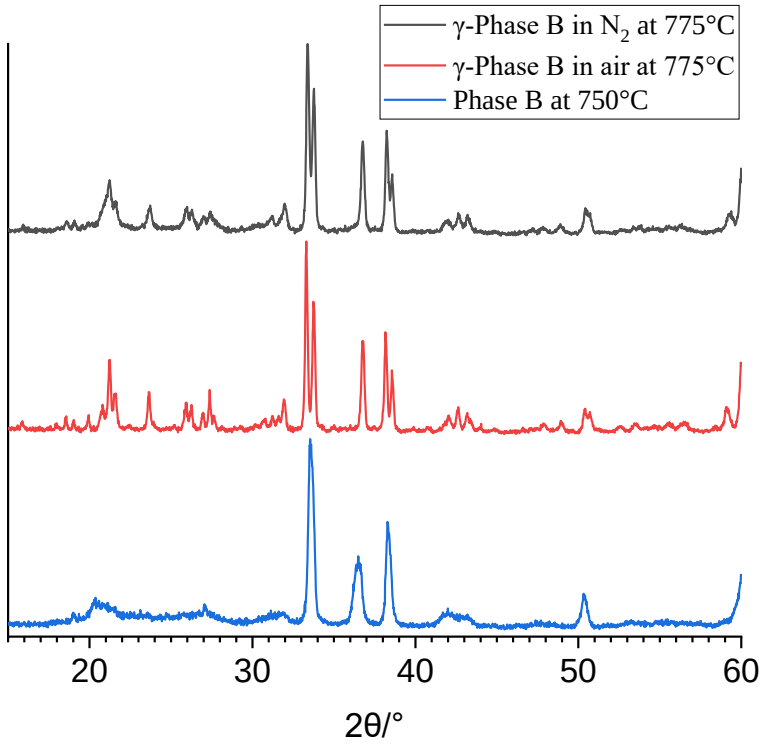

Fig 5.6. Phase B with composition Li_2O:SiO_2:LiF=47:28:25 (composition 17) transited to γ-Phase B when heated in air or N_2.

The sample of Phase B, with composition Li_2O:SiO_2:LiF=47:28:25 (17), was heated at 775 °C in either air or N_2. The diffraction patterns are essentially the same in the two atmospheres, Fig 5.6. At 775 °C, some lines of Phase B are still present, but others split into two peaks. In addition, instead of the broad supercell lines in Phase B, sharp peaks are present, especially at low 2θ angles. This indicates the formation of a more ordered polymorph of Phase B at 775 °C, labelled as γ-Phase B.

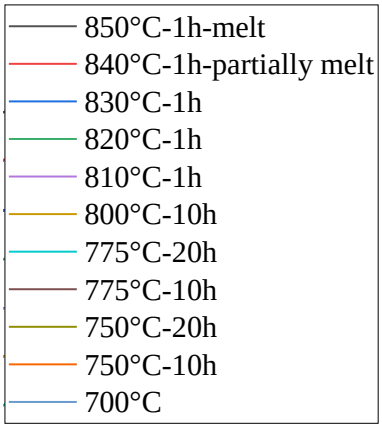

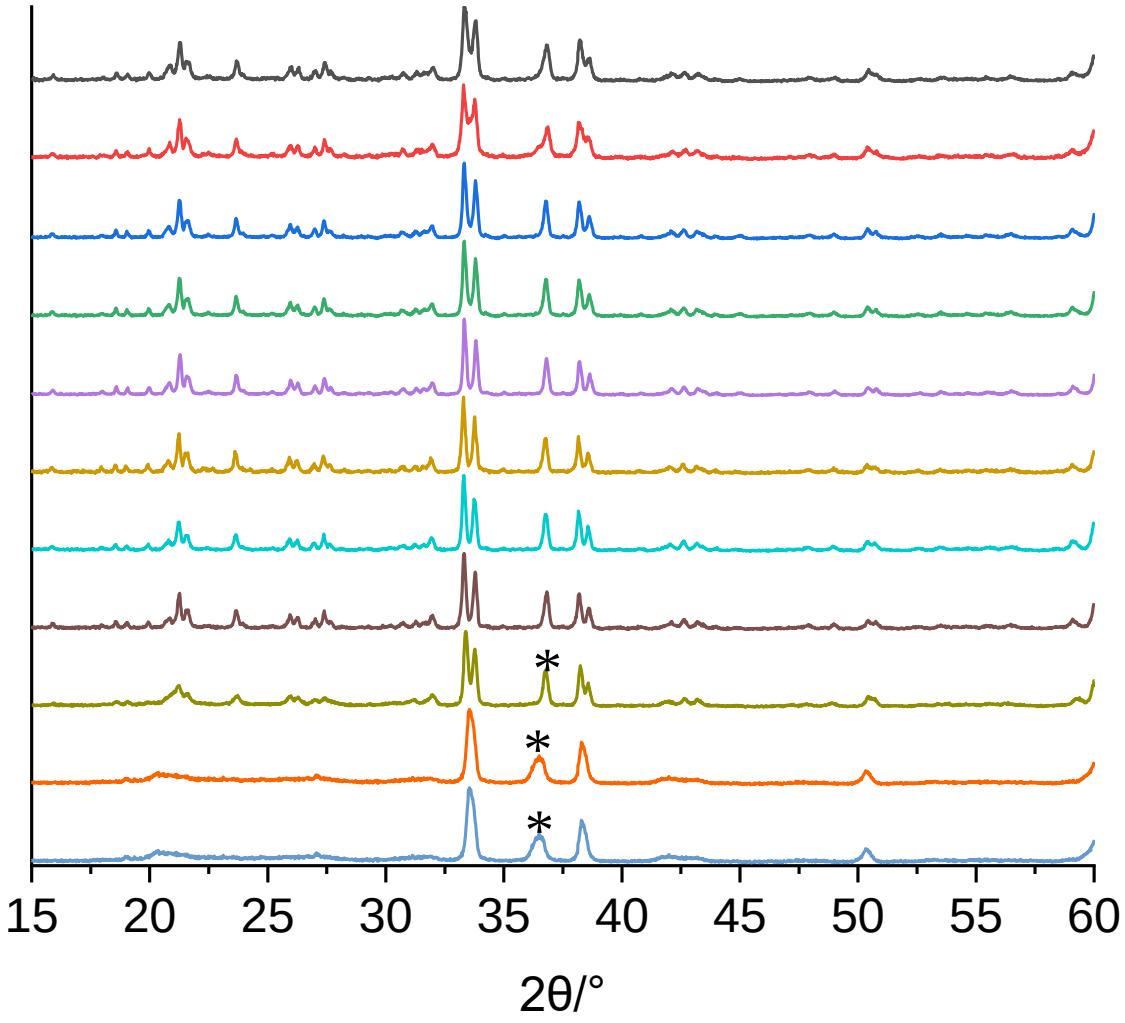

Fig 5.7. Composition Li_2O:SiO_2:LiF=47:28:25 heated at 700 °C to 850 °C, Phase B forms at 700-750 °C; γ-Phase B forms at 775-830 °C; γ-Phase B sample melt at 840 °C and 850 °C by observation but give unchanged diffraction patterns after cooling back to room temperature.

In order to study the transformation from Phase B to γ-Phase B, samples of Phase B were heated at different temperature, with results shown in Fig 5.7. At 700-750 °C, the patterns correspond to Phase B, but at 750 °C for a longer heating time and temperatures up to 830 °C, the pattern corresponds to γ-Phase B. On heating at 840 °C, samples showed signs of melting by observation which was much more apparent at 850 °C. Nevertheless, the XRD pattern of cooled samples corresponds to γ-Phase B which probably means the melting of γ-Phase B is congruent, giving a liquid of similar composition, that re-crystallised to γ-Phase B on cooling. Thus the poorer quality of XRD patterns at 840-850 °C can be attributed to the less-than-perfect crystallinity when cooling from liquid. In addition, the (0 0 2) peak in Phase B, marked by an

asterisk, moved to higher 2θ angle when the transition to γ-Phase B occurred at ~750 °C. No further changes in the diffraction patterns were observed at higher temperatures.

5.2.1.2.2. DSC tests and possible melting behaviours of Phase B, γ-Phase B, α-Li_5SiO_4F and γ-Li_5SiO_4F

(a)

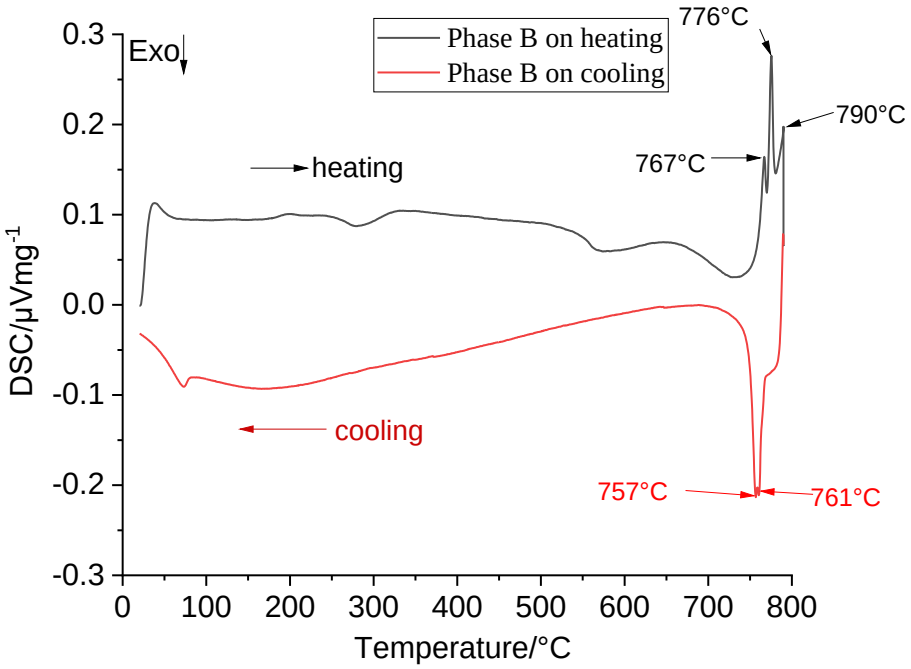

(b)

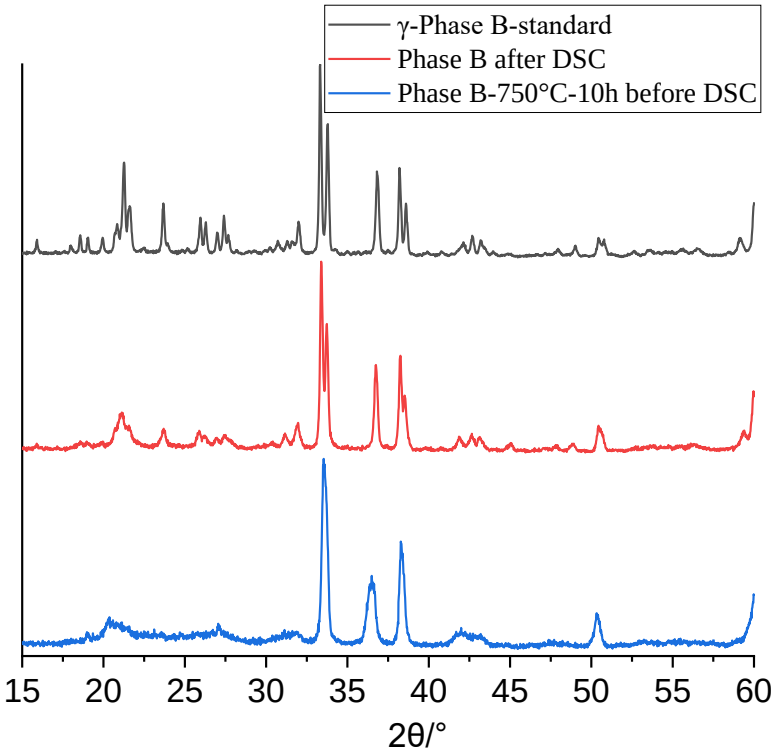

(c)

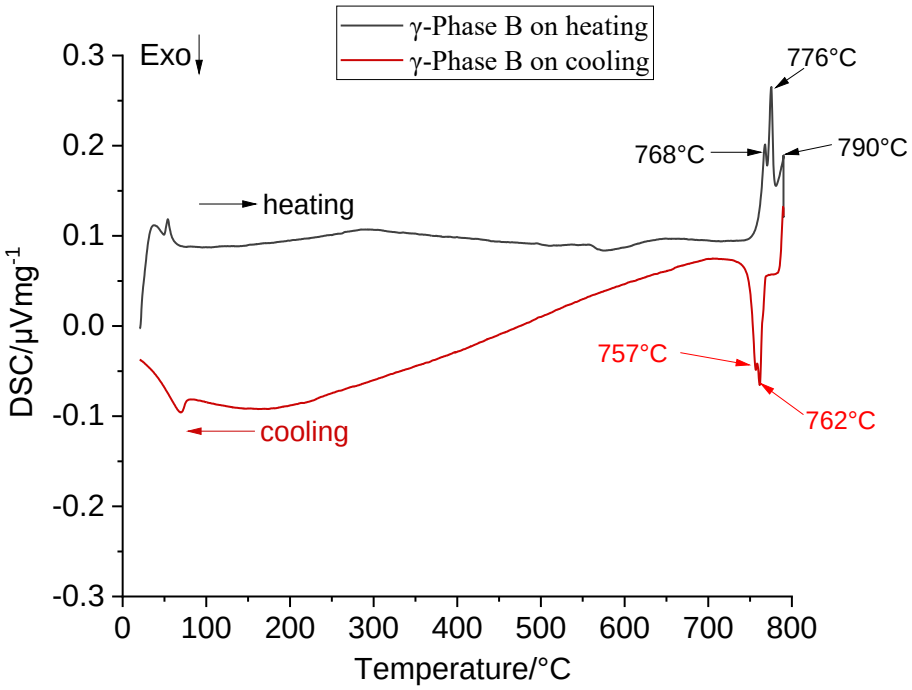

(d)

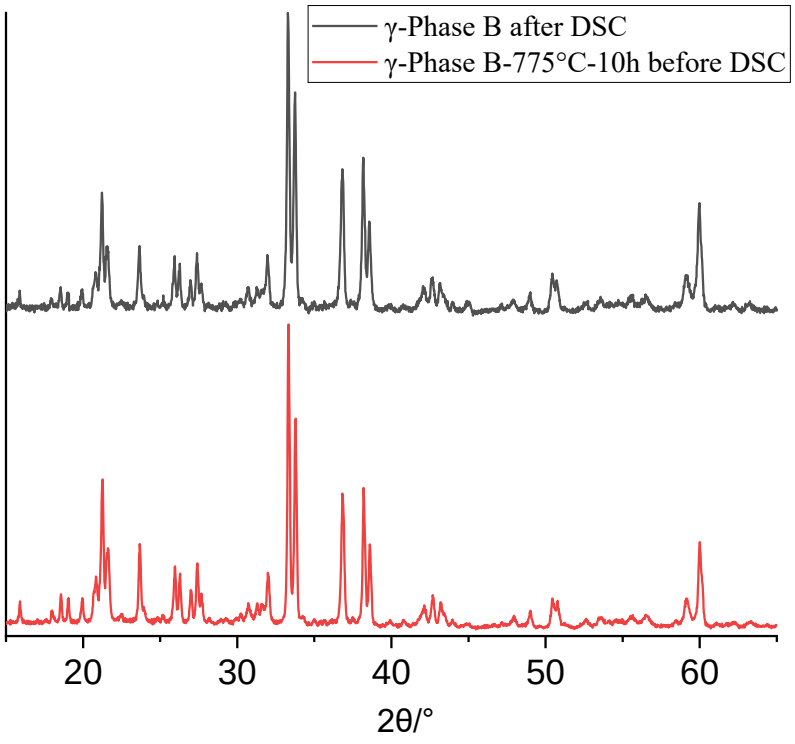

Fig 5.8 (a) DSC results for Phase B with (b) XRD for Phase B before/after the DSC test and (c) DSC results for γ-Phase B with (d) XRD for γ-Phase B before/after the DSC test

Both Phase B and γ-Phase B samples are composition 17.

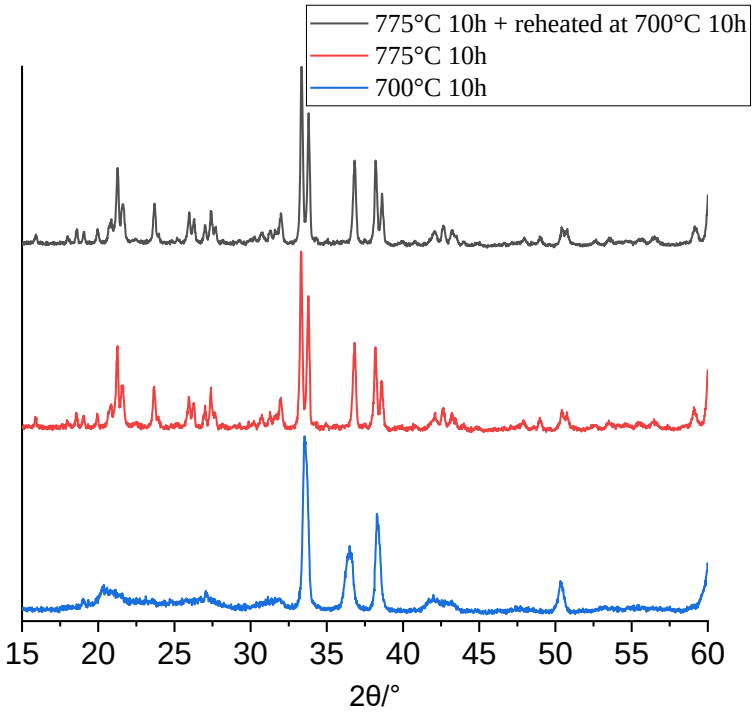

Fig 5.9. Composition 17: Li_2O:SiO_2:LiF=47:28:25 heated at different temperatures.

Samples of Phase B and γ-Phase B with the same composition Li_2O:SiO_2:LiF=47:28:25 (17), were analysed by DSC over the range of temperature, 20-790 °C, with results shown in Fig 5.8 (a) and (c). For Phase B, in (a), doublet endothermic peaks are observed at 767-776 °C on heating and corresponding exothermic peaks at 757-761 °C on cooling with a small hysteresis. The XRD results of Phase B in (b) show partial transformation to γ-Phase B after heating/cooling. For γ-Phase B, in (c), similar reversible exothermic/endothermic peaks with small hysteresis are observed. The XRD results of γ-Phase B in Fig 5.8 (d) show no change before and after the DSC. There are three possibilities for this: (a) either a rapidly reversible phase transition from Phase B and γ-Phase B to another high temperature polymorph, for which we have no XRD data at present, we speculate that this is a simple hexagonal, ZnO-like structure without any superlattice; (b) or congruent melting on heating and recrystallisation on cooling; (c) or γ-Phase B has partially decomposition / incongruent melting at that temperature, which is not likely due to reversibility and no changes in XRD results before/after, Fig 5.8. In order to check the possible reversibility of the Phase B to γ-Phase B transition, a sample of γ-Phase B prepared at 775 °C was reheated at 700 °C. There was no transformation back to Phase B according to the XRD results shown in Fig 5.9. This indicates that probably Phase B is a

metastable phase produced by low temperature synthesis and would not, therefore, appear on an equilibrium phase diagram. The diagram shown in Fig 5.3 is unlikely to represent thermodynamic equilibrium although γ-Phase B is likely to be thermodynamically stable.

(a)

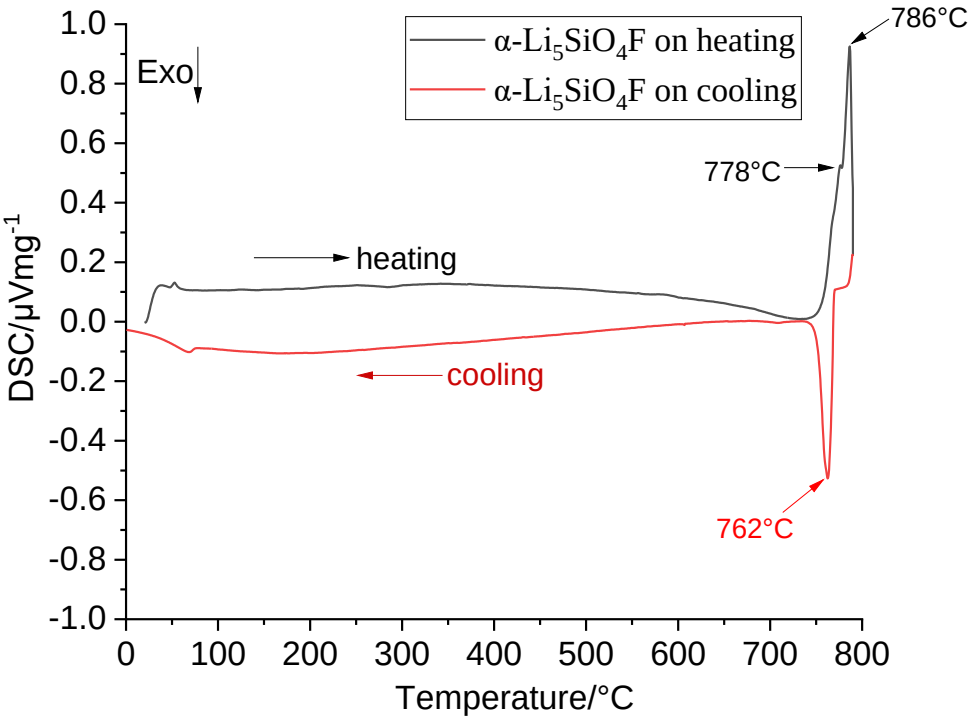

(b)

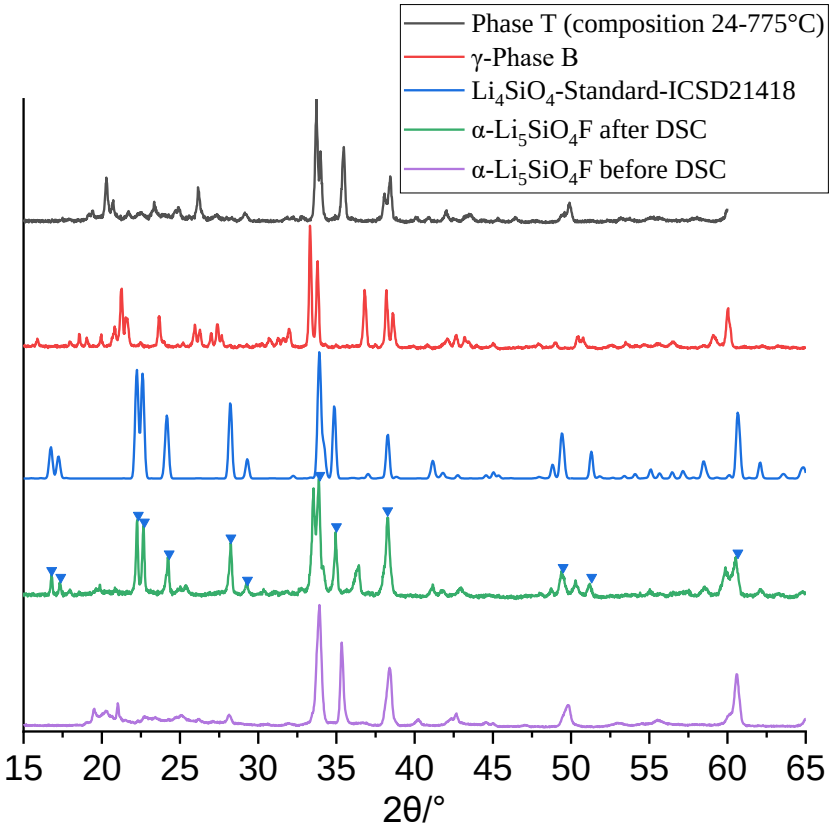
Phase T (composition 24-775°C)
γ-Phase B
Li4SiO4-Standard-ICSD21418
α-Li5SiO4F after DSC
α-Li5SiO4F before DSC
15 20 25 30 35 40 45 50 55 60 65
2θ/°

(c)

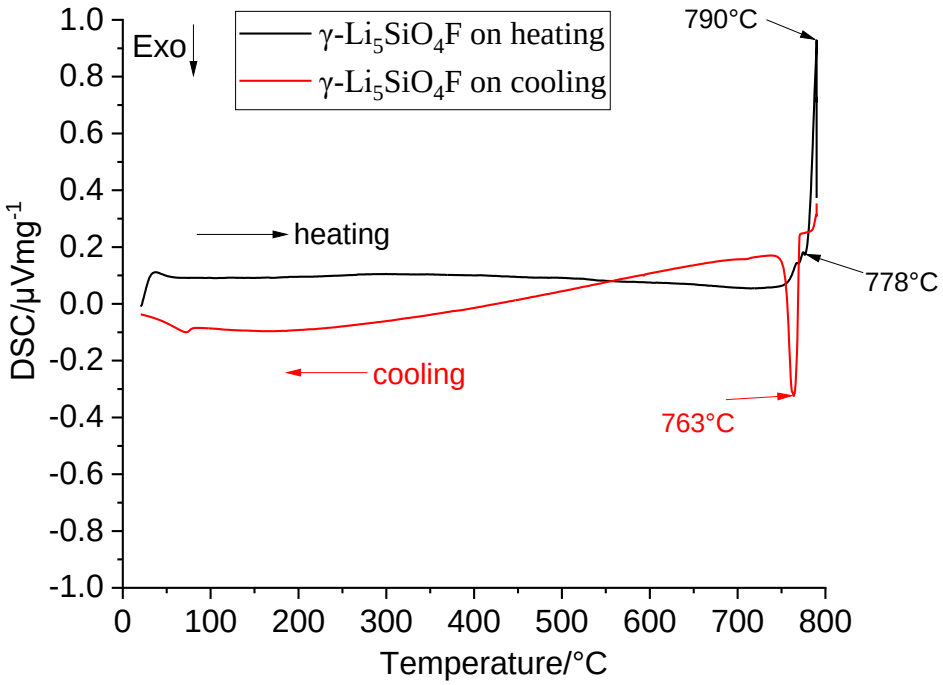
Exo
γ-Li5SiO4F on heating
γ-Li5SiO4F on cooling
790°C
778°C
763°C
heating
cooling
DSC/μVmg-1
1.0 0.8 0.6 0.4 0.2 0.0 -0.2 -0.4 -0.6 -0.8 -1.0
0 100 200 300 400 500 600 700 800
Temperature/°C

(d)

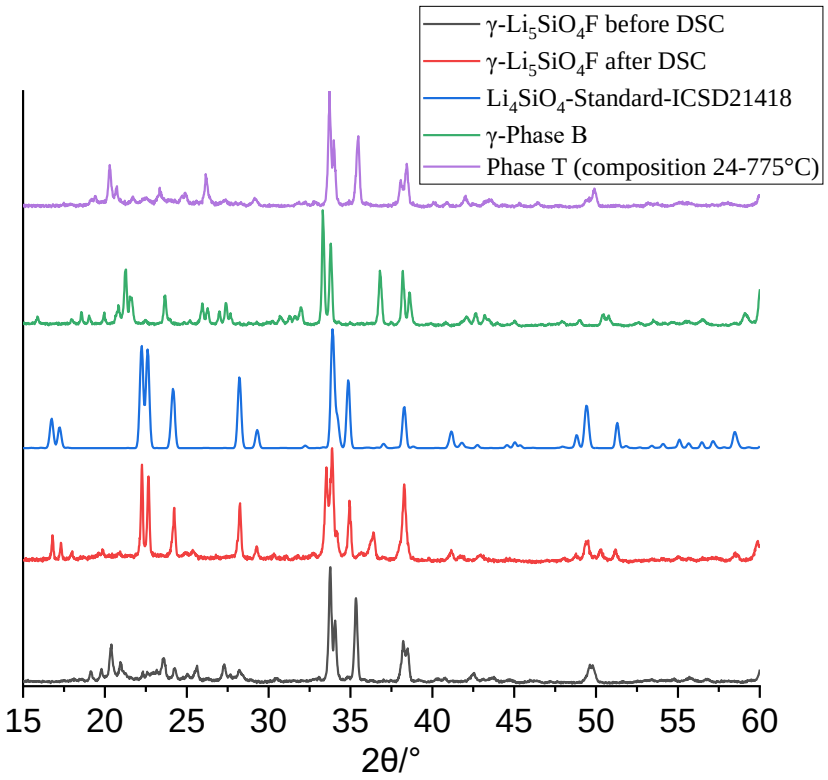

Fig 5.10. (a) DSC for α-Li_5SiO_4F with (b) XRD before/after the DSC test; and

(c) DSC for γ-Li_5SiO_4F with (d) XRD before/after the DSC test.

DSC results for α-Li_5SiO_4F in Fig 5.10 (a) show two endothermic peaks at 778 °C and 786 °C on heating and an exothermic peak at 762 °C on cooling. DSC results for γ-Li_5SiO_4F in (c) clearly show a pair of reversible peaks: endothermic peaks at 790 °C on heating and exothermic peak at 763 °C on cooling. There seems exists a partially resolved endothermic peak at 778 °C on heating. The XRD results of both α-Li_5SiO_4F and γ-Li_5SiO_4F in (b) and (d) show a mixture of Li_4SiO_4 and unidentified phase which clearly belong to same general family as Phase B type and Phase T type but different to those known phases given by its peak at ~36.6 °2θ. The reversible peaks at ~790 °C on heating and ~763 °C on cooling probably indicate an incongruent melting of γ-Li_5SiO_4F. The large difference in XRD patterns before/after DSC and the major present of Li_4SiO_4 indicates that, probably, α- and γ-Li_5SiO_4F melt incongruently to Li_4SiO_4 + liquid at ~790 °C. Some of the liquid may volatilise and anyway, the incongruent is not readily reversible on cooling.

5.2.1.2.3. Indexing results of γ-Phase B, identification of possible subcell

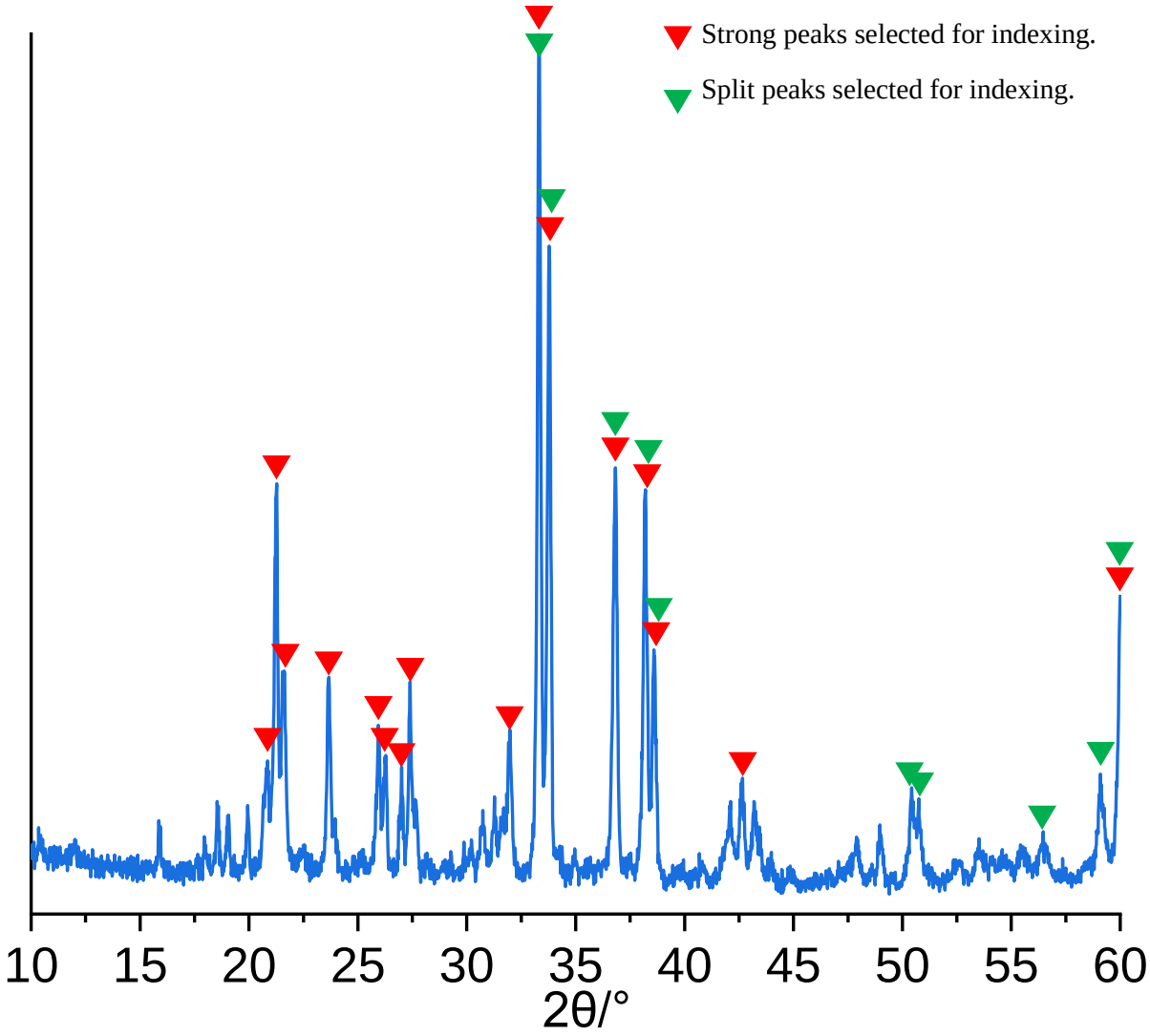

Fig 5.11. Peaks in γ-Phase B selected for indexing.

Table 5.4. Indexed results for γ-Phase B with peaks marked with green triangles in Fig 5.11.

(a)

2θ observed	2θ indexed	2θ dif	h	k	l
33.33	33.28	0.04	1	0	1
33.78	33.74	0.04	2	0	0
36.81	36.80	0.01	0	2	0
38.20	38.17	0.03	1	1	1
38.60	38.58	0.02	2	1	0
50.46	50.46	0.00	1	2	1
50.74	50.78	-0.04	2	2	0
56.53	56.52	0.01	0	3	0
59.16	59.18	-0.02	0	0	2
60.03	60.06	-0.03	3	0	1
Orthorhombic lattice: *a*=3.120(1) Å, *b*=5.309(3) Å, *c*=4.881(2) Å, V=80.83 Å^3					

(b)

2θ observed	2θ indexed	2θ dif	h	k	l
33.33	33.35	-0.02	1	0	-1
33.78	33.78	0.00	1	0	1
36.81	36.82	-0.01	0	2	0
38.20	38.23	-0.03	1	1	-1
38.60	38.62	-0.02	1	1	1
50.46	50.49	-0.03	1	2	-1
50.74	50.79	-0.05	1	2	1
56.53	56.52	0.01	0	3	0
59.16	59.14	0.02	1	1	-2
60.03	60.02	0.01	2	2	0
Monoclinic system: *a*=3.973(4) Å, *b*=3.602(3) Å, *c*=4.882(2) Å, *γ*=90.70(6)°, V=69.85 Å^3					

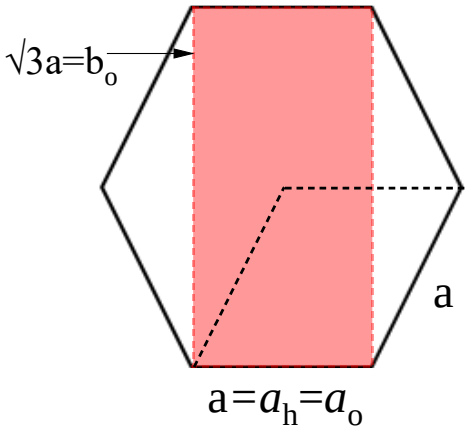

Fig 5.12. geometric relationship between the hexagonal subcell in Phase B and the orthorhombic subcell in γ-Phase B

The attempt to index the complete pattern of γ-Phase B was unsuccessful. Then, the split peaks in similar position to those in Phase B together with 3 extra lines, marked with green triangles in Fig 5.11, were successfully indexed on an orthorhombic subcell as shown in Table 5.4 (a). There is a close relationship between this orthorhombic subcell of γ-Phase B and the hexagonal subcell of Phase B: a_o equals a_h, b_o equals $\sqrt{3}\, a_h$, and c_o equals c_h, as illustrated in Fig 5.12. The orthorhombic subcell has a doubled subcell volume of V=80.83 $Å^3$ compared to that of hexagonal subcell with ~40 $Å^3$, which could be suitable for a mixture of 4 anions: O^{2-} and F^-. Alternatively, a small monoclinic lattice with lower symmetry was also obtained by the indexing software with results shown in Table 5.4 (b). However, the volume of this monoclinic lattice, 69.85 $Å^3$, does not show any simple geometric relationship to that of the hexagonal subcell. Nevertheless, c_m in the monoclinic cell roughly equals c in both Phase B and γ-Phase B.

Table 5.5. Indexed results for γ-Phase B with peaks marked with red triangles in Fig 5.11.

(a)

2θ observed	2θ indexed	2θ dif	h	k	l	2θ observed	2θ indexed	2θ dif	h	k	l
20.82	20.93	-0.11	0	3	0	**33.33**	33.24	0.09	2	0	4
	20.77	0.05	2	2	1	**33.78**	33.88	-0.10	2	3	3
21.24	21.34	-0.10	2	1	2		33.86	-0.08	5	0	0
	21.31	-0.07	3	1	0		33.6	0.18	3	2	3
21.57	21.60	-0.03	1	2	2	**36.81**	36.73	0.08	1	5	1
	21.50	0.07	3	0	1		36.76	0.05	5	2	0
23.66	23.66	0.00	0	1	3		36.63	0.18	3	0	4
	23.59	0.07	1	0	3	**38.2**	38.11	0.09	0	0	5
25.95	25.85	0.10	0	3	2		38.24	-0.04	4	2	3

	26.05	-0.10	2	3	1	**38.6**	38.63	-0.03	2	5	1
26.27	26.35	-0.08	2	0	3	**42.65**	42.59	0.06	0	6	0
	26.17	0.10	3	1	2		42.56	0.09	3	3	4
26.98	26.94	0.04	4	0	0	**59.16**	59.08	0.08	3	1	7
27.39	27.48	-0.09	1	2	3		59.12	0.04	6	2	5
	27.28	0.11	2	1	3		58.92	0.24	0	3	7
31.97	31.94	0.03	0	4	2		59.02	0.14	3	4	6
	31.85	0.12	1	1	4		58.93	0.23	5	1	6
Orthorhombic system: *a*=13.226(8) Å, *b*=12.726(1) Å, *c*=11.796(9) Å, V=1985.70 Å^3											

(b)

2θ observed	**2θ indexed**	**2θ dif**	**h**	**k**	**l**	**2θ observed**	**2θ indexed**	**2θ dif**	**h**	**k**	**l**
20.82	20.88	-0.06	1	1	1	**33.33**	33.29	0.04	1	2	-1
21.24	21.15	0.09	0	0	2	**33.78**	33.83	-0.05	1	0	3
21.57	21.55	0.02	2	0	-1	**36.81**	36.82	-0.01	2	0	-3
23.66	23.62	0.04	1	0	2	**38.20**	38.12	0.08	1	2	-2
25.95	25.97	-0.02	0	1	2		38.26	-0.06	2	0	3
26.27	26.30	-0.03	2	1	-1	**38.60**	38.59	0.01	1	2	2
26.98	26.96	0.02	2	1	1		38.60	0.00	3	1	-2
27.39	27.42	-0.03	1	1	-2	**42.65**	42.70	-0.05	3	0	-3
31.97	31.95	0.02	0	0	3	**59.16**	59.18	-0.02	3	3	-2
	31.94	0.03	0	2	1						
	31.95	0.02	2	1	-2						
Monoclinic system: *a*=9.25(2) Å, *b*=5.94(1) Å, *c*=8.403(9) Å, *β*=92.4(1)°, V=461.03 Å^3											

Further indexing was attempted using additional strong peaks in γ-Phase B marked with red triangles in Fig 5.11. The indexed results suggest (a) either a very large orthorhombic unit cell with *a*= 13.23 Å, *b*= 12.73 Å, *c*= 11.80 Å, and V= 1985.70 Å^3, Table 5.5 (a); or (b) a monoclinic unit cell with *a*= 9.25 Å, *b*= 5.94 Å, *c*= 8.40 Å, *β*=92.4 (1) °, and V= 461.03 Å^3, Table 5.5 (b). The general agreement of the monoclinic cell is significantly better than that of the orthorhombic cell. This may indicate that the symmetry of γ-Phase B is a monoclinic, slight distortion of the orthorhombic cell because the *β* angle close to 90°. Further work is required, ideally using single crystal XRD or electron diffraction as there are several other XRD reflections that were not included in the trial and error indexing attempts.

5.2.1.2.4. Possible subcell of γ-Li_5SiO_4F

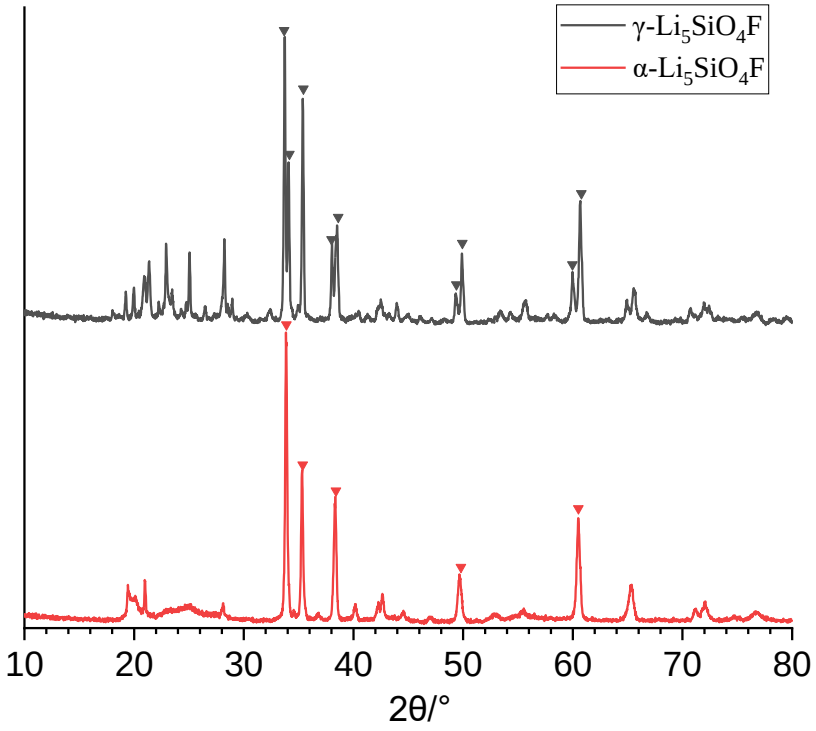

Fig 5.13. Peaks of α-Li_5SiO_4F and γ-Li_5SiO_4F used for indexing, results for α-Li_5SiO_4F are shown in Table 5.2. Some peaks in α-Li_5SiO_4F split in γ-Li_5SiO_4F.

Table 5.6. (a) Indexed results for γ-Li_5SiO_4F with split peaks (b) comparison of subcell of γ-Li_5SiO_4F and γ-Phase B

(a)

2θ observed	**2θ indexed**	**2θ dif**	**h**	**k**	**l**
33. 766	33.711	0.055	0	1	1
34.113	34.061	0.052	0	2	0
35.415	35.404	0.011	2	0	0
38.077	38.051	0.026	1	1	-1
38.519	38.536	-0.017	1	2	0
49.396	49.412	-0.016	2	1	-1
49.943	49.944	-0.001	2	2	0
60.044	60.07	-0.026	0	0	2
60.743	60.743	0	0	3	1
Monoclinic system: *a*=3.078(2) Å, *b*=5.260(3) Å, *c*=5.067(4) Å,					

β=90.69(9)°, V=82.04Å^3

(b)

Indexed subcell	Type	a (Å)	b (Å)	c (Å)	B (°)	V (Å^3)
γ-Li_5SiO_4F	monoclinic	3.078(2)	5.260(3)	5.067(4)	90.69(9)°	82.04
γ-Phase B	orthorhombic	3.0539(9)	5.309(3)	4.881(2)	90	80.83

Following the identification of a hexagonal subcell for both Phase B and α-Li_5SiO_4F, together with a related orthorhombic subcell for γ-Phase B, the XRD pattern of γ-Li_5SiO_4F was reinvestigated. Some peaks of γ-Li_5SiO_4F are probably related to those intense lines in similar 2θ positions in α-Li_5SiO_4F, as shown in Fig 5.13. The hexagonal subcell of α-Li_5SiO_4F is shown in Table 5.2. The indexed results for γ-Li_5SiO_4F with those split peaks suggest a monoclinic subcell as shown in Table 5.6. This is approximately twice as large, V=82.04 Å^3, as the hexagonal subcell of α-Li_5SiO_4F, V=40.98 Å^3. Within acceptable error, a_m equals a_h, c_m equals c_h and b_m equals $\sqrt{3}\ a_h$. As β in the monoclinic subcell is quite close to 90°, the monoclinic subcell of γ-Li_5SiO_4F is likely to be based on a minor distortion of the hexagonal subcell of α-Li_5SiO_4F. There is a similarity between the orthorhombic subcell of γ-Phase B and the monoclinic subcell of γ-Li_5SiO_4F including similar *a* and *b* values and slightly distorted β angle. The main difference is the *c*-axis, which is used to distinguish the general β/γ families in Li_3PO_4-related materials.

5.2.1.2.5. Densities of α/γ-Li_5SiO_4F, Phase B and γ-Phase B

Table 5.7. Density for α-Li_5SiO_4F, Phase B, and ZnO

3 hexagonal unit cell	*a* (Å)	*c* (Å)	*c*/*a* ratio (1.633*)	Lattice volume (Å^3)	Theoretical/hypothesised density (gcm^{-3})
ZnO [25]	3.289	5.307	1.614	49.716	5.434
α-Li_5SiO_4F	3.0539(9)	5.074(3)	1.661	40.981	2.382
Phase B	3.089(2)	4.917(4)	1.592	40.632	2.404

* c/a ratio for ideal hexagonal cell; 1 Å=10^{-8} cm; 1 amu=1.67377×10^{-24} g

Table 5.8. The pellet density, measured powder density and theoretical density for different materials

	Diameter (mm)	Thickness (mm)	Volume (mm^3)	Weight (g)	Pellet Density (gcm^{-3})	Theoretical/ hypothesised density (gcm^{-3})	Measured density (gcm^{-3})
α-Li_5SiO_4F	9.95	1.21	94.08	0.135	1.435	2.382	-
Phase B-com 17-hot press	10.09	1.14	91.15	0.1511	1.658	2.404	2.437(5)
γ-Phase B-com 17-cold press	9.29	1.19	80.66	0.1307	1.62	2.404	2.458(5)
γ-Phase B-com 17- hot press	9.64	1.55	113.13	0.2249	1.99	2.404	-

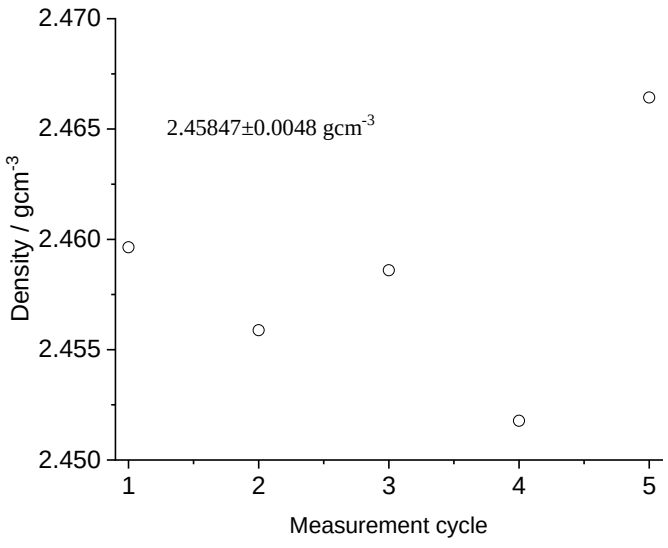

Fig 5.14. Loose powder density of γ-Phase B measured by gas displacement pycnometer, 5 cycles.

As the indexing results of the low temperature phases, α-Li_5SiO_4F and Phase B, suggest a basic ZnO-like hexagonal subcell, the density of these phases was calculated as shown in Table 5.7. The ZnO hexagonal cell has two Zn^{2+} and two O^{2-}, the number of cations and anions were calculated according to the formula of Li_5SiO_4F and the possible stoichiometric composition Phase B, Li_2O:SiO_2:LiF=47:28:25. For Li_5SiO_4F, the average cations are 1.67 Li^+ and 0.33 Si^{4+}; while the average anions are 1.6 O^{2-} and 0.4 F^-. For Phase B, the cations are 1.62 Li^+ and 0.38 Si^{4+}; while the anions are 1.61 O^{2-} and 0.39 F^-. The volume of the lattice is calculated by: $V = 0.866 \times a^2 \times c$, where a and c are the indexed lattice parameters. Then, the density of the pellet and loose powder of different materials are summarised in Table 5.8. The pellet density is calculated by the measured weight, thickness and diameter of the pellets. The pellet density should have some errors as the sample pellets are not perfectly symmetric in its dimensions. The pellet density will be lower than the theoretical density as the sample pellets are always porous. The porosity of the sample can also be assumed by the difference between the pellet density and theoretical density of the sample. The loose powder density is measured by a gas displacement pycnometer. The results of γ-Phase B are illustrated in Fig 5.14. The measured loose powder densities for both Phase B and γ-Phase B are slightly higher than the theoretical density. Probably, the is a higher Si content in the stoichiometric Phase B which offer a higher density.

5.2.1.2.6. Identification of γ-Phase B solid solution

(a)

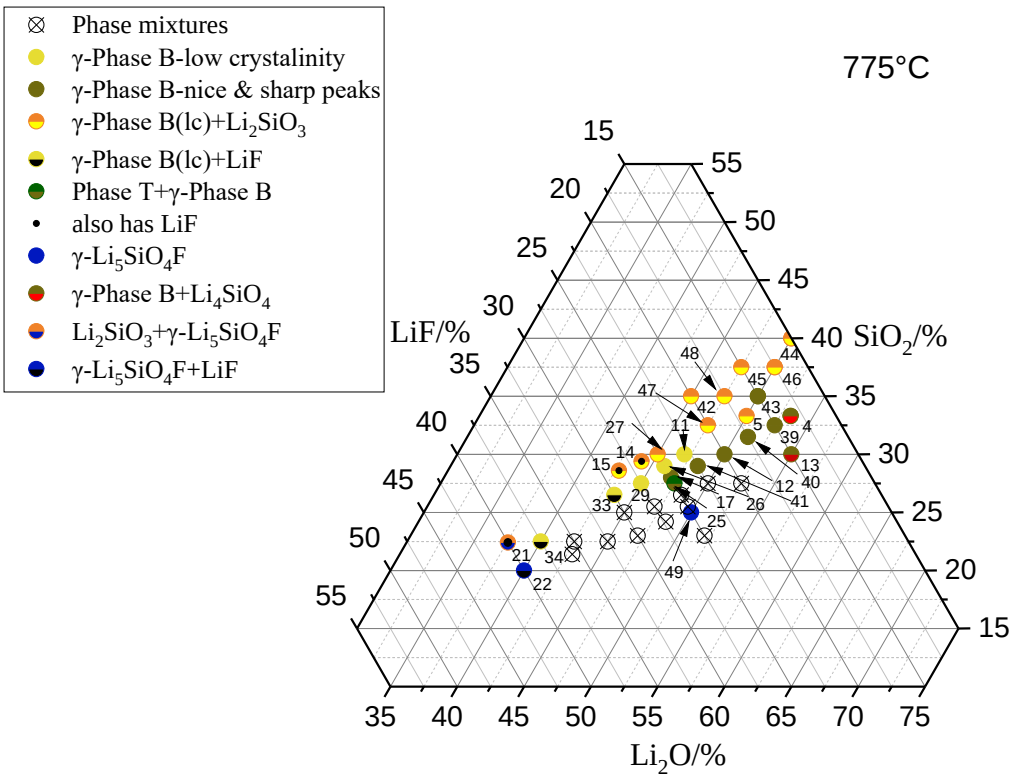
Phase mixtures
γ-Phase B-low crystalinity
γ-Phase B-nice & sharp peaks
γ-Phase B(lc)+Li2SiO3
γ-Phase B(lc)+LiF
Phase T+γ-Phase B
also has LiF
γ-Li5SiO4F
γ-Phase B+Li4SiO4
Li2SiO3+γ-Li5SiO4F
γ-Li5SiO4F+LiF
775°C
LiF/%
SiO2/%
Li2O/%

(b)

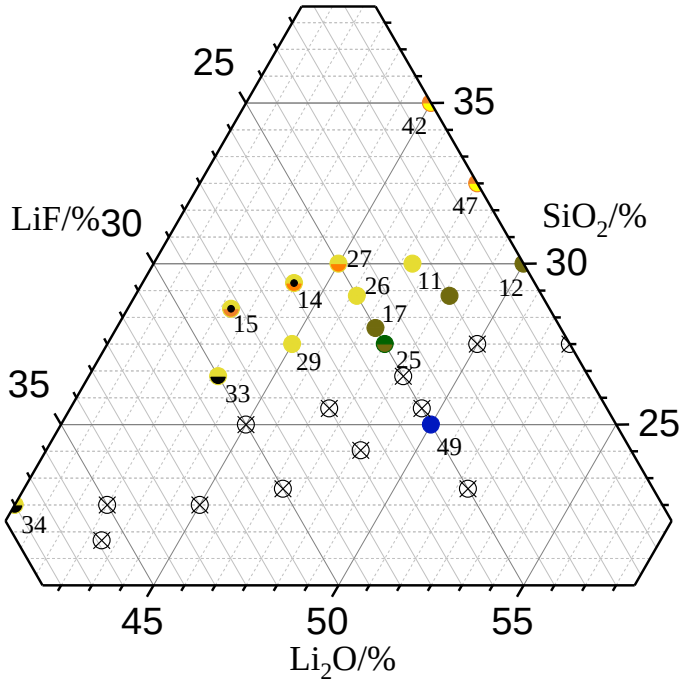
LiF/%
SiO2/%
Li2O/%

(c)

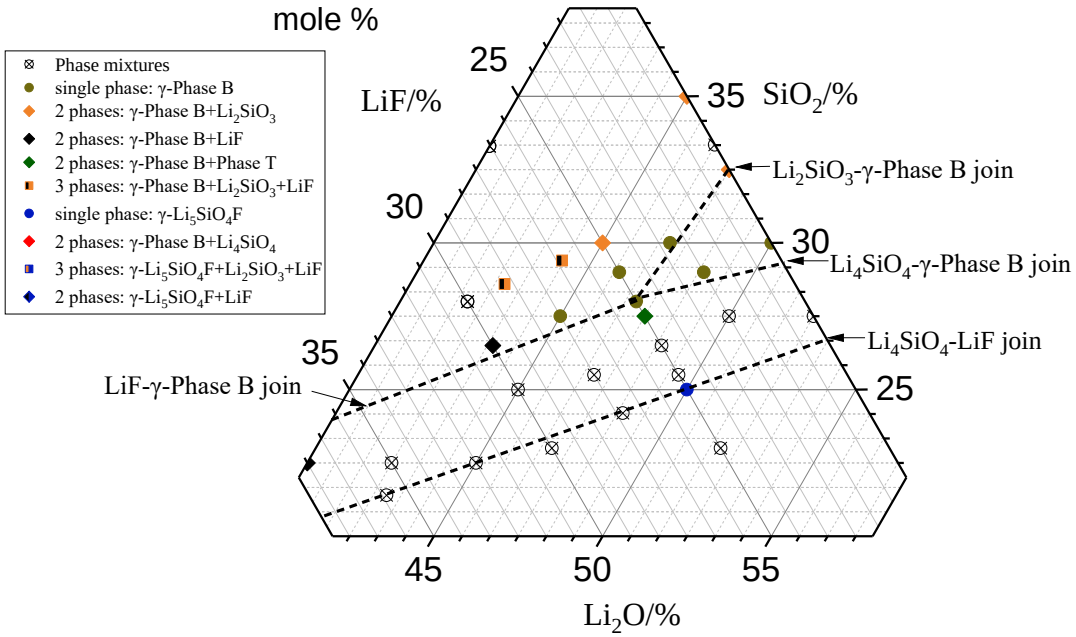

(d)

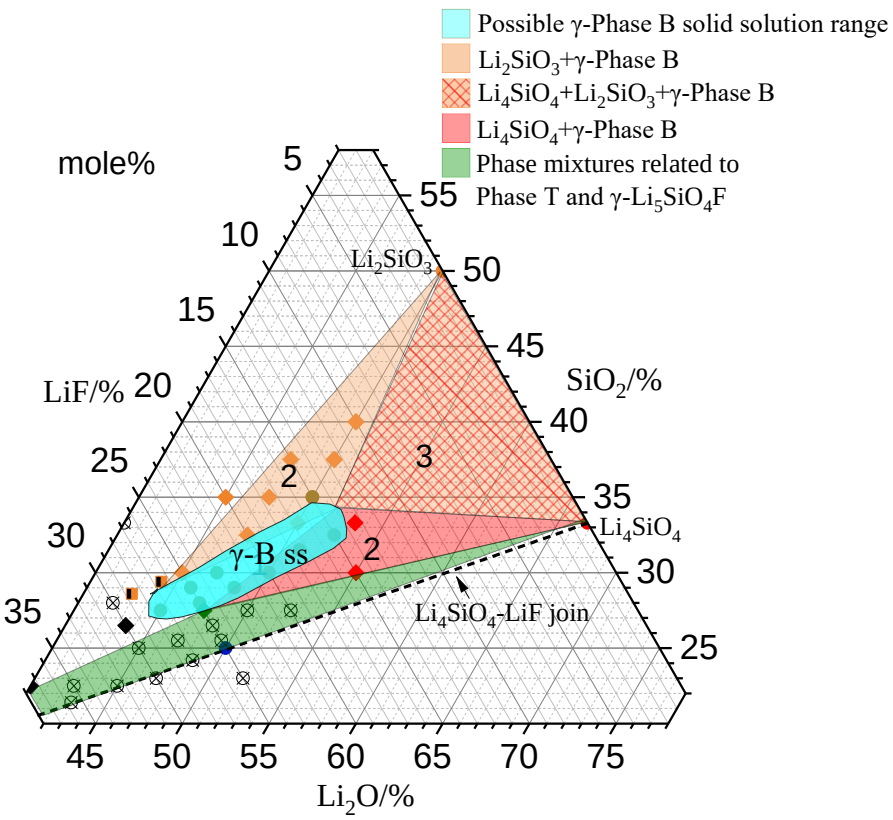

Fig 5.15. (a-b) Compositions and phase(s) present in ternary system Li_2O-SiO_2-LiF at 775 °C; (c) number of phase(s) present; (d) the possible solid solution range of γ-Phase B.

During the overview of phase formation in composition inside the area Li_4SiO_4-Li_2SiO_3-LiF, a number of compositions gave patterns of γ-Phase B without any second phase, indicating the possible formation of a range of γ-Phase B solid solution. These results are summarised for synthesis at 775 °C in Fig 5.15 (a-b) and Table 5.S1. Compositions 12, 17, 39, 40, 41, and 43 gave phase-pure γ-Phase B while compositions 11, 26, and 29 are also regarded as γ-Phase B but with lower crystallinity according to their XRD results. This shows that γ-Phase B forms a solid solution over the approximate range 15-28 mole% LiF and 45-53 mole% Li_2O, as illustrated in (d). Based on the results summarised in (c), possible compatibility triangles (regions) at 775 °C are also illustrated in (d). The results are similar to those at 750 °C as shown in Fig 5.3 (d), but now contain a solid solution area for γ-Phase B instead of a single composition for Phase B. So far, whether the solid solution range of γ-Phase B changes with temperature need further confirmation. If the solid solution range of γ-Phase B changes with temperature, the huge difference in possible solid solution range between Phase B and γ-Phase B may be explained by the different synthesis temperatures used. If not, then either the solid solution range of γ-Phase B is temperature dependent, or the reactions at 750 °C may be incomplete. γ-Phase B solid solution would have a dimer structure, while α- and γ-Li_5SiO_4F may has isolated SiO_4 tetrahedra. XRD results of some representative compositions are summarised in Fig 5.S2.

On comparing of the XRD results for heat treatment at 750°C and 775°C, it is clear that, at 750°C, the main new phase product in this composition range is Phase B with highly disordered structure; at 775°C, however, the product with much better crystallinity is the γ-Phase B solid solution. It is possible that formation of Phase B is the first product of reaction which is metastable and forms as an example of Ostwald's law of successive reactions. But higher temperatures are needed to form the equilibrium γ-Phase B solid solutions. Thus, we have no evidence that γ-Phase B can transform to Phase B on reheating at lower temperatures.

5.2.1.3. Phase T

5.2.1.3.1. Synthesis and identification of Phase T

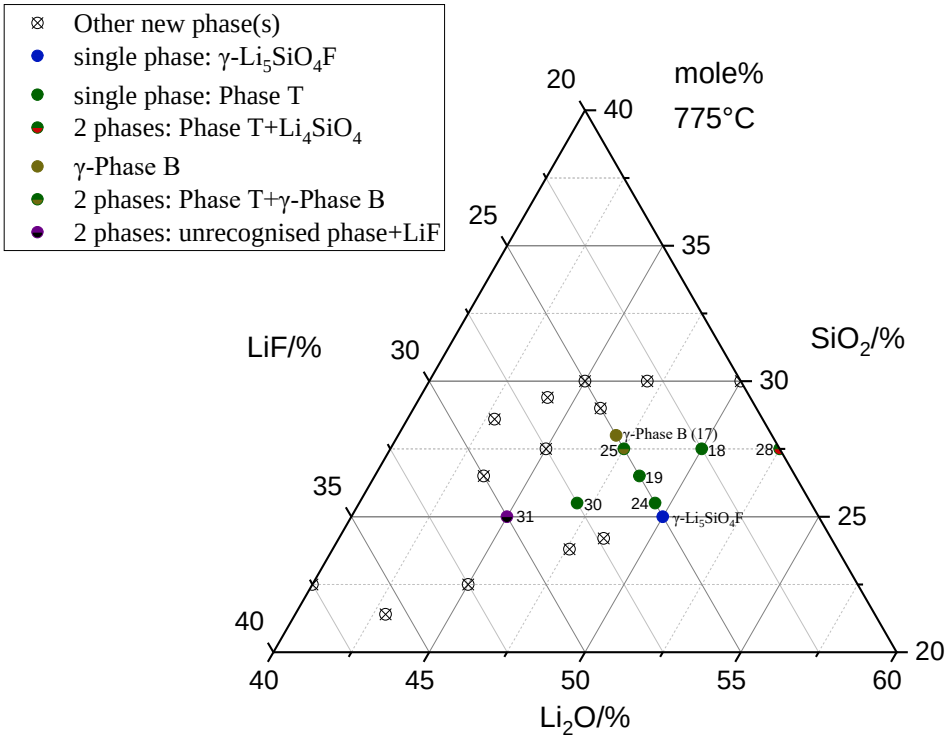

Fig 5.16. Phase T in the Li_2O-SiO_2-LiF system at 775 °C

Some compositions around γ-Phase B and Li_5SiO_4F prepared at 650-800 °C whose XRD patterns indicated the existence of another new phase, labelled Phase T, are summarised in Fig 5.16. Phase T may form a solid solution over a narrow range 47.5-50 %/mole Li_2O, 22.5-25 %/mole LiF. However, reactions at lower temperatures, 700-750 °C, may not complete, Therefore, the phase diagram representing thermodynamic equilibrium at lower temperatures needs further work.

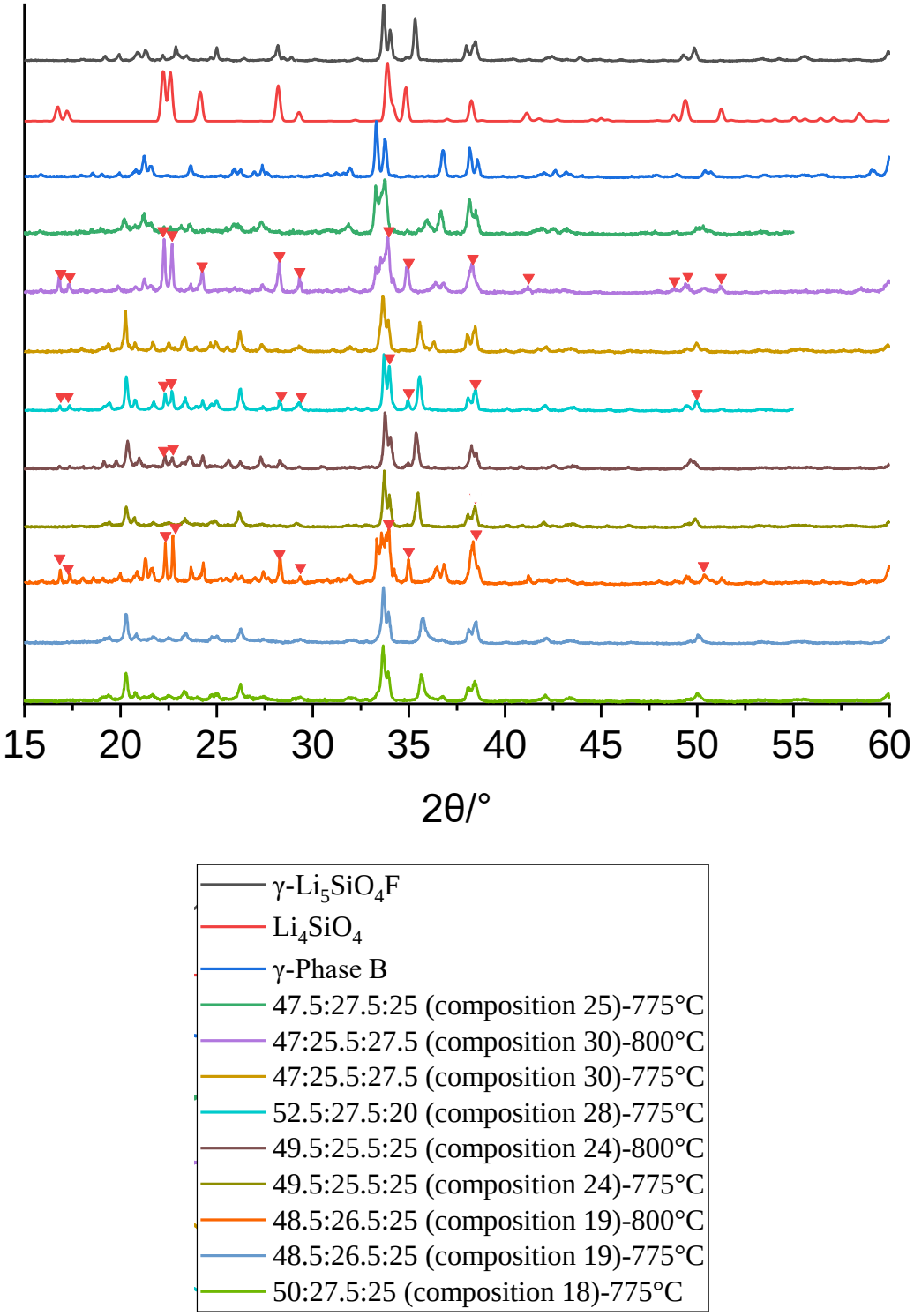

Fig 5.17. XRD results of Phase T related compositions, some compositions show Li_4SiO_4 with other phase(s) in the product.

Compositions 18, 19, 24 and 30 show a main phase which differ to neither γ-Phase B, nor Li_5SiO_4F, Fig 5.17 and Table 5.S1. The most significant difference between γ-Phase B and Phase T is the position of the (0 0 2) peak, at ~35°2θ and ~37°2θ, respectively. The main difference between Phase T and γ-Li_5SiO_4F is the peaks at low 2θ angles, at ~18-28 °2θ.

When compositions 24 and 28, Phase T, were heated at higher temperatures, 775-~800°C, their XRD results show the existence of Li_4SiO_4, which indicates an incongruent melting of Phase T at ~800°C.

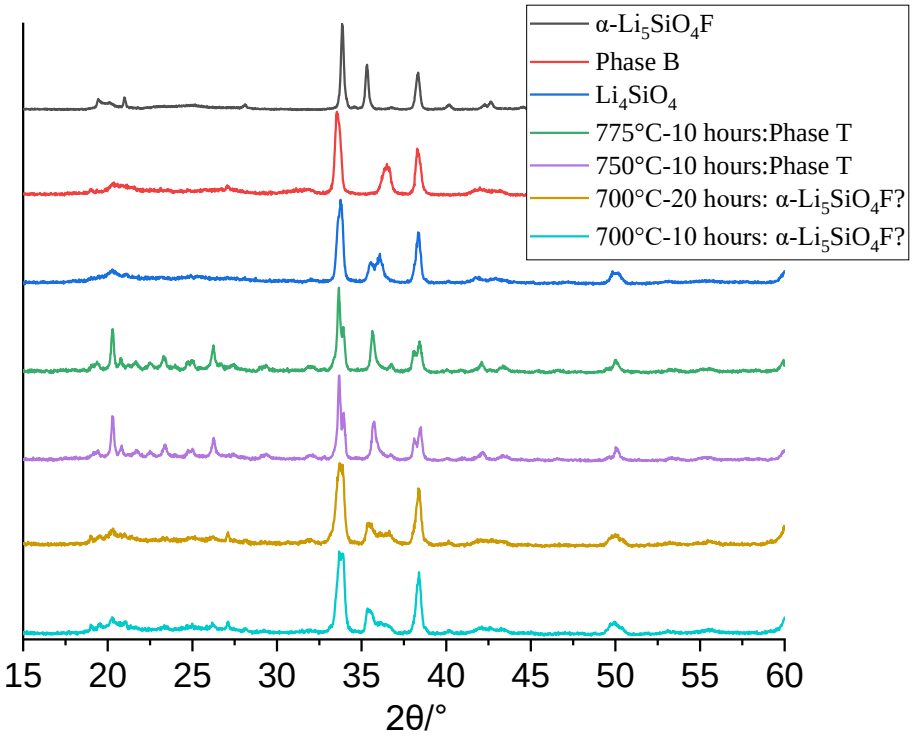

Fig 5.18. XRD results of Li_2O:SiO_2:LiF=48.5:26.5:25 (composition 19) at different temperatures, showing: α-Li_5SiO_4F+probably Phase B at 700°C; Phase T at 750-775°C.

Composition 19, Fig 5.18, shows a low-crystallinity mixture of α-Li_5SiO_4F and Phase B at 700 °C; pure-phase Phase T at 750-775°C. In specific, at 700 °C, the broad peak at ~ 35-37°2θ is likely to be overlapped (0 0 2) peaks in both Phase B and α-Li_5SiO_4F. So far, compositions between Phase B (composition 17) and Li_5SiO_4F do not show any other thermodynamically

stable phase besides the two low-temperature polymorphs: α-Li_5SiO_4F and Phase B at 700°C-750°.

5.2.1.3.2. Possible α-Li_5SiO_4F solid solution

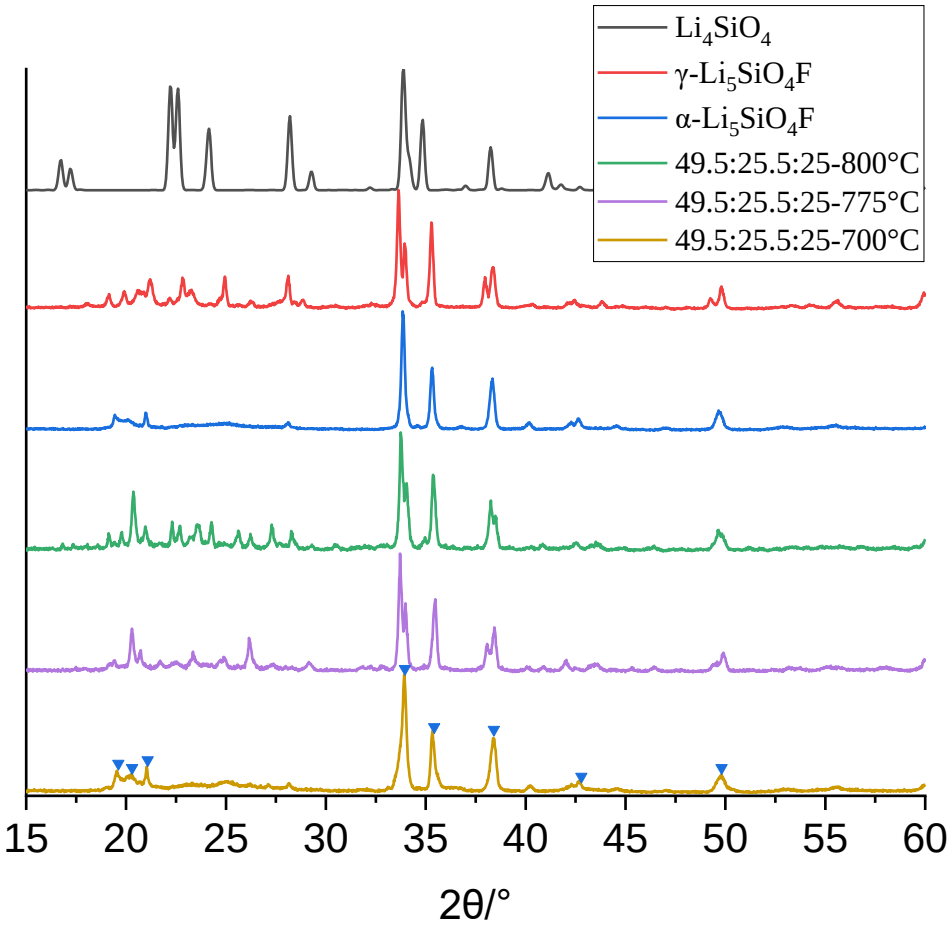

Fig 5.19. Composition 24 synthesised at different temperatures. An α-Li_5SiO_4F solid solution shows at 700°C; while Phase T shows at 775°C.

Previous study on Li_5SiO_4F suggested specific composition, Li_2O:SiO_2:LiF=2:1:1, to form α-Li_5SiO_4F [5], however, this study may suggest a α-Li_5SiO_4F solid solution. In specific, in Chapter 3, the synthesis of Li_5SiO_4F, either α- or γ-, with flexible ratio between Li_4SiO_4 and LiF as starting material do not show any solid solution of Li_5SiO_4F formed on Li_4SiO_4-LiF join. However, composition 24, shows α- Li_5SiO_4F at 700 °C but Phase T at 775 °C, Fig 5.19. It indicates that α-Li_5SiO_4F can has a narrow solid solution region with varied Li:Si ratio and

steady F content at ~700 °C. There is no evidence of the solid solution of the high-temperature polymorph, γ-Li_5SiO_4F.

5.2.1.3.3. Indexing attempt on Phase T

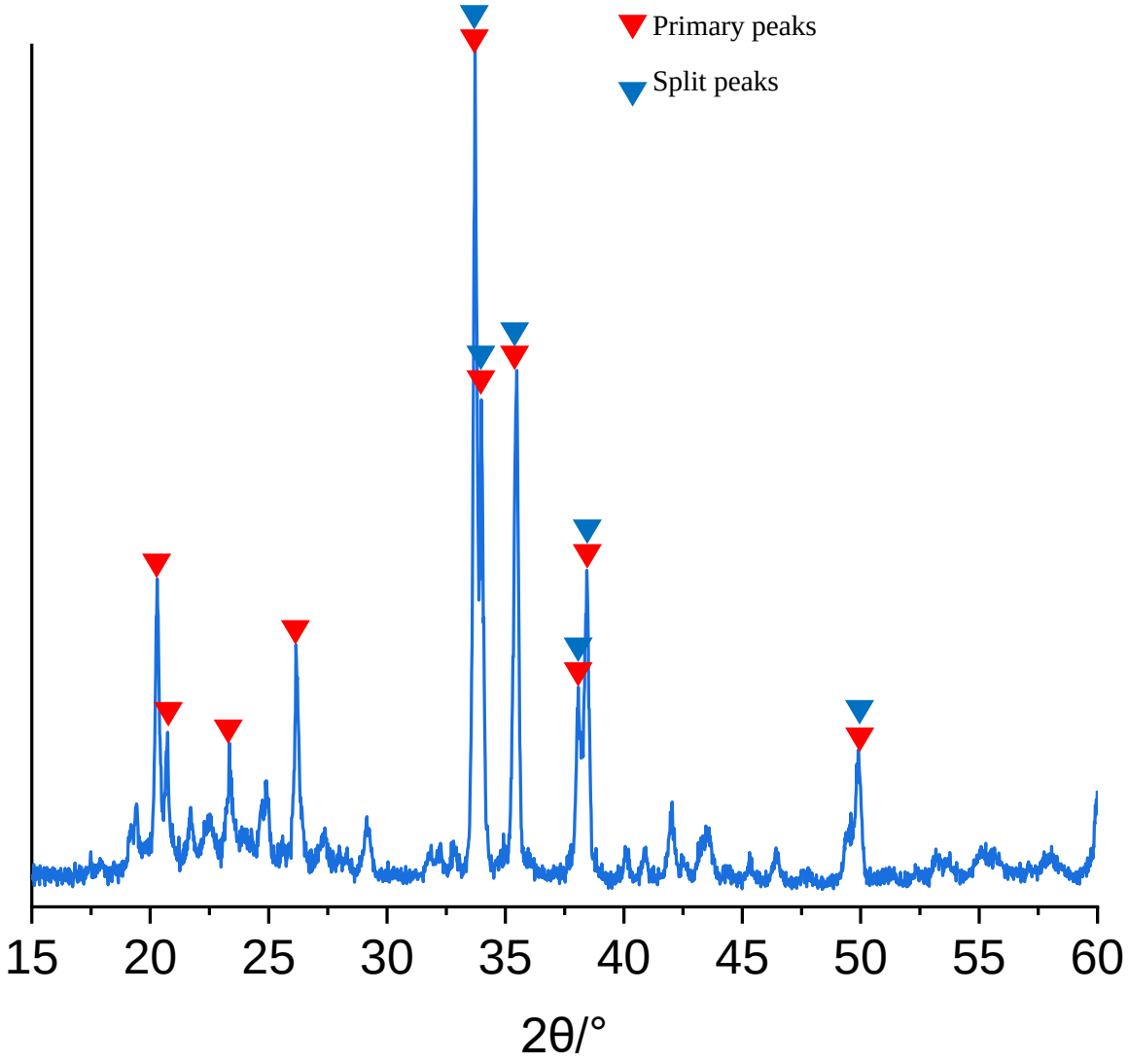

Fig 5.20. Peaks in Phase T selected for indexing.

Table 5.9. (a) Indexed results with split peaks in Phase T, (b) compared to γ-Phase B and γ-Li_5SiO_4F

(a)

h	**k**	**l**	**2θ-obs**	**2θ-cal**	**2θ-dif**
0	0	1	33.670	33.670	0.000
0	1	0	33.935	33.916	-0.019
2	0	0	35.709	35.704	-0.005
1	0	-1	38.181	38.181	0.000
1	1	0	38.456	38.477	0.021
2	1	0	50.085	50.067	-0.018
Monoclinic: *a*=2.641 (2) Å, *b*=5.026(4), *c*=2.660(2) Å, γ=90.3(1), V=35.30 Å^3					

(b)

Indexed subcell	Type	a (Å)	b (Å)	c (Å)	B (°)	V (Å^3)
γ-Li_5SiO_4F	monoclinic	3.078(2)	5.260(3)	5.067(4)	90.69(9)°	82.04
γ-Phase B	orthorhombic	3.0539(9)	5.309(3)	4.881(2)	90	80.83
Phase T	monoclinic	2.641 (2)	2.660(2)	5.026(4)	90.3(1)	35.30

The initial trial to determine the potential subcell in Phase T use two groups of peaks in Phase T, Fig 5.20, for indexing. The split peaks (marked by blue triangles) in Phase T can be indexed in a monoclinic subcell, Table 5.9. It shows the subcell of Phase T is similar to those in γ-Phase B and γ-Li_5SiO_4F, but half value of the *b*-axis, (b).

Table 5.10. Index results for Phase T with primary peaks

(a)

2θ observed	**2θ indexed**	**2θ dif**	**h**	**k**	**l**
20.302	20.351	-0.049	2	1	1
20.719	20.670	0.049	0	2	1
23.368	23.314	0.054	3	0	0
26.180	26.178	0.002	2	1	2
33.741	33.722	0.019	0	3	2
34.005	34.050	-0.045	0	2	3
	34.033	-0.028	4	1	1
35.485	35.529	-0.044	3	2	2
38.100	38.095	0.005	1	4	0
38.471	38.494	-0.023	0	4	1
49.948	49.942	0.006	1	1	5
Orthorhombic system: *a*=11.44 (2) Å, *b*=9.649 (7) Å, *c*= 9.416(8) Å, V=1039.13 Å^3					

(b)

2θ observed	**2θ indexed**	**2θ dif**	**h**	**k**	**l**
20.302	20.300	0.002	2	0	1
20.719	20.703	0.016	0	1	-1
	20.742	-0.023	0	2	0
23.368	23.365	0.003	1	2	0
26.180	26.216	-0.036	1	2	-1
33.741	33.738	0.003	2	1	-2
34.005	33.995	0.010	3	1	0
35.485	35.448	0.037	3	2	-1
38.100	38.128	-0.028	4	0	-1
38.471	38.466	0.005	2	2	-2
49.948	49.966	-0.018	5	1	-1
Monoclinic system: *a*=9.454 (6) Å, *b*=8.558 (9) Å, *c*= 5.636(5) Å, β=118.5(1)°, V=400.72 Å^3					

The indexed results with more peaks, as marked by red triangles in Fig 5.20, show either (1) an orthorhombic lattice with *a*=11.44 (2) Å, *b*=9.649 (7) Å, *c*= 9.416(8) Å, V=1039.13 Å^3, in Table 5.10 (a); or (2) a smaller monoclinic lattice with *a*=9.454 (6) Å, *b*=8.558 (9) Å, *c*= 5.636(5) Å, β=118.5(1) °, V=400.72 Å^3, in Table 5.10 (b). There is no clear multiplicity shown between the possible monoclinic subcell and these possible supercell structures.

5.2.1.4. Phase N

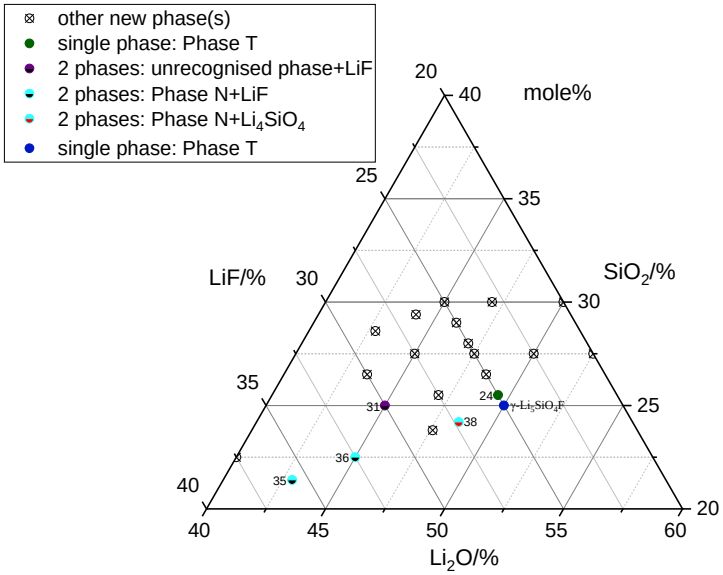

Fig 5.21. Phase N in the Li_2O-SiO_2-LiF system at 775 °C.

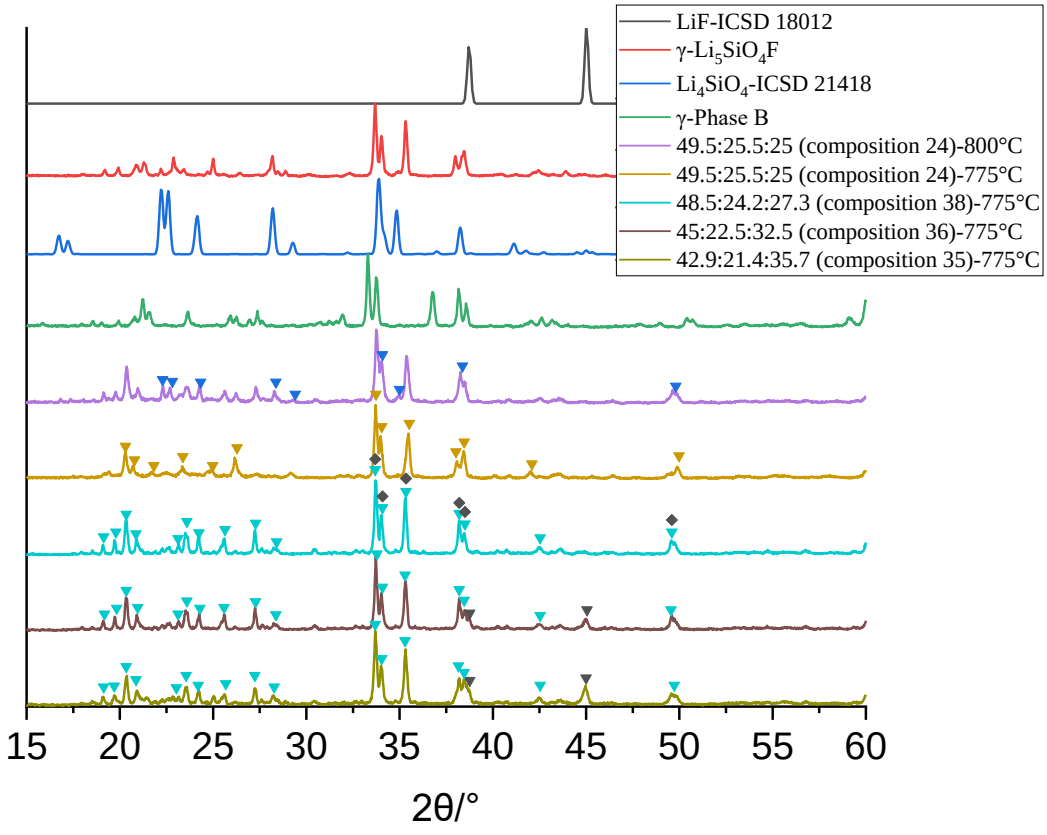

Fig 5.22. XRD results of Phase N related compositions.

Some compositions between Li_5SiO_4F and LiF synthesised at 775 °C show another possible new phase, labelled as Phase N, Fig 5.21. The main difference between Phase T (24, yellow triangles) and Phase N (35, 36 and 38, light blue triangles) is the different intensity ratio between the pair peaks at ~38°2θ, and ~38.5°2θ, Fig 5.22. The main difference between Phase N and γ-Li_5SiO_4F is the peaks at low 2θ angles, ~17-30°2θ.

Table 5.11. Indexed results with split peaks in Phase N

h	k	l	2θ-obs	2θ-cal	2θ-dif	d-obs	d-cal	d-dif
1	0	0	33.751	33.747	-0.004	2.65356	2.65380	0.00024
0	0	1	34.052	34.045	-0.007	2.63078	2.63126	0.00048
0	2	0	35.337	35.335	-0.002	2.53798	2.53815	0.00017
1	1	0	38.235	38.238	0.003	2.35202	2.35181	-0.00021
0	1	1	38.499	38.506	0.007	2.33650	2.33608	-0.00042
1	0	1	49.638	49.638	0	1.83514	1.83514	0
Monoclinic: a=2.6556 (5) Å, b=5.076(1) Å, c=2.6330(5) Å, γ=92.10(2), V=35.47 Å^3								

Preliminary attempt to index the subcell of Phase N used the peaks marked by black diamonds in Fig 5.22, with results shown in Table 5.11. The possible monoclinic subcell of Phase N is almost same to the monoclinic subcell of Phase T, in Table 5.9, indicating same basic 'block cell' to establish different supercell structures.

5.2.2. Impedance analysis of three new phases: Phase B, γ-Phase B, and Phase T and Arrhenius plot

5.2.2.1. Phase B

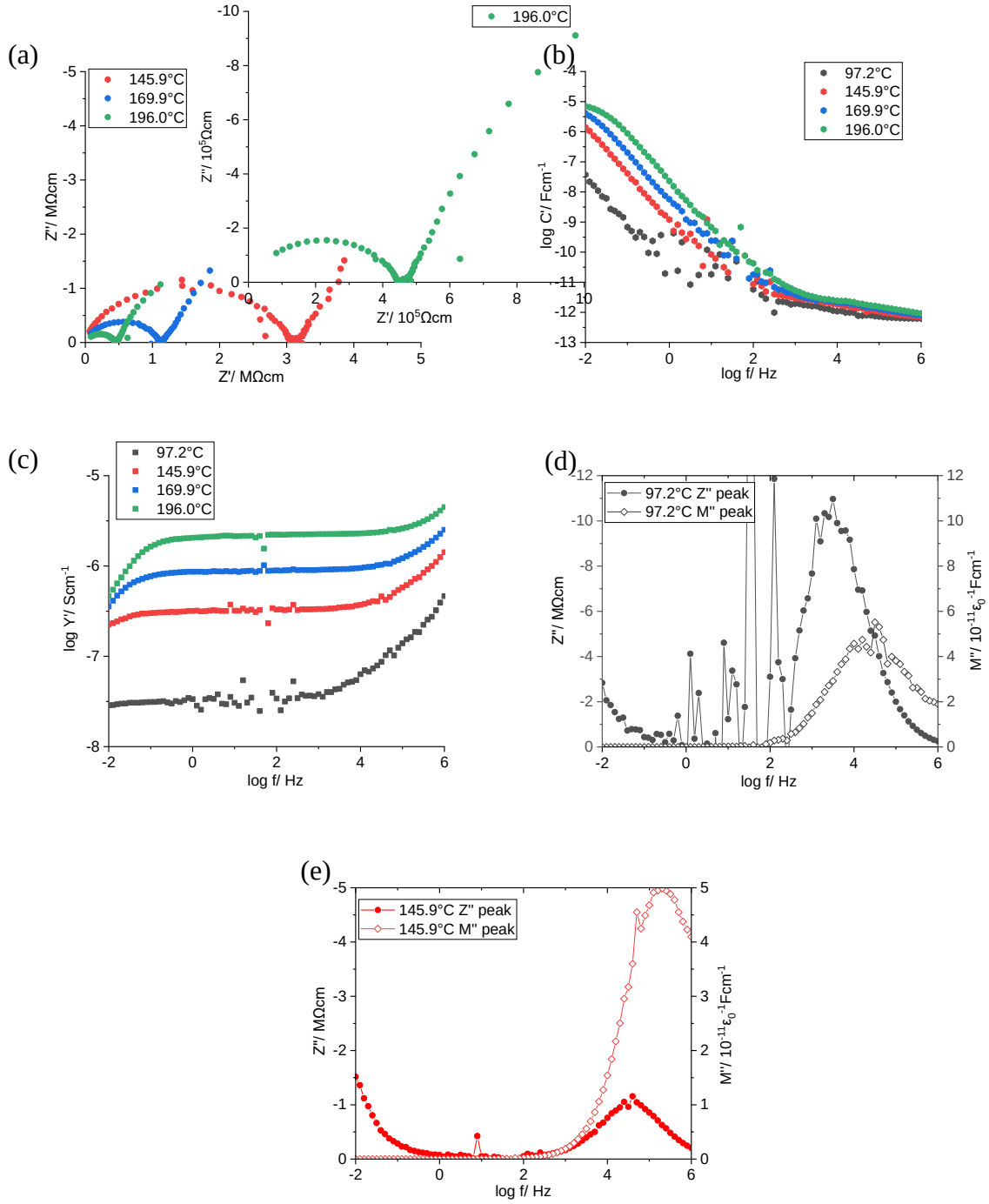

Fig 5.23. Impedance dataset for composition Li_2O:SiO_2:LiF=47:28:25

(Synthesised at 750 °C, 10 hours, coated with Au, primary phase of Phase B)

(a) $Z^{''}$-$Z^{'}$ complex plane plot, spectroscopic plots of (b) capacitance C', (c) admittance Y', (d) $Z^{''}M^{''}$ at 97.2 °C, and (e) $Z^{''}M^{''}$ at 145.9 °C

Pellet with composition 17, the stoichiometric composition of Phase B, was prepared by cold press and sintered at 750°C for 10 h, coated with Au electrodes and reheated at 750°C for 6 h.

Some impedance datasets for Phase B are shown in four different complementary formats in Fig 5.23. The impedance complex plane plot in (a) consists of squashed semicircles and a large spike with a total resistance of 4.42×10^5 Ω cm at 196.0 °C. The spike in (a) and the high values of the low frequency capacitance of ~10^{-6} F/cm in (b) are indications of a significant sample-electrode capacitance and therefore, of ionic conduction in the sample. Spectroscopic plots of $C^{'}$ in (b) show 2 clear plateaux at ~10^{-6}-10^{-5} F/cm and ~10^{-12} F/cm. The possible intermediate plateau at ~5×10^{-11} F/cm should not be considered as a grain boundary capacitance as the typical value of grain boundary capacitance is 2-3 orders of magnitude higher than that of bulk capacitance. From the high frequency bulk capacitance, ~10^{-12} F/cm, the bulk permittivity of the sample, given by $\varepsilon' = C/e_0$, is 11.3. The log $Y^{'}$-log f plot in (c) shows a distorted total conductivity plateau over the range ~10^0-10^4 Hz with additional significant dispersions at both low and high frequency ends. The sample-electrode interface is responsible for the low frequency dispersion, while the high frequency dispersion can be attributed to Jonscher Law behaviour. The high frequency $Z^{''}$ peak and $M^{''}$ peak in (d-e) are nearly coincident on the frequency scale, thus the high frequency semi-circle in (a) and the high frequency capacitance plateau at ~10^{-12} F/cm in (b) can be attributed to the bulk response. The sample may be not well sintered because the full width at half maximum of the $M^{''}$ peaks are roughly 2 orders of magnitude on frequency scale, which is higher than the typical value of 1.13. As the sample is pressed into pellet with loose powder covered before the synthesis at 750 °C, the possible reason for that is the relevantly low temperature but limited by the phase transition from Phase B to γ-Phase B at 750-775 °C.

5.2.2.2. γ-Phase B

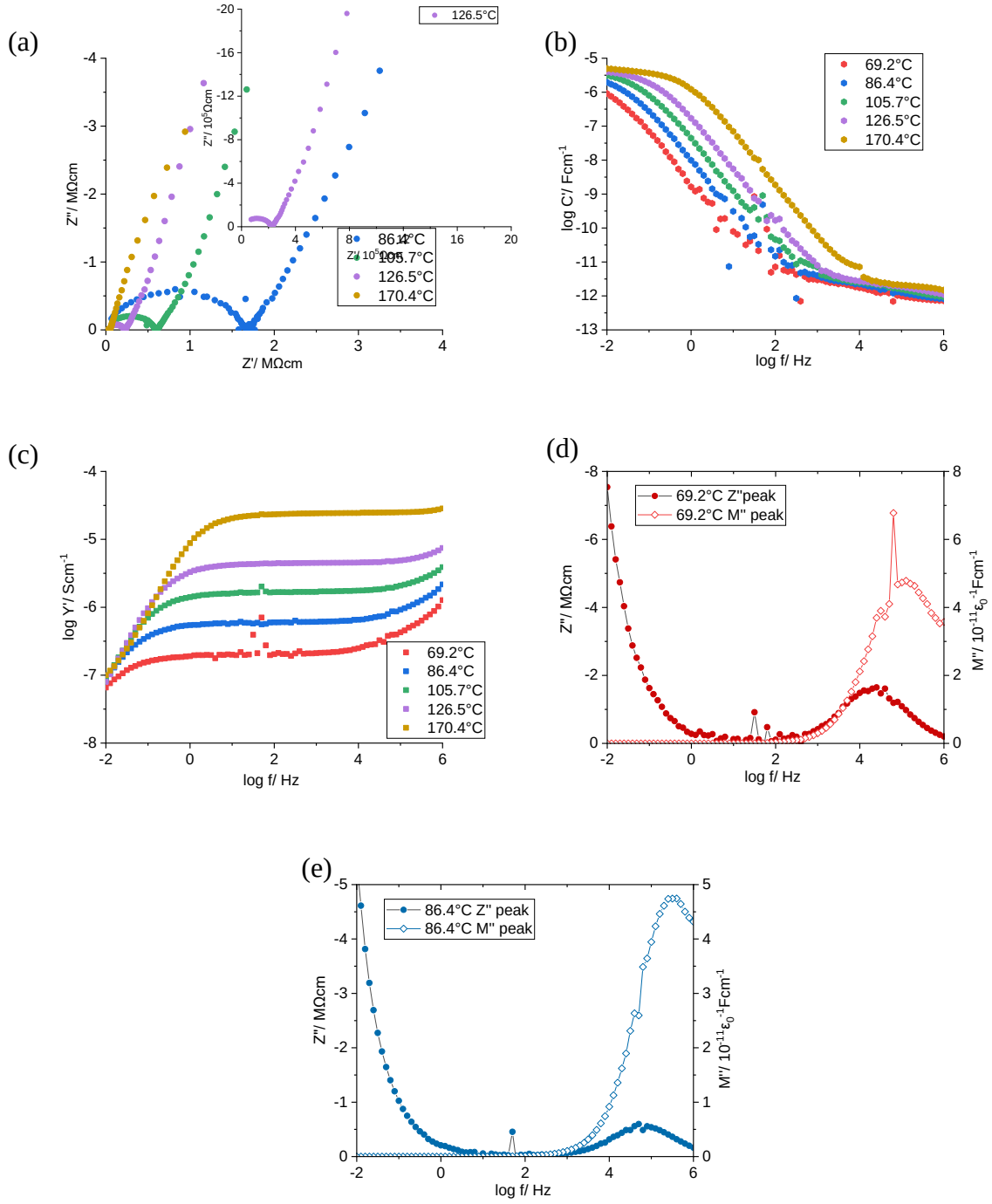

Fig 5.24. Impedance dataset for composition Li_2O:SiO_2:LiF=47:28:25

(Synthesised at 775 °C, 10 hours, coated with Au, primary phase of γ-Phase B)

(a) Z''-Z' complex plane plot, spectroscopic plots of (b) capacitance C', (c) admittance Y', (d) Z''M'' at 69.2 °C, and (e) Z''M'' at 86.4 °C

Impedance datasets for sample composition 17 prepared at 775 °C, with main phase of γ-Phase B, Fig 5.24, show similar ionic conductor response to Phase B, Fig 5.23. The pellets of Phase B and γ-Phase B were also prepared by hot press, with similar impedance datasets shown in Figs 5.S3-S4.

5.2.2.3. Arrhenius plot for Phase B and γ-Phase B, with equivalent circuit.

Table 5.12. Pellets density for Phase B and γ-phase B prepared by either cold press or hot press.

Sample	Density/ gcm^{-3}
Phase B-composition 17-cold pressed	1.62
Phase B-composition 17-hot pressed	1.66
γ-Phase B-composition 17-cold pressed	1.81
γ-Phase B-composition 17-hot pressed	1.99

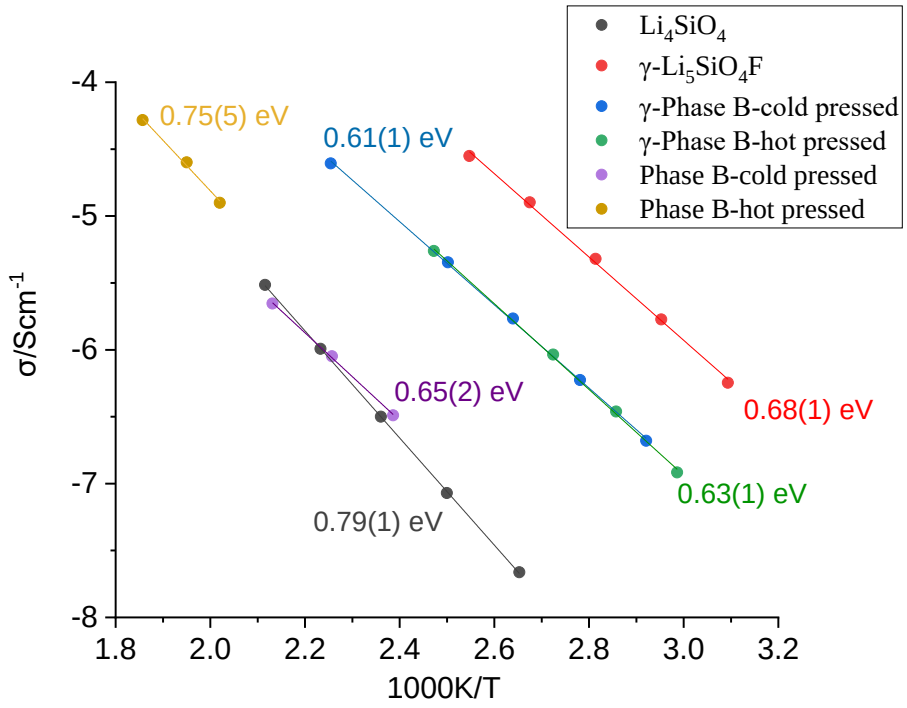

Fig 5.25. Arrhenius plot for phase B and γ-phase B prepared by either cold press or hot press.

The Arrhenius plot in Fig 5.25 clearly shows that there is barely no difference in the impedance responses of samples prepared by either cold press or hot press. However, pellets prepared by hot press do have a slight increased density, with a comparison shown in Table 5.12.

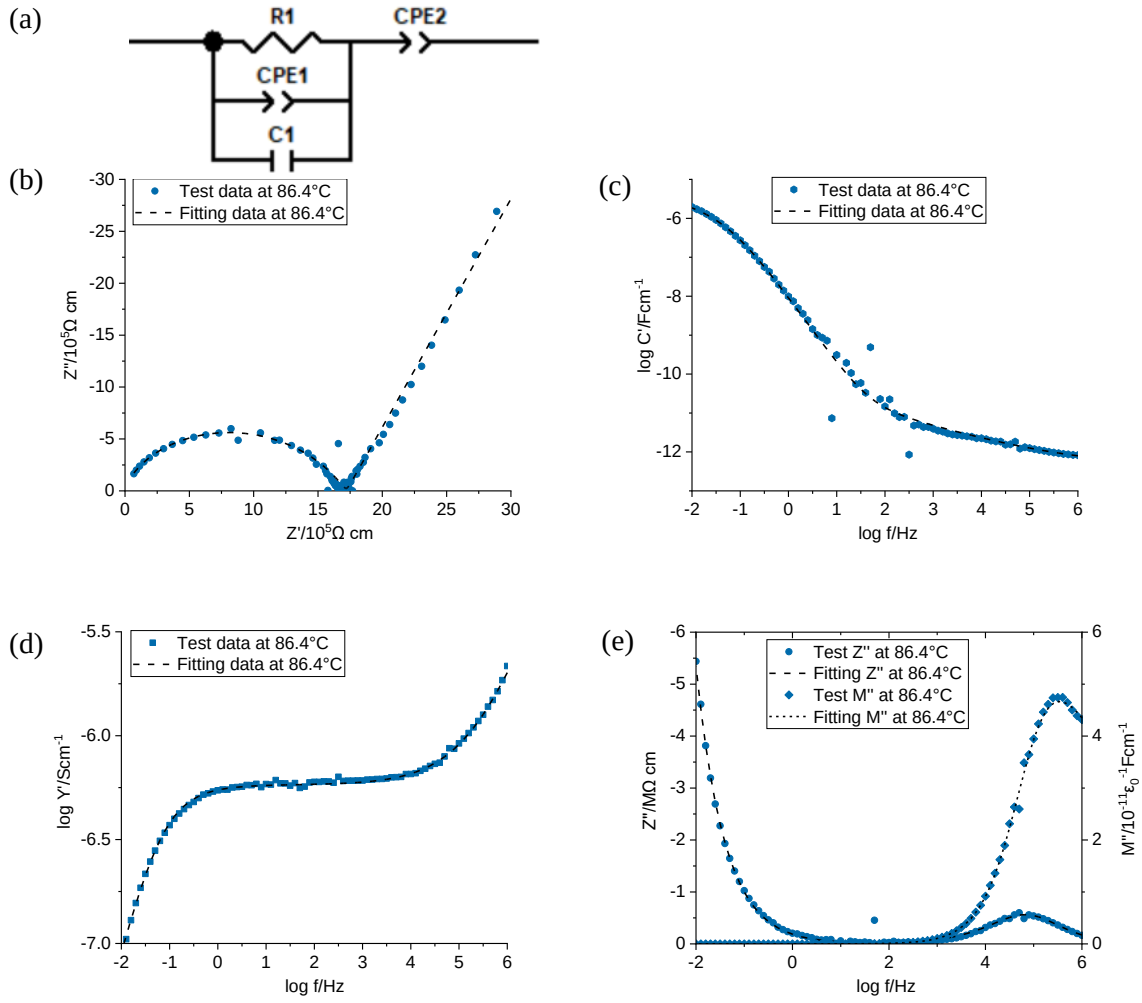

Fig 5.26. Equivalent circuit fitted to the impedance data at 86.4 °C.

Since the impedance data indicate possible overlapping components in bulk response, an equivalent circuit, Fig 5.26 (a) was used to fit the results at 86.4 °C in Fig 5.24. The equivalent circuit consists of two elements in series: R_1, C_1 and CPE_1 in parallel, which is the standard circuit used to fit bulk data of ionic conductors, and CPE_2 to fit the sample-electrode response. Exclude several 'bad points' on log frequency range of 4.5-4.8 Hz, the circuit fit the results at 86.4°C well. The fitted bulk C_b=4.38×10^{-13} F/cm, while the bulk R_b=1.72×10^6 Ω. Similar fitting results for the bulk/overall response at 69.2°C and at 105.7°C are respectively shown in Figs

5.S5-S6 and Figs 5.S7-S8. The parameters in equivalent circuit fitting are summarised in Table 5.S2.

5.2.2.4. Phase T

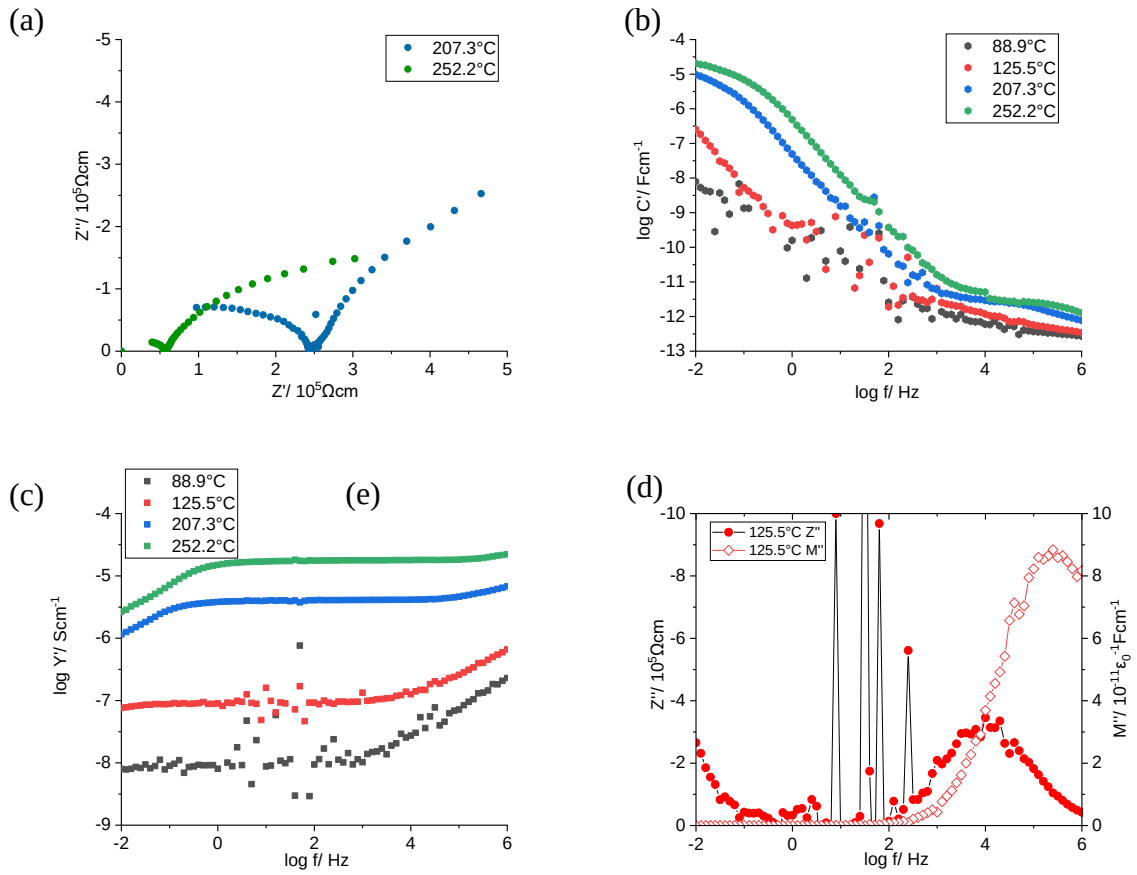

Fig 5.27. Impedance dataset for composition Li_2O:SiO_2:LiF=48.5:26.5:25 (19)

(Synthesised at 775°C, 10 hours, coated with Au, primary phase of Phase T)

(a) $Z^{''}$-$Z^{'}$ complex plane plot, spectroscopic plots of (b) capacitance C', (c) admittance Y', (d) $Z^{''}M^{''}$ at 125.5°C

Impedance datasets for composition 19, with main phase of Phase T, Fig 5.27, show a squashed semicircles with a total resistance of ~2.5×10^5 Ω cm at 207.3 °C, followed by a quite curved spike in (a). The low frequency sample-electrode capacitance at ~10^{-6}-10^{-5} F/cm in (b) and the spike in (a) indicates the ionic conductivity of the sample. $C^{'}$ plot, (b), show 2 clear plateaux at ~10^{-6}-10^{-5} F/cm and ~10^{-12} F/cm, which are sample-electrode capacitance and bulk capacitance,

respectively. There is another intermediate plateau at ~5×10^{-11} F/cm, which should not be regarded as the grain boundary capacitance, which is commonly ~2 orders of magnitude higher than bulk capacitance. Admittance plot, (c), shows a distorted total conductivity plateau over the range ~10^0-10^4 Hz with significant dispersions at both low and high frequency ends at high temperatures. The high frequency Z'' peak and M'' peak, (d), are not well overlapped on frequency scale, which may indicate an electrically inhomogeneous sample.

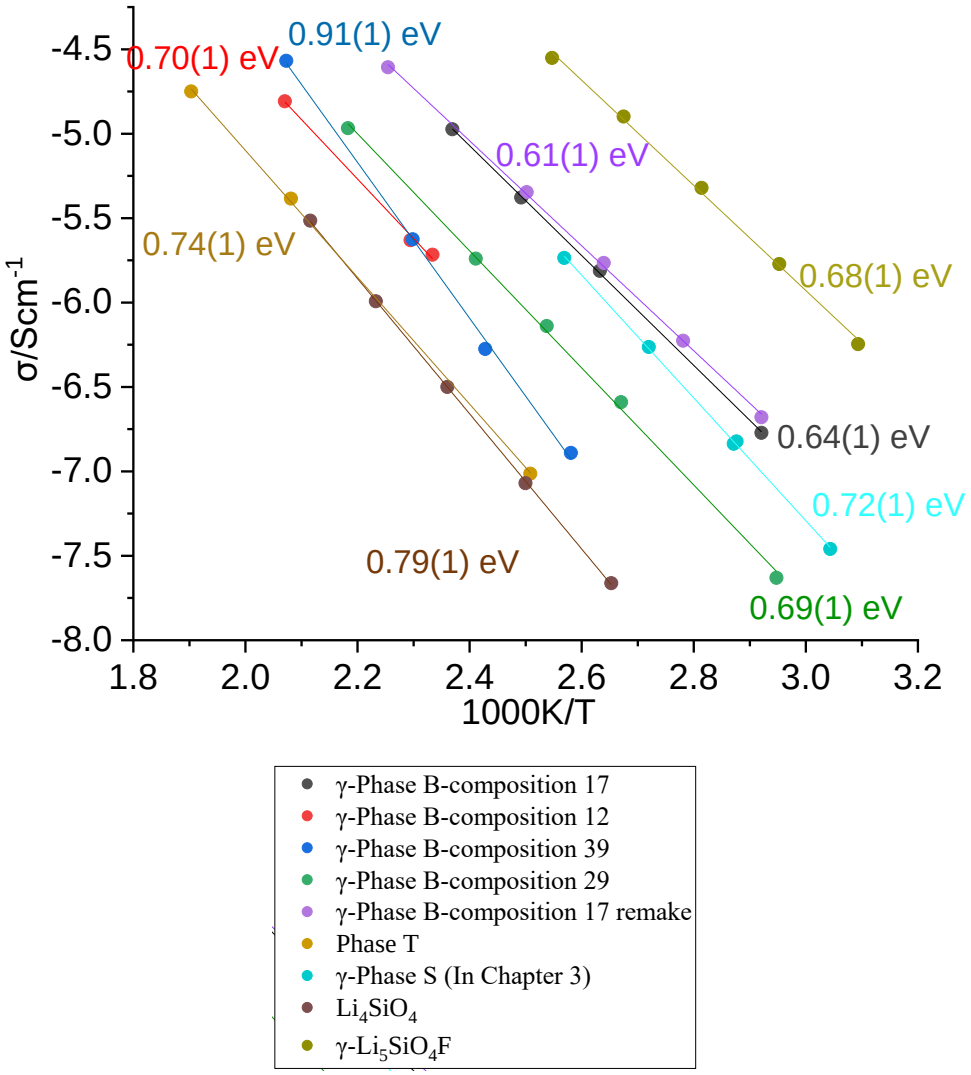

Fig 5.28. Arrhenius plot for new phase B, T, and other phases in Li_2O-SiO_2-LiF system

The ionic conductivity and activation energy of some important compositions are summarised in the Arrhenius plot, Fig 5.28. Three compositions 12, 17 and 39 show γ-phase B solid solution

with high crystallinity. Composition 17 has a higher fluorine content than compositions 12 and 39. Composition 17 is also the only composition give pure Phase B at 750 °C. Composition 17 has the highest ionic conductivity with ~5×10^{-5} Ωcm^{-1} at 100°C, which is ~1 orders of magnitude higher than those of other γ-Phase B solid solution compositions. γ-Phase B has an average ionic conductivity that ~2 orders of magnitude higher than that of Li_4SiO_4. However, the ionic conductivity of γ-Phase B is ~1 orders of magnitude lower than that of γ-Li_5SiO_4F, discovered by Dong [5]. Composition 17 also show a lowest activation energy with ~0.61 eV compared to other solid solution compositions. The activation energy of γ-Phase B is similar to that of γ-Li_5SiO_4F with either 0.68(1) eV as tested, or 0.57 eV as reported. Composition 29 with a low crystallinity γ-Phase B solid solution has an ionic conductivity several times lower than that of composition 17. Phase T only show a poor ionic conductivity similar to that of Li_4SiO_4.

References

[1] I. M. Hodge, M. Ingram, and A.R. West, "Ionic conductivity of Li_4SiO_4, Li_4GeO_4, and their solid solutions," *Journal of the American Ceramic Society*, vol. 59, no. 7-8, pp. 360–366, 1976.

[2] A. Khorassani and A.R. West, "New Li+ Ion Conductors in the system Li_4SiO_4–Li_3AsO_4," *Solid State Ionics*, vol. 7, no. 1, pp. 1–8, 1982.

[3] M. Dissanayake and A. R. West, "Structure and conductivity of an Li_4SiO_4–Li_2SO_4 solid solution phase," *J. Mater. Chem*, vol. 1, no. 6, pp. 1023–1025, 1991

[4] "Database of ionic radii," Shannon Radii. [Online]. Available: http://abulafia.mt.ic.ac.uk/shannon/ptable.php. [Accessed: 07-Dec-2022].

[5] B. Dong, J. Yan, B. Walkley, K. K. Inglis, F. Blanc, S. Hull, and A. R. West, "Synthesis and characterisation of the new oxyfluoride Li^+ ion conductor, Li_5SiO_4F," *Solid State Ionics*, vol. 327, pp. 64–70, 2018.

[6] B. Konar, M. Van Ende, and I. Jung, "Critical evaluation and thermodynamic optimization of the Li-O, and Li_2O-SiO_2 systems," *Journal of the European Ceramic Society*, vol. 37, no. 5, pp. 2189–2207, 2017.

[7] C. Mühle and M. Jansen, "Zur Löslichkeit von Cobalt(IV) in Li_8SiO_6," *Zeitschrift für anorganische und allgemeine Chemie*, vol. 634, no. 1, pp. 37–38, 2008.

[8] F. Durán-Muñoz, I. C. Romero-Ibarra, and H. Pfeiffer, "Analysis of the CO_2 chemisorption reaction mechanism in lithium oxosilicate (Li_8SiO_6): a new option for high-temperature CO_2 capture," *Journal of Materials Chemistry A*, vol. 1, no. 12, p. 3919, 2013.

[9] A. R. West, "Lithium ion conductors," in *Solid state chemistry and its applications, Chichester*, UK: John Wiley & Sons, 1990, pp. 193-194.

[10] X. Yan, Y. Li, X. Ma, J. Zhao, and Z. Wang, "Performance of Li_4SiO_4 Material for CO_2 Capture: A Review," *International Journal of Molecular Sciences*, vol. 20, no. 4, p. 928, 2019.

[11] Y. Gong, X. Yu, M. Yang, J. Wei, Y. Shi, Z. Huang, T. Lu, and W. Huang, "A facile approach to fabricate Li_4SiO_4 ceramic pebbles as tritium breeding materials," *Materials Letters*, vol. 159, pp. 245–248, 2015.

[12] A. R. West, "Lithium battery," in *Solid state chemistry and its applications, Chichester*, UK: John Wiley & Sons, 1990, pp. 418-420.

[13] A. D. Robertson, A. R. West, and A. G. Ritchie, "Review of crystalline lithium-ion conductors suitable for high temperature battery applications," *Solid State Ionics*, vol. 104, no. 1-2, pp. 1–11, 1997.

[14] B. L. Dubey and A. R. West, "Crystal Chemistry of Li_4XO_4 phases: X = Si, Ge, Ti," *Journal of Inorganic and Nuclear Chemistry*, vol. 35, no. 11, pp. 3713–3717, 1973.

[15] S. Adnan and N. S. Mohamed, "Effects of Sn substitution on the properties of Li_4SiO_4 ceramic electrolyte," *Solid State Ionics*, vol. 262, pp. 559–562, 2014.

[16] A. Khorassani and A. R. West, "Li^+ ion conductivity in the system Li_4SiO_4-Li_3VO_4," *Journal of Solid State Chemistry*, vol. 53, no. 3, pp. 369–375, 1984.

[17] Y. Saito, "Ionic conductivity of Li^+ ion conductors, $Li_{4.2}M_xSi_{1-x}O_4$ (M: B^{3+}, Al^{3+}, Ga^{3+}, Cr^{3+}, Fe^{3+}, Co^{2+}, Ni^{2+})," *Solid State Ionics*, vol. 40-41, pp. 34–37, 1990.

[18] N. T. Han, V. K. Dien, N. T. Thuy Tran, D. K. Nguyen, W.-P. Su, and M.-F. Lin, "First-principles studies of electronic properties in lithium metasilicate (Li_2SiO_3)," RSC Advances, vol. 10, no. 41, pp. 24721–24729, 2020.

[19] K. Gao, S.-X. Zhao, S.-T. Guo, and C.-W. Nan, "Improving rate capacity and cycling performance of lithium-rich high-mn $Li_{1.8}[Mn_{0.7}Co_{0.15}Ni_{0.15}]O_{2.675}$ cathode materials by Li_2SiO_3 coating," *Electrochimica Acta*, vol. 206, pp. 1–9, 2016.

[20] Y. Xiao, G. Wang, S. Zhou, Y. Sun, Q. Zhao, Y. Gong, T. Lu, C. Luo, and K. Yan, "Enhanced electrochemical performance and decreased strain of graphite anode by Li_2SiO_3 and Li_2CO_3 co-modifying," *Electrochimica Acta*, vol. 223, pp. 8–20, 2017.

[21] H. Zhang and J. Yang, "Hollow Li_2SiO_3 architectures with tunable secondary nanostructures and their potential application for the removal of heavy metal ions," Journal of Materials Science, vol. 55, no. 9, pp. 3845–3859, 2019.

[22] S. D. Stookey, "Catalyzed crystallization of glass in theory and Practice," *Industrial & Engineering Chemistry*, vol. 51, no. 7, pp. 805–808, 1959.

[23] M. Dittmer, C. Ritzberger, W. Höland, and M. Rampf, "Controlled precipitation of lithium disilicate ($Li_2Si_2O_5$) and lithium niobate ($LiNbO_3$) or lithium tantalate ($LiTaO_3$) in glass-ceramics," *Journal of the European Ceramic Society*, vol. 38, no. 1, pp. 263–269, 2018.

[24] T. J. Headley and R. E. Loehman, "Crystallization of a glass-ceramic by epitaxial growth," *Journal of the American Ceramic Society*, vol. 67, no. 9, pp. 620–625, 1984.

[25] A. R. West, “Silicate structures ,” in *Solid state chemistry and its applications, Chichester*, UK: John Wiley & Sons, 1990, pp. 81–82.

[26] “MP-2133: ZnO (hexagonal, $P6_3mc$, 186),” Materials Project. [Online]. Available: https://materialsproject.org/materials/mp-2133. [Accessed: 07-Dec-2022].

[27] T. Ungár, “Microstructural parameters from X-ray diffraction peak broadening,” *Scripta Materialia*, vol. 51, no. 8, pp. 777–781, 2004.

[28] R. K. Biswas et al., “Study of short range structure of amorphous silica from PDF using AG radiation in laboratory XRD System, Raman and NEXAFS,” *Journal of Non-Crystalline Solids*, vol. 488, pp. 1–9, 2018. doi:10.1016/j.jnoncrysol.2018.02.037

Appendix

(a)

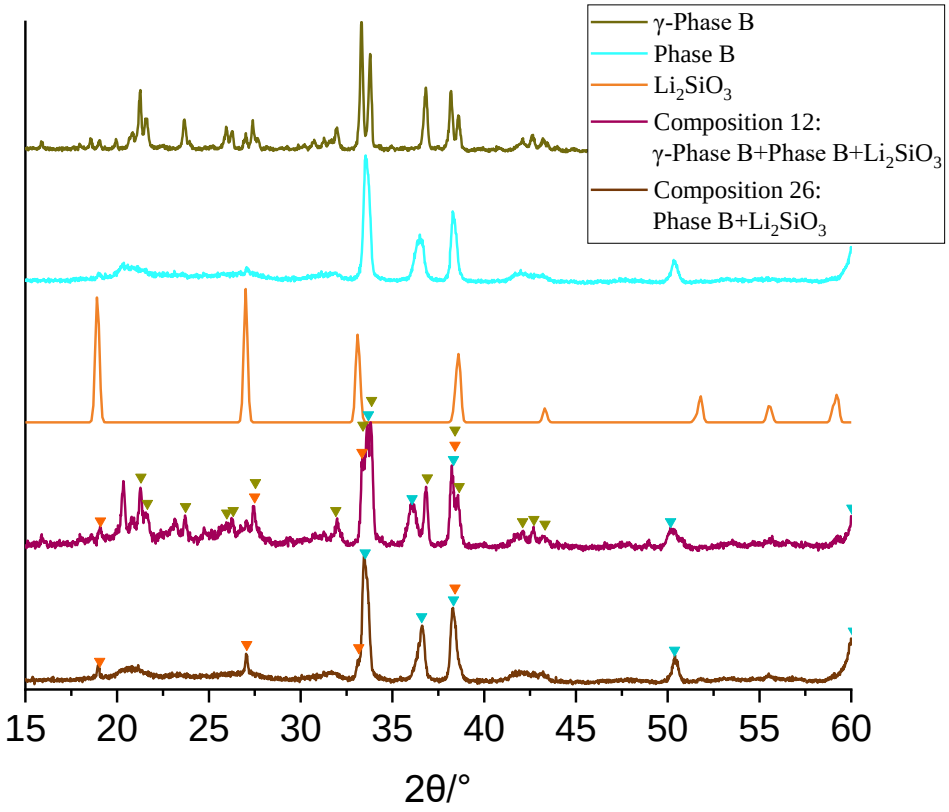
γ-Phase B
Phase B
Li2SiO3
Composition 12:
γ-Phase B+Phase B+Li2SiO3
Composition 26:
Phase B+Li2SiO3
15
20
25
30
35
40
45
50
55
60
2θ/°

(b)

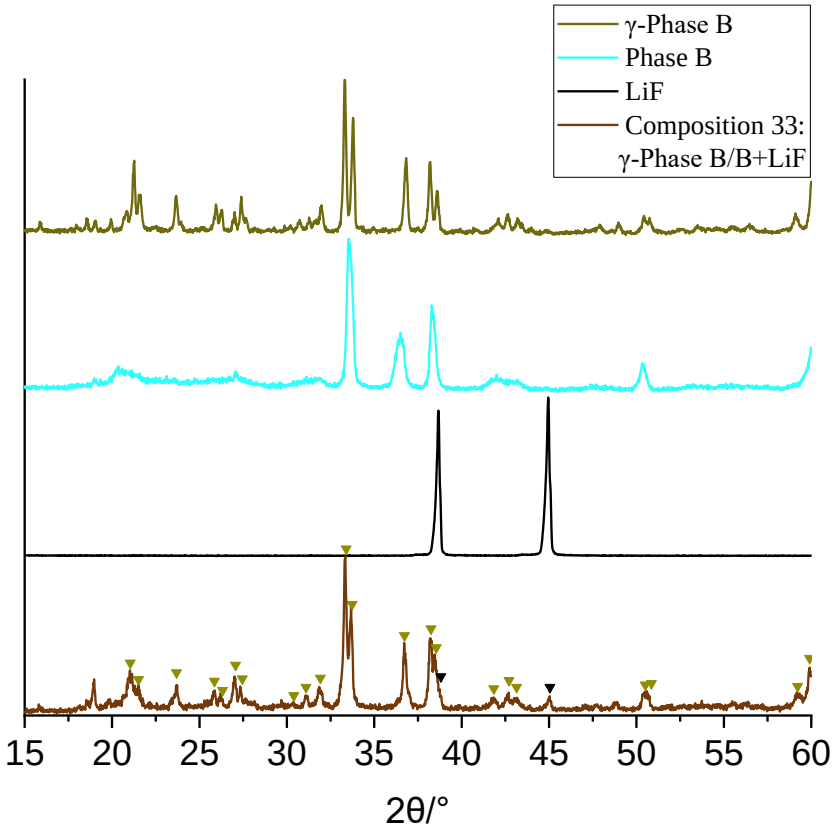
γ-Phase B
Phase B
LiF
Composition 33:
γ-Phase B/B+LiF
15
20
25
30
35
40
45
50
55
60
2θ/°

(c)

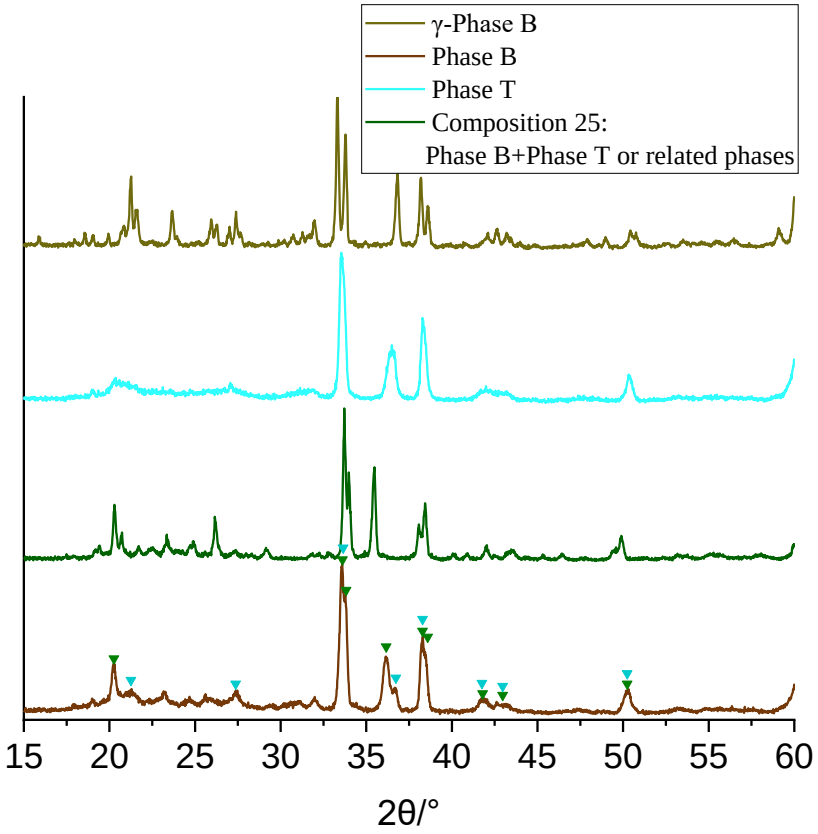
γ-Phase B
Phase B
Phase T
Composition 25:
Phase B+Phase T or related phases
15
20
25
30
35
40
45
50
55
60
2θ/°

(d)

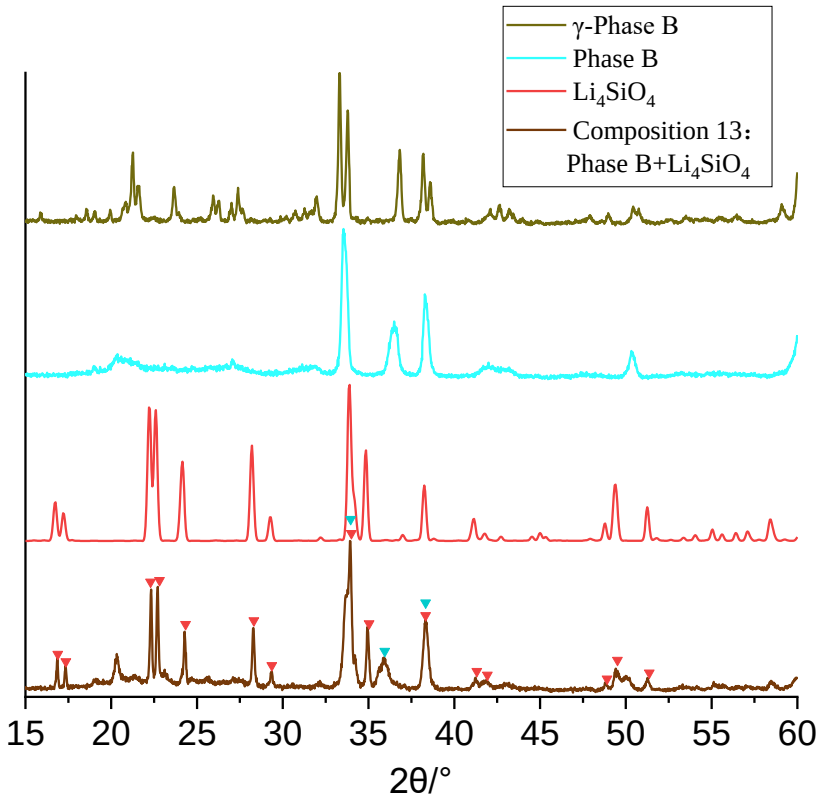
γ-Phase B
Phase B
Li4SiO4
Composition 13:
Phase B+Li4SiO4
15 20 25 30 35 40 45 50 55 60
2θ/°

(e)

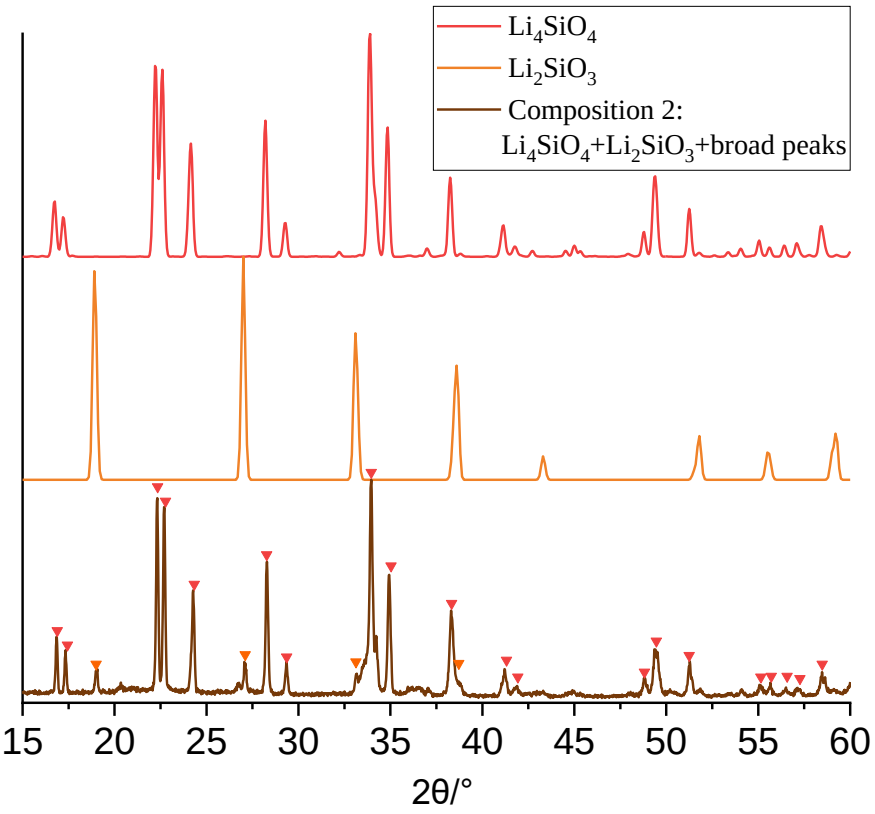
Li4SiO4
Li2SiO3
Composition 2:
Li4SiO4+Li2SiO3+broad peaks
15 20 25 30 35 40 45 50 55 60
2θ/°

(f)

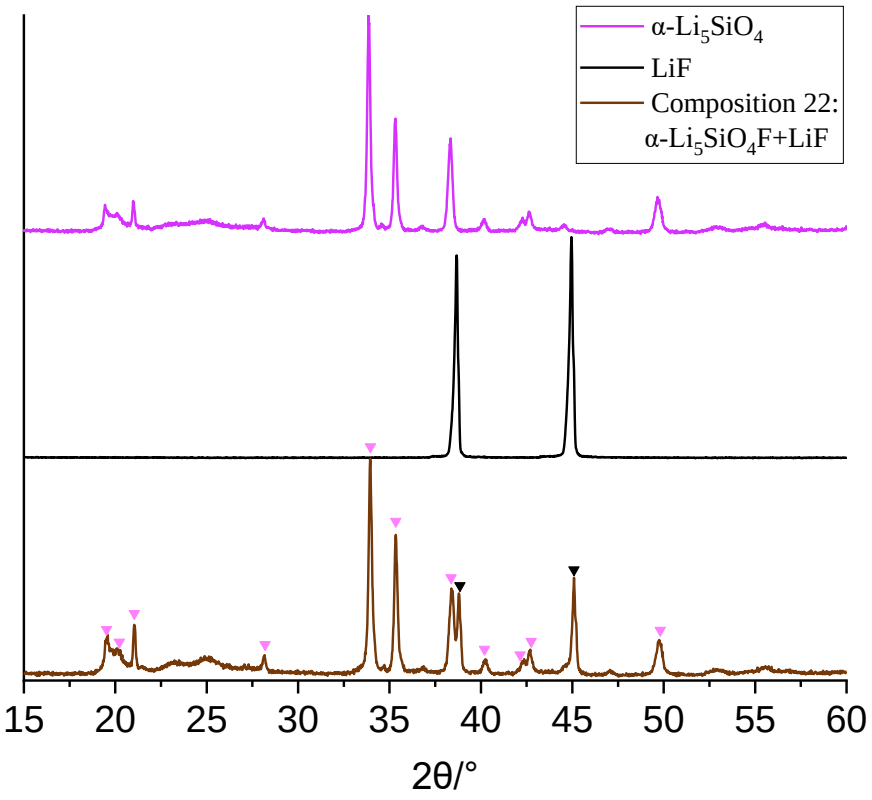
α-Li5SiO4
LiF
Composition 22:
α-Li5SiO4F+LiF
15
20
25
30
35
40
45
50
55
60
2θ/°

(g)

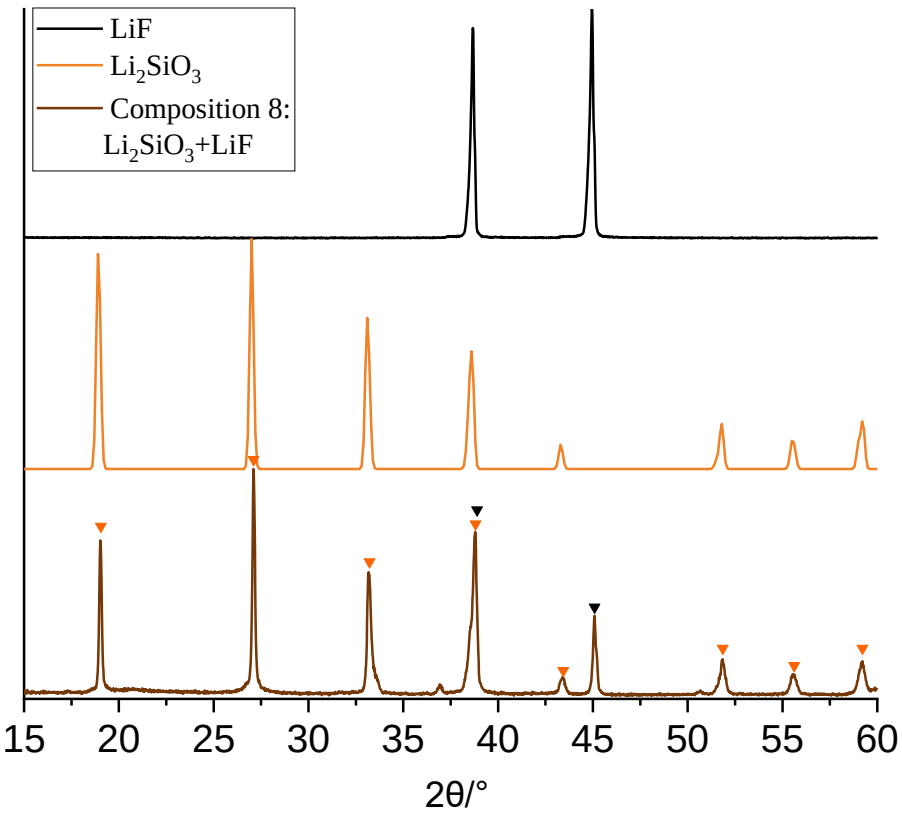
LiF
Li2SiO3
Composition 8:
Li2SiO3+LiF
15
20
25
30
35
40
45
50
55
60
2θ/°

(h)

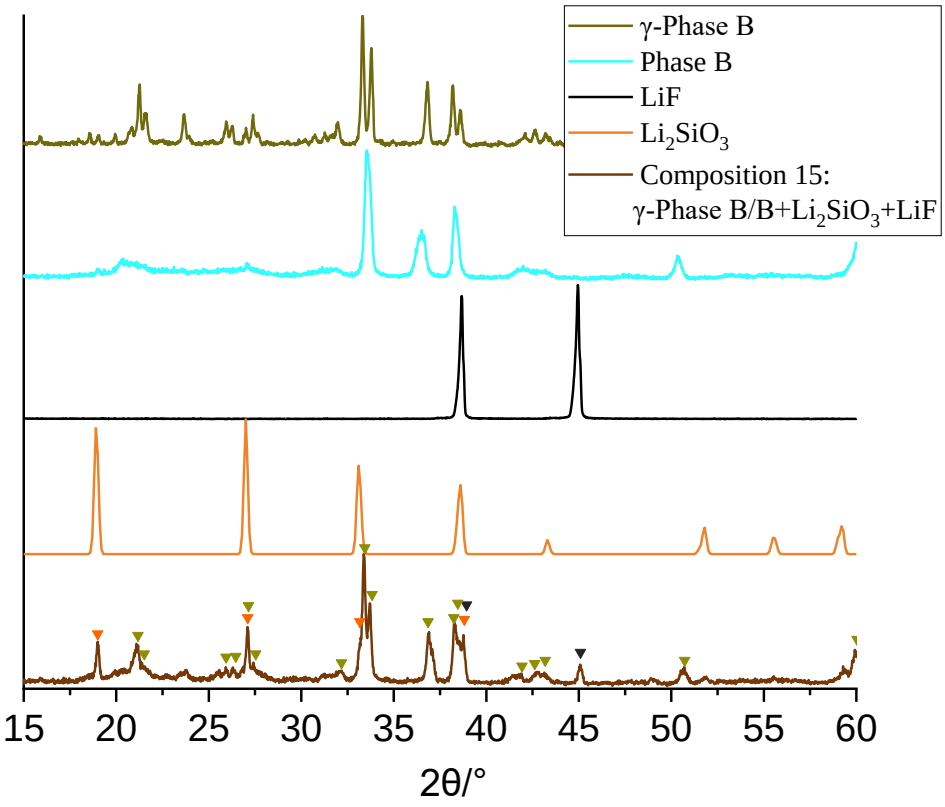

(i)

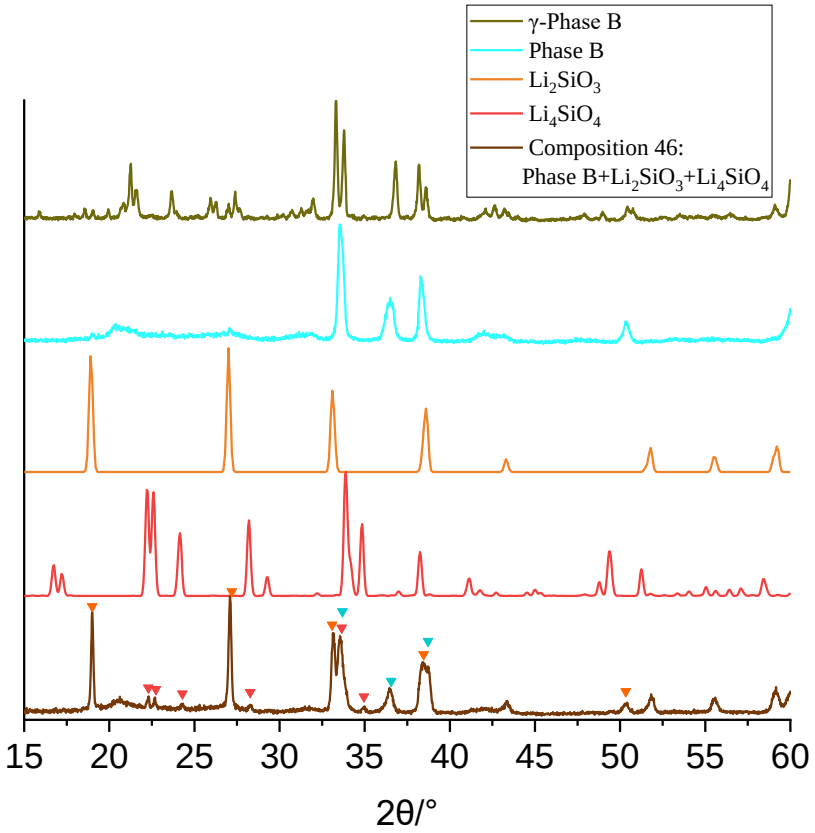

Fig 5.S1. XRD patterns for some representative compositions at 750 °:

(a) 26: Li_2SiO_3+B; 12: γ-B+B+Li_2SiO_3; (b) 33:LiF+γ-B/B

(c) 25: T+B or related phases; (d) 13: Li_4SiO_4+B

(e) 2: Li_4SiO_4+ Li_2SiO_3+broad peaks related to B; (f) 22: α-Li_5SiO_4F+LiF

(g) 8: Li_2SiO_3+LiF;

(h) 15: B/γ-B+Li_2SiO_3+LiF (i) 46: Li_2SiO_3+Li_4SiO_4+B

Table 5.S1. A summary of compositions studied, synthesis conditions and phase(s) present given by XRD.

(a)

	Compositions Li_2CO_3:SiO_2:LiF	Synthesis temperature & time	Phase(s) present
1	~63.3:33.3:3.3	750°C, 20 hours	Li_4SiO_4+Li_2SiO_3(tiny)
2	~60.3:33.3:6.3	750°C, 20 hours	Li_4SiO_4+Li_2SiO_3(tiny)
3	~56.6:33.3:10	750°C, 20 hours	Li_4SiO_4+Li_2SiO_3+(γ-)Phase B
4	~53.3:33.3:13.3	750°C, 20 hours	Li_4SiO_4+Li_2SiO_3+(γ-)Phase B
		775°C, 10 hours	Li_4SiO_4+ γ-Phase B
		775°C, 20 hours	Li_4SiO_4+ γ-Phase B
5	~50:33.3:16.7	750°C, 20 hours	(γ-)Phase B +Li_2SiO_3+Li_4SiO_4(tiny)
		775°C, 20 hours	γ-Phase B+ Li_2SiO_3
6	~46.6:33.3:20	750°C, 20 hours	Unknown peaks+Li_2SiO_3
7	~40:33.3:26.7	750°C, 10 hours	(γ-)Phase B+Li_2SiO_3+LiF
8	~33.3:33.3:33.3	750°C, 10 hours	Li_2SiO_3+LiF
9	48:36:16	650°C, 10 hours	Li_2SiO_3+ α-Li_5SiO_4F?+Li_4SiO_4
		750°C, 10 hours	Li_2SiO_3+(γ-)Phase B

10	52:36:12	650°C, 10 hours	α-Li_5SiO_4F+LiF+Li_4SiO_4(tiny)
		750°C, 10 hours	Li_4SiO_4+Li_2SiO_3+(γ-)Phase B
11	47:30:23	750°C, 10 hours	γ-Phase B-lower crystallinity+Li_2SiO_3(tiny)
		775°C, 10 hours	γ-Phase B-lower crystallinity +Li_2SiO_3(tiny)
12	50:30:20	750°C, 10 hours	(γ-)Phase B
		775°C, 10 hours	γ-Phase B
13	55:30:15	650°C, 10 hours	α-Li_5SiO_4F+Li_4SiO_4 + (γ-)Phase B
		750°C, 10 hours	Li_4SiO_4 + (γ-)Phase+extra peak
		775°C, 10 hours	Li_4SiO_4 + γ-Phase B
14	44.1:29.4:26.5	750°C, 10 hours	(γ-)Phase B +Li_2SiO_3 (t)+LiF(t)
		775°C, 10 hours	(γ-)Phase B +Li_2SiO_3(t)+LiF(t)

(b)

	Compositions Li_2CO_3:SiO_2:LiF	Synthesis temperature & time	Phase(s) present
15	42.8:28.6:28.6	750°C, 10 hours	(γ-)Phase B +Li_2SiO_3 (t)+LiF(t)
		775°C, 10 hours	(γ-)Phase B +Li_2SiO_3 (t)+LiF(t)
16	42:28:30	750°C, 10 hours	α-Li_5SiO_4F + Li_2SiO_3+LiF ?
		775°C, 10 hours	Unknown peaks + Li_2SiO_3+LiF ?
17	47:28:25	700°C, 10 hours	Phase B
		750°C, 10 hours	Phase B
		750°C, 20 hours	(γ)-Phase B
		775°C, 10 hours	γ-Phase B
		775°C, 20 hours	γ-Phase B
		800°C, 10 hours	γ-Phase B
		810°C, 1 hour	γ-Phase B
		820°C, 1 hour	γ-Phase B
		830°C, 1 hour	γ-Phase B

		840°C, 1 hour	γ-Phase B partial melt?
		850°C, 1 hour	γ-Phase B melt
18	50:27.5:22.5	750°C, 10 hours	Phase T
		775°C, 10 hours	Phase T+ unknown peak (melt?)
19	48.5:26.5:25	750°C, 10 hours	Phase T
		775°C, 10 hours	Phase T
20	47:23:30	750°C, 10 hours	α-Li_5SiO_4F+LiF
		775°C, 10 hours	γ -Li_5SiO_4F+LiF
		775°C, 20 hours	γ-Phase B type?
21	37.6:22.4:40	750°C, 10 hours	α-Li_5SiO_4F + Li_2SiO_3+LiF
		775°C, 10 hours	γ -Li_5SiO_4F+ Li_2SiO_3+LiF
22	40:20:40	750°C, 10 hours	α-Li_5SiO_4F+LiF
		775°C, 10 hours	γ -Li_5SiO_4F+LiF
23	52:23:25	750°C, 10 hours	(α-γ)-Li_5SiO_4F+Li_2CO_3-peaks
		775°C, 20 hours	γ-Li_5SiO_4F+Li_2CO_3-peaks
		800°C, 10 hours	melt? Li_4SiO_4+Li_2CO_3-peaks

(c)

	Compositions Li_2CO_3:SiO_2:LiF	Synthesis temperature & time	Phase(s) present
24	49.5:25.5:25	700°C, 10 hours	α-Li_5SiO_4F-type
		750°C, 10 hours	Phase T
		775°C, 20 hours	Phase T (higher crystallinity)
		800°C, 10 hours	Phase T (higher crystallinity)+Li_4SiO_4
25	47.5:27.5:25	750°C, 10 hours	Phase T+ Phase B
		775°C, 20 hours	Phase T+ γ-Phase B
		800°C, 10 hours	Phase T+ γ-Phase B
26	46:29:25	750°C, 10 hours	Li_2SiO_3+Phase B
		775°C, 20 hours	γ-Phase B-lower crystallinity
		800°C, 10 hours	γ-Phase B-lower crystallinity
27	45:30:25	750°C, 10 hours	Li_2SiO_3+γ-Phase B-lower crystallinity

		775°C, 20 hours	Li_2SiO_3 +γ-Phase B-lower crystallinity
		800°C, 10 hours	γ-Phase B-lower crystallinity
28	52.5:27.5:20	750°C, 10 hours	Phase T+Li_4SiO_4
		775°C, 20 hours	Phase T+Li_4SiO_4
		800°C, 10 hours	Phase T+Li_4SiO_4
29	45:27.5:27.5	750°C, 10 hours	Li_2SiO_3 (tiny)+Phase B
		775°C, 20 hours	γ-Phase B-lower crystallinity
		800°C, 10 hours	γ-Phase B-lower crystallinity
30	47:25.5:27.5	750°C, 10 hours	Phase B+ unknown peak
		775°C, 20 hours	Phase T+ unknown peak Li_2SiO_3?
		800°C, 10 hours	Phase T+ unknown peak Li_2SiO_3?
31	45:25:30	775°C, 10 hours	Unknown phase
		800°C, 6 hours	Phase T+LiF
32	42.5:22.5:35	775°C, 10 hours	Unknown phase
		800°C, 6 hours	Phase T-like+LiF+Li_4SiO_4
33	43.5:26.5:30	750°C, 10 hours	γ-Phase B+LiF+extra peak
		775°C, 20 hours	γ-Phase B+LiF

(d)

	Compositions Li_2CO_3:SiO_2:LiF	Synthesis temperature & time	Phase(s) present
34	40:22.5:37.5	750°C, 10 hours	γ-Phase B+LiF+extra peak
		775°C, 20 hours	γ-Phase B+LiF
35	42.9:21.4:35.7	775°C, 20 hours	Phase T-type+LiF
36	45:22.5:32.5	775°C, 20 hours	Phase T-type+LiF
37	47.6:23.8:28.6	750°C, 10 hours	(γ)-Phase B type
		775°C, 20 hours	(γ)-Phase B type
38	48.5:24.2:27.3	775°C, 20 hours	Phase T-type
39	52.5:32.5:15	750°C, 10 hours	Li_2SiO_3+Phase B
		775°C, 10 hours	γ-Phase B
40	51:31.5:17.5	750°C, 10 hours	Li_2SiO_3+Phase B
		775°C, 10 hours	γ-Phase B

41	48.5:29:22.5	750°C, 10 hours	Li_2SiO_3+Phase B
		775°C, 10 hours	γ-Phase B
42	45:35:20	750°C, 10 hours	Li_2SiO_3+Phase B
		775°C, 10 hours	Li_2SiO_3+Phase B type
43	50:35:15	750°C, 10 hours	Li_2SiO_3++Li_4SiO_4+Phase B
		775°C, 10 hours	γ-Phase B
44	50:40:10	750°C, 10 hours	Li_2SiO_3++Li_4SiO_4+Phase B
		775°C, 10 hours	γ-Phase B-lower crystallinity + Li_2SiO_3
45	47.5:37.5:15	750°C, 10 hours	Li_2SiO_3+ Phase B
		775°C, 10 hours	γ-Phase B-lower crystallinity + Li_2SiO_3
46	50:37.5:12.5	750°C, 10 hours	Li_2SiO_3+Li_4SiO_4+Phase B
		775°C, 10 hours	γ-Phase B-lower crystallinity + Li_2SiO_3
47	47.5:32.5:20	750°C, 10 hours	γ-Phase B- lower crystallinity + Li_2SiO_3
		775°C, 10 hours	γ-Phase B-lower crystallinity + Li_2SiO_3

(e)

	Compositions Li_2CO_3:SiO_2:LiF	Synthesis temperature & time	Phase(s) present
48	47.5:35:17.5	750°C, 10 hours	γ-Phase B-lower crystallinity + Li_2SiO_3
		775°C, 10 hours	γ-Phase B-lower crystallinity + Li_2SiO_3
49	50:25:25	650°C, 20 hours	α-Li_5SiO_4F
		700°C, 10 hours	α-Li_5SiO_4F
		750°C, 10 hours	γ-Li_5SiO_4F
		775°C, 10 hours	γ-Li_5SiO_4F
		775°C, 20 hours	γ-Li_5SiO_4F
		800°C, 10 hours	γ-Li_5SiO_4F
50	50:50:0	800°, 10 hours	Li_2SiO_3

51	~66.66:33.33:0	800°, 10 hours	Li_4SiO_4

(a)

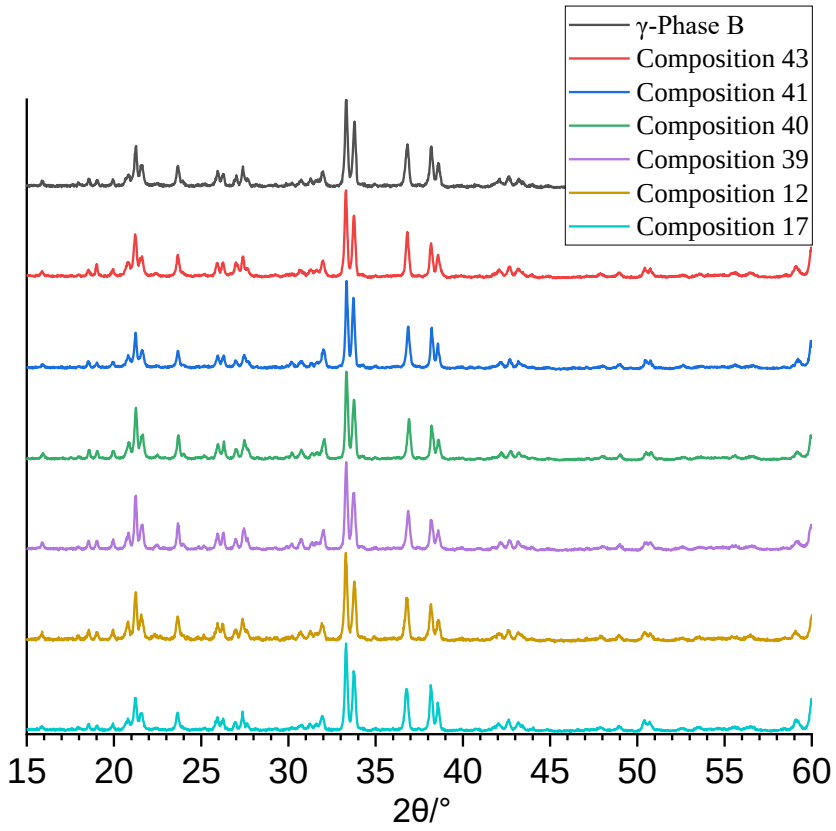
γ-Phase B
Composition 43
Composition 41
Composition 40
Composition 39
Composition 12
Composition 17
15
20
25
30
35
40
45
50
55
60
2θ/°

(b)

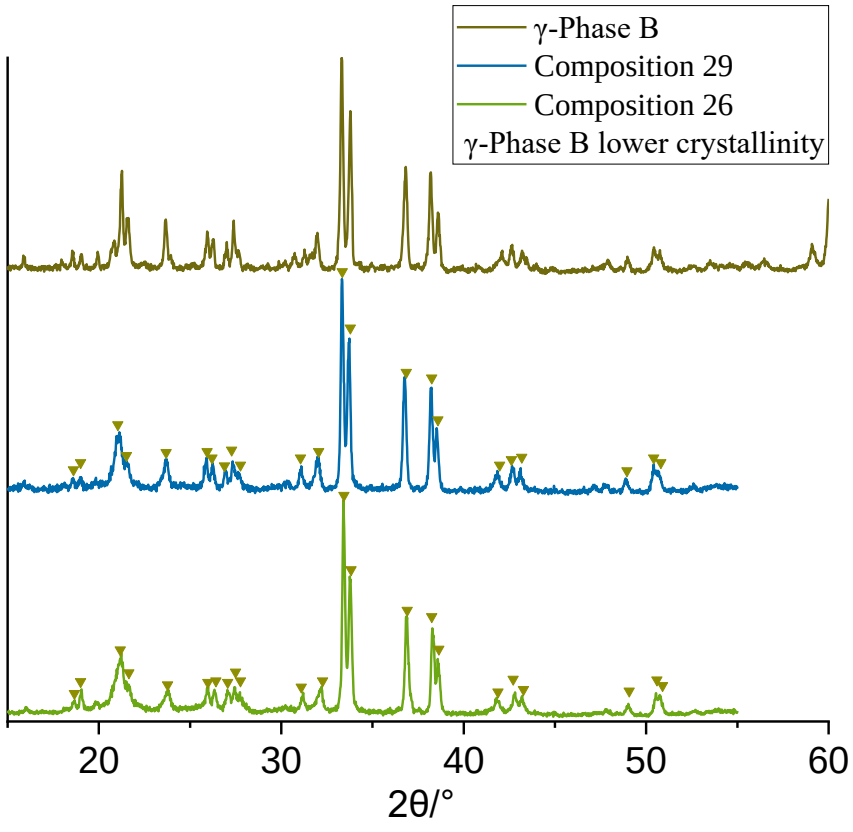
γ-Phase B
Composition 29
Composition 26
γ-Phase B lower crystallinity
20
30
40
50
60
2θ/°

(c)

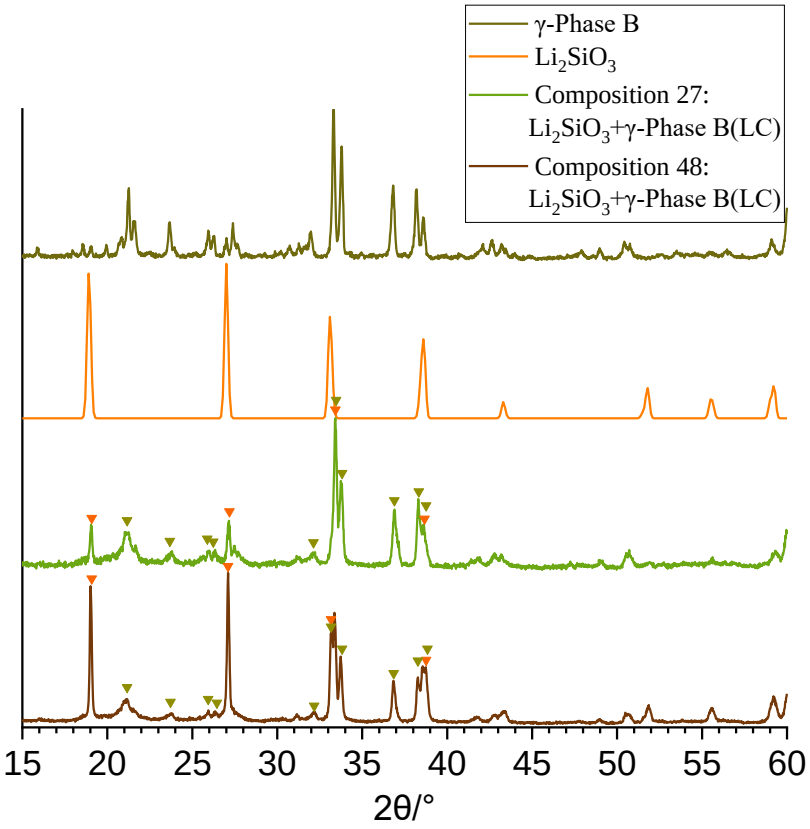
γ-Phase B
Li2SiO3
Composition 27:
Li2SiO3+γ-Phase B(LC)
Composition 48:
Li2SiO3+γ-Phase B(LC)
15 20 25 30 35 40 45 50 55 60
2θ/°

(d)

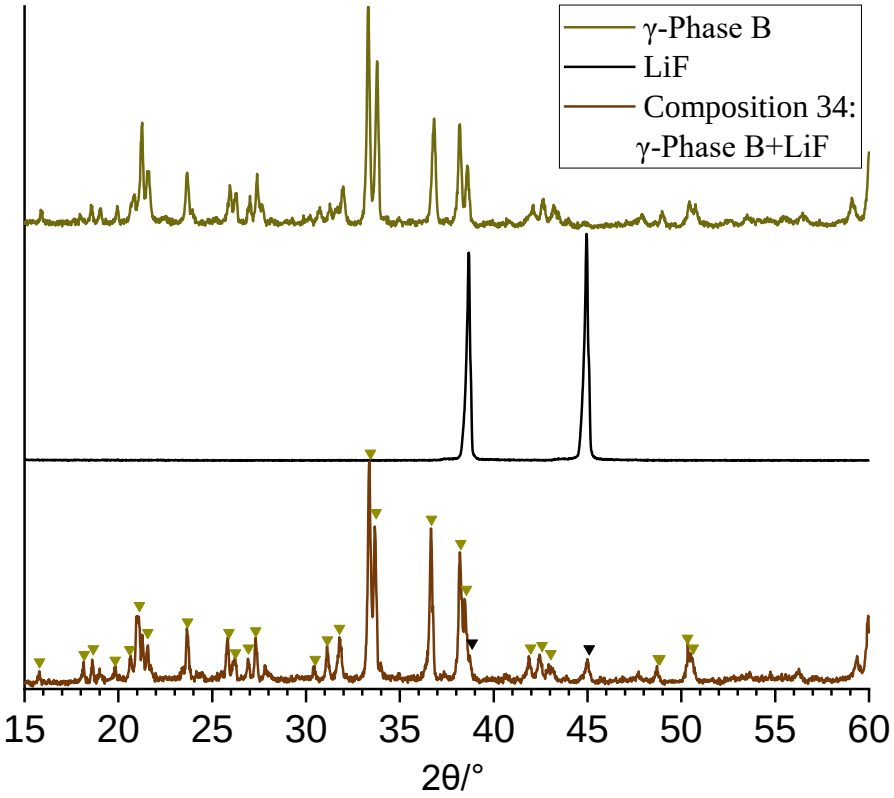
γ-Phase B
LiF
Composition 34:
γ-Phase B+LiF
15 20 25 30 35 40 45 50 55 60
2θ/°

(e)

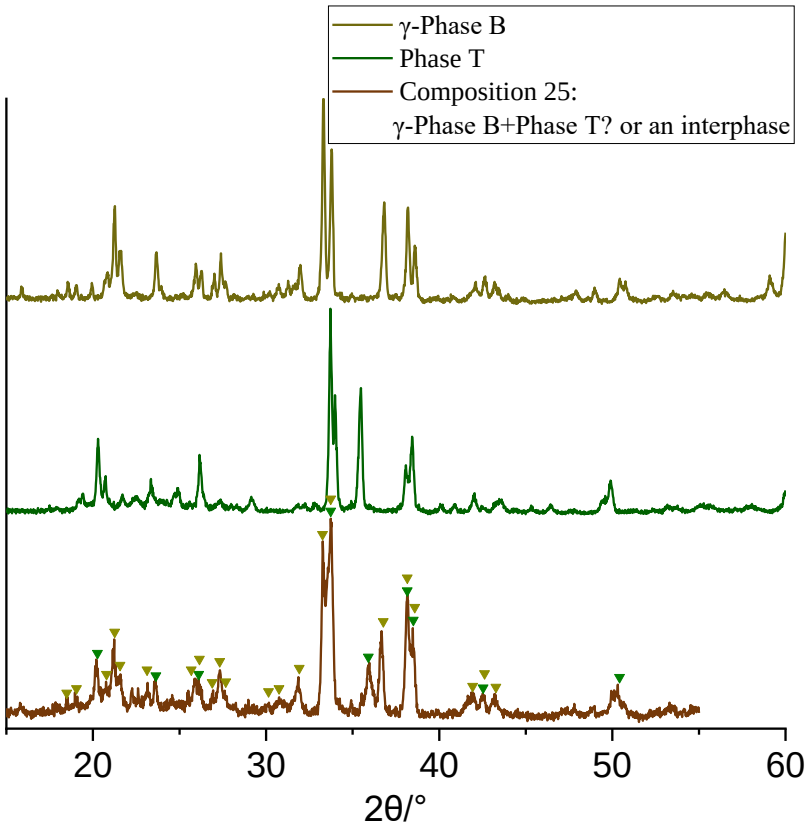
γ-Phase B
Phase T
Composition 25:
γ-Phase B+Phase T? or an interphase
20
30
40
50
60
2θ/°

(f)

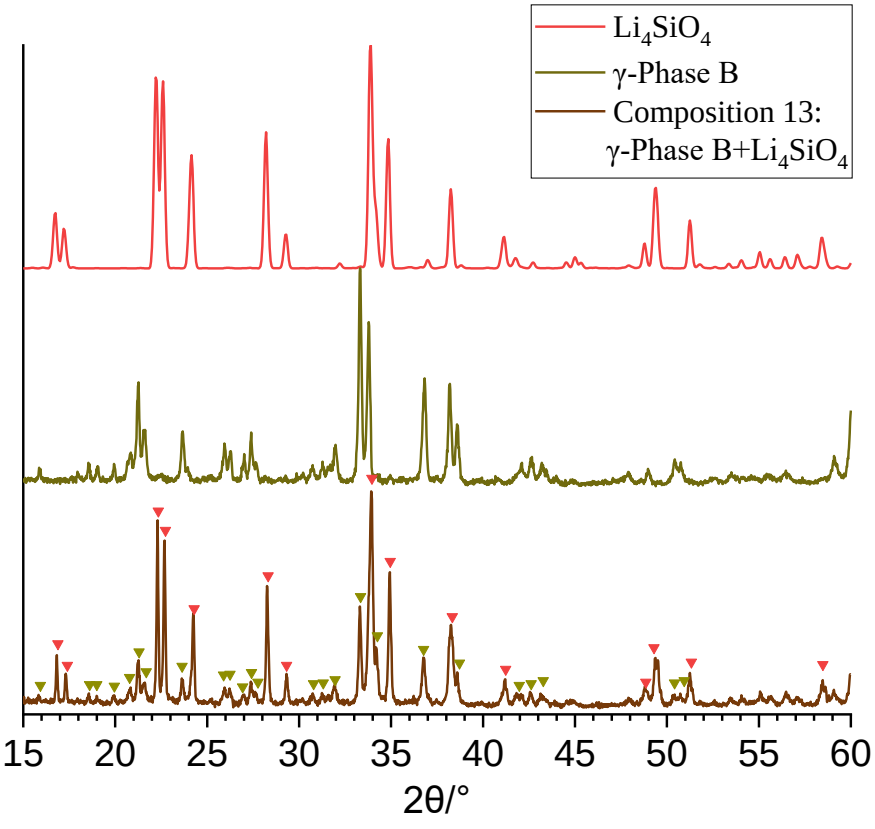
Li4SiO4
γ-Phase B
Composition 13:
γ-Phase B+Li4SiO4
15
20
25
30
35
40
45
50
55
60
2θ/°

(g)

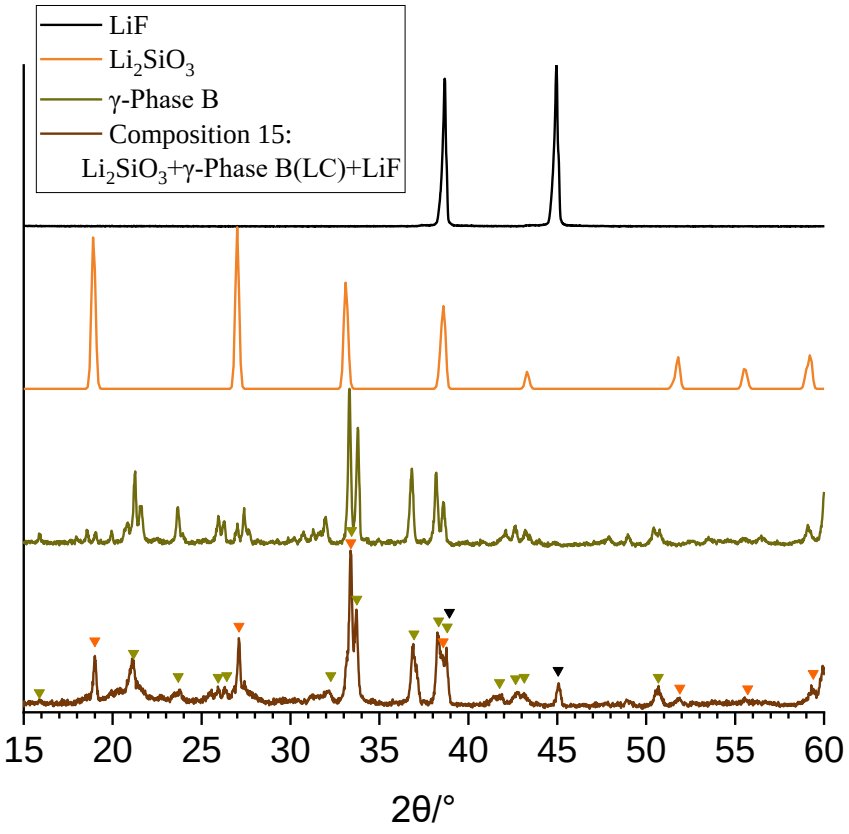

.

Fig 5.S2. XRD patterns for some representative compositions at 775°: (a) 12, 17, 39, 40, 41, and 43: γ-B; (b) 26, and 29: γ-B-lower crystallinity

(c) 48, 27: γ-B-LC+ Li_2SiO_3; (d) 24: γ-B+LiF (e) 25: γ-B+T(or an intermediate phase); (f) 13: γ-B+ Li_4SiO_4

(g) 15: γ-B+Li_2SiO_3+LiF

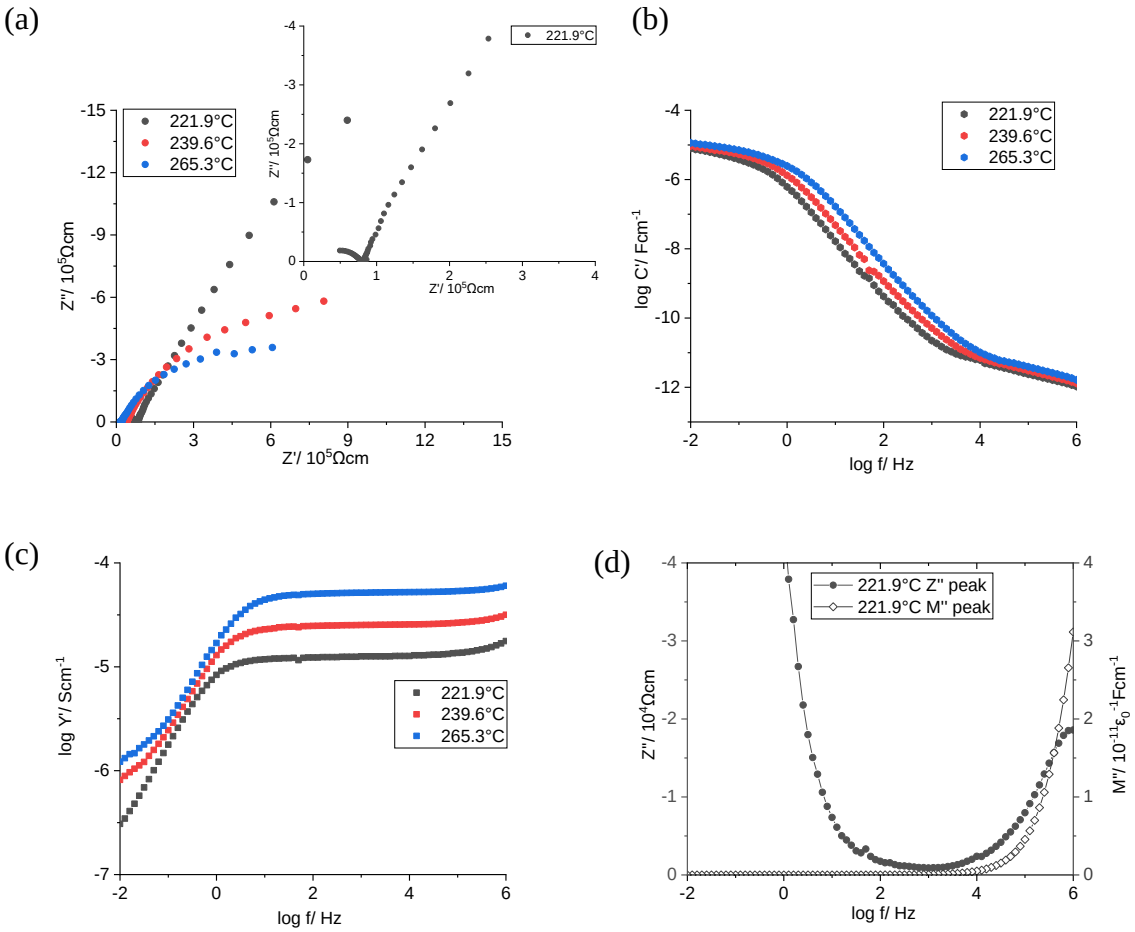

Fig 5.S3. Impedance dataset for composition Li_2O:SiO_2:LiF=47:28:25

(Hot pressed pellet at 300°C, synthesised at 700°C, 10 hours, coated with Au, primary phase of Phase B)

(a) $Z^{''}$-$Z^{'}$ complex plane plot, spectroscopic plots of (b) capacitance $C^{'}$, (c) admittance $Y^{'}$, (d) $Z^{''}M^{''}$ at 221.9°C

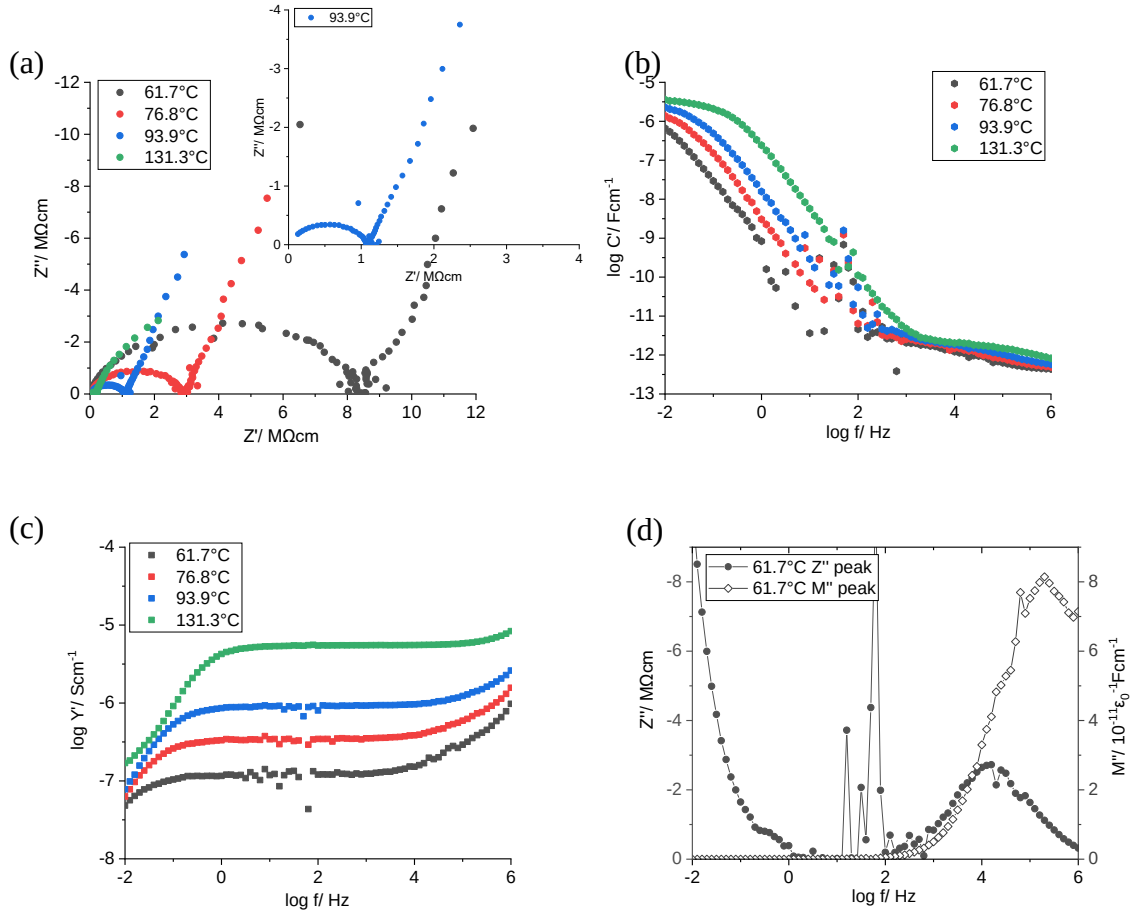

Fig 5.S4. Impedance dataset for composition Li_2O:SiO_2:LiF=47:28:25

(Hot pressed pellet at 300°C, synthesised at 775°C, 10 hours, coated with Au, primary phase of γ-Phase B)

(a) Z''-Z' complex plane plot, spectroscopic plots of (b) capacitance C', (c) admittance Y', (d) $Z''M''$ at 61.7°C

Table 5.S2. Parameters for the equivalent circuits fitted to the bulk/overall response of γ-Phase B

	R_1/ Ω	C_1/ Fcm^{-1}	CPE_1-T	CPE_1-P	CPE_2-T	CPE_2-P
69.2°C	5.10×10^{6}	5.42×10^{-13}	1.99×10^{-10}	0.56105	8.64×10^{-7}	0.71877
86.4°C	1.72×10^{6}	4.38×10^{-13}	1.21×10^{-10}	0.63897	1.28×10^{-6}	0.72839
105.7°C	594670	1.28×10^{-13}	4.94×10^{-11}	0.74156	1.83×10^{-6}	0.74507
126.5°C	225240	1.64×10^{-12}	1.48×10^{-11}	0.89323	-	-
170.4°C	40625	2.75×10^{-10}	2.82×10^{-10}	0.9987	-	-
Equivalent circuits are only fitted to the bulk response for high temperature samples						

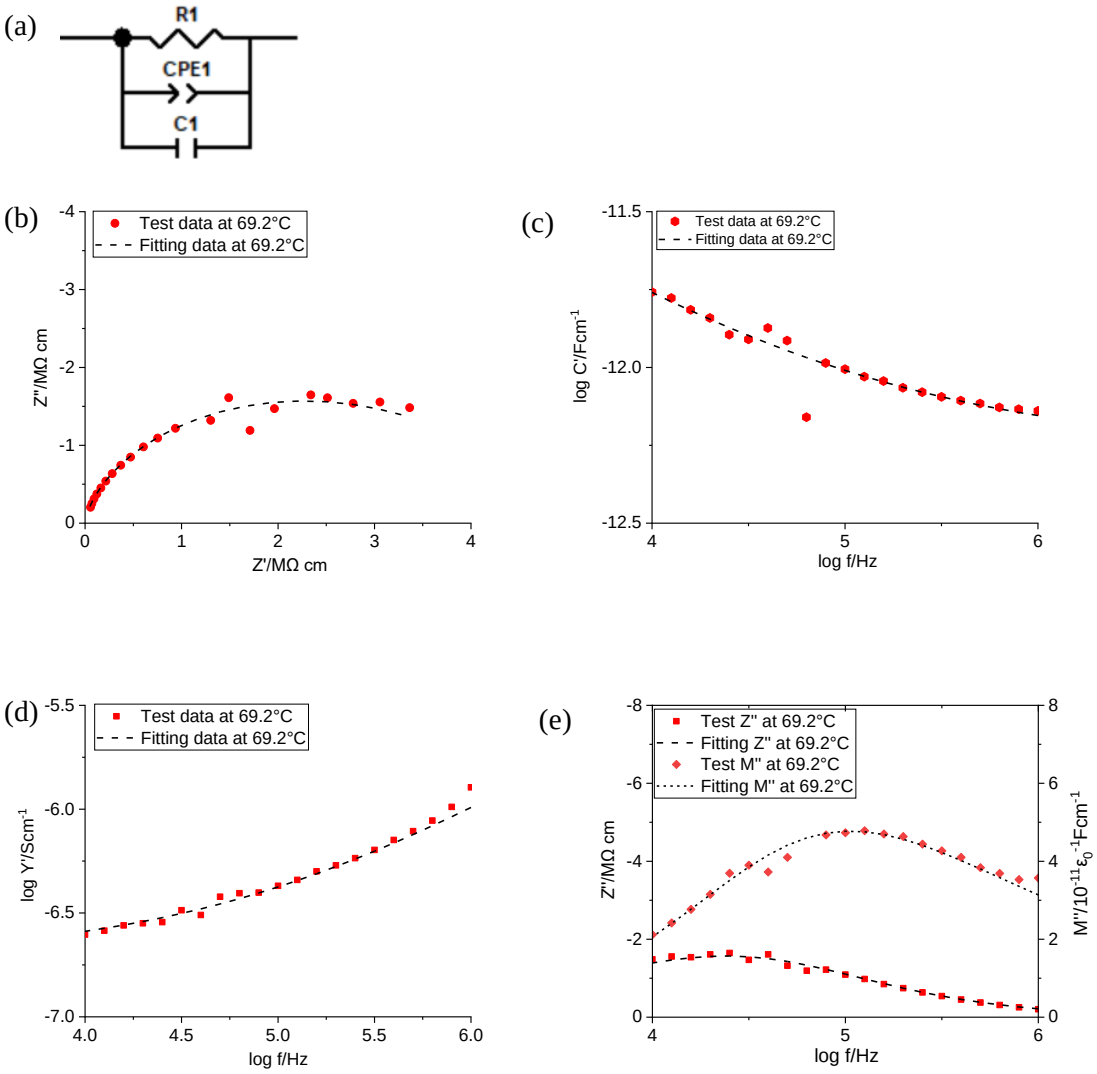

Fig 5.S5. Equivalent circuit fitted to the bulk response at 69.2°C.

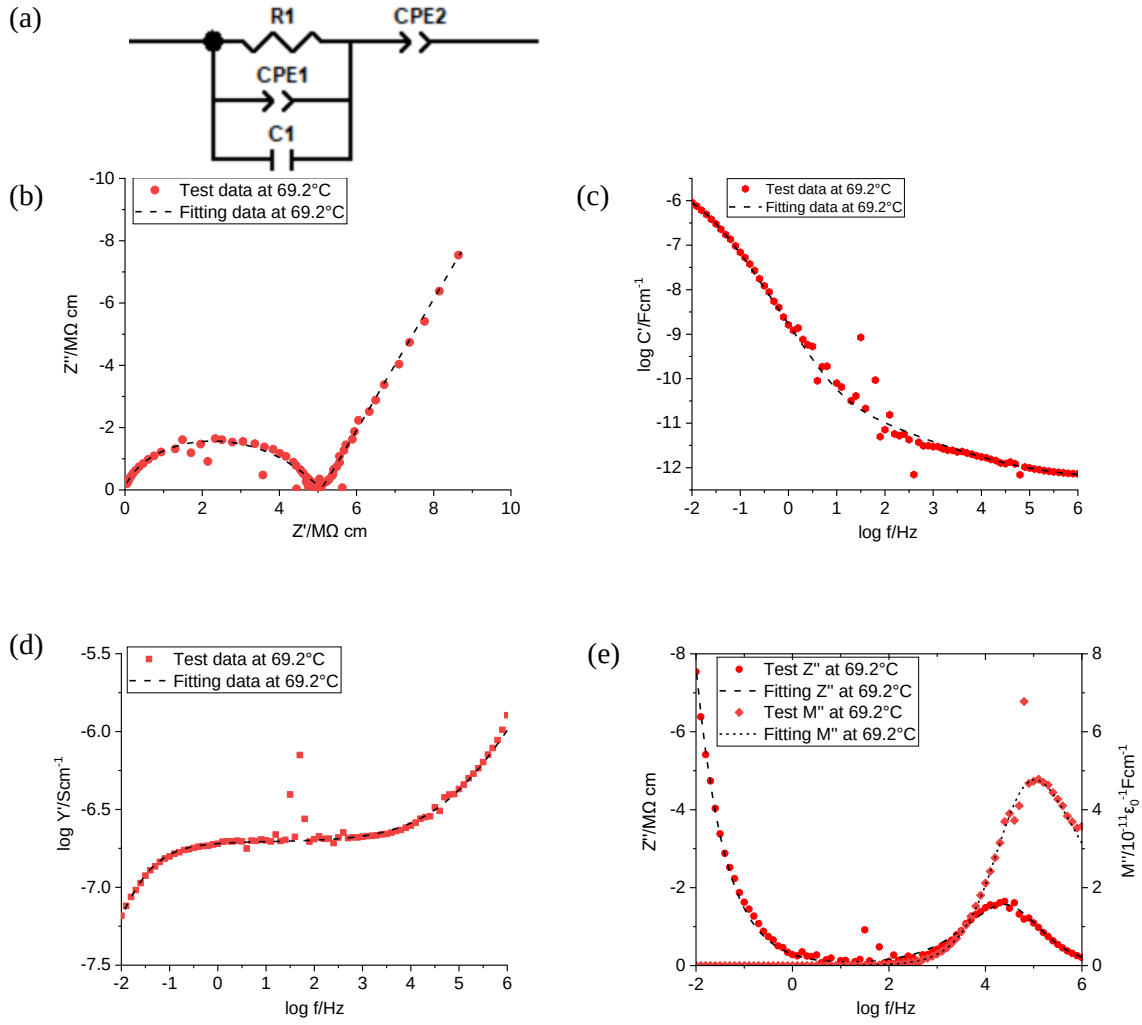

Fig 5.S6. Equivalent circuit fitted to the impedance data at 69.2°C.

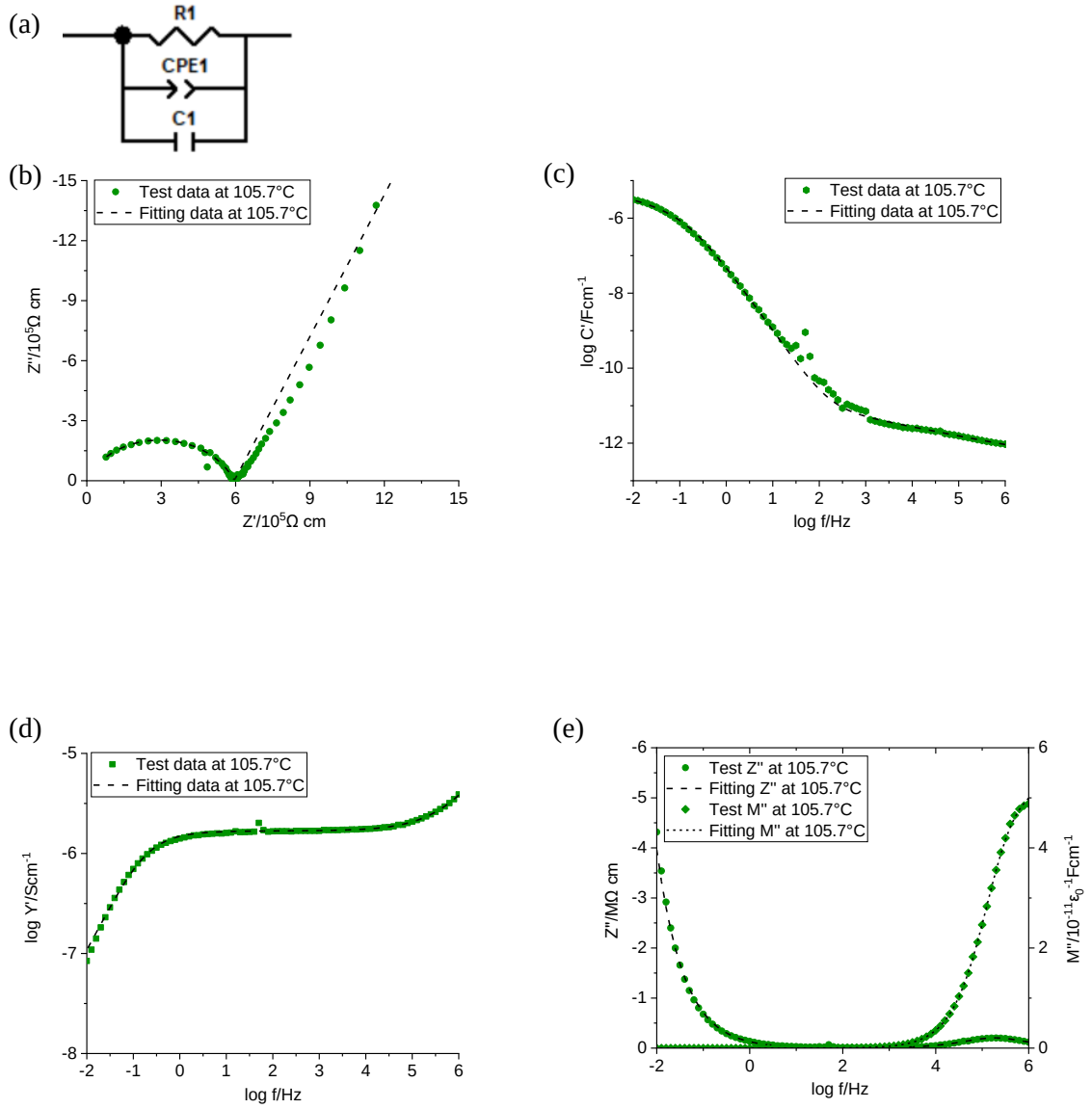

Fig 5.S7. Equivalent circuit fitted to the impedance data at 105.7°C.

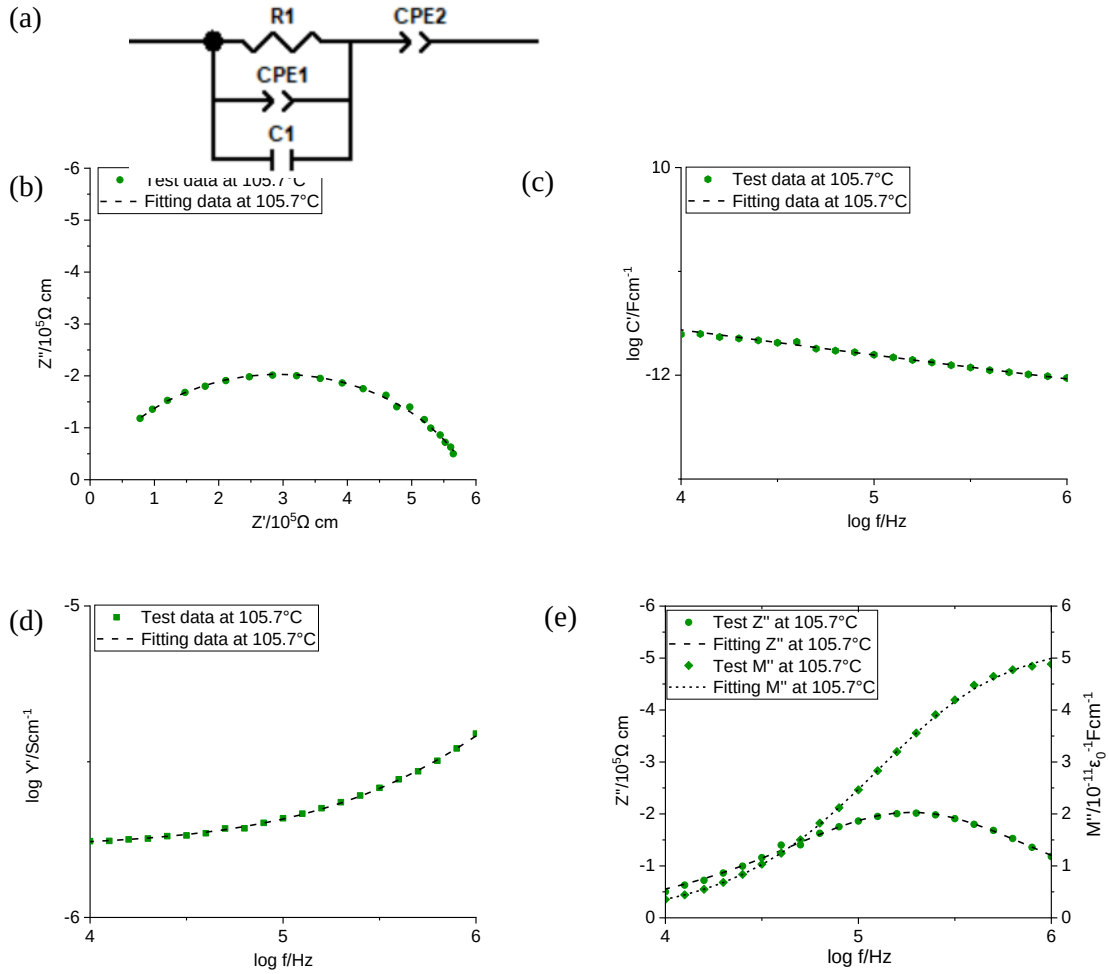

Fig 5.S8. Equivalent circuit fitted to the bulk response at 105.7°C.

Chapter 6. Phase formation in the ternary system Li_4SiO_4-Li_3PO_4-LiF

Summary

Three possible new phases, Phase S, γ-Phase S and Phase A were found in the ternary system Li_4SiO_4-Li_3PO_4-LiF. Phase S is synthesised at low temperatures, ~650-750 °C. γ-Phase S is synthesised at 750-775 °C and appears to be a metastable phase which easily transform in Phase A, at 750°C-800 °C. Phase S has a ZnO-like hexagonal subcell. Phase S and Phase A only exhibit a poor ionic conductivity similar to bulk Li_4SiO_4; while γ-phase S show an ionic conductivity which is approximately 2 orders of magnitude lower than that of γ-Li_5SiO_4F. There is evidence of F^- doped Li_4SiO_4-Li_3PO_4 solid solution, which possibly exhibit a good ionic conductivity comparable to that of γ- Li_5SiO_4F.

6.1. Introduction

The Li_4SiO_4-Li_3PO_4 edge in the ternary system Li_4SiO_4-Li_3PO_4-LiF was well investigated for many years as a solid solution system, in which both end-member phases and some specific compositions were regarded as potential solid electrolytes [1-2]. Although bulk Li_4SiO_4 only has a modest ionic conductivity with ~2.5×10^{-6} S/cm at 573 K, it shows thermal stability and compatibility in contact with a wide range of electrodes including lithium metal and graphite [3]. Bulk Li_3PO_4 exhibits an ionic conductivity with ~10^{-8} S/cm at 573 K and is not commonly used as an electrolyte; however, it can be coated on spinel cathode materials. The strong covalency of the PO_4 group offers cathode materials enhanced thermal stability, the P-O bonds can simultaneously offer better chemical resistance against acidic electrolytes with less dissolution of transition metal ions into electrolyte [4].

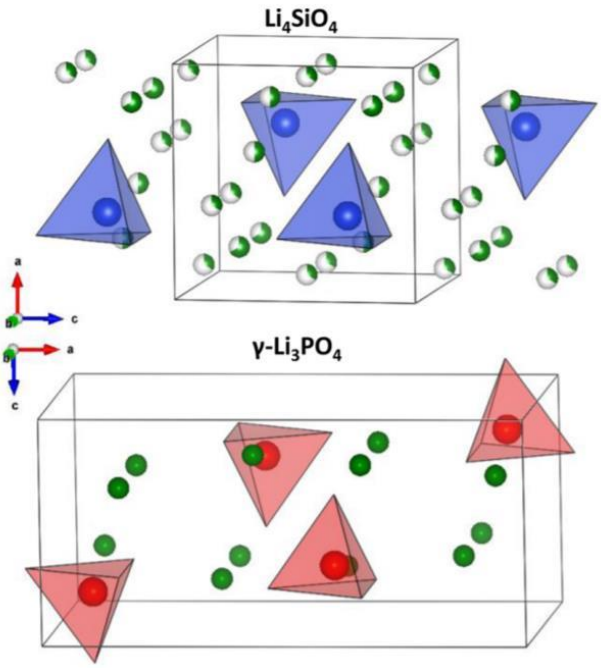

Fig 6.1. Crystal structures of Li_4SiO_4 and Li_3PO_4,

Isolated SiO_4 and PO_4 tetrahedra shown in blue and red; lithium ions in green.

Copied with permission from Y. Deng (2015) [2]. Copyright 2015 American Chemical Society.

Li_4SiO_4 has a monoclinic α-phase and a triclinic γ-phase [2]. Li_3PO_4 is a representative member of the A_3XO_4 family, Li_3MO_4 (M=P, As, V) and Li_2AXO_4 (A=Zn, Mg, Co; X=Si, Ge), with related derivative structures, which commonly show polymorphism. The family normally has a β-structure at low temperatures while a γ-structure at high temperatures. There is no transition phase shown in the β/γ inversion of Li_3PO_4 [5]. Both β and γ-Li_3PO_4 are orthorhombic [6]. Both monoclinic Li_4SiO_4 and Li_3PO_4 adopt a crystal structure built of XO_4 ($X=Si^{4+}$ or P^{5+}) tetrahedral with Li^+ partially occupied the interstitial sites, but different tetrahedral orientations as shown in Fig 6.1 [2].

The two end members each forms a limited range of solid solution where there may be disagreement over the limiting composition of each solid solution. The first limits reported by West in 1981 suggested ~42 %mole and 88 %mole of Li_4SiO_4 by solid state reactions, while the existence of single phase $Li_{3.5}Si_{0.5}P_{0.5}O_4$ remained uncertain [1]. Another study prepared Li_4SiO_4-Li_3PO_4 solid solution by both solid reaction and spark-plasma-sintering (SPS) suggested solid solution limits of ~40 %mole and 60 %mole of

Li_4SiO_4, in which it appears to give a monoclinic Li_4SiO_4-type phase with 60-100 %mole of Li_4SiO_4, while an orthorhombic phase arising from Li_3PO_4 when with 0-40 %mole of Li_4SiO_4. Sample with 50 %mole of Li_4SiO_4, $Li_{3.5}Si_{0.5}P_{0.5}O_4$, was successfully prepared by spark-plasma-sintering [7]. More recent research suggested solid solution limits of ~35 %mole and 45 %mole of Li_4SiO_4 [2]. The middle composition, $Li_{3.5}Si_{0.5}P_{0.5}O_4$ has a Li_3PO_4-like orthorhombic lattice cell which is demonstrated as isolated XO_4 tetrahedra with lithium atoms settled in different crystallographic sites [2].

Li_5SiO_4F is the only single phase that has been reported on the Li_4SiO_4-LiF edge, which has two polymorphs: α-form at low temperature and γ-form at high temperature [8]. The electrical properties and crystal structure of Li_5SiO_4F have been discussed in Chapter 3-4.

No phases have been reported on the Li_3PO_4-LiF edge. The binary phase diagram of Li_3PO_4-LiF suggests a simple eutectic system with coordinates of 800±5 °C and 8±1 %mole of Li_3PO_4. The formation of solid solution is proposed based on the substitution of $(PO_4)^{3-}$ by $(LiF_4)^{3-}$, similar to the substitution of tetrahedra $(SO_4)^{2-}$ by $(BeF_4)^{2-}$ [9].

There are many disordered crystal structures in electrolyte and cathode materials. One possible approach to increase the ionic conductivity of electrolyte materials is by introducing defects such as interstitial/substitutional elements and vacancies. For instance, disordered $Li_{10}GeP_2S_{12}$ (LGPS) has partially occupied cation sites with disordered P^{5+} and Ge^{4+} and ordered anion sites. The anti-site Ge_P defects have a lower concentration than P_{Ge}. P_{Ge} defects are dominant in enhancing its ionic conductivity plausibly due to the removal of local structural distortion [10]. A disordered structure was also seen in cathode materials like olivine-type $LiFePO_4$ and layered rock salt $LiCoO_2$ [11]. The representative material in hexagonal perovskite family, $Ba_7Nb_4MoO_{20}$, as an O^{2-} conductor, shows disordered cations with large difference in their ionic size, which then change some octahedral units to be face-sharing instead of corner-sharing. The mixed corner-sharing and face-sharing octahedra can give rise to hexagonal perovskite derivatives with both cationic and anionic vacancies [12].

In this chapter, the possible formation of solid solutions of F^- doped Li_4SiO_4-Li_3PO_4 was investigated. Several compositions in the ternary system Li_4SiO_4-Li_3PO_4-LiF were prepared in order to gain a general overview of the system.

6.2. Results and discussion

6.2.1. Possible F doped Li_4SiO_4-Li_3PO_4 solid solution

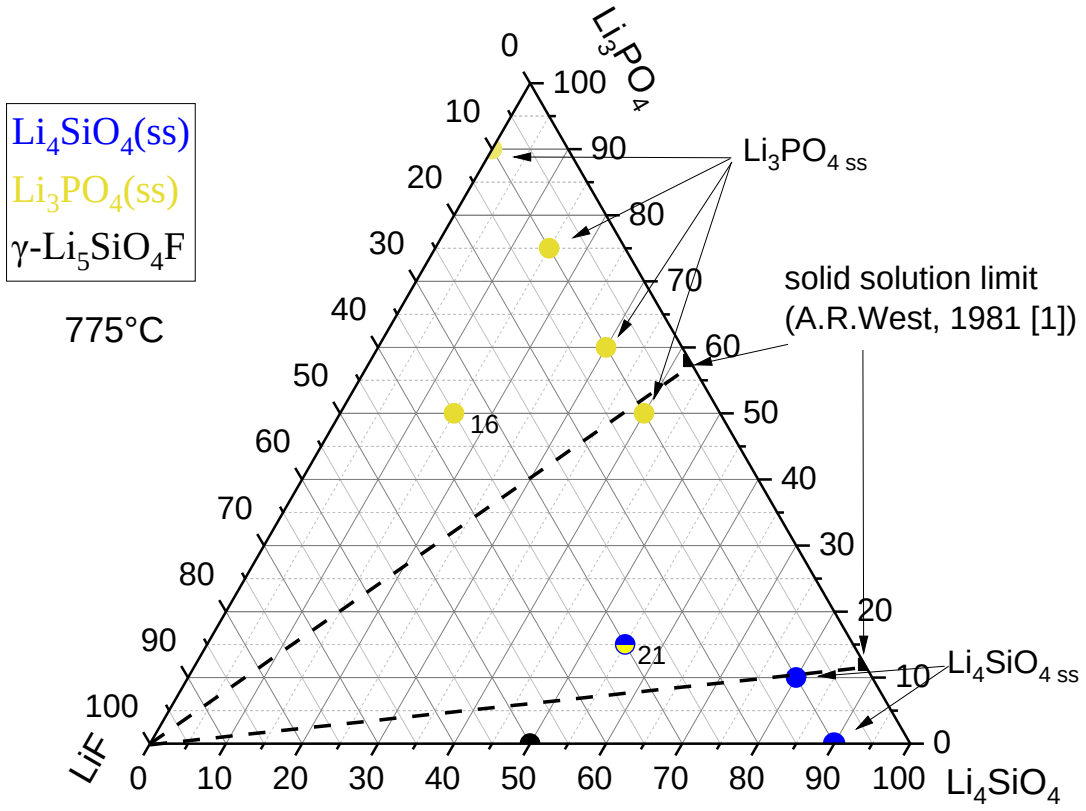

Fig 6.2. Some compositions and products at 775°C in ternary system Li_4SiO_4-Li_3PO_4-LiF, with either Li_4SiO_4 solid solution, Li_3PO_4 solid solution or a mixture of both.

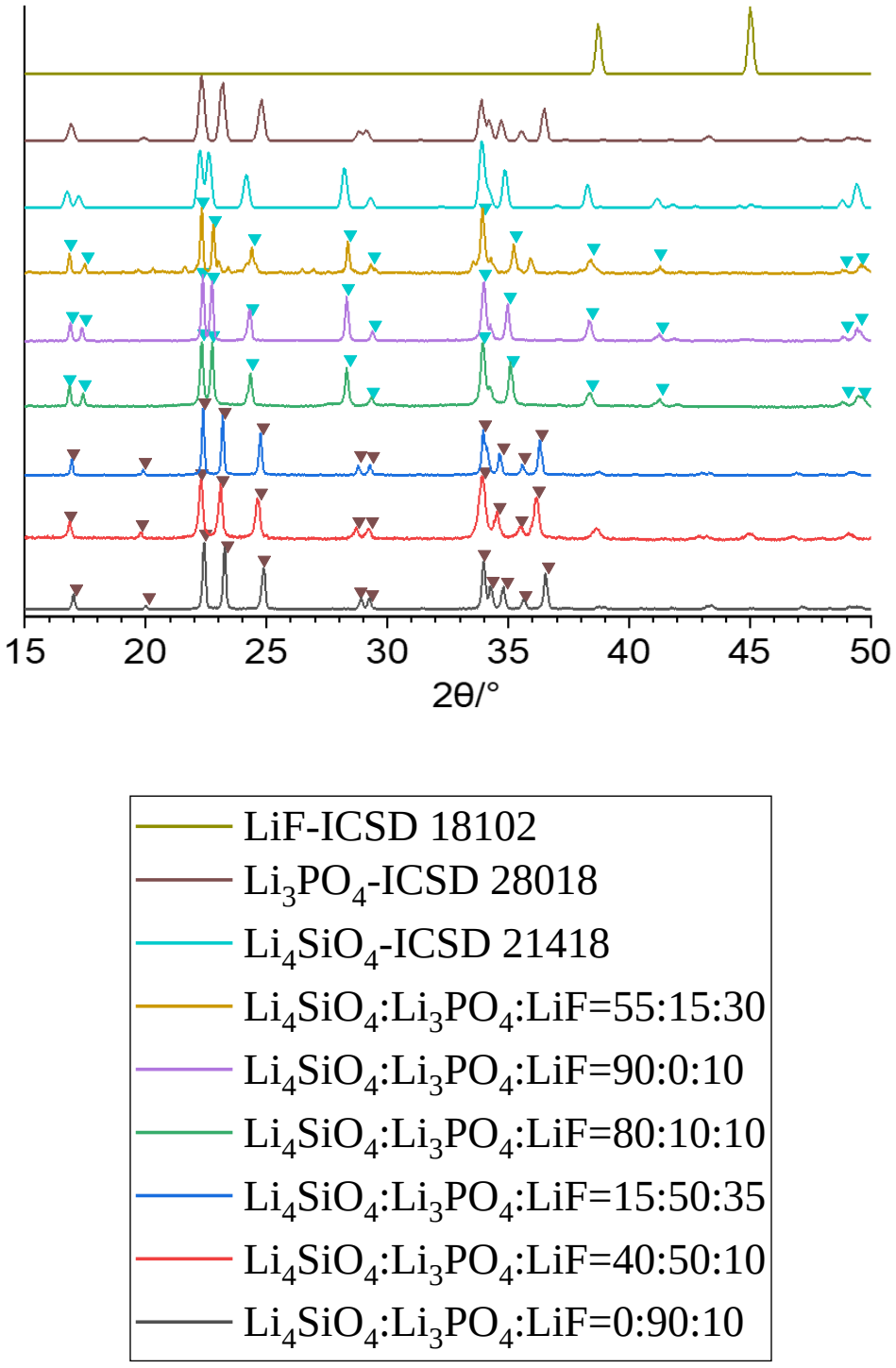

Fig 6.3. XRD results of some compositions in the ternary system Li_4SiO_4-Li_3PO_4-LiF, compared to standard patterns. Some of which are Li_3PO_4 solid solution, some are Li_4SiO_4 solid solution.

A preliminary study was made on some compositions in the ternary system Li_4SiO_4-Li_3PO_4-LiF which were reacted at different temperatures, with results summarised in Fig 6.2 and Table 6.1. With 10 %mole of LiF, the products were either Li_3PO_{4ss} or Li_4SiO_{4ss} with no existence of

LiF, Fig 6.3. As Li_4SiO_4:Li_3PO_4:LiF=15:50:35 (16) show a Li_3PO_{4ss} with no LiF, it more likely to show a F^- doped Li_3PO_{4ss} or Li_4SiO_{4ss} instead of possible losing of LiF during heat treatment. The possible solid solution limits with 10 %mole of LiF is ~15 %mole and 60 %mole of Li_3PO_4 at experimental temperatures, 700-775 °C, close to the value found by West [1]. Li_4SiO_4:Li_3PO_4:LiF=90:0:10 do not show any trace of Li_5SiO_4F, maybe its composition is too low to be detected by D2-XRD.

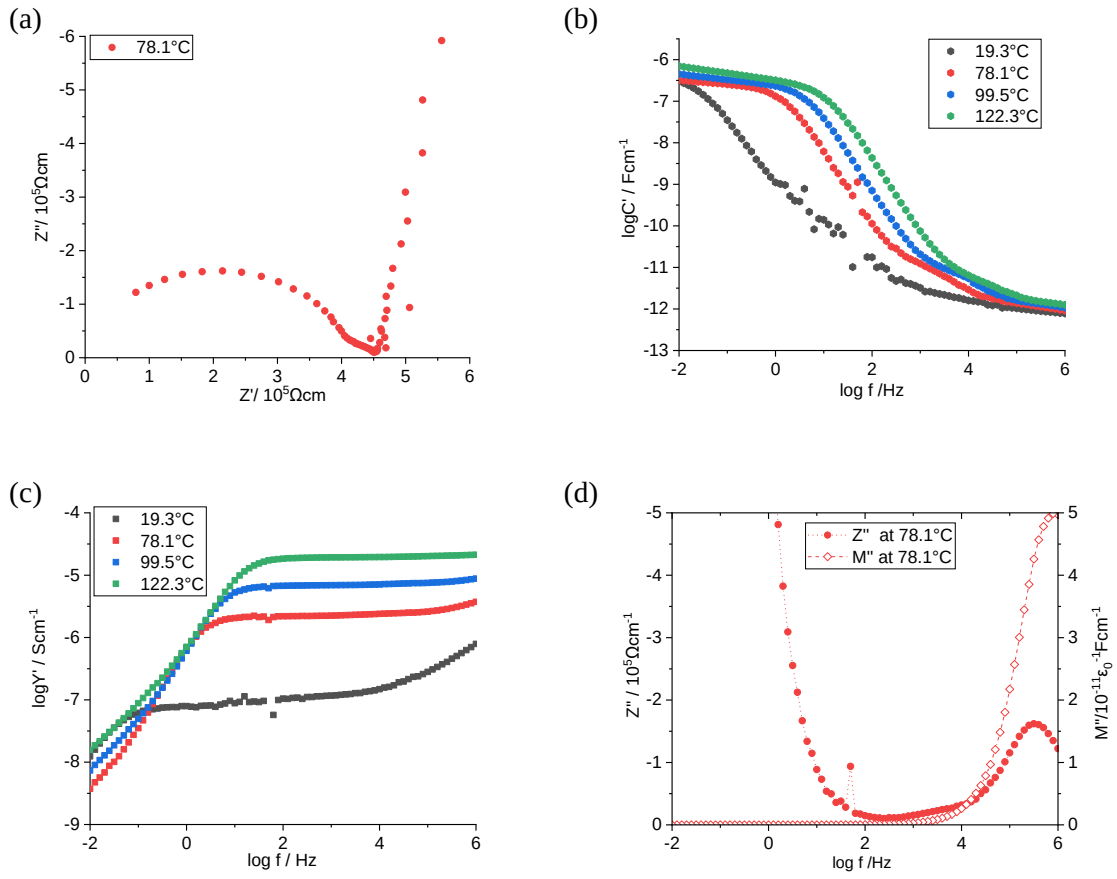

Fig 6.4. The impedance dataset for Li_4SiO_4:Li_3PO_4:LiF=15:75:10 (sintered at 750 °C, 10 h), (a) impedance complex plane plot, spectroscopic plots of (b) capacitance C', (c) admittance Y', and (d) Z''-M'' at 78.1 °C

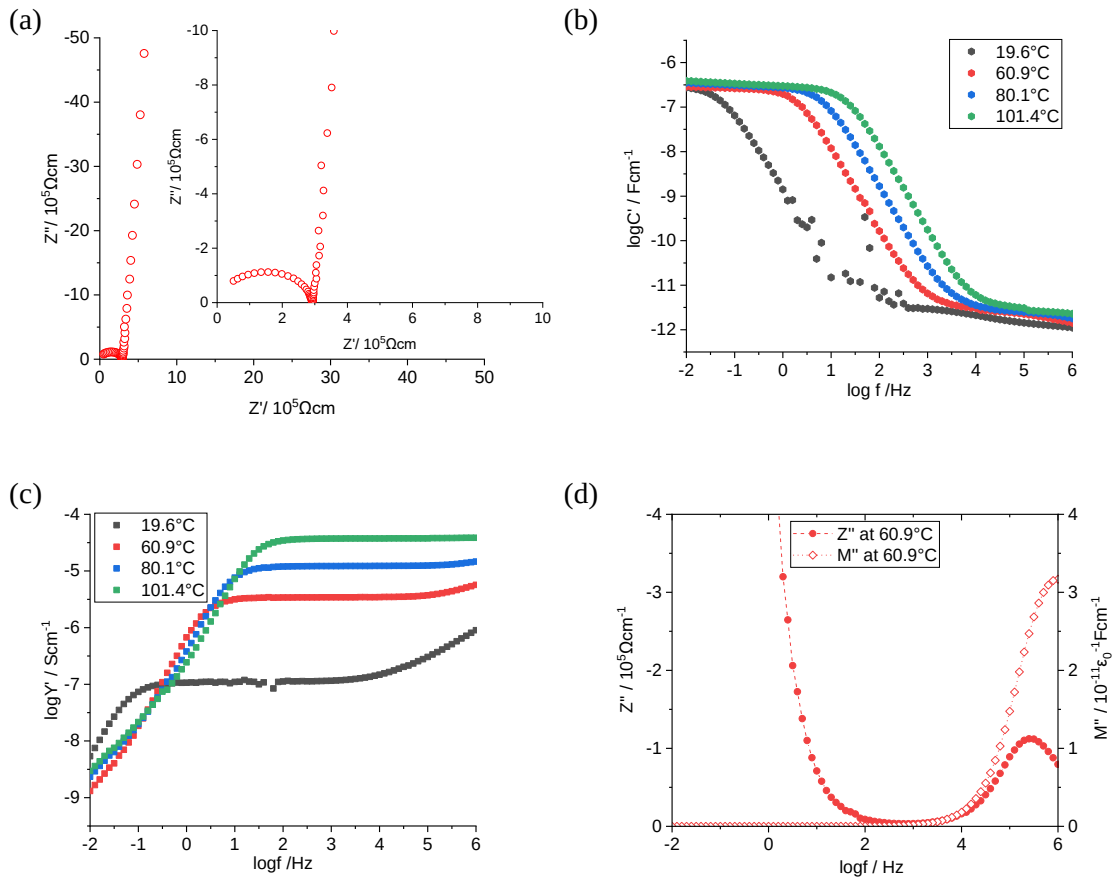

Fig 6.5. The impedance dataset for Li_4SiO_4:Li_3PO_4:LiF=80:10:10 (sintered at 750 °C, 10 h), (a) impedance complex plane plot at 60.9 °C , spectroscopic plots of (b) capacitance C', (c) admittance Y', and (d) Z''-M'' at 60.9 °C

The impedance results of Li_3PO_{4ss} and Li_3PO_{4ss} are shown in Fig 6.4 and Fig 6.5 respectively. The complex plane plots in Fig 6.4 (a) consist of a semicircle followed by a high frequency spike, which correspond to the high frequency capacitance plateau in (b), indicating the ionic conductivity of the sample. The asymmetrical semicircle in (a) and partially resolved capacitance plateau at ~10^{-11} Fcm^{-1} in (b) show a possible grain boundary response. The total resistance at 78.1 °C is ~4.5×10^5 Ω. The log Y'-log f plot in (c) shows a distorted total conductivity plateau over the range ~10^0-10^4 Hz with dispersions at both low and high frequency ends. The sample-electrode interface is responsible for the low frequency dispersion, while the high frequency dispersion can be attributed to Jonscher Law behaviour. The Z'' peak and M'' peak in (d) are nearly coincident on frequency scale. Li_3PO_{4SS}, Fig 6.5, show similar impedance responses but without any grain boundary effects.

6.2.2. Three possible new phases: Phase S, γ-Phase S and Phase A in ternary system Li_4SiO_4-Li_3PO_4-LiF

(a)

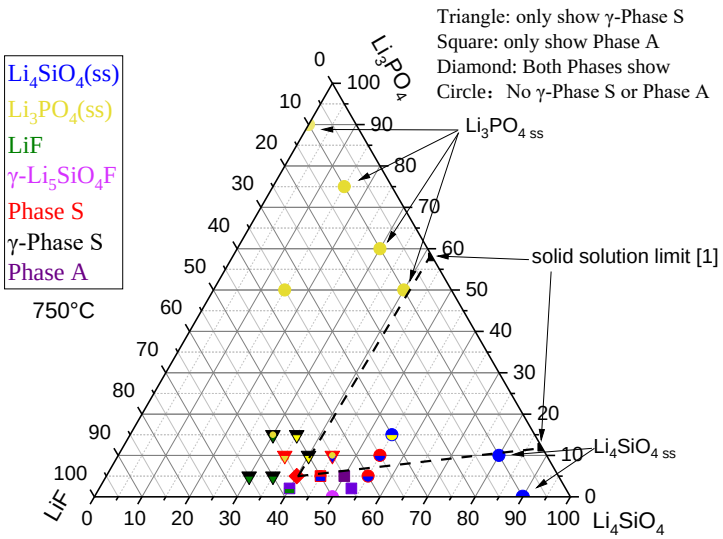

(b)

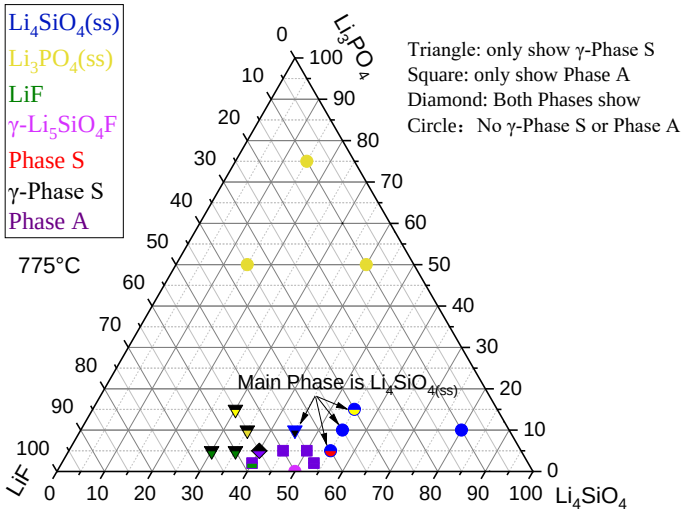

Fig 6.6. Compositions and products in the ternary system Li_4SiO_4-Li_3PO_4-LiF (a) at 750 °C and (b) at 775 °C

Table 6.1. A summary of compositions, experimental conditions and products

(a)

Compositions Li_4SiO_4:Li_3PO_4:LiF	Synthesis temperature & time	Phase(s) present
50:0:50	650°C, 10 hours	α-Li_5SiO_4F
	750°C, 10 hours	γ-Li_5SiO_4F
0:50:50	650°C, 10 hours	$Li_3PO_{4\ (ss)}$+LiF
	750°C, 10 hours	$Li_3PO_{4\ (ss)}$+LiF
40:02:58	650°C, 10 hours	α-Li_5SiO_4F+LiF+Li_4SiO_4(tiny)
	700°C, 10 hours	α-Li_5SiO_4F+LiF
	750°C, 10 hours	Phase A+LiF
	775°C, 10 hours	Phase A+LiF
The primary phase at 650°C is more likely to be α-Li_5SiO_4F instead of Phase S; the primary phase at 700°C is clearly α-Li_5SiO_4F		
53:02:45	650°C, 10 hours	Li_4SiO_4+α-Li_5SiO4F
	700°C, 10 hours	Li_4SiO_4+α-Li_5SiO4F
	750°C, 10 hours	Phase A
	775°C, 10 hours	Phase A
30:05:65	600°C, 10 hours	Phase S+LiF
	650°C, 10 hours	Phase S+LiF
	700°C, 10 hours	Phase S+LiF
	750°C, 10 hours	γ-Phase S+LiF
	775°C, 10 hours	γ-Phase S+LiF
35:05:60	600°C, 10 hours	Phase S+LiF
	650°C, 10 hours	Phase S+LiF
	700°C, 10 hours	Phase S+LiF
	750°C, 10 hours	γ-Phase S+LiF
	775°C, 10 hours	γ-Phase S+LiF
40:05:55	600°C, 10 hours	Phase S (some samples take longer time)
	650°C, 10 hours	Phase S
	700°C, 10 hours	Phase S
	750°C, 10 hours	Phase S
	750°C, 20 hours	γ-Phase S
	775°C, 10 hours	γ-Phase S
	775°C, 20 hours	γ-Phase S+Phase A
	800°C, 10 hours	γ-Phase S+Phase A
	820°C, 1 hour	γ-Phase S+Phase A
	820°C, 10 hours	γ-Phase S+Phase A
	830°C, 1 hour	γ-Phase S+Phase A
	840°C, 1 hour	Li_4SiO_4
45:05:50	600°C, 10 hours	Phase S+Li_4SiO_4
	650°C, 10 hours	Phase S+Li_4SiO_4
	700°C, 10 hours	Phase S+Li_4SiO_4
	750°C, 10 hours	Phase S-like +Li_4SiO_4
	775°C, 10 hours	Phase A
The Phase S-like product at 750°C show more broader peaks at low 2θ angles		

(b)

Compositions Li_4SiO_4:Li_3PO_4:LiF	Synthesis temperature & time	Phase(s) present
55:05:40	600°C, 10 hours	Li_4SiO_4+Li_2CO_3+LiF
	650°C, 10 hours	Phase S+Li_4SiO_4
	700°C, 10 hours	Phase S+Li_4SiO_4
	750°C, 10 hours	Phase S+Li_4SiO_4
	775°C, 10 hours	Phase S+Li_4SiO_4
35:10:55	650°C, 10 hours	Phase S+LiF+Li_3PO_4
	700°C, 10 hours	Phase S +LiF(tiny)+Li_3PO_4(tiny)
	750°C, 10 hours	Phase S +Li_3PO_4(tiny)
	775°C, 10 hours	γ-Phase S +Li_3PO_4(tiny)
40:10:50	650°C, 10 hours	Phase S +Li_3PO_4
	700°C, 10 hours	Phase S +Li_3PO_4
	750°C, 10 hours	γ-Phase S +Li_3PO_4
45:10:45	600°C, 10 hours	Li_4SiO_4+Li_2CO_3+LiF+Li_3PO_4
	650°C, 10 hours	Phase S+Li_4SiO_4+ Li_3PO_4
	700°C, 10 hours	Phase S+Li_4SiO_4+Li_3PO_4
	750°C, 10 hours	Phase S+Li_4SiO_4
	775°C, 10 hours	γ-Phase S + Li_4SiO_4
55:10:35	600°C, 10 hours	Li_4SiO_4+Li_2CO_3+LiF+Li_3PO_4
	650°C, 10 hours	Phase S+Li_4SiO_4+ Li_3PO_4
	700°C, 10 hours	Phase S+Li_4SiO_4 +Li_3PO_4
	750°C, 10 hours	Phase S+Li_4SiO_4
	775°C, 10 hours	Phase S+Li_4SiO_4
80:10:10	650°C, 10 hours	$Li_4SiO_{4\ (ss)}$
	700°C, 10 hours	$Li_4SiO_{4\ (ss)}$
	750°C, 10 hours	$Li_4SiO_{4\ (ss)}$
	775°C, 10 hours	$Li_4SiO_{4\ (ss)}$
30:15:55	600°C, 10 hours	Li_4SiO_4+Li_2CO_3+LiF+Li_3PO_4
	650°C, 10 hours	Li_4SiO_4+Phase S+LiF+Li_3PO_4
	700°C, 10 hours	Phase S+Li_3PO_4+LiF
	750°C, 10 hours	γ-Phase S+Li_3PO_4+LiF
	775°C, 10 hours	γ-Phase S+Li_3PO_4+LiF
35:15:50	650°C, 10 hours	Phase S+ Li_3PO_4
	700°C, 10 hours	Phase S+ Li_3PO_4
	750°C, 10 hours	Phase S+ Li_3PO_4
	775°C, 10 hours	Li_3PO_4 and an intermediate phase between Phase S and γ-Phase S.
15:50:35	650°C, 10 hours	$Li_3PO_{4\ (ss)}$+LiF
	700°C, 10 hours	$Li_3PO_{4\ (ss)}$+LiF
	750°C, 10 hours	$Li_3PO_{4\ (ss)}$
	775°C, 10 hours	$Li_3PO_{4\ (ss)}$
40:50:10	650°C, 10 hours	$Li_3PO_{4\ (ss)}$
	700°C, 10 hours	$Li_3PO_{4\ (ss)}$
	750°C, 10 hours	$Li_3PO_{4\ (ss)}$
	775°C, 10 hours	$Li_3PO_{4\ (ss)}$

(c)

Compositions Li_4SiO_4:Li_3PO_4:LiF	Synthesis temperature & time	Phase(s) present
90:0:10	650°C, 10 hours	$Li_4SiO_{4(ss)}$
	750°C, 10 hours	$Li_4SiO_{4(ss)}$
30:60:10	650°C, 10 hours	$Li_3PO_{4\ (ss)}$ + tiny $Li_4SiO_{4(ss)}$
	750°C, 10 hours	$Li_3PO_{4\ (ss)}$ + tiny $Li_4SiO_{4(ss)}$
0:90:10	650°C, 10 hours	$Li_3PO_{4\ (ss)}$
	750°C, 10 hours	$Li_3PO_{4\ (ss)}$
50:05:45	600°C, 10 hours	Phase S+Li_4SiO_4+Li_2CO_3
	650°C, 10 hours	Phase S+Li_4SiO_4
	700°C, 10 hours	Phase S+Li_4SiO_4
	750°C, 10 hours	Phase A
	775°C, 10 hours	Phase A
15:75:10	650°C, 10 hours	$Li_3PO_{4\ (ss)}$
	700°C, 10 hours	$Li_3PO_{4\ (ss)}$
	750°C, 10 hours	$Li_3PO_{4\ (ss)}$
	775°C, 10 hours	$Li_3PO_{4\ (ss)}$
25:50:25	650°C, 10 hours	$Li_3PO_{4\ (ss)}$
	750°C, 10 hours	$Li_3PO_{4\ (ss)}$

Several compositions with 5, 10 and 15 %mole Li_3PO_4 in the ternary system Li_4SiO_4-Li_3PO_4-LiF were prepared at different temperatures, with results illustrated in Fig 6.6 and summarised in Table 6.1. There are 3 possible new phases labelled as: (1) Phase S, which is synthesised at low temperatures, ~650-750 °C ; (2) γ-Phase S, which is synthesised at 750-775 °C; and (3) Phase A, which is synthesised at 750°C-800 °C. Single phases of both Phase S and γ-Phase S were obtained only in composition Li_4SiO_4:Li_3PO_4:LiF=40:5:55, while Phase A is likely to have a solid solution range near Phase S and Li_5SiO_4F, in Fig 6.6 (b).

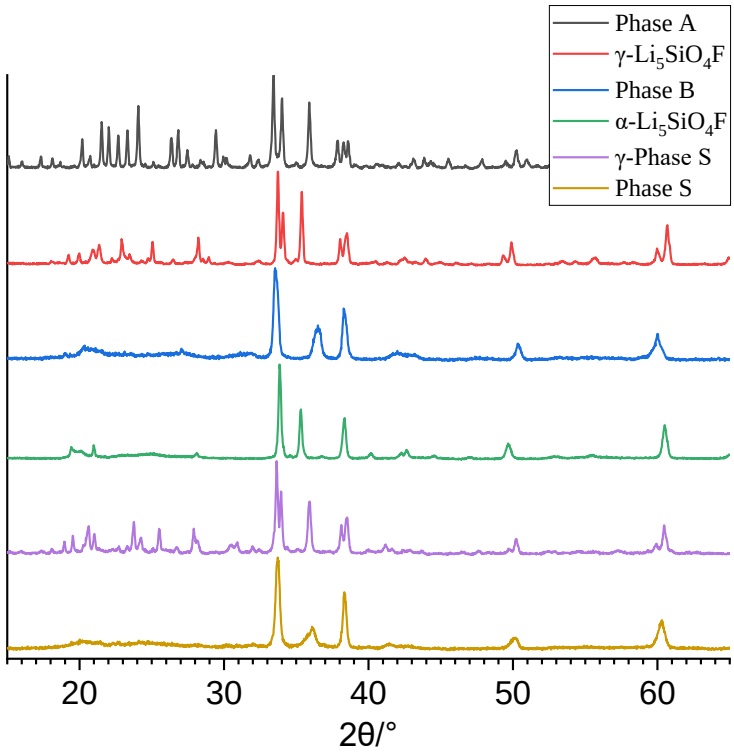

Fig 6.7. XRD results of the possible new phases compared to standard patterns.

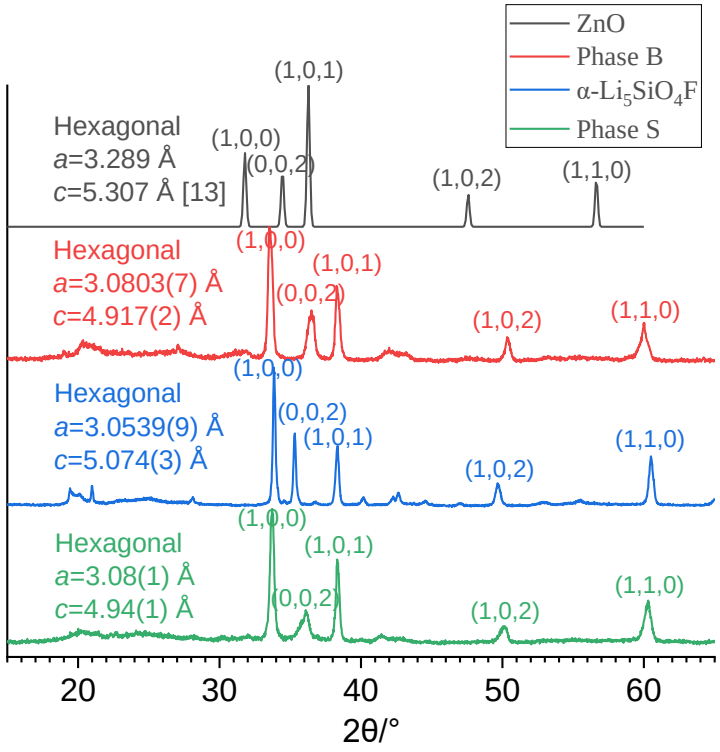

Fig 6.8. Three phases can be indexed on similar hexagonal subcells: Phase S, α-Li_5SiO_4F and Phase B, compared to ZnO [13]

The XRD results of these three possible new phases, Fig 6.7, firstly show that Phase S has a simple diffraction pattern similar to Phase B, which has been discussed in detail in Chapter 5, and to α-Li_5SiO_4F. These ZnO-like phases are successfully indexed on similar hexagonal subcells, Fig 6.8. The value of the parameter *c* varies significantly as shown by the different positions of the (0 0 2) peak. We take this as a diagnostic characteristic to distinguish different ZnO-like phases. The broad peaks at low 2θ angles in Phase S and Phase B probably indicate the existence of poorly-defined superstructures.

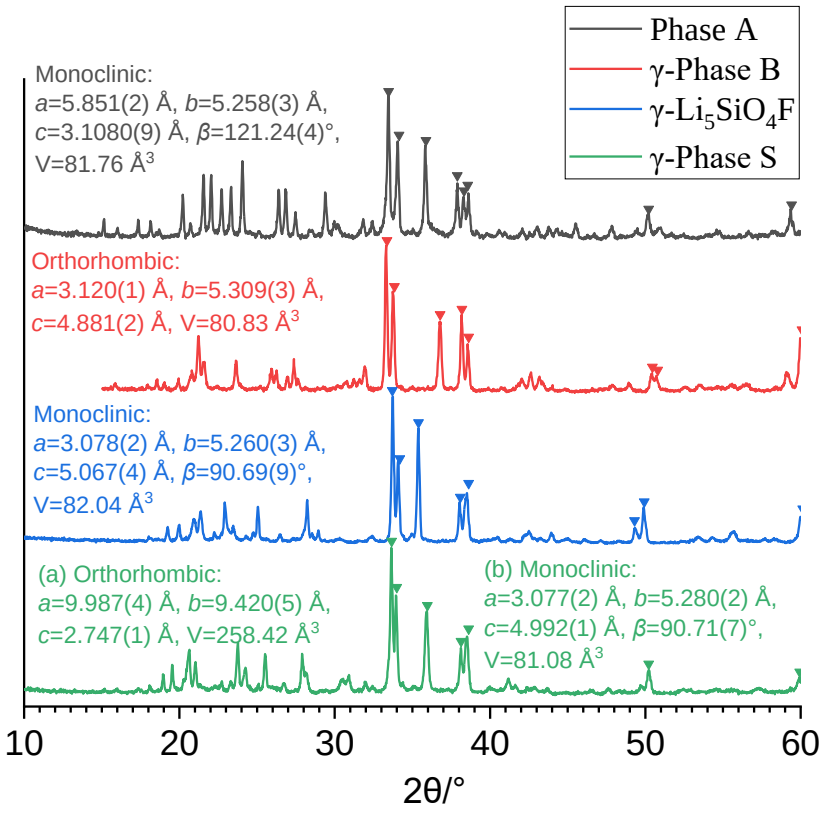

Fig 6.9. Three γ-type phases with indexed subcell structure: γ-Phase S, γ-Li_5SiO_4F and γ-Phase B compared to Phase A; peaks selected for indexing are marked.

Table 6.2. (a-b) Indexed results for possible subcell of γ-Phase S; (c) Indexed result for possible subcell of Phase A.

(a)

h	k	l	2θ-obs	2θ-cal	2θ-dif	d-obs	d-cal	d-dif
2	3	0	33.697	33.691	0.007	2.65762	2.65815	-0.00054
0	1	1	33.997	33.968	0.029	2.63491	2.63708	-0.00217
4	0	0	35.946	35.942	0.005	2.49634	2.49664	-0.00030
0	4	0	38.178	38.184	-0.006	2.35539	2.35505	0.00034
2	1	1	38.550	38.579	-0.029	2.33352	2.33186	0.00166
4	1	1	50.272	50.285	-0.013	1.81345	1.81301	0.00044
5	2	1	60.554	60.544	0.010	1.52782	1.52805	-0.00022
Monoclinic: *a*=9.987 (4) Å, *b*=9.420(5) Å, *c*=2.747(1) Å, V=258.42 Å^3								

(b)

h	k	l	2θ-obs	2θ-cal	2θ-dif	d-obs	d-cal	d-dif
0	1	1	33.697	33.692	0.006	2.65762	2.65806	-0.00044
1	0	-1	33.997	34.015	-0.019	2.63491	2.63350	0.00141
2	0	0	35.946	35.954	-0.08	2.49634	2.49581	0.00053
1	1	-1	38.178	38.157	0.021	2.35539	2.35662	-0.00123
1	2	0	38.550	38.548	0.002	2.33352	2.33364	-0.00012
2	2	0	50.272	50.268	0.005	1.81345	1.81361	-0.00016
0	3	1	60.554	60.563	-0.009	1.52782	1.52762	0.00021
Monoclinic: *a*=4.992 (1) Å, *b*=5.280(2) Å, *c*=3.077(2) Å, *β*=90.71(7), V=81.08 Å^3								

(c)

h	k	l	2θ-obs	2θ-cal	2θ-dif	d-obs	d-cal	d-dif
1	1	1	33.488	33.467	0.20	2.67379	2.67536	-0.00157
0	2	0	34.076	34.073	0.04	2.62892	2.62921	-0.00029
2	0	0	35.873	35.873	-0.09	2.50190	2.50126	0.00064
0	1	-1	37.905	37.905	0.17	2.37068	2.37172	-0.00104
2	1	-1	38.323	38.323	0.00	2.34684	2.34682	0.00002
1	2	0	38.656	38.656	-0.12	2.32805	2.32734	0.00071
3	1	-1	50.207	50.207	0.11	1.81528	1.81565	-0.00037
2	0	-2	59.438	59.438	-0.17	1.55422	1.55382	0.00040
Monoclinic: *a*=5.851 (2) Å, *b*=5.258 (3) Å, *c*=3.1080 (9) Å, *β*=121.24 (4), V=81.76 Å^3								

Secondly, γ-Phase S is closely related to Phase S, given by the split peaks at ~34 °/2θ and 38 °/2θ, Fig 6.9. The transition between them may be similar to the transition between α-/γ-

Li_5SiO_4F. However, γ-Phase S only exists at a single composition within a limited temperature range: 750-775 °C. γ-Phase S may be a thermodynamically metastable phase, since it quickly decomposes/transfers to Phase A during longer heat treatment or at higher temperatures. Whether there is any loss of element, Li^+ and/or F^- during the transition between γ-Phase S and Phase A is unknown, but the successive reheating Phase A at lower temperatures shows that the transition between γ-Phase S and Phase A is irreversible.

γ-Phase S, Fig 6.9, can be indexed on an orthorhombic subcell, Table 6.2 (a), or a smaller monoclinic subcell, Table 6.2 (b), which is similar to the subcell of γ-Phase B with reduced parameter *c*. The third possible new phase, Phase A, can be indexed on a monoclinic subcell, Table 6.2 (c). The possible monoclinic subcell of Phase A is different to those in γ-Phase S and γ-Li_5SiO_4F. The additional peak at 37-38.5°/2θ in Phase A may be a supercell peak, however, the attempts to index the pattern without this peak did not reach a convincing result with good agreements.

At this stage, the suitable conditions for transition from Phase S or γ-Phase S to Phase A are not clear.

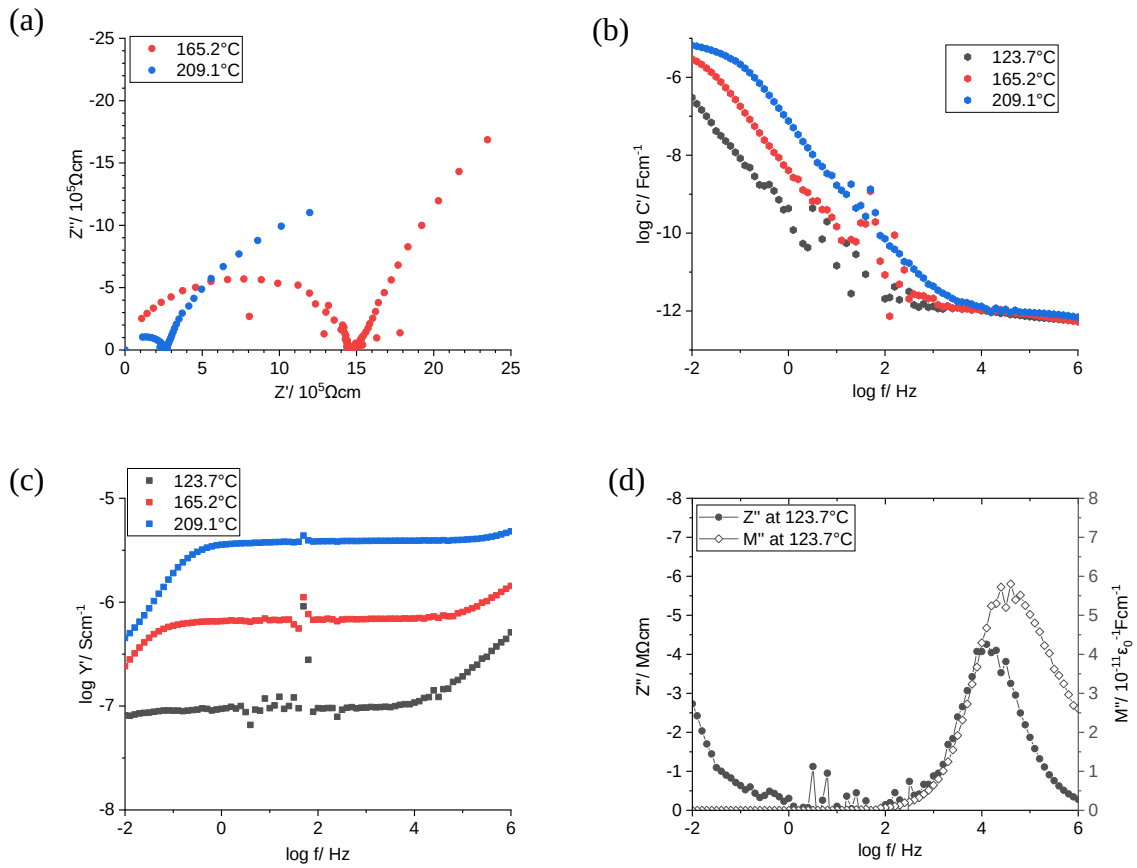

Fig 6.10. Impedance dataset for composition Li_4SiO_4:Li_3PO_4:LiF=40:05:55

(synthesised at 700 °C, 10 hours, coated with Au, primary phase of Phase S)

(a) $Z^{''}$-$Z^{'}$ complex plane plot, spectroscopic plots of (b) capacitance C', (c) admittance Y', (d) $Z^{''}M^{''}$ at 123.7 °C

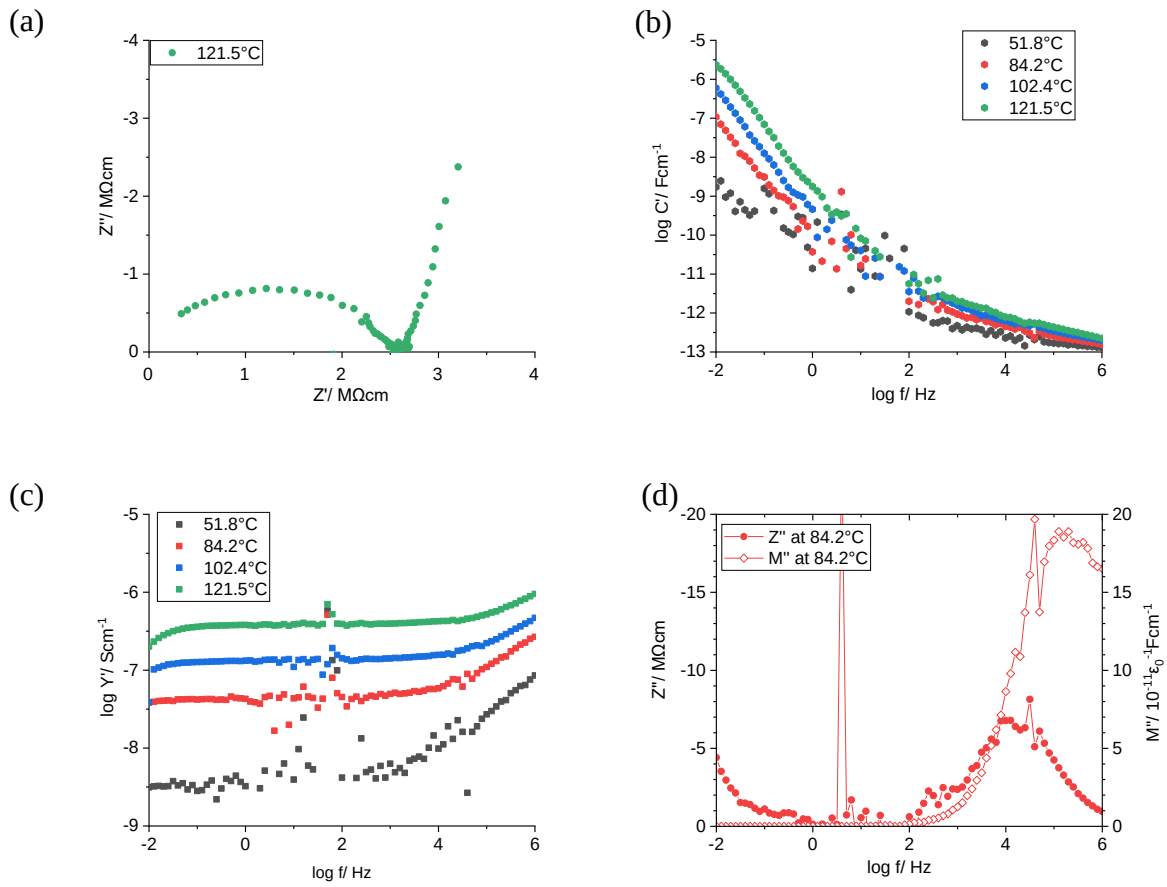

Fig 6.11. Impedance dataset for composition Li_4SiO_4:Li_3PO_4:LiF=40:05:55

(synthesised at 775 °C, 10 hours, coated with Au, primary phase of γ-Phase S)

(a) $Z^{''}$-$Z^{'}$ complex plane plot, spectroscopic plots of (b) capacitance C', (c) admittance Y', (d) $Z^{''}M^{''}$ at 84.2 °C

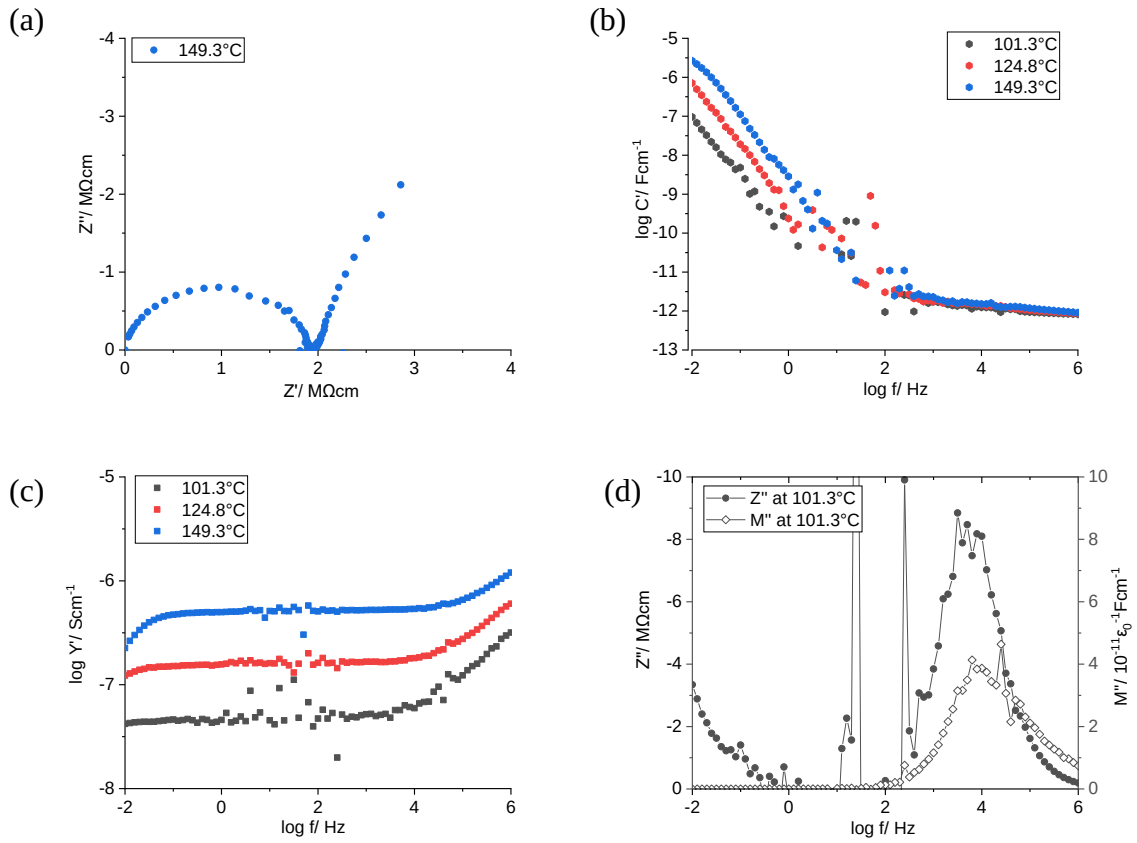

Fig 6.12. Impedance dataset for composition Li_4SiO_4:Li_3PO_4:LiF=40:05:55

(Synthesised at 800 °C, 10 hours, coated with Au, primary phase of Phase A)

(a) $Z^{''}$-$Z^{'}$ complex plane plot, spectroscopic plots of (b) capacitance C', (c) admittance Y', (d) $Z^{''}M^{''}$ at 101.3 °C

The impedance datasets for Phase S, γ-Phase S and Phase A, shown in Fig 6.10-6.12, show a typical ionic conductor impedance response. The impedance complex plane plots in (a), consist of a semicircle and a large spike, which corresponds to the high capacitance plateau in (b) indicating a significant sample-electrode capacitance and therefore, the ionic conduction in the sample. The capacitance plateaux at 10^{-12} F/cm in (b) are typical bulk response. There is no significant grain boundary plateau shown in spectroscopic capacitance plots. The log $Y^{'}$-log f plots in (c) show a distorted conductivity plateau over the range ~10^0-10^4 Hz with clear dispersions at both low and high frequency ends. The low frequency dispersion can be attributed to the sample-electrode interface, while the high frequency dispersion is the common

Jonscher Law behaviour. The Z'' peaks and M'' peaks in (d) are nearly coincident on the frequency scale but not perfect.

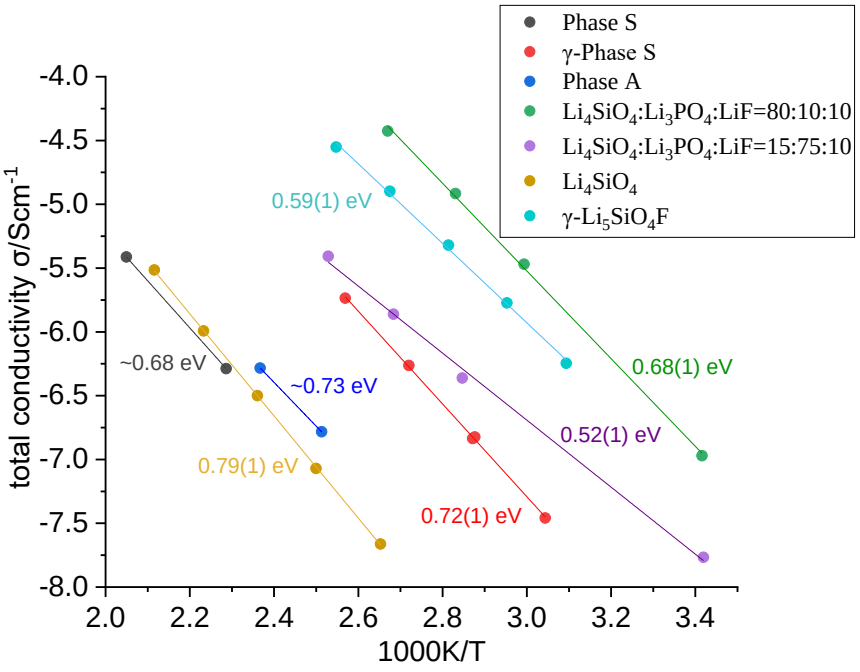

Fig 6.13. The Arrhenius plots for different compositions in the Li_4SiO_4-Li_3PO_4-LiF system

The Arrhenius plots in Fig 6.13 shows: (a) Phase S and Phase A only exhibit a poor ionic conductivity similar to bulk Li_4SiO_4; (b) γ-phase S show an ionic conductivity which is approximately 2 orders of magnitude lower than that of γ-Li_5SiO_4F; (c) the possible F-doped Li_3PO_4-Li_4SiO_4 solid solution has a promising ionic conductivity. In specific, the ionic conductivity at 573K of Li_4SiO_4, Li_3PO_4 and $Li_{3.5}P_{0.5}SiO_4$ are 2.5×10^{-6} S/cm, 1.2×10^{-8} S/cm and 2.5×10^{-3} S/cm, respectively [2]. Composition Li_4SiO_4:Li_3PO_4:LiF=80:10:10, with a main phase of Li_4SiO_{4ss}, Fig 6.3, has an ionic conductivity of ~8×10^{-2} S/cm at 573K, which is higher than those of γ-Li_5SiO_4F and $Li_{3.5}P_{0.5}SiO_4$; composition Li_4SiO_4:Li_3PO_4:LiF=15:75:10, with a main phase of Li_3PO_{4ss}, Fig 6.3, show an ionic conductivity of ~4×10^{-4} S/cm at 573K, which is ~ 1 order of magnitude lower than that of γ-Li_5SiO_4F. As the Li_3PO_4-Li_4SiO_4 solid solution has been well studied, the possible F-doping of that deserves further investigation.

6.2.3. Possible doping on Li_3PO_4 by LiF

As a previous study on possible anion doping of Li_4SiO_4 by LiF found the new phase Li_5SiO_4F [8], a similar doping study was conducted on Li_3PO_4. There are two possible mechanisms to dope Li_3PO_4 by LiF: (a) either partially replace O^{2-} by F^- in $Li_{3-x}PO_{4-x}F_x$, in which lithium vacancies will be created due to charge compensation; or (b) F^- may be directly doped in available sites in $Li_{3+y}PO_4F_y$, in which additional Li^+ is needed to maintain electrical neutrality.

Composition Li_4SiO_4:Li_3PO_4:LiF=0:90:10, synthesised at 750°C for 20 hours, show a single phase of Li_3PO_4, Fig 6.14, indicating the possibility to somehow dope Li_3PO_4 by LiF.

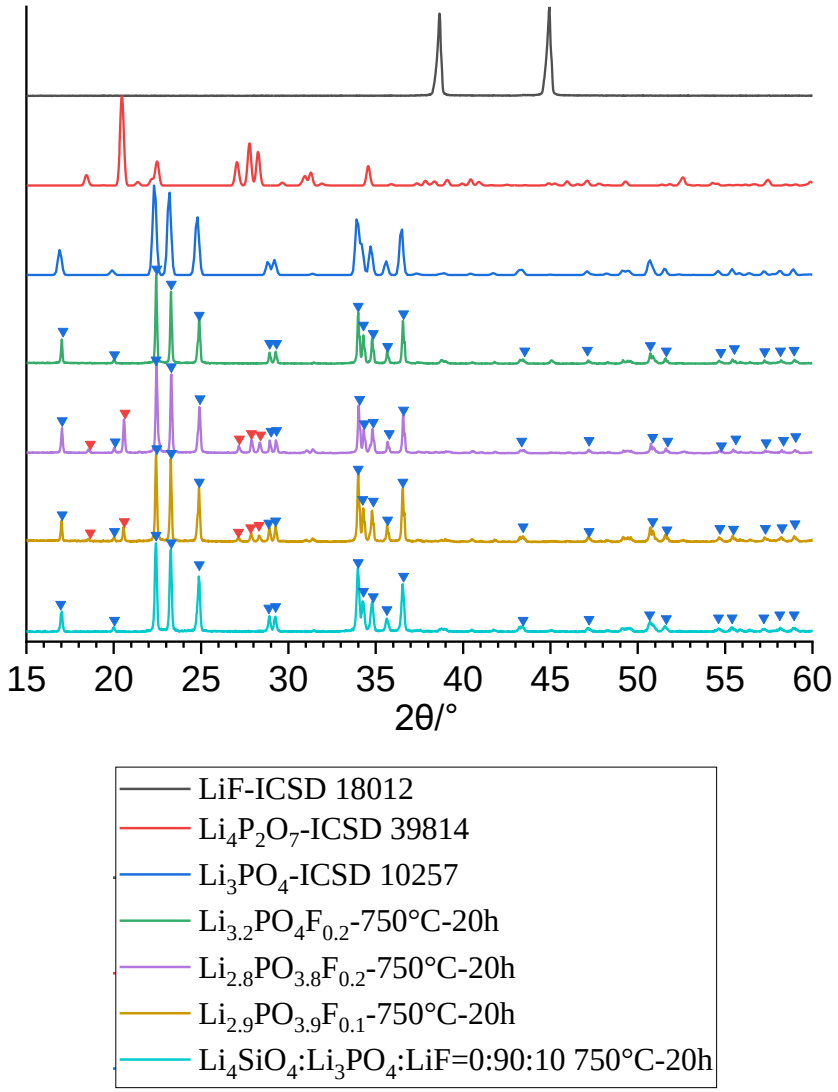

Fig 6.14. XRD results for some LiF doped Li_3PO_4 samples: $Li_{3-x}PO_{4-x}F_x$ samples show a mixture of Li_3PO_4 and $Li_4P_2O_7$ when x=0.1 and 0.2; $Li_{3+y}PO_4F_y$ shows only Li_3PO_4.

The XRD results by mechanism A, with x=0.1 and 0.2, Fig 6.14, show a mixture of Li_3PO_4 and $Li_4P_2O_7$. The amount of $Li_4P_2O_7$ increases with larger x value, which then show a clear secondary phase of $Li_4P_2O_7$ in x=0.2 sample.

The XRD result by mechanism B, with y=0.2, show a single phase of Li_3PO_4. There is no existence of LiF in the product, and there is no clear peak shift of Li_3PO_4 can be seen. Thus, it is hard to determine whether F^- has been successfully doped in Li_3PO_4 by mechanism B, but it probably indicates that there is no single phase exists on Li_3PO_4-LiF edge besides the two end members.

There is another doping possibility to replace $(PO_4)^{3-}$ by $(LiF_4)^{3-}$ [9], with a general formula will be $Li_{3+x}P_{1-x}O_{4-4x}F_{4x}$. The compositions by this mechanism will still on the Li_3PO_4-LiF join and there will be no lithium vacancy nor interstitial lithium.

References

[1] A. Khorassani, G. Izquierdo, and A. R. West, "The solid electrolyte system, Li_3PO_4-Li_4SiO_4" *Materials Research Bulletin*, vol. 16, no. 12, pp. 1561–1567, 1981.

[2] Y. Deng, C. Eames, J.-N. Chotard, F. Lalère, V. Seznec, S. Emge, O. Pecher, C. P. Grey, C. Masquelier, and M. S. Islam, "Structural and mechanistic insights into fast lithium-ion conduction in Li_4SiO_4– Li_3PO_4 solid electrolytes," *Journal of the American Chemical Society*, vol. 137, no. 28, pp. 9136–9145, 2015.

[3] A. D. Robertson, A. R. West, and A. G. Ritchie, "Review of crystalline lithium-ion conductors suitable for high temperature battery applications," *Solid State Ionics,* vol. 104, no. 1-2, pp. 1–11, 1997.

[4] Y. Wu, L. Ben, H. Yu, W. Qi, Y. Zhan, W. Zhao, and X. Huang, "Understanding the effect of atomic-scale surface migration of bridging ions in binding Li_3PO_4 to the surface of spinel cathode materials," *ACS Applied Materials & Interfaces,* vol. 11, no. 7, pp. 6937–6947, 2018.

[5] A. R. West and F. P. Glasser, "Preparation and crystal chemistry of some tetrahedral Li_3PO_4 -type compounds," *Journal of Solid State Chemistry,* vol. 4, no. 1, pp. 20–28, 1972.

[6] C. Keffer, A. D. Mighell, F. Mauer, H. E. Swanson, and S. Block, "Crystal structure of twinned low-temperature lithium phosphate," *Inorganic Chemistry,* vol. 6, no. 1, pp. 119–125, 1967.

[7] Y. Arachi, Y. Higuchi, R. Nakamura, Y. Takagi, and M. Tabuchi, "Synthesis and electrical property of $Li_{2-x}FeSi_{1-x}P_xO_4$ as positive electrodes by spark-plasma-sintering process," *Journal of Power Sources,* vol. 244, pp. 631–635, 2013.

[8] B. Dong, J. Yan, B. Walkley, K. K. Inglis, F. Blanc, S. Hull, and A. R. West, "Synthesis and characterisation of the new oxyfluoride Li^+ ion conductor, Li_5SiO_4F," *Solid State Ionics,* vol. 327, pp. 64–70, 2018.

[9] G. V. Zimina, M. Tsygankova, M. Sadykova, F. M. Spiridonov, V. V. Fomichev, and P. P. Fedorov, "Phase diagram of LiF-Li_3PO_4 system: A new mechanism of heterovalent anionic isomorphism," *MRS Advances,* vol. 3, no. 23, pp. 1309–1317, 2017.

[10] P. Gorai, H. Long, E. Jones, S. Santhanagopalan, and V. Stevanovic, "Defect chemistry of disordered solid-state electrolyte $Li_{10}GeP_2S_{12}$," *Journal of Materials Chemistry A,* vol. 2020, no. 07, 2019.

[11] J. Lee, W. Zhou, J. C. Idrobo, S. J. Pennycook, and S. T. Pantelides, "Vacancy-driven anisotropic defect distribution in the battery-cathode material $LiFePO_4$", *Physical Review Letters*, vol. 107, no. 8, 2011.

[12] S. Fop, K. S. McCombie, E. J. Wildman, J. M. Skakle, J. T. Irvine, P. A. Connor, C. Savaniu, C. Ritter, and A. C. Mclaughlin, "High oxide ion and proton conductivity in a disordered hexagonal perovskite," *Nature Materials*, vol. 19, no. 7, pp. 752–757, 2020.

[13] "MP-2133: ZnO (hexagonal, $P6_3mc$, 186)," *Materials Project*. [Online]. Available: https://materialsproject.org/materials/mp-2133. [Accessed: 01-Jan-2023].

Chapter 7 Conclusion and Discussion

7.1. Li_5SiO_4F

There is a more insightful study on Li_5SiO_4F in Chapter 3. α-Li_5SiO_4F and γ-Li_5SiO_4F were synthesised at 650-700 °C and at 750-775 °C, as suggested by previous research [1]. Beyond the previous report [1], there are several new findings for α-Li_5SiO_4F and γ-Li_5SiO_4F: (1) the possible subcells of the two polymorphs of Li_5SiO_4F have been determined for the first time. There are a ZnO-like hexagonal subcell of α-Li_5SiO_4F and a monoclinic subcell of γ-Li_5SiO_4F. Their supercell structure still needs further investigation. The geometry relationship between the subcell of two polymorphs are also seen between Phase B and γ-Phase B, in Chapter 5. The transition from hexagonal subcell of low temperature polymorph to orthorhombic (or slightly distorted monoclinic) subcell of high temperature polymorph may exist on a wider field of oxyfluoride material derived from ZnO structure.

(2) The DSC tests on Li_5SiO_4F indicated an incongruent melting of γ-Li_5SiO_4F at ~790°C, at which some of the liquid may volatilise. The impedance results showed clear evidence of a very thin layer of Li_4SiO_4 in γ-Li_5SiO_4F especially after long heat treatment at higher temperatures close to its possible melting temperature, which indicates loss of LiF by volatilisation. The Li_4SiO_4 layer had a capacitance value which was 2-3 orders of magnitude higher than a typical grain boundary response. This is not only an extended study on Li_5SiO_4F, but a good example to analysis impedance responses from different components by their capacitance and how to distinguish between a grain boundary response and a secondary bulk response.

(3) The impedance responses of same γ-Li_5SiO_4F pellet samples coated with either gold electrodes or silver electrodes were measured. A possible ion exchange between Li^+ and Ag^+ occurred from low temperatures, <70°C, while an electrochemical redox reaction occurred and became significant at high temperatures, >200°C. This should be a good example of how silver electrodes can react with Li^+ containing materials and lead to clear influence in impedance measurement.

(4) In equivalent circuit analysis on the bulk response of γ-Li_5SiO_4F, a circuit consists of R_1-C_1-CPE_1-R_0C_0 in parallel, in which R_0C_0 is the dipole element, gave a better fitting of its impedance results, which made Li_5SiO_4F a representative material with clear dipole effect in the bulk.

(5) The cation doping study of γ-Li_5SiO_4F, in Chapter 4, tried a series of cations with valence from +2 to +5. The possible doping mechanisms include either creating lithium vacancies or introducing interstitial lithium. The attempts to dope γ-Li_5SiO_4F had three groups of outcomes. Firstly, some cation candidates such as Al^{3+} and Ga^{3+} were successfully doped in γ-Li_5SiO_4F given by XRD results. However, the doped samples did not show a better ionic conductivity compared to undoped bulk γ-Li_5SiO_4F. The mechanism behind may deserve further investigation. So far, no doped sample with a better ionic conductivity compared to bulk γ-Li_5SiO_4F has been found. Further work may possibly focus on co-doping on Li_4SiO_4, such as Zn^{2+} and F^-. Secondly, most dopants gave a significant number of secondary phases in the product indicating an unsuccessful doping. Thirdly, some dopants lead to the synthesis of new phases and further research on different ternary phases systems form the Chapters 5-6 of this thesis.

7.2. New phases

(i) Zn doping of γ-Li_5SiO_4F lead to a very preliminary survey of compositions in the system Zn_2SiO_4-Li_4SiO_4-LiF, in section 4.2.9. There are already some evidences of possible new phases in $Li_{5-2x}Zn_xSiO_4F$ system and a possible solid solution between Li_2ZnSiO_4 (*a*:*b*=1:0) and Li_3ZnSiO_4F (*a*:*b*=1:1). As most of compositions in $Li_{5-2x}Zn_xSiO_4F$ showed the existence of LiF in the final product, further research on compositions with less LiF in Zn_2SiO_4-Li_4SiO_4-LiF may be interesting.

(ii) Four new phases have been synthesised and characterised in the ternary system: Li_2O-SiO_2-LiF, in Chapter 5. Phase B was prepared at the approximate stoichiometry Li_2O:SiO_2:LiF=47:28:25 by solid state reaction at ~750 °C. It shows a ZnO-type hexagonal subcell, and has a modest ionic conductivity of ~5.6×10^{-8} Scm^{-1} at 100 °C.

γ-Phase B appears to be a more ordered polymorph related to Phase B, that forms over a wide solid solution range. The crystal structure of γ-Phase B appears to have an orthorhombic subcell derived from that of hexagonal ZnO type cell and presumably involves an ordered arrangement of the cations and/or anions. Its ionic conductivity is ~1.1×10^{-6} Scm^{-1} at 100 °C.

Phases T and N have similar composition to previously-reported Li_5SiO_4F but significantly different XRD patterns and electrical properties. Phase T forms a solid solution within a narrow area in the Li_2O-SiO_2-LiF system but shows a poor ionic conductivity, similar to that of Li_4SiO_4. As yet, no composition giving single phase N has been found.

(iii) As discussed in Chapter 6, P doping of γ-Li_5SiO_4F lead to a general survey of the Li_3PO_4-Li_4SiO_4-LiF system, in which three possible new phases: Phase S, γ-Phase S and Phase A were found. Phase S was indexed on a ZnO-like hexagonal subcell, with a=3.08(1) Å and c=4.94(1) Å. γ-Phase S is closely related to Phase S and is probably a thermodynamically metastable phase which quickly decomposes/transforms to Phase A. Similar transitions can be seen on the representative β-t-γ transition of Li_3PO_4 [2]. Indexing results suggested either a monoclinic or an orthorhombic subcell for γ-Phase S and a monoclinic subcell for Phase A. Impedance results showed that Phase S and Phase A have only poor ionic conductivity similar to that of bulk Li_4SiO_4; γ-phase S shows an ionic conductivity which is approximately 2 orders of magnitude lower than that of γ-Li_5SiO_4F.

(iv) Some compositions that were studied in the Li_3PO_4-Li_4SiO_4-LiF system may be F^- doped Li_3PO_4-Li_4SiO_4 solid solution. Although there are limited number of compositions were prepared in this study, some compositions show promising ionic conductivity, for instance, composition Li_4SiO_4:Li_3PO_4:LiF=80:10:10 shows an ionic conductivity with ~10^{-4} Scm^{-1} at 100°C. A more general survey on F^- doped Li_3PO_4-Li_4SiO_4 solid solution require more further works.

Most of the new phases including Phase B, γ-Phase B, Phase T in Li_2O-SiO_2-LiF and Phase S, γ-Phase S in Li_3PO_4-Li_4SiO_4-LiF appear to have similar ZnO-like hexagonal subcells, which indicates a possible new family, discussed in detail in section 7.3. Most materials in this family of structures are non-stoichiometric and do not have simple cation:anion ratios. However, in most cases, the cation:anion ratio is slightly greater than 1 which means that the materials contain extra Li+ ions and these are responsible for the high levels of ionic conductivity as they presumably occupy interstitial sites in an interconnected conduction pathway. The specific conduction mechanism cannot be given now because of the unknown superstructures. The

possible further work should begin with the determination on the unit cells of the superstructures, either by single crystal XRD, or by selected area electron diffraction or by trial and error indexing of high quality XRD / neutron diffraction data, then use the available software to attempt solution of the crystal structures. Phase S, γ-Phase S in Li_3PO_4-Li_4SiO_4-LiF in Chapter 6 may be P-doped materials similar to the phases shown in Li_2O-SiO_2-LiF in Chapter 5. Further investigation on the possible solid solution limit and different phase(s) with varied P composition may be worth trying. At this stage, these possible new fluoro-LISICON materials still need further modifications to meet the basic requirements for ionic conductivity with $>10^{-3}$ Scm^{-1} at room temperature to be commercially feasible in the real world [1]. However, this research discovered a possible new family of solid electrolyte material and suggested possible further anion-doping in similar materials in the future.

7.3. Structural considerations: ZnO-based subcell structures

The general investigations on ternary phases in the systems: Li_2O-SiO_2-LiF and Li_3PO_4-Li_4SiO_4-LiF, has shown the formation of several possible new phases. Although their possible formulae are rather complicated, we have confidence in their composition with the 0 that their Li contents may be slightly in error. Their detailed crystal structures are not yet known, but there is clear evidence that similar hexagonal subcells derived from ZnO may be a common feature, especially for the low-temperature structures, α-Li_5SiO_4F and Phase B. The high temperature structures such as γ-Li_5SiO_4F and γ-Phase B may have subcell that are orthorhombic or monoclinic distortion of the hexagonal subcells. There is a clear geometric relationship between the subcells of low/high-temperature structures.

Possibly, these new phases can be categorised into a general β/γ-family of LISICON materials. Generally, LISICONs cover a wide range of oxides with two polymorphs, a low temperature β-form and a high temperature γ-form [2-3]. The typical oxide families include (a) Li_3AO_4: A=P, As, V, Cr, Mn; (b) XYO_2: X=Li, Na and Y=Al, Ga; and some of the (c) A_2BCO_4 material: A=Li, Na, B= B = Be, Mg, Mn, Fe, Co, Zn, Cd and C = Si, Ge [3].

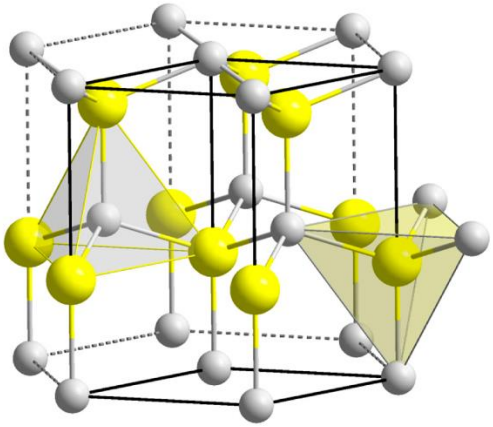

Figure 7.1. ZnO wurtzite, Zn cations shown in yellow, O atoms shown in grey, tetrahedral coordination for Zn is shown in light yellow [4]

In a structure consisting of hcp oxide ions, there are two sets of tetrahedral sites which have their triangular base in one oxide layer and the apex in the adjacent oxide layer. The two sets of sites may be distinguished by whether their apex is the layer above or the layer below, giving rise to the nomenclative T_+ and T_-. In the structure shown in Fig 7.1, a ZnO_4 tetrahedron is shown with its apex in the layer below. All other ZnO_4 tetrahedra therefore have the same orientation, which are called T_- sites. The β-structures are derived from wurtzite ZnO, in Fig 7.1, with different cation ordering sequences. As yet, there are no known examples of LISICONs that have a fully disordered cation arrangement and a simple hexagonal cell. A cation disordered β-structure would have a hexagonal close packing sequence, -ABABAB-, with alternating close packed O atoms layer and ordered cations layer in one set of the tetrahedral sites. The constitution of the second oxygen-cation layers is the same as the first layers, but with different orientation and position. Each cation and 4 oxygen anions form a MO_4 tetrahedron which is connected to other three tetrahedra by sharing its corners [3-4]. The c unit cell dimension in these hexagonal cells spans two oxygen layers and two cation layers [4]. The representative β-family materials include (a) ZnO and BeO; (b) β-$NaXO_2$, X=Fe, Ga and Al; (c) β_{II}-Li_3PO_4, β_{II}-Li_3AsO_4, and β_{II}-Li_3VO_4; and (d) β_{II}-Li_2MXO_4, such as) β_{II}-Li_2BeSiO_4 [3-4].

The family of γ-structures also has hexagonal close-packed oxygen layers [5]. For available tetrahedral sites, three anions, like O atoms, build the base of the tetrahedron on the close

packed layer. If the tetrahedron has the vertex pointing upwards along the stacking axis, the site is T_+; while the tetrahedron with a vertex oriented downward is T_- [6]. The cations in γ-structure are equally distributed over both T_- and T_+ sites. As there are variable full/empty sequences for these tetrahedral sites, theoretically, there is a large family of possible single γ-structures [4]. Instead of having only corner-sharing tetrahedra in the β-structures, there are edge-sharing tetrahedra in γ-structures. For instance, every LiO_4 tetrahedra shares an edge with AlO_4 tetrahedra in γ-$LiAlO_2$ [4]. The representatives of the γ-family materials include (a) γ-$LiAlO_2$, γ-$NaAlO_2$ and γ-$NaFeO_2$; (b) γ_{II}-Li_3XO_4, X=P, V and As; and (c) γ_{II}-Li_2MXO_4, such as γ_{II}-Li_2ZnSiO_4 [3-4].

The β-γ transition in the same composition may be viewed as cation migration through intact oxygen layers [4]. There may also exist an intermediate phase, T, in the β-T-γ transition, in some materials such as Li_3PO_4, Li_3AsO_4 and Li_2MgGeO_4. The atomic movements involved in both β-T and T-γ transitions are necessary for the complete transition [4].

(a)

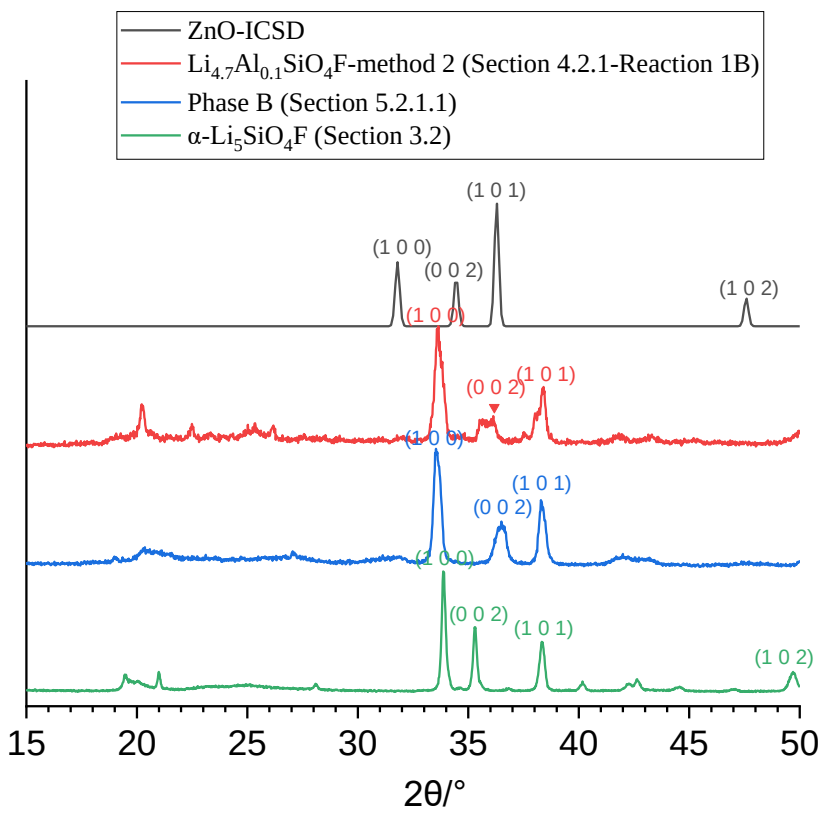

(b)

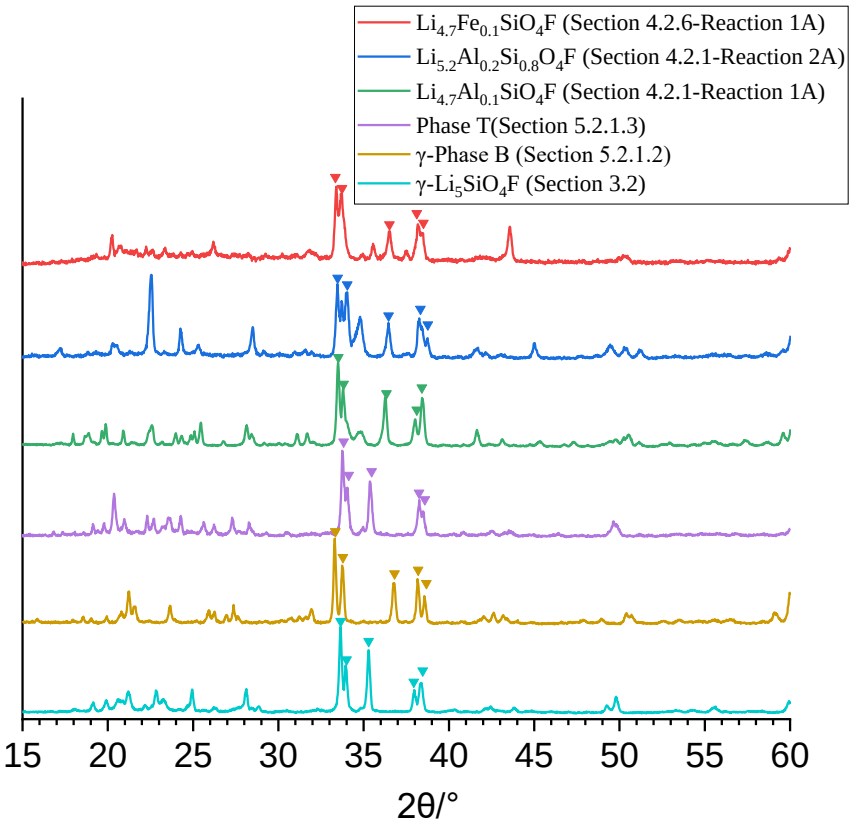

Fig 7.2. Some compositions may belong to β-/γ- families: Possible β-phase in (a) and possible γ-phase with characteristic peaks marked in (b)

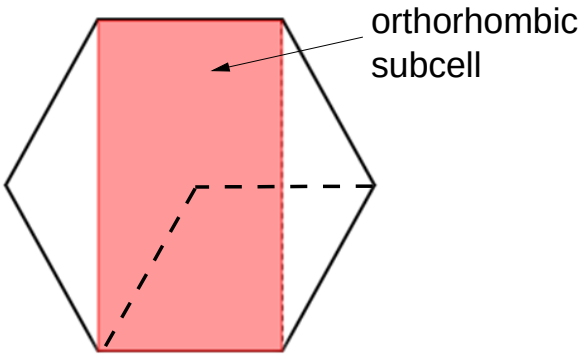

Fig 7.3. Orthorhombic subcell derived from hexagonal close packed layers.

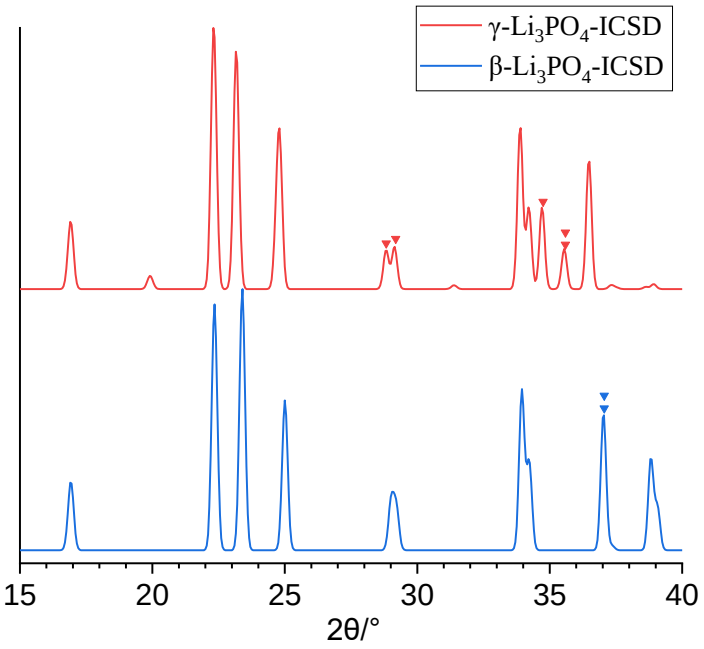

Fig 7.4. Standard patterns of β-/γ-Li_3PO_4, peaks with single triangle are additional supercell lines in γ while the shift of (0 0 2) peak is marked by double triangles.

XRD data for the possible β-/γ- materials in this study are summarised in Fig 7.2. Two polymorphs Phase B and γ-Phase B are similar to previously reported α/γ-Li_5SiO_4F. The phase transition is charactered by two pairs of the peak splitting at 33-34 and 38-39°/2θ and the shift of the (0 0 2) peak at 35-37.5°/2θ. Both low temperature phases, Phase B and α-Li_5SiO_4F have a hexagonal subcell, Table 5.3. Although their supercell structures are rather complex to be categorised as typical β-structure, their subcell structure may possibly belong to β-family, in which cations, Li^+ and Si^{4+}, are randomly distributed in one set of the tetrahedral sites. Whether F can replace some of the oxygen atoms in MO_4 tetrahedra to give MO_3F; or isolated F atoms can form LiF_4, or SiF_4 somewhere in the close packed layers are unknown. The preliminary hypothesis is that the corresponding high temperature phases, γ-Li_5SiO_4F and γ-Phase B have a similar orthorhombic subcell (slightly distorted in γ-Li_5SiO_4F, giving a monoclinic subcell), which may be built on the hexagonal close packed layers, Fig 7.3. Cations in these two γ-family phases possibly become ordered and occupy both T_+ and T_- sites, resulting in expanded c axis, thus a reduced 2θ angle of the (0 0 2) peak. The ordering of cations possibly leads to a complex supercell structure, giving by the lines at low 2θ angles in both γ-Li_5SiO_4F and γ-Phase B. Similar circumstances can be seen in Li_3PO_4, in which the transition from β to γ corresponds

to a shift of the peak marked with double triangles, Fig 7.4 and the presence of additional supercell lines marked with single triangles.

Although the basic hexagonal subcell of Phase T has not been clarified, its possible (0 0 2) peak is at lower 2θ angle compared to Phase B/γ-Phase B, indicating a larger *c* parameter value for its hexagonal subcell.

Some possible other new phases were observed during the attempts to dope Li_5SiO_4F, usually shown as a mixture with other phases. It is too early to speculate on their structure before obtaining single phase samples, however, generally, a (0 0 2) subcell peak at relevantly lower 2θ angles in the same or similar compositions may indicate a γ-structure as the occupancy of cations in a γ-family over both tetrahedral sites is more complicated and often results in a larger parameter *c* value. In $Li_{4.7}Al_{0.1}SiO_4F$ and $Li_{4.7}Fe_{0.1}SiO_4F$, Fig 7.2 (b), several lines between the two pairs of doublet peaks at ~35-38°/2θ may indicate either a phase mixture, or more likely an unknown γ-type phase.

7.4. Possible anion mixing in Li_5SiO_4F.

In the anion doping study of Li_3PO_4 by LiF, in section 6.2.3, the possible compensation mechanisms include either (i) the replacement of O^{2-} by F^-, $Li_{3-x}PO_{4-x}F_x$, or (ii) direct insertion of F^- into available sites, $Li_{3+y}PO_4F_y$. A recent study suggested a new possible doping mechanism, (iii) in which $(PO_4)^{3-}$ tetrahedra are replaced as a group by $(LiF_4)^{3-}$ without any interstitial lithium or lithium vacancy creation [6]. The promising aspects of this new doping mechanisms are (a) the compositions from doping mechanisms (i) and (ii) are not on the Li_3PO_4-LiF join, while mechanism (iii) $Li_3(PO_4)_{1-x}(LiF_4)_x$ is; (b) mechanisms (i) and (ii) do not have a clear conclusion on whether F^- is replacing O^{2-} in $(PO_4)^{3-}$ tetrahedra to give $(PO_{4-x}F_x)$ with less negative charge, which possibly further leads to lithium vacancies for charge balance, or F^- is isolated from PO_4 tetrahedra. Thus, this isovalent double-substitution method deserves further investigation.

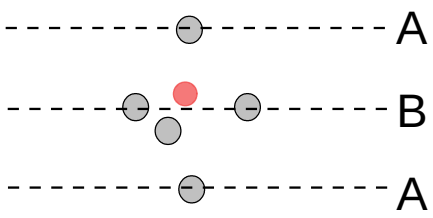

Fig 7.5. The possible pentagonal bipyramid structure in Li_5SiO_4F, O^{2-} in grey, Li^+ in red

The low temperature structures of Li_5SiO_4F and other possible new phases appears to have a subcell derived from ZnO, in which there are isolated SiO_4 tetrahedra formed between alternative -ABABA- layers. A preliminary hypothesis of the crystal structure of Li_5SiO_4F is that it contains a pentagonal bipyramid unit, Fig 7.5. The four O atoms in SiO_4 tetrahedra with another O atom formed a bipyramid and one of the O sites may be occupied by F, thus giving a $(SiO_4F)^{5-}$ bipyramid. By sharing common corner(s) and/or edge(s) with other bipyramids, or possibly F^- can occupy more than 1 O site, the composition ratio between Si, O and F may be more flexible. This is a completely new model for Si with a coordination number of 5 instead of 4 in the common SiO_4 tetrahedra. The existence of $(SiO_4F)^{5-}$ bipyramid would also fit very well with the formula of Li_5SiO_4F. Although we have confidence in the rough compositions of these new phases in the ternary phase diagram Li_2O-SiO_2-LiF, there remains uncertainty of losing some Li^+ and F^- during high temperature synthesis. The composition of Phase B, Li_2O:SiO_2:LiF=47:28:25, gives its formula, $Li_{119}Si_{28}O_{103}F_{25}$. Based on the pentagonal bipyramid model, there is a possible simplified formula for Phase B, $3Li_2O{\cdot}2SiO_2{\cdot}2LiF$, which possibly consists of two different polyhedra: SiO_4 tetrahedra and $Si(O,F)_5$ dipyramid. The $(SiO_4F)^{5-}$ bipyramid is just a hypothetical model at this stage, but it offers a new Si-O structure with a coordination number of 5, which may be testified and accepted in further investigations.

7.5. Conclusions and potential future work.

In summary, in order to find potential solid state electrolyte candidates, a series of materials had been prepared by solid state synthesis method and further investigated with a set of technologies: phase determination by XRD and/or STOE with PDF-4 software and ISCD database; crystal structure analysis by indexing with WinXpow software using the Louer's

algorithm (DICVOL); composition analysis by XRF; melting behaviours by DSC; and microstructure and electrical properties analysis by impedance measurement and equivalent circuit analysis.

There are several new findings summarised as follows:

(a) Extended study on Li_5SiO_4F:

(1) Validation of Synthesis Method: The previously reported synthesis method of two polymorphs of Li_5SiO_4F [2] has been testified (section 3.2).

(2) Incongruent Melting Behaviour: An incongruent melting of γ-Li_5SiO_4F probably at ~790°C was identified (section 5.2.1.2.2).

(3) Formation of Li_4SiO_4 Layer: After prolonged heat treatment, a thin layer of Li_4SiO_4 was observed in γ-Li_5SiO_4F sample, exhibiting a capacitance approximately 10^2 times larger than a typical grain boundary, highlighting the importance of considering fluorine sustainability in processing F-containing materials processing (section 3.2.2.4). It can be a representative case of how impedance spectroscopy is useful in interpreting different electrical regions, which commonly include bulk, grain boundary and sample-electrode responses, especially in investigations on electroceramics.

(4) Dipole Effect: a clear dipole effect in bulk γ-Li_5SiO_4F was proved by fitting its impedance results to an equivalent circuit consists of a common RC-CPE circuit and a R_0C_0 dipole element in parallel (section 3.3.2.1). When dipole effect exists in bulk material, the main differences in impedance spectroscopy include a slightly higher admittance $Y^{'}$ value against frequency and a broadened $M^{''}$ peak at high frequency end instead of a standard Debye-like peak. Similar dipole effect is also shown in yttria-stabilised zirconia and probably in other electroceramics, it may worth further investigating how the existence of dipole effect varies the bulk response and wider electrical properties of materials.

(5) Electrode Influence: Impedance responses varied significantly between γ-Li_5SiO_4F pellets coated with Au and Ag electrodes, indicating that Ag electrodes may not be suitable for Li-containing materials due to the Ag^+-Li^+ exchange near sample-electrodes interface which may also happened in Na-contained materials especially at high temperatures at which significant electrochemical redox reactions happen (sections 3.3.1.1-3.3.1.2)..

(6) Cation Dopants: Different cation dopants with valence from +2 to +5 have been tried on parent γ-Li_5SiO_4F. Li_5SiO_4F can only be partially doped by Al^{3+} and Ga^{3+}, with no improvement on ionic conductivity, the mechanisms behind that are still unclear (Chapter 4). Other cation candidate cannot be doped into Li_5SiO_4F either leaving a clear secondary phase(s) or leaving a completely different main phase(s) instead of Li_5SiO_4F nor Li_4SiO_4 which lead to a more general survey on other ternary phases systems (Chapters 5-6). Further research can focus on possible co-doping methods by different cations or possible anion-doping by partially replace F^- or O^{2-} by other halide ions like Cl^- or N^{3-}.

(7) Subcell Structures: α-Li_5SiO_4F possibly has a hexagonal subcell with *a*=3.0539(9) Å and *c*=5.074(4) Å; while γ-Li_5SiO_4F has a monoclinic subcell (or regarded as a slightly distorted orthorhombic subcell) with *a*=3.078(2) Å, b=5.260(3) Å, *c*=5.067(4) Å and β=90.69(9) ° (section 5.2.1.2).

(8) Possible new Si-O Structure: There is a hypothesis that Li_5SiO_4F may contain a $(SiO_4F)^{5-}$ pentagonal bipyramid unit, which offers a new Si-O structure with a coordination number of 5 (section 7.4). Further research, for example, neutron diffraction may testify it.

(9) Possible multiple new phases: during the Zn^{2+} doping attempt on Li_5SiO_4F, there are at least 4 possible new phases, which named as Phases L, M, H and HH with a different Li:Zn ratio, have been observed in XRD results (section 4.2.9). At this stage, most of the compositions contained a small amount of LiF in the final product, further investigations probably on ternary systems between Li_4SiO_4-Zn_2SiO_4-LiF may testify the possibility to dope $Li_{4-2x}ZnSiO_4$ solid solution by LiF in which good Li-ion conductor may exist.

(b) a series of possible new oxyfluoride phases:

In the general survey in different ternary phases systems, this research found many possible new phases: Phase B, γ-Phase B, Phase N and Phase T in Li_2O-SiO_2-LiF system (Chapter 5). Phase B appeared to be the low-temperature polymorph with a fixed composition while γ-Phase B appeared to be the high-temperature polymorph which can form a solid solution within a certain range. Phase T formed a solid solution roughly between Phase B and Li_5SiO_4F. The single phase of Phase N had been found yet. Phase S, γ-Phase S and Phase A were found in Li_4SiO_4-Li_3PO_4-LiF system (Chapter 6). Phase S seemed to be the low temperature polymorph; γ-Phase S seemed to be a metastable intermediate phase which easily transformed in Phase A.

The stoichiometric formulae for these new phases have not been fully determined, while their detailed supercell structures are still uncertain. However, based on the preliminary study on their XRD and impedance results, some commonalities and differences can be concluded as follows:

(1) There are some similarities in their possible subcell structures: (i) the low temperature phases in different systems including Phase B, α-Li_5SiO_4F, Phase S show hexagonal subcells similar to ZnO. These hexagonal subcells have similar lattice parameter *a* value but varied parameter *c*. (ii) the high temperature phases including γ-Phase B, Phase T, γ-Li_5SiO_4F and γ-Phase S show similar orthorhombic subcell with similar lattice parameters *a* and *b* values but different lattice parameter *c* value (γ-Li_5SiO_4F has a distorted monoclinic subcell with β=90.69(9)°). (iii) There is a clear geometric relationship between the hexagonal subcells from low temperature phases and the orthorhombic subcells from high temperature phases: $a_{orthorhombic}$ equals $a_{hexagonal}$, $b_{orthorhombic}$ equals $\sqrt{3}$ $a_{hexagonal}$, $c_{orthorhombic}$ equals $c_{hexagonal}$ and orthorhombic subcells have a doubled lattice volume of ~80 $Å^3$ compared to those of hexagonal subcells with ~40 $Å^3$, which could be suitable for a mixture of 4 anions: O^{2-} and F^-. This is the first time the subcell structure of two polymorphs are related geometrically, similar circumstances may also happen in a wider field of materials.

(2) As the subcell structures of these new phases were regarded to be commonly derived from the same ZnO-type unit, they can be categorised into a wider β/γ-family of LISICON materials as discussed in section 7.3. The easiest way to distinguish them is the position of their (0 0 2) peaks when indexing their XRD results, which directly determine the value of the parameter *c* value. Generally, in typical β-type materials, cations only occupy one set of the tetrahedral sites. The low temperature phases (Phase B, Phase S and α-Li_5SiO_4F), whose subcell structures were categorised in β-family, may have Li^+ and Si^{4+} (probably partial P^{5+} in Phase S) randomly settled in T_+ sites. On the other hand, the high temperature phases (γ-Phase B, Phase T, γ-Li_5SiO_4F and γ-Phase S), whose subcell structures were categorised in γ-family, may have ordered cations in both T+ and T- sites, resulting in expanded *c* axis, thus a reduced 2θ angle of the (0 0 2) peak in their XRD. The ordering of cations possibly leads to a complex supercell structure, leading to different peaks in low 2θ angle regions in their XRD. Further investigation requires more detailed studies on their crystal structure, especially their supercell structures. Beyond the current hypothesis on the distribution of their cations, the main uncertainty is the position of F^- in these oxyfluoride phases, whether F^- can replace some O^{2-} in MO_4 tetrahedra

to give MO_3F; or isolated F^- can form LiF_4, or SiF_4 somewhere in the close packed layers deserve further research.

(3) As the original purpose of this study is to find some potential solid state electrolyte materials, the ionic conductivity of these new oxyfluoride phases with ~10^{-8}-10^{-6} S/cm at room temperature, is not high enough to be possibly used in future commercial market which commonly requires an ionic conductivity of >10^{-3} S/cm at ambient temperature. However, there remains a wide possibility to dope them with different cations or anions.

References

[1] J. Janek and W. G. Zeier, "Challenges in speeding up solid-state battery development," *Nature Energy*, vol. 8, no. 3, pp. 230–240, 2023.

[2] B. Dong, J. Yan, B. Walkley, K. K. Inglis, F. Blanc, S. Hull, and A. R. West, "Synthesis and characterisation of the new oxyfluoride Li^+ ion conductor, Li_5SiO_4F," *Solid State Ionics*, vol. 327, pp. 64–70, 2018.

[3] A. R. West and F. P. Glasser, "Crystallisation of lithium zinc silicates," *Journal of Materials Science*, vol. 5, no. 7, pp. 557–565, 1970.

[4] A. R. West, "Crystal Chemistry of some tetrahedral oxides," *Zeitschrift für Kristallographie*, vol. 141, no. 5-6, pp. 422–436, 1975.

[5] M. A. Borysiewicz, "ZnO as a functional material, a review," *Crystals*, vol. 9, no. 10, p. 505, 2019.

[6] A.R. West Tetrahedral and octahedral sites in '*Solid State Chemistry and Its Applications, 2th edition*'. John Wiley & Sons. West Sussex, pp.26-28.

[7] G. V. Zimina, M. Tsygankova, M. Sadykova, F. M. Spiridonov, V. V. Fomichev, and P. P. Fedorov, "Phase diagram of LiF-Li_3PO_4 system: A new mechanism of heterovalent anionic isomorphism," *MRS Advances*, vol. 3, no. 23, pp. 1309–1317, 2017.